Skeletal muscles facilitate all types of human movement through contraction, which generates force. Muscle characteristics regarding the internal architecture or external shape can be linked to the muscle's force-generating capacities. Therefore, experimental assessment of such characteristics can provide valuable insights into the muscle's functionality. This thesis presents novel methods for the controlled acquisition and 3D reconstruction of such muscle characteristics, e.g., muscle volume, length, cross-sectional area and pennation angle. A key contribution is the development and validation of an automated 3D ultrasound system for enabling controlled and reproducible ultrasound data acquisition. Moreover, an image processing algorithm is developed and employed to compute the fascicle direction for each volume element derived from ultrasound images of the tibialis anterior muscle. This methodology enables the determination of the pennation angle in three dimensions and allows for the examination of architectural characteristics of the muscle in high contraction levels. Furthermore, a methodology for the acquisition of volumetric ultrasound data of the tibialis anterior muscle during dynamic movement and an algorithm for 3D reconstruction of the collected dynamic images are presented. This methodology enables the investigation of shape changes of the tibialis anterior during dynamic movement. The methods introduced in this thesis provide a novel way to investigate muscle architecture and contraction behavior, yielding valuable additional information about muscle functionality.

Annika Sahrmann

ISBN 978-3-946412-13-7

A. Sahrmann

Automated 3D Ultrasound Imaging of Skeletal Muscle

CBM-14 (2024)

Automated 3D Ultrasound Imaging for Investigating Skeletal Muscle in Static and Dynamic Conditions

Annika Sahrmann

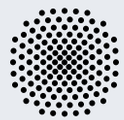

vorgelegt an der
Universität Stuttgart

Automated 3D Ultrasound Imaging for Investigating Skeletal Muscle in Static and Dynamic Conditions

Von der Fakultät Bau- und Umweltingenieurwissenschaften
der Universität Stuttgart
zur Erlangung der Würde eines Doktor-Ingenieurs (Dr.-Ing.)
genehmigte Abhandlung

Vorgelegt von

Annika Stephanie Sahrmann, M.Sc.

aus Waiblingen

Hauptberichter:	Prof. Oliver Röhrle, Ph.D.
Mitberichter:	Prof. Dr. Tobias Siebert
	Prof. Thor Besier, Ph.D.

Tag der mündlichen Prüfung: 19. April 2024

Institut für Modellierung und Simulation Biomechanischer Systeme
der Universität Stuttgart
2024

Report No.: CBM-14 (2024)
Institute for Modelling and Simulation of Biomechanical Systems
Continuum Biomechanics and Mechanobiology Research Group
University of Stuttgart, Germany, 2024

Editor:
Prof. O. Röhrle, PhD

University of Stuttgart
Institute for Modelling and Simulation of Biomechanical Systems
Continuum Biomechanics and Mechanobiology Research Group
Pfaffenwaldring 5a
70569 Stuttgart, Germany

ISBN 978-3-946412-13-7
(D 93 – Dissertation, Universität Stuttgart)

Declaration of Originality

I hereby declare that this thesis and the work reported herein was composed by and originated entirely from me. Information derived from the published and unpublished work of others has been acknowledged in the text and references are given in the list of sources.

Stuttgart, June 2024

Annika Stephanie Sahrmann

Acknowledgements

The work presented in this thesis was carried out between 2019 and 2024 during my time as a research assistant at the Institute for Modelling and Simulation of Biomechanical Systems. Many people have contributed to this work in various ways throughout this journey, and I am very grateful to all of them.

I would like to begin by expressing my gratitude to my supervisor, Prof. Oliver Röhrle, for affording me the opportunity to conduct research for my Ph.D. in this environment. I appreciate your advice, guidance and insights, and I am thankful for your trust in me by giving me the freedom to realize my own ideas throughout my Ph.D. time.

I would like to thank Prof. Tobias Siebert and Prof. Thor Besier for their efforts in co-chairing my Ph.D. examination. Tobias, I enjoyed our discussions and the insights you have provided regarding my work on muscle physiology. I am convinced that they have added a lot of value to my work. Thor, I am happy that I got the opportunity to conduct research in your group at the Auckland Bioengineering Institute on two occasions during my masters and Ph.D., which were both great and enriching experiences.

Another huge thank you goes to Leonardo Gizzi for his incredible support and patience with my experiments in the lab. Leo, I am so grateful for your guidance in setting them up. I am not sure I would have been able to do this without your help.

Furthermore, I am grateful to Geoffrey Handsfield for his advisory support throughout my Ph.D. time, which included fruitful discussions on data processing, imaging and muscle biomechanics, and also solutions for challenging paper reviews. Geoff, I am glad that we maintained our regular meetings and stayed in touch, even after my two research stays in New Zealand.

I am happy that I was able to work in such a pleasant group with so many great colleagues at CBM, who helped me a lot through the ups and downs of my Ph.D. time. I really appreciated the group atmosphere, where I could discuss problems with my colleagues, if I was stuck on a topic (this applies to both the good old times in 4F and later in 5A, where I was friendly adopted). I also appreciated all of our little (or bigger) coffee and snack breaks, where we could often just switch off, but where sometimes new project ideas were born as well.

A big thank you goes to all my friends for all the great moments where we enjoyed life outside of work and for being there and listening patiently. Scarlett, I admire that you volunteered to proofread parts of this thesis. Further, thanks to everyone who participated in my studies (Chrissi and colleagues) spending hours in the windowless lab, so that I could collect data.

Ultimately, I want to express my gratitude to my family for all their support, understanding and love. There are simply no words to describe how deeply thankful I am for having you all. Andreas, I am especially thankful for your never-ending support and your everlasting patience with me (which probably was not always easy), and that you always believed in me.

Stuttgart, June 2024 Annika Sahrmann

Contents

Abstract v

Deutsche Zusammenfassung vii

Nomenclature xi

1 Introduction 1
- 1.1 Motivation . . . 1
- 1.2 State of the Art . . . 5
  - 1.2.1 Imaging-Based Assessment of Muscle Volume and Architecture . . . 5
  - 1.2.2 Automated and Force-Integrated Ultrasound Systems . . . 9
- 1.3 Thesis Outline . . . 12
- 1.4 List of Publications . . . 13

I Physiological and Technological Background 15

2 Fundamentals of the Musculoskeletal System 17
- 2.1 Hierarchical Structure of Skeletal Muscles . . . 17
- 2.2 Muscle Contraction . . . 19
  - 2.2.1 Excitation-Contraction Coupling . . . 19
  - 2.2.2 Force-Length and Force-Velocity Relationship . . . 20
- 2.3 Skeletal Muscle Architecture . . . 21
- 2.4 Tibialis Anterior Muscle . . . 22

3 Technological Background 25
- 3.1 General Principles of Medical Ultrasound Imaging . . . 25
  - 3.1.1 Basic Physics of Ultrasound Imaging . . . 25
  - 3.1.2 Ultrasound Probe . . . 27
  - 3.1.3 Imaging Modes . . . 29
- 3.2 3D Ultrasound Imaging . . . 29
  - 3.2.1 3D Ultrasound Data Acquisition . . . 30
  - 3.2.2 Spatial Calibration . . . 32
  - 3.2.3 Temporal Calibration . . . 36
  - 3.2.4 Volume Reconstruction . . . 36
  - 3.2.5 3D Visualization . . . 38
- 3.3 Motion Capture . . . 40

II The Automated 3D Ultrasound System 43

4 Development of an Automated 3D Ultrasound System 45
4.1 System Preparation . . . 45
4.1.1 Ultrasound . . . 45
4.1.2 Motion Capture . . . 46
4.2 The Automated 3D Ultrasound System . . . 47
4.2.1 Functional Requirements . . . 47
4.2.2 System Overview . . . 48
4.2.3 Force Control . . . 50
4.2.4 Device Control . . . 51
4.2.5 Synchronization . . . 53
4.2.6 System Calibration . . . 53
4.2.7 Coordinate Transformations . . . 58
4.3 3D Reconstruction . . . 60
4.3.1 Reconstruction Volume Determination . . . 60
4.3.2 Filling the Volume . . . 62
4.3.3 Data Export . . . 64
4.3.4 Segmentation . . . 64
4.4 3D Reconstruction using Stradwin . . . 64
4.5 Volume Analysis . . . 65

5 Validation and Application of the Automated 3D Ultrasound System 67
5.1 Ultrasound Phantoms . . . 67
5.2 Methods . . . 68
5.2.1 Experimental Setup . . . 68
5.2.2 3D Reconstruction and Image Segmentation . . . 69
5.2.3 Statistical Analysis . . . 70
5.3 Results . . . 70
5.3.1 Volume and Length . . . 72
5.3.2 Reproducibility . . . 73
5.4 Discussion . . . 79
5.4.1 Operator Dependency . . . 79
5.4.2 Combination with Additional Techniques . . . 80
5.4.3 Safety . . . 80
5.4.4 Contact Force . . . 81
5.4.5 Limitations . . . 81
5.5 Conclusion . . . 81

III Determining Skeletal Muscle Parameters in Static and Dynamic Conditions 83

6 Fascicle Detection from 3D Ultrasound Imaging 85
6.1 Methods . . . 85
6.1.1 Fascicle Phantom . . . 85

6.1.2 Experimental Setup . . . 87
6.1.3 3D Reconstruction and Image Segmentation . . . 88
6.1.4 Fascicle Detection Algorithm . . . 88
6.1.5 Angle Determination . . . 90
6.1.6 Statistical Analysis . . . 90
6.2 Results . . . 92
6.2.1 Phantom Study . . . 92
6.2.2 Muscle Volume Reconstruction . . . 92
6.2.3 Muscle Fascicle Reconstruction . . . 94
6.3 Discussion . . . 100
6.3.1 Muscle Volume . . . 100
6.3.2 Pennation Angle . . . 100
6.3.3 Limitations/Outlook . . . 103
6.4 Conclusion . . . 103

7 Dynamic 3D Ultrasound Imaging of the Tibialis Anterior 105
7.1 Methods . . . 105
7.1.1 Experimental Setup . . . 105
7.1.2 Angle Intervals . . . 108
7.1.3 3D Reconstruction and Image Segmentation . . . 111
7.1.4 Ellipsoid Prediction . . . 111
7.1.5 Statistical Analysis . . . 113
7.2 Results . . . 113
7.2.1 Muscle Volume and Length . . . 113
7.2.2 Cross-Sectional Area . . . 113
7.3 Discussion . . . 119
7.3.1 Comparison with a Simple Ellipsoidal Muscle Model . . . 119
7.3.2 Comparison of 2D and 3D Ultrasound . . . 119
7.3.3 Impact of Movement Condition on CSA . . . 120
7.3.4 Limitations . . . 121
7.4 Conclusion . . . 121

8 Discussion & Outlook 123
8.1 Potentials and Challenges . . . 123
8.2 Outlook . . . 127

A Experimentally Determined Force Values 129

B Setup of a 3D Freehand Ultrasound Workflow 131

C Pennation Angles over Resting Position Muscle Length 135

Bibliography 139

Abstract

Through contraction, skeletal muscles facilitate all kinds of human movement, such as walking, running, standing, speaking, or even breathing. Muscle contraction enables these movements by generating force. A skeletal muscle is made up of many fibers, which are bundled into structures called fascicles. In some muscles, the fascicles are oriented in line with the muscle's direction of contraction, from the muscle's origin to its insertion, whereas in other muscles, the fascicles are arranged at an angle to its line of action, which is referred to as a pennate muscle. The internal arrangement of fibers is called muscle architecture. Muscle characteristics regarding the internal architecture or external shape can be linked to the muscle's force-generating capacities. Therefore, experimental assessment of such characteristics can provide valuable insights into the muscle's functionality. Furthermore, computational models of muscles can complement experimental methods by predicting internal and external forces, which can be useful for applications, such as prosthesis fitting or surgery planning. In order to make correct predictions, it is essential that such models are adapted to the appropriate anatomy of the respective patient. Thus, there is a need for patient-specific computational models.

The commonly employed imaging-based methods are capable of obtaining a variety of muscle characteristics, which can serve as an input for computational models. They are, however, restricted either in the ability of illustrating 3D structures or dynamic conditions. Furthermore, most ultrasound-based methods are operator-dependent, which is due to manual probe movement and may result in inconsistent tissue deformation. In this thesis, 3D ultrasound-based methods for the controlled assessment of muscle characteristics, i.e., deformation and muscle architecture, in both static and dynamic conditions, are developed to alleviate the common restrictions and extend the current application domain.

As a key contribution, an automated 3D ultrasound system for enabling controlled and reproducible 3D ultrasound data acquisition is developed. The system is comprised of a custom-designed device, a control cabinet with an industrial PC for control, an ultrasound machine and a video capture device. The custom-designed device consists of three axes, with the ultrasound probe mounted on one of the axis. In this configuration, the probe can move along all three axes. One of the axes is realized in semicircular shape, which is similar to a tomographic system. Since all axes contain encoders for determining the position of the ultrasound probe, there is no need for additional position sensing. A synchronization algorithm enables simultaneous recording of image and encoder data. Furthermore, the system has a built-in force control mechanism, such that measurements with the custom-designed device ensure a consistent tissue deformation along the scanning trajectory. For 3D reconstruction of acquired image and position data, as well as segmentation and volume analysis, two different methods are implemented and presented. The principle is to align the images according to the position information of the encoder data by applying a series of coordinate transformations. The proposed system is capable of controlled scanning trajectories while applying a consistent contact force, therefore enabling automated and

controlled 3D ultrasound measurements.

The automated 3D ultrasound system is evaluated in a validation study (by using custom-designed phantoms) and an *in vivo* application study on a human tibialis anterior (TA) muscle. Here, the computed phantom volumes show small errors compared to the known phantom geometries. This indicates a high accuracy of reconstructions based on data acquired with the automated 3D ultrasound system. Moreover, the automated method is compared to 3D freehand ultrasound imaging. The results show lower standard deviations in computed phantom length, volume and thickness for the automated method. Furthermore, the coefficients of variation for thickness computations are higher for the freehand trials (for both phantom and TA data). This reveals the benefits of the integrated force control system. The findings show that the automated method is capable of conducting fast 3D ultrasound measurements with a higher reproducibility than freehand ultrasound methods.

In a second part of this thesis, 3D ultrasound data sets acquired with the automated 3D ultrasound system are used for determination of 3D muscle architecture. For this, an image processing algorithm is developed based on a multiscale vessel enhancement filter, which allows computation of the fascicle direction for each volume element. The method is validated using a custom-designed wire phantom, where small absolute errors (below 1°) of the angle between the wires are observed. The small errors demonstrate that the method is capable of computing pennation angles with a high accuracy. In an application study with 10 human subjects, the TA is investigated for different foot positions, i.e., different muscle lengths. Here, decreases in pennation angle for increasing muscle length can be observed, which is consistent with previous literature. This indicates that the method is suitable for 3D architecture determination. As such, the proposed algorithm provides new means to investigate muscle architecture even at high muscle contraction levels, whereas the currently employed methods are restricted to relatively low muscle contraction levels.

Moreover, a method for acquisition of 3D ultrasound data of the TA during dynamic movement is developed and applied to a study with five human subjects. While the subjects periodically flex and extend their foot, the automated 3D ultrasound system oscillates the ultrasound probe along the TA's longitudinal axis. The ankle joint angle is measured by using reflective markers. Therefore, each 2D image has a corresponding position and ankle joint angle. An algorithm is developed which enables 3D reconstruction of the collected dynamic images. Results of muscle deformation analysis, i.e., the cross-sectional area, show similar findings to previous literature. This indicates that the method enables acquisition of volumetric muscle data during dynamic movements, whereas this would be highly restricted or impossible with the current imaging modalities. Hence, the proposed method provides a novel way to investigate muscle contraction behavior, yielding valuable additional information about muscle functionality.

In future applications, the developed methods can be combined. Here, data sets with information on the 3D pennation angle and the volumetric deformation, may be acquired during dynamic movements. On the one hand, this can provide novel information about the characteristics of muscles and lead to a generally improved understanding of the muscle's functionality. Furthermore, the gained information can lead to the improvement of existing computational models of the muscle or entirely new models. This may help answer previously unresolved research questions and lead to novel therapy approaches.

Deutsche Zusammenfassung

Durch Kontraktion ermöglichen Skelettmuskeln sämtliche Arten der menschlichen Bewegung wie etwa das Gehen, Laufen, Stehen, Sprechen und sogar Atmen. Die Kontraktion der Muskeln ermöglicht diese Bewegungen, indem sie Kraft erzeugt. Ein Skelettmuskel besteht aus vielen Fasern, die in Strukturen, genannt Faszikel, gebündelt sind. Bei einigen Muskeln sind die Faszikel in einer Linie mit der Kontraktionsrichtung des Muskels, vom Muskelursprung bis zum Ansatz, ausgerichtet, während bei anderen Muskeln die Faszikel in einem Winkel zur Wirkungsrichtung angeordnet sind, was als gefiedert bezeichnet wird. Die innere Anordnung der Fasern wird als Muskelarchitektur bezeichnet. Muskeleigenschaften, die sich auf die innere Architektur oder die äußere Form beziehen, können mit den kraftgenerierenden Fähigkeiten des Muskels in Verbindung gebracht werden. Daher kann die experimentelle Bewertung solcher Merkmale wertvolle Informationen über die Funktion des Muskels liefern. Darüber hinaus können Simulationsmodelle von Muskeln die experimentellen Methoden ergänzen, indem sie innere und äußere Kräfte vorhersagen, was für Anwendungen wie die Anpassung von Prothesen oder die Planung von Operationen nützlich sein kann. Um korrekte Vorhersagen machen zu können, müssen die Modelle unbedingt an die entsprechende Anatomie des jeweiligen Patienten angepasst werden. Somit besteht hier ein Bedarf an patientenspezifischen Simulationsmodellen.

Die derzeit verwendeten bildgebenden Verfahren können eine Vielzahl von Muskelmerkmalen erfassen, die als Eingabe für solche Simulationsmodelle dienen können. Sie sind jedoch in ihrer Fähigkeit eingeschränkt, 3D-Strukturen oder dynamische Bedingungen abzubilden. Des Weiteren sind ultraschallbasierte Methoden bedienerabhängig, was auf die manuelle Bewegung des Schallkopfs zurückzuführen ist und zu einer inkonsistenten Gewebedeformation führen kann. In dieser Arbeit werden 3D-Ultraschallmethoden für die kontrollierte Erhebung von Muskeleigenschaften, d. h. Verformung und Muskelarchitektur, sowohl unter statischen als auch unter dynamischen Bedingungen, entwickelt, um die bisherigen Einschränkungen zu reduzieren und den aktuellen Anwendungsbereich zu erweitern.

Ein wesentlicher Beitrag ist die Entwicklung eines automatisierten 3D-Ultraschallsystems, das eine kontrollierte und reproduzierbare 3D-Ultraschalldatenerhebung ermöglicht. Das System besteht aus einem anwendungsspezifisch entwickelten Gerät, einem Schaltschrank mit einem Industrie-PC zur Steuerung, einem Ultraschallgerät und einem Videoaufnahmegerät. Das Gerät besteht aus drei Achsen, wobei der Ultraschallkopf an einer der Achsen montiert ist. In dieser Konfiguration kann sich der Schallkopf entlang der drei Achsen bewegen. Eine der Achsen ist halbkreisförmig ausgeführt, ähnlich wie bei einem Tomographiesystem. Da alle Achsen Encoder zur Bestimmung der Position der Ultraschallsonde enthalten, ist kein zusätzlicher Positionssensor erforderlich. Ein Synchronisationsalgorithmus ermöglicht die gleichzeitige Erfassung von Bild- und Encoderdaten. Darüber hinaus verfügt das System über einen eingebauten Kraftregelungsmechanismus, so dass die Messungen mit dem Gerät eine

gleichmäßige Gewebedeformation über die gesamte Abtasttrajektorie gewährleisten. Für die 3D-Rekonstruktion der erfassten Bild- und Positionsdaten sowie für die Segmentierung und Volumenanalyse werden zwei unterschiedliche Verfahren entwickelt und eingesetzt. Das Prinzip besteht darin, die Bilder anhand der Positionsinformationen der Encoderdaten durch Anwendung einer Reihe von Koordinatentransformationen auszurichten. Das System ist in der Lage, kontrollierte Abtasttrajektorien zu fahren und dabei eine konsistente Kontaktkraft anzuwenden, wodurch automatisierte und kontrollierte 3D-Ultraschallmessungen ermöglicht werden.

Das automatisierte 3D-Ultraschallsystem wird in einer Validierungsstudie (unter Verwendung von speziell angefertigten Phantomen) und einer *in vivo* Anwendungsstudie an einem menschlichen Musculus tibialis anterior (TA) evaluiert. Hier weisen die berechneten Phantomvolumina geringe Fehler im Vergleich zu den bekannten Phantomgeometrien auf. Dies deutet auf eine hohe Genauigkeit der Rekonstruktionen auf der Grundlage von Daten hin, die mit dem automatischen 3D-Ultraschallsystem erhoben wurden. Darüber hinaus wird die automatisierte Methode mit der 3D Freihand-Ultraschalltechnik verglichen. Die Ergebnisse zeigen geringere Standardabweichungen bei den berechneten Phantomlängen, -volumina und -dicken für die automatisierte Methode. Zudem sind die Variationskoeffizienten für die Berechnung der Phantomdicke bei den Freihandversuchen höher (sowohl für Phantom- als auch für TA-Daten). Dies verdeutlicht die Vorteile der integrierten Kraftregelung. Die Ergebnisse zeigen, dass die automatisierte Methode in der Lage ist, schnelle 3D-Ultraschallmessungen mit höherer Reproduzierbarkeit durchzuführen als Freihand-Ultraschallmethoden.

In einem zweiten Teil dieser Arbeit werden 3D-Ultraschalldatensätze, die mit dem automatisierten 3D-Ultraschallsystem aufgenommen wurden, zur Bestimmung der 3D-Muskelarchitektur verwendet. Hierfür wird ein Bildverarbeitungsalgorithmus entwickelt, der auf einem „Multiscale vessel enhancement“ Filter basiert und die Berechnung der Faszikelrichtung für jedes Volumenelement ermöglicht. Die Methode wird zur Validierung an einem speziell konstruierten Drahtphantom angewandt, welche geringe absolute Fehler (unter 1°) des Winkels zwischen den Drähten aufweisen. Die geringen Fehler zeigen, dass die Methode in der Lage ist, die Fiederwinkel mit hoher Genauigkeit zu berechnen. In einer Anwendungsstudie mit 10 Probanden wird der TA für verschiedene Fußpositionen, das heißt unterschiedliche Muskellängen, untersucht. Hier ist eine Abnahme des Fiederwinkels bei zunehmender Muskellänge zu beobachten, was mit der bisherigen Literatur übereinstimmt. Dies zeigt, dass die Methode für die Bestimmung der 3D-Architektur geeignet ist. Der Algorithmus bietet neue Möglichkeiten zur Untersuchung der Muskelarchitektur, auch bei hohen Muskelkontraktionswerten, wohingegen die derzeit verwendeten Methoden auf relativ niedrige Muskelkontraktionswerte beschränkt sind.

Darüber hinaus wird eine Methode zur Erhebung von 3D-Ultraschalldaten des TA während dynamischer Bewegungen entwickelt und in einer Studie mit fünf Probanden angewandt. Während die Probanden ihren Fuß periodisch beugen und strecken, pendelt der Ultraschallkopf entlang der longitudinaleln Achse des TA. Der Sprunggelenkwinkel wird mit Hilfe von reflektierenden Markern bestimmt. Daher besitzt jedes 2D-Bild eine entsprechende Position und einen Sprunggelenkwinkel. Es wird ein Algorithmus entwickelt, der im Anschluss eine 3D-Rekonstruktion der gesammelten dynamischen Bilder ermöglicht. Die Ergebnisse der Muskeldeformationsanalyse, das heißt der Querschnittsfläche, zeigen ähnliche Ergebnisse wie in der Literatur. Dies deutet darauf hin, dass die

Methode die Erfassung volumetrischer Muskeldaten während dynamischer Bewegungen ermöglicht, während dies mit den derzeitigen Bildgebungsmodalitäten nur sehr eingeschränkt oder nicht möglich ist. Daher bietet die vorgeschlagene Methode eine neuartige Möglichkeit zur Untersuchung des Muskelkontraktionsverhaltens, durch die wertvolle zusätzliche Informationen über die Muskelfunktion gewonnen werden können.

In zukünftigen Anwendungen können die entwickelten Methoden kombiniert werden. Damit könnten Datensätze mit Informationen über den 3D-Fiederungswinkel und die volumetrische Verformung bei dynamischen Bewegungen erfasst werden. Dies kann zum einen neue Informationen über die Eigenschaften von Muskeln liefern und zu einem allgemein verbesserten Verständnis der Funktionsweise des Muskels führen. Zum anderen können die gewonnenen Informationen zur Verbesserung bestehender oder zur Erstellung neuer Simulationsmodelle des Muskels führen. Dies kann dazu beitragen, bisher ungelöste Forschungsfragen zu beantworten und neue Therapieansätze zu finden.

Nomenclature

Abbreviation	Description
2D	Two-dimensional
3D	Three-dimensional
ACSA	Anatomical cross-sectional area
BMI	Body mass index
CoV	Coefficient of variation
CR	Calibration reproducibility
CSA	Cross-sectional area
CT	Computer tomography
DOF	Degree of freedom
DTI	Diffusion tensor imaging
EMG	Electromyography
FBM	Function-based methods
FE	Finite elements
HD EMG	High density electromyography
MRI	Magnetic resonance imaging
MVC	Maximum voluntary contraction
MVEF	Multiscale vessel enhancement filter
PBM	Pixel-based methods
PCA	Principal component analysis
PCSA	Physiological cross-sectional area
PNN	Pixel nearest neighbor
PRA	Point reconstruction accuracy
RANSAC	Random sample consensus
ROM	Range of motion
SR	Sarcoplasmatic reticulum
TA	Tibialis anterior
VBM	Voxel-based methods
VNN	Voxel nearest neighbor

Anatomical Terminologies

In the course of this thesis, some anatomical location descriptions are used:

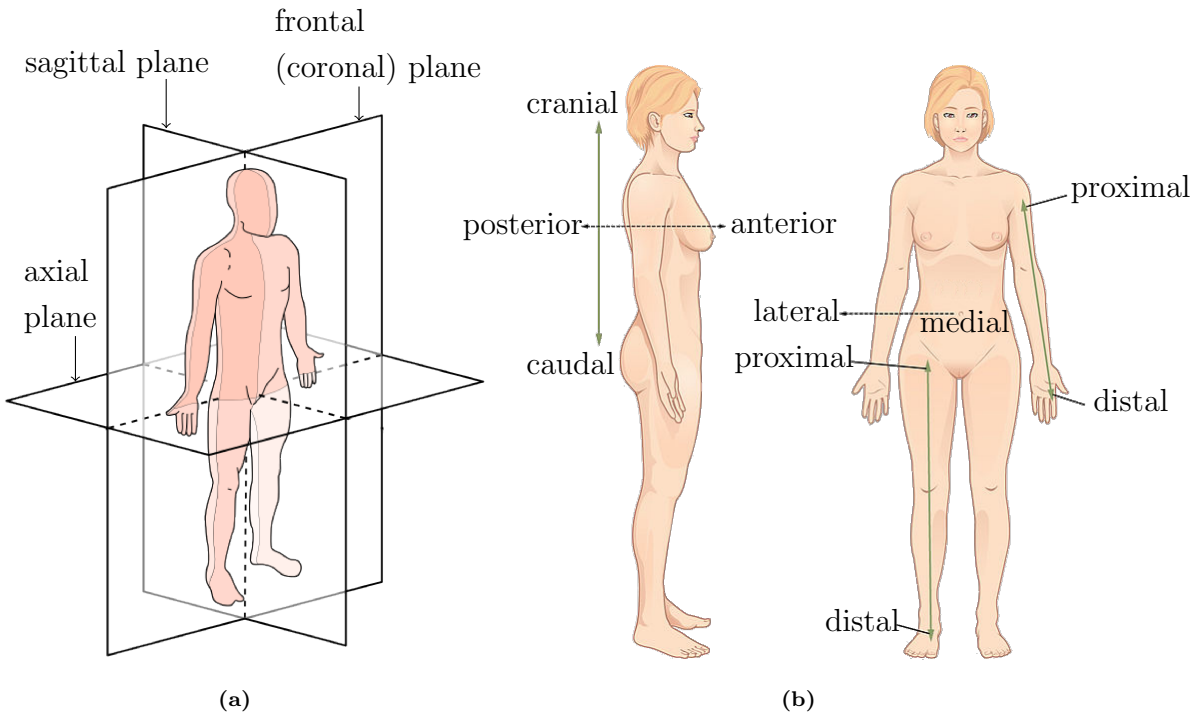

Figure 1: Anatomical terminologies. (a) Anatomical planes, image adapted from [1] (licensed under CC BY-SA 3.0). (b) Definition of anatomical directions and locations, image adapted from [2] (licensed under CC BY 3.0).

1 Introduction

1.1 Motivation

For humans, or any kind of mammals, skeletal muscles are essential for survival as they facilitate various types of movement such as walking, running, standing, speaking, or even breathing [154]. Such movement is enabled by muscle contraction, which generates force. A skeletal muscle is made up of many muscle fibers, that can be arranged in various ways, being referred to as muscle architecture. This architecture defines the total number of fibers a muscle can comprise. Thus, assuming that more fibers can exert a larger amount of force, the inner muscle architecture plays a crucial role for force-generation. During contraction, muscle fibers shorten and due to the incompressibility property of skeletal muscle tissue [104], the muscle shape changes, e.g., the muscle belly bulges. Specific characteristics of skeletal muscle related to its shape and architecture can be directly or indirectly linked to the force-generating capacities of the muscle, thus being important determinants of the muscle's functionality. Assessment of these characteristics can therefore provide important information about, for example, the progression of neuromuscular diseases or predict the benefit of therapies.

Muscle characteristics can be estimated by employing various experimental methods. Computational models of the muscle can complement them by predicting internal forces. Such model predictions can be used for, e.g., planning of surgeries [49], simulating and predicting injuries [232] or fitting of prostheses [191, 202]. Often, the parameters for such computational models were taken from *ex vivo*[1] studies in which individual muscles have been dissected [6, 11]. However, such cadaver studies are limited in their ability to study muscle contractions, especially active ones. Moreover, the results from such studies may differ from living tissue [72], i.e., *in vivo* studies. Consequently, there is a need for patient-specific, data-driven computational models of skeletal muscles which accurately represent the respective muscle geometry and its internal structure, providing accurate predictions of muscle deformation and force generation during muscle contractions [215, 228]. Experimental methods which can determine these parameters *in vivo* are crucial to enable such patient-specific muscle models.

Various medical imaging methods have proven to be a valid tool for obtaining a number of muscle characteristics. Magnetic resonance imaging (MRI) is an established technique for *in vivo* estimations of muscle length and volume [190]. It makes use of strong magnetic fields and radio waves for acquiring detailed two-dimensional (2D) anatomical images of the body. By combining multiple 2D images, three-dimensional (3D) data sets can be produced. Conventional anatomical MRI scans lack, however, the ability to visualize the internal structure of a given muscle, i.e., its architectural structure. Thus, considering

[1]The term *ex vivo* can be translated from Latin as "out of the living" and describes experiments outside of the living organism, or using dead tissue or organs. *In vivo* is translated as "within the living" and refers to experimental conditions using the whole living organism, e.g., experiments on living humans.

not only the external shape of the muscle, but also the arrangement of muscle fibers, diffusion tensor imaging (DTI) can be a useful tool. DTI is an MRI-based technique determining the direction of diffusion of water molecules within tissue. It can be used for the reconstruction of muscle architecture since water diffusion occurs primarily along the fiber direction. Yet, MRI and DTI are expensive techniques which require long acquisition times, making it prohibitive to collect data in some cases. Thus, experimental conditions are limited where a participant would be required to maintain a high muscle contraction level during imaging. Moreover, due to the size and requirements of an MRI system, it is stationary and not suitable for studies where imaging might take place in a variety of settings. Further limitations are due to the narrow space of the imaging bore, and difficulties with patients with metal implants can occur. Additionally, DTI has a poor resolution, typically in a range of 1-3mm for musculoskeletal examinations [170], such that an additional anatomical MRI scan is needed if the segmentation of a skeletal muscle is required.

On the other hand, ultrasound imaging is a widely-used and clinically established tool for investigating skeletal muscle architectural parameters. In contrast to MRI, ultrasound is less expensive, enables faster acquisitions and is portable. A 2D ultrasound image is created by an ultrasound probe sending out sound waves into the tissue where the amount of reflected waves determines the grayscale level of the image. The spatial resolution of ultrasound images is dependent on the operating frequency [178]. With high frequency ultrasound probes, a spatial resolution of approximately 100µm and below is possible, in contrast to anatomical MRI scans, which commonly employ resolutions of 0.5-1mm for musculoskeletal applications [170]. In sagittal view, skeletal muscles appear in a stripe pattern, due to their acoustic properties. The fiber bundles are displayed in black and the connective tissue between fascicles is white. Conventional 2D ultrasound images, however, do not allow examination in 3D without post-processing. 3D freehand ultrasound techniques have been developed for more than three decades to allow acquisition of volumetric images [67, 192]. In this technique, the probe is equipped with some form of position sensor, e.g., reflective motion capture markers. A human operator then scans along the longitudinal axis of the muscle, taking several cross-sectional images. From the position and orientation of the ultrasound probe of each taken 2D image, one can apply a series of coordinate transformations to reconstruct a 3D volume. Since a 3D freehand ultrasound measurement of a muscle has a relatively short acquisition time (less than 60 seconds), measurements with static muscle contractions are viable in a wider spectrum compared to MRI.

Many 3D freehand ultrasound applications use a motion capture system with optical reflective markers for accurate determination of the position and orientation of the probe, e.g., [19, 40, 57, 200]. This usually requires a costly laboratory setting that is mostly not highly portable due to its size and configuration. Further, reflective markers have to be visible at all times to the infrared cameras. When manually moving the ultrasound probe, the contact force exerted by the operator may vary, for instance due to the natural curvature of the human body. Variations in contact force may lead to inconsistent deformation of muscle tissue along the scanning trajectory. Moreover, manual movement of the probe generally leads to variation in scanning trajectories and velocity, thus resulting in a decrease in reproducibility of the method. Further, 3D freehand ultrasound requires training of the operator to ensure an acquisition of the whole muscle and to avoid large

gaps between adjacent frames [72].

While MRI is capable of acquiring 3D data sets of skeletal muscles without contraction or with low contraction levels, with 3D freehand ultrasound imaging, such images can be obtained at high contraction levels. Yet, the contractions are limited to static conditions, i.e., isometric contractions where the muscle length does not change. If one considers human movement such as gait, compared to holding an object or standing still, these are dynamic movements that occur frequently in everyday life and are therefore highly relevant. Dynamic contractions can be examined using 2D ultrasound for observing muscle thickness or fibers during movement. However, such investigations are restricted to plane images. Thus, there is a need for an experimental method allowing acquisition of 3D images of skeletal muscles during dynamic contractions.

A key contribution of this thesis is the development of a novel portable automated 3D ultrasound system which enables ultrasound scans with controllable movement trajectories of the probe by using motors which electrically move the probe. By incorporating encoders, there is no need for an additional position sensor on the ultrasound probe. An integrated force control mechanism ensures a constant contact force between the probe and the skin. Further, algorithms for reconstructing 3D volumes are developed and implemented.

Subsequently, the automated 3D ultrasound system is applied in two studies in this thesis (Chapter 6 and Chapter 7). The first study focuses on the development of an algorithm for determination of 3D fascicle orientations presenting an alternative to imaging modalities such as DTI. First, static images of phantom data and muscle data are acquired. After 3D reconstruction, the fascicle orientation algorithm is applied and evaluated. The second study presents a novel method for acquisition of 3D ultrasound data sets of skeletal muscle during dynamic movement, which is applied to five human subjects. An algorithm for 3D reconstruction of the dynamic data is developed and presented, enabling determination of 3D muscle deformation during active contractions. Figure 1.1 shows a comparison of the capabilities of current imaging methods and the proposed methods in this thesis, illustrating the added benefit of the new technique.

The methods developed within this thesis present new techniques for determining morphological and architectural muscle parameters that can be used to generate patient-specific computational models. In addition, the proposed methods can determine the deformation of the muscle during movement, which inform computational models and enable respective validation studies.

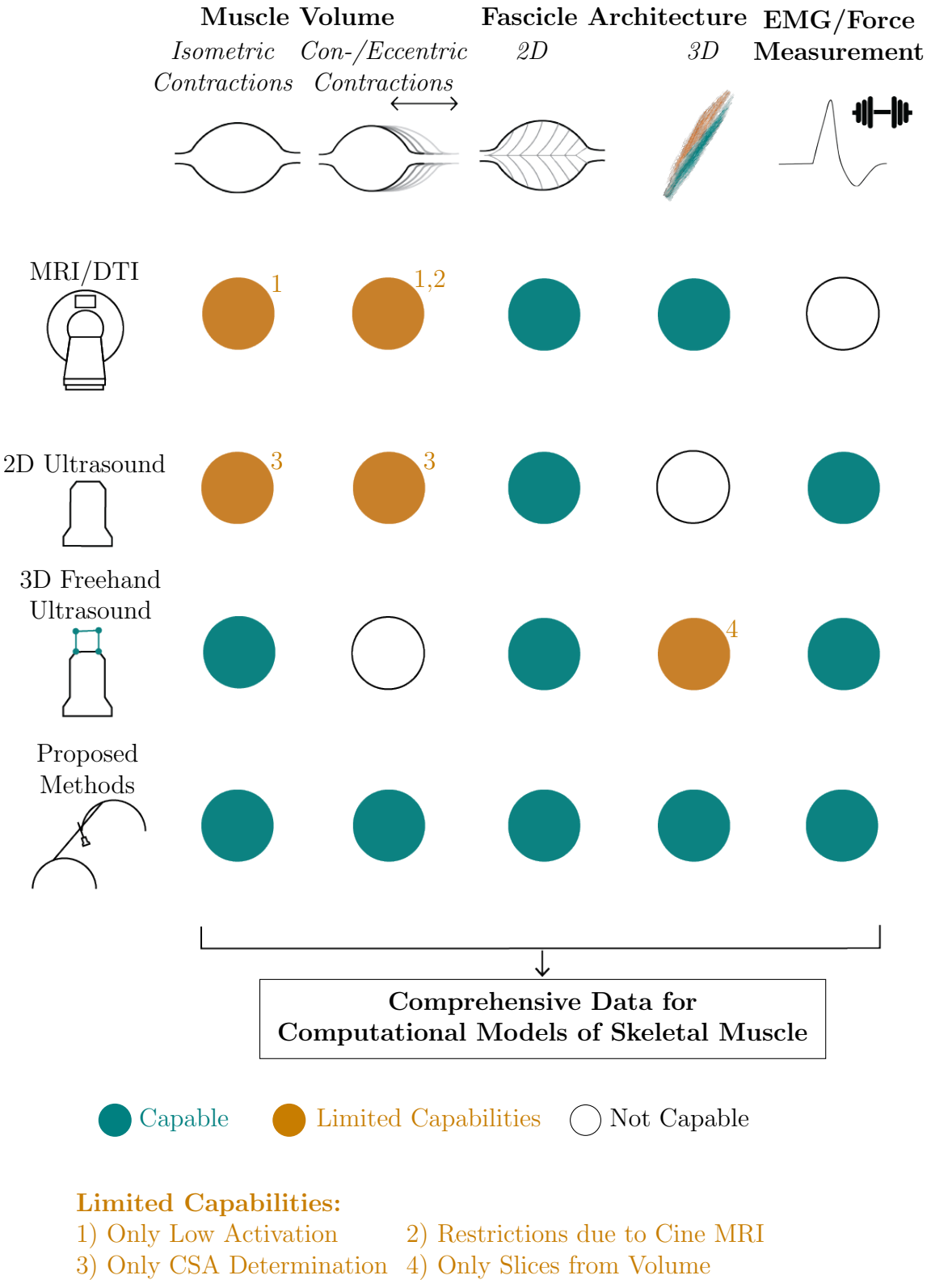

Figure 1.1: Comparison of current imaging methods with the proposed automated 3D ultrasound technique and methods for determining muscle volume and architecture. CSA: Cross-sectional area.

1.2 State of the Art

In this thesis, an automated 3D ultrasound device as well as two different methods for investigation of skeletal muscles are developed and presented. In the following, an overview of previous studies determining muscle shape and architectural characteristics is given, as well as a summary of existing automated ultrasound systems.

1.2.1 Imaging-Based Assessment of Muscle Volume and Architecture

Muscle characteristics in the context of this thesis can be divided into such concerning the muscle anatomically and architecturally. While anatomical characteristics refer to the external shape of the muscle including muscle volume, muscle length and muscle thickness, architectural characteristics refer to the internal fiber arrangement of the muscle. The architecture characteristics primarily include the fiber or fascicle length, where a fascicle refers to a bundle of muscle fibers, and the so-called pennation angle, which describes the orientation of the fibers, see Figure 1.2.

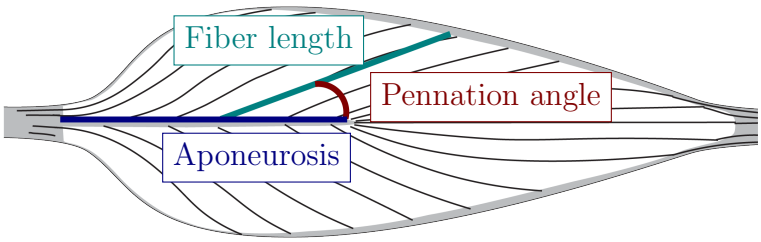

Figure 1.2: Schematic of a pennate muscle with fibers running from an internal plane referred to as aponeurosis (blue). The pennation angle is displayed in red and the fiber/fascicle length in green.

For both MRI and 3D ultrasound data, muscle volume can be determined by segmenting either all or a subset of the acquired 2D images. The volume of the muscle can thus be determined via the resolution of the volume elements in the 3D image. Using this technique on MRI-based examinations, previous studies showed that muscle volume is proportional to the joint torque of a muscle, revealing a correlation of muscle volume and force [79, 108]. MRI-based techniques have been used extensively to study muscle volume and showed that it is an important morphological parameter to infer age [66, 107, 156, 171], training [8, 139, 185] and growth processes [236]. Such MRI techniques have been applied to study differences in muscle volumes of healthy muscles and different clinical conditions such as cerebral palsy, e.g., [95, 179, 211, 218]. Significantly smaller volumes have been documented for clinical conditions, establishing it as an important measure for monitoring diseases.

3D freehand ultrasound techniques have been applied to muscles for investigation of muscle volume in both healthy [19, 200, 267] and clinical conditions [77, 181, 226]. Further, ultrasound phantoms are objects with known geometry and acoustic properties that can be used for validation and/or testing of ultrasound methods, or for training purpose. Such phantoms have been used for validating 3D freehand ultrasound techniques regarding volume reconstruction accuracy. Barber et al. [19], Cenni et al. [40] and Obst et al. [182] validated the 3D freehand method using water-filled latex condoms, water-filled balloons,

and acrylic tubes filled with a gelatin mixture, respectively. The studies found volume errors in the reconstruction of values below 3%. Other validation approaches compared the 3D freehand ultrasound technique with MRI measurements of the same subjects and found differences in muscle or tendon volume determination of approximately 7% [65], 1.1% [19, 57], up to 1.4% [18] and 16% [153]. Both validation methods showed a high accuracy and good repeatability of the 3D freehand ultrasound method for volume reconstruction.

The previous section demonstrated that MRI- and 3D freehand ultrasound-based methods are valid methods for volume reconstruction, i.e., the external shape of a muscle. Knowledge on the muscle's internal structure, however, also plays a major role in the understanding of force production. Considering two muscles with the same volume and shape, where in one of them, the fibers run straight from one end to the other. In the second muscle, an internal plane called aponeurosis acts as a division of the fibers, which is illustrated as a blue line in Figure 1.2. They run from the aponeurosis in different directions, e.g., like a fan. The second muscle is referred to as a pennate muscle. As a consequence, in the second muscle, the fibers are shorter and the muscle can contain more fibers, thus being able to exert more force. The characteristics of such fiber arrangement can be directly related to the muscle's force-generating capacities [150], providing valuable information on the muscle's functionality. It is thus crucial to experimentally obtain such architectural characteristics in addition to the anatomical characteristics. Due to the clearly visible striped appearance in longitudinal view, 2D ultrasound is a commonly used tool for investigating muscle architecture, see Figure 1.3a.

Parameters such as the pennation angle or the fascicle length have been investigated using 2D ultrasound, applied in either healthy [56, 78, 106, 242] or clinical conditions, such as cerebral palsy [26, 233], stroke [83] or Duchenne muscle dystrophy [129]. It has been shown that length changes in fascicles derived from ultrasound and sarcomeres, i.e., the smallest contractile units of the muscle, are correlated [148]. Kwah et al. [141] demonstrated the reliability and validity of ultrasound-determined fascicle lengths and pennation angles. In a more recent systematic review, van Hooren et al. [110] showed that these characteristics derived from 2D ultrasound data are reliable for movements such as locomotion, jumping or cycling. In a particularly recent study from 2023, Martin-Rodriguez et al. [162] used 2D ultrasound for investigating the tibialis anterior (TA) muscle for a total of 109 subjects, which revealed significant differences in pennation angle between genders and muscle compartments, i.e., compartments divided by the aponeurosis.

Fascicle length and pennation angle (see Figure 1.2) can be determined manually from the ultrasound images. Such manual determination is, however, time consuming, especially when a long time series of images is recorded or a large number of images is obtained. Therefore, computational methods for automatic detection of such characteristics have been proposed. Rana et al. [204] presented an approach for automatic detection of the pennation angle from 2D ultrasound data using a multiscale vessel enhancement filter (MVEF). The MVEF computes the Hessian matrix of a 2D scalar ultrasound image and its eigenvalues and eigenvectors for enhancement of fascicle position. The study further combined the MVEF with a Radon and wavelet transform. Testing on synthetically generated images using the combined method revealed errors of less than 0.6° for the artificial pennation angle. In a comparison study, Cunningham et al. [52] used a deep residual network approach which outperformed the method of Rana et al. [204]. A residual network has also been used by Zheng et al. [278] with errors of around 1°.

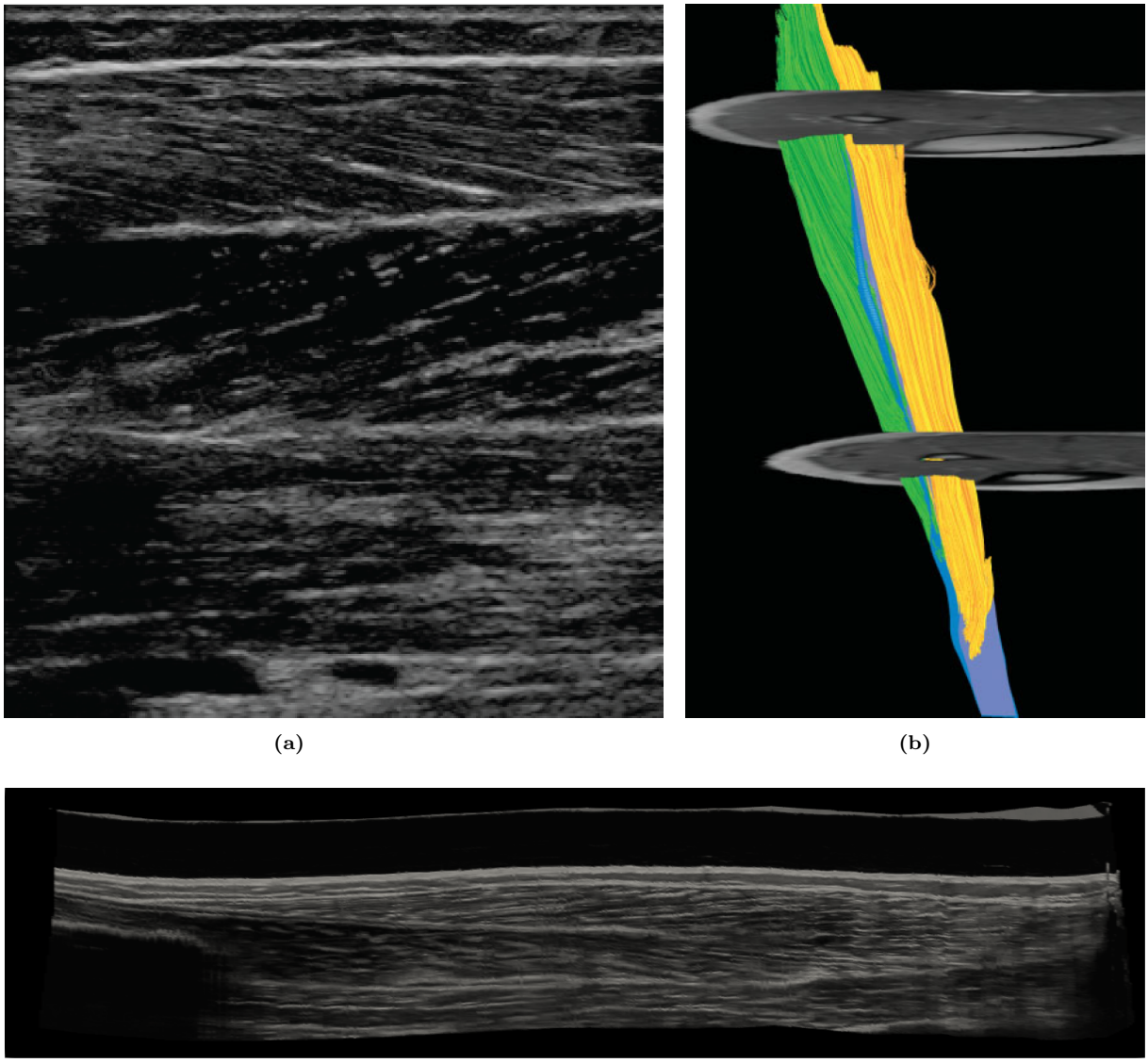

Figure 1.3: Visualization of current imaging methods, examples shown on the tibialis anterior (TA) muscle. (a) 2D ultrasound imaging in sagittal view, showing the fascicles in a striped pattern. (b) Example of a DTI reconstruction, overlayed with anatomical MRI images. The blue line shows the aponeurosis, green and yellow illustrate the muscle compartments. Image from [99], with permission. (c) Sagittal image slice of a reconstructed volume from 3D freehand ultrasound of the TA.

Further methods include Kalman filters [152, 276] and Gabor filters [279] for enhancement of fascicles or detection of fascicle directions. Some studies also provided open-source software tools such as TimTrack [260] or Simple Muscle Architecture Analysis (SMA) [229] for automatic computation of fascicle characteristics. Computational approaches are reliable methods for determining the pennation angle in 2D. On the other hand, the computed angles are in-plane results and lack spatial information of the fascicle orientations. Bénard et al. [22] and Bolsterlee et al. [30] showed that determination of pennation angles from 2D images is highly dependent on the correct alignment and orientation of the ultrasound probe as the image should optimally lie in the fascicle plane. Pennation angles may show, however, a high variance within a muscle [224] and regional differences in pennation angles

may occur [162]. This renders a correct measurement from a 2D image difficult.

It is further possible to determine in-plane fascicle lengths or pennation angles from 3D freehand-based data sets, e.g., [140, 200, 265, 267]. In such studies, a representative sagittal slice, where the striped pattern of the fascicles is visible, which appears similar to longitudinal 2D ultrasound images of skeletal muscle, is taken out of the reconstructed 3D volume, as shown in Figure 1.3c. From this slice, pennation angle and fascicle length can be determined the same way as for conventional longitudinal 2D ultrasound images. For determination of 3D fascicle architecture instead of in-plane parameters, DTI is a commonly used method, e.g., [29, 94, 99, 142], see Figure 1.3b. DTI requires, however, long acquisition times of approximately 15 minutes for a scan of the TA [99] and is therefore limited in imaging of muscle contractions. In a previous *ex vivo* study, Damon et al. [54] compared DTI measurements of a rat's lateral gastrocnemius with manual dissection and found no significant differences in pennation angle between both methods. In another DTI validation study using manual digitization on a rabbit's soleus, Schenk et al. [224] found, however, significant differences in pennation angles, but not in fascicle lengths. Comparing architectural characteristics based on 3D ultrasound in-plane angles and DTI measurements, Wang et al. [265] determined fascicle lengths and pennation angles of the TA and gastrocnemius medialis (GM) muscle. The results revealed statistically insignificant overestimates in fascicle length computation in both TA and GM. Pennation angle were significantly smaller for the TA in 3D freehand ultrasound compared to DTI. Another comparison of DTI and conventional 2D ultrasound imaging on the GM has been evaluated by Bolsterlee et al. [31] regarding fascicle length and pennation angle. No statistically significant differences between mean values of fascicle lengths were found, however, the authors reported substantial differences between individual pairs and significantly larger pennation angles for the DTI method. In comparison to cadaver studies [266], pennation angles were significantly larger for both 2D ultrasound and DTI.

Rana and Wakeling [207] developed a method for determining fascicle orientations from 2D ultrasound images and simultaneously using optical motion capture to define 3D direction cosines from the 2D directions. The method relied on the correct orientation of the probe and took up to 120 seconds for acquisition. In a later study, the method was employed for quantifying 3D architecture of the triceps surae. Here, the computed pennation angles differed from previously obtained angles from 2D images [205]. This may be caused by the different method of the pennation angle definition, which is mostly defined as the angle between the fascicles and the aponeurosis, however in [205], the pennation angle is the angle relative to the major axis of the muscle.

As mentioned above, most of the acquisition methods capable of obtaining 3D data are limited to static conditions. While 2D ultrasound is able to image muscle architecture characteristics in dynamic conditions [110], it is restricted to single-plane investigations and therefore does not consider changes in fascicle orientation at different locations in the muscle. 3D freehand imaging enables 3D acquisition, but is limited to static conditions, i.e., isometric contractions. In cardiac MRI, cine imaging enables dynamic acquisitions. In cine imaging, the MRI sequences are timed to echocardiogram signals over multiple cardiac cycles, such that time-resolved images of a beating heart can be acquired [188]. Tissue motion, e.g., due to the patient's breath, may lead to artifacts in MRI images. To reduce such motion artifacts in cardiac cine MRI, patients are often instructed to hold their breath [165, 188], yielding a more complex method. Another cine MRI-based tech-

nique employs spatially selective saturation pulses for physically tagging tissue, thus being referred to as MRI tagging [53]. MRI tagging enables measurement of tissue displacement. Cine imaging and MRI tagging have been used for quantifying muscle positions and strains in skeletal muscle, e.g., [13, 130, 163]. Dynamic imaging methods such as cine MRI are, however, restricted due to the size of the MRI bore and the interactions with metal parts. Thus it is challenging to acquire data under "physiological joint loading conditions" [32]. Furthermore, image quality is reduced for dynamic conditions in comparison to static ones thereby reducing the reliability of such images [165].

1.2.2 Automated and Force-Integrated Ultrasound Systems

Ultrasound has been shown to be a valid method for investigations of skeletal muscle in both 2D and 3D imaging [72, 110, 141]. In order to achieve an adequate acoustic signal, ultrasound gel and a certain amount of contact force are essential. However, variation in contact force exerted by the operator caused by manual movement of the probe may occur, for instance due to the natural curvature of the lower limb. Changes in characteristics such as muscle thickness and pennation angle caused by external forces like muscle compression have been reported [213, 264]. Schimmoeller et al. [225] found a total tissue compression of 18%, measured at the anterior central lower leg and arm, for indentation forces of 10.74N. Therefore, keeping constant contact force during the whole scanning procedure can help improving the scanning process.

In order to measure the contact force exerted by the operator, approaches for hand-held ultrasound probe attachments or instrumentations have been presented, e.g., [89, 98, 180, 225]. Using such instrumentations, various studies quantified commonly used contact forces for different body part examinations. Table 1.1 lists applied force levels from previous studies employed on different body parts. Using a force sensor mounted to an ultrasound probe for vascular imaging, Triboulet and Dauzat [255] showed a reduction of measured arterial diameter with an increase in applied contact force. For abdominal examinations, mean values of 7N [89] and 8N [61] were found, which is within the defined range of 5N-20N that Smith-Guérin et al. [237] defined for abdominal, cardiac and renal evaluations.

Investigating the effects of contact force on skeletal muscle tissue, Lee et al. [145] found significant differences in TA muscle thickness between applied forces of 1N, 2N and 4N. Another study on the transversus abdominis muscle found significant changes in muscle thickness for small forces below 2N [127].

	Exerted Force [N]	Application
Dhyani et al. [61]	8.2±4.3	Abdominal
Gilbertson and Anthony [89]	7±3	Abdominal
Ishida and Watanabe [127]	0.5-4	Transversus abdominis
Lee et al. [145]	1-4	Tibialis anterior
Smith-Guérin et al. [237]	5-20	Abdominal, cardiac, renal
Triboulet and Dauzat [255]	2.6-3.1	Arterial

Table 1.1: Applied contact force levels from previous studies, with application on different body parts.

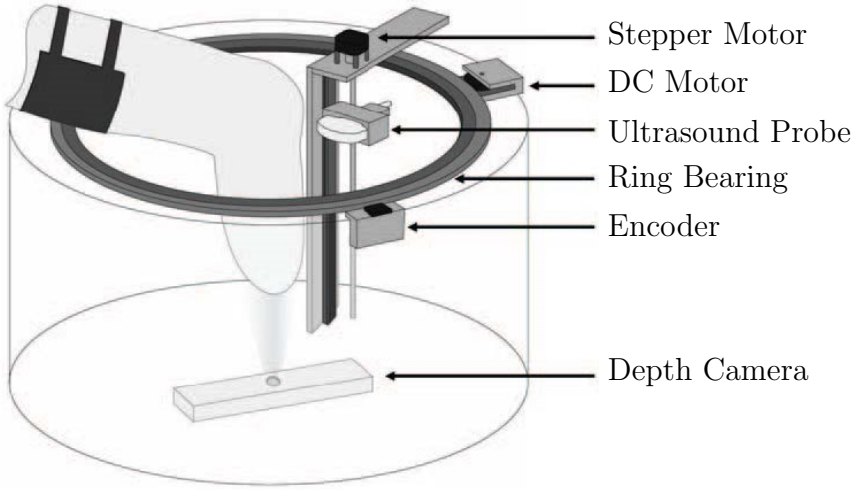

Figure 1.4: Tomographic ultrasound device, as proposed by Ranger et al. [208]. Image adapted from [208], with permission (©2017 IEEE). DC: Direct current

Other systems, which are primarily designed for 2D ultrasound imaging, have an integrated passive mechanism to maintain a contact force realized by a spring [128, 258, 259]. Passive systems enable a constant contact force in the vertical downward direction; in cases where the contact angle of the probe may change - such as while traversing the skin over a skeletal muscle - passive systems would not maintain a constant normal contact force [259]. For reducing inconsistent soft tissue deformation during 3D freehand ultrasound, Thomare et al. [249] proposed a large gel pad for GM examinations, which covered the length of the calf. Reconstructions using the large gel pad demonstrated reliable results for muscle volume estimates. Another approach for reducing muscle tissue deformations was presented by Cenni et al. [42]. In their study, a specially designed attachment was employed to mount a gel pad to the ultrasound probe. While a reduction in muscle deformation was observed, variances in volume estimates were not significantly different between the attachment and the conventional approach with the probe directly on the skin. Thus, muscle volume estimations were not more reliable than using the probe directly on skin.

Gilbertson and Anthony [90] developed a hand held force controlled ultrasound probe used for 2D imaging facilitating constant contact force between the ultrasound probe and skin. The probe is positioned via a servo motor with a rotary encoder which records the probe position. An included load cell measures the contact force and an implemented control algorithms enables maintenance of a constant force over a 5cm range of motion. The force controlled ultrasound probe has been used in a study by Pigula et al. [189], where differences in muscle compressibility between patients with Duchenne muscular dystrophy and healthy subjects have been assessed.

Another method for full avoidance of muscle deformation caused by the probe contact force is to conduct ultrasound scanning in a water tank, since there is no strong reflection between tissue and water, compared to air. Zhang et al. [277] designed a tomographic ultrasound scanner for 3D imaging of stumps of lower limb amputees. The stump is lowered into a cylindrical vessel filled with water. In the vessel, the probe moves along a circle, actuated by a stepper motor, whereby upward and downward movements are

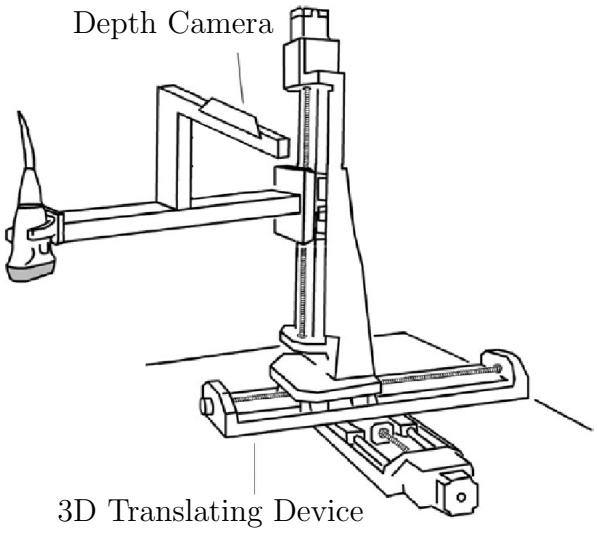

Figure 1.5: Automated ultrasound system with three translational degrees of freedom, as proposed by Huang et al. [119]. Image adapted from [119], with permission (©2018 IEEE).

also possible. This allows the probe to scan the stump from all directions without any contact. The scanner was extended by Ranger et al. [208, 209] to include a depth camera for tracking the limb and probe to compensate for movement, as shown in Figure 1.4.

Measurements in water tanks avoid tissue deformation. When recording in a water bath, however, simultaneous electronic measurements such as electromyography (EMG) readings using electrodes, with which contraction levels can be determined, are prohibitive.

In 3D freehand ultrasound, manual movement of the probe is accompanied not only by a variation of the applied contact force, but also by a variation of the scanning trajectory, thus reducing the reproducibility of the method. For enabling controlled scanning trajectories, assisted approaches for holding and moving the probe with one or more degrees of freedom (DOF) exist. Huang et al. [122] introduced a one DOF system where the ultrasound probe was mounted on a linear axis along which it could be moved manually by the operator. The linear axis was realized as a digital caliper, providing the position of the ultrasound probe. The same group developed a relatively small-sized system, where the probe was mounted on a rig comprising three linear axes, which facilitate the translational DOFs [121]. In their proposed system, the position of the ultrasound probe was recorded by an electromagnetic measurement system. A more sophisticated version of the system was proposed in 2018 [119] using a digital 3D translating device comprising three linear axis, thus enabling three translational DOFs, and a depth camera for obtaining the contours of the tissue surface. The system enabled automated 3D ultrasound measurements, with the ultrasound probe attached in a vertical direction, as illustrated in Figure 1.5.

Such linear position systems enable controlled movement trajectories. They prohibit, however, scanning from oblique angles making certain measurements difficult, particularly on the curved surfaces of limbs.

Another proposed small system [176] contains a motorized assembly attached to the ultrasound probe which enables tilting motion in a tilt range of -30° to 30° and linear motions in a 3cm range. Yet, this range would not enable acquisition of the whole volume for most muscles.

Robotic ultrasound systems can enable scanning from oblique angles. Such systems can have advantages in "accuracy, consistency, dexterity and maneuverability" [198]. An early robotic ultrasound system using a robot arm with linked joints was proposed in 1999 by Salcudean et al. [221] for carotid artery examinations. Since then, robotic arms have been used for 3D ultrasound imaging in a variety of applications such as spine imaging [262], acoustic radiation force elastography [21, 186], abdominal examinations [175], or general imaging applications [117]. While robotic arms are capable of scanning tissue surfaces from oblique angles due to their DOFs, they are mostly not easily portable, rather expensive and implementation can be relatively complex. For a more detailed description of the current state of the art in robotic ultrasound system, which is beyond the scope of this thesis, the interested reader is referred to [131] and [198].

1.3 Thesis Outline

After examination of the existing methods for the determination of muscle characteristics, and the developed automated ultrasound system, methods for enabling controlled 3D ultrasound measurements are developed within the scope of this thesis. Further, a method for the assessment of muscle characteristics of 3D fascicle architecture is presented, which can be employed during higher contraction levels. In addition, a method for volumetric data acquisition during dynamic movements is introduced. The developed methods overcome limitations of currently employed imaging methods, such as MRI.

This thesis is structured as follows:

Part I presents the underlying physiological and technological principles of this work, which are necessary to understand the techniques developed and applied. **Chapter 2** introduces the basics of the musculoskeletal system, involving muscle structure with hierarchical organization and architectural concepts. Further, the fundamental mechanisms of muscle contraction, which enable human movement, are described and basics on the muscle investigated in this thesis, i.e., the TA, are explained. **Chapter 3** provides a description of the underlying technological concepts used within this thesis, namely ultrasound imaging and motion capture. The general principle of medical ultrasound imaging is explained and the technology of 3D ultrasound including different methodologies for data acquisition, volume reconstruction and visualization are described. Moreover, a brief explanation on motion capture methods is provided.

In **Part II**, the development of an automated 3D ultrasound system, the corresponding reconstruction methods and a validation of the workflow are presented. **Chapter 4** shows the necessary measurement preparations and introduces the automated 3D ultrasound system. The chapter gives a detailed description of the system and includes a listing of the associated components and modes of operation. The chapter further describes the post-processing steps which are necessary for reconstruction of a 3D volume. For 3D reconstruction, two implemented and employed methods are presented, i.e., a custom-written one and one using a freely available software called Stradwin. The segmentation and volume analysis methods are also presented. **Chapter 5** describes a validation study of the method presented in Chapter 4. The automated 3D ultrasound system is applied on phantom and TA data. Furthermore, it is compared to data acquisition using freehand ultrasound imaging.

In **Part III**, the methods from Part II are applied to skeletal muscles for investigating

architectural parameters and dynamic conditions. **Chapter 6** presents a method for 3D fascicle orientation detection from volumetric ultrasound images, applied on phantom and TA data. The fascicle detection algorithm is first applied to phantom data for validation purpose. Secondly, an *in vivo* study on the TA of 10 human subjects is conducted for computation of 3D pennation angles. In **Chapter 7**, a method for obtaining volumetric ultrasound data of the TA deformation during movement of the foot is introduced, which is applied to five human subjects. First, the experimental methods for collecting dynamic 3D ultrasound data are described. Secondly, the post-processing steps for reconstructing volumes from dynamic imaging data are explained.

Chapter 8 provides an overall discussion of the topics covered in this thesis. Potentials and challenges are discussed. Further, future applications are considered and an overall outlook is given.

1.4 List of Publications

Journal Publications

A. S. Sahrmann, G. G. Handsfield, L. Gizzi, J. Gerlach, A. Verl, T. F. Besier, O. Röhrle, A System for Reproducible 3D Ultrasound Measurements of Skeletal Muscles, *IEEE Transactions on Biomedical Engineering*, 2024

A. S. Sahrmann, L. Vosse, T. Siebert, G. G. Handsfield, O. Röhrle, 3D Ultrasound based Determination of Skeletal Muscle Fascicle Orientations, *Biomechanics and Modeling in Mechanobiology*, 2024

A. S. Sahrmann, L. Vosse, T. Siebert, G. G. Handsfield, O. Röhrle,Determination of Muscle Shape Deformations of the Tibialis Anterior during Dynamic Contractions Using 3D Ultrasound, *Frontiers in Bioengineering and Biotechnology*, 2024

Conference Proceedings

A. S. Sahrmann, L. Gizzi, A. Zanker, G. G. Handsfield and O. Röhrle, Dynamic 3D Ultrasound Imaging of the Tibialis Anterior Muscle, *44th Annual International Conference of the IEEE Engineering in Medicine & Biology Society (EMBC)*, Glasgow, Scotland, United Kingdom, 2022, pp. 3899-3902

J. R. Walter, H. Saini, B. Maier, N. Mostashiri, J. L. Aguayo, H. Zarshenas, C. Hinze, S. Shuva, J. Köhler, **A. S. Sahrmann**, C. Chang, A. Csiszar, S. Galliani, L. K.Cheng, O. Röhrle, Comparative Study of a Biomechanical Model-based and Black-box Approach for Subject-Specific Movement Prediction, *42nd Annual International Conference of the IEEE Engineering in Medicine & Biology Society (EMBC)*, Montreal, QC, Canada, 2020, pp. 4775-4778

Patent

A. S. Sahrmann, G. G. Handsfield, T. F. Besier, O. Röhrle, Ultrasound system, method for taking a 3D- and/or 4D-ultrasound image, and computer program product, DE 10 2022 206 137

Part I

Physiological and Technological Background

2 Fundamentals of the Musculoskeletal System

The human body is able to perform a variety of movements, such as running fast, carrying and lifting heavy objects, or fine motor executions such as drawing. Due to their ability to contract and generate force, skeletal muscles enable the body to perform such movements.

The human body is comprised of over 600 muscles that account for approximately 40% [75] of the body weight. The high diversity of different skeletal muscles in the body enables the variety of movements humans may perform. This chapter introduces the basics of the musculoskeletal system and explains how the structure and function of muscles can generate force and perform movements.

2.1 Hierarchical Structure of Skeletal Muscles

The muscle-tendon complex refers to a muscle attached to the bones via tendons. The muscle itself consists of many muscle fibers. The number of fibers of a given muscle may range from a few hundred to over a million [154]. The fibers vary from 10 to 60µm in diameter [64, 81] and 1 to 400mm in length [64]. A three-level network of connective tissue, which consists of collagen, connects muscle fibers and hierarchically organizes the muscle's structure, see Figure 2.1a. The three connective tissue layers are epimysium, perimysium and endomysium. Skeletal muscles are enveloped by the epimysium, which is a network of collageneous connective tissue [154], separating muscles from each other. A bundle of approximately 20-80 muscle fibers [137] is called a fascicle. Each fascicle is covered by the perimysium which paves the way for larger blood vessels and nerves. The perimysium and the epimysium are connected. The endomysium is composed of a dense network of collagen fibrils encapsulating each muscle fiber [154]. The membrane of each muscle fiber is called sarcolemma, which encloses also the sarcoplasm, i.e., the fluid enclosed within the fiber. The membrane system consists of the sarcoplasmatic reticulum (SR), the terminal cisternae and the transverse tubules. The SR is a Calcium (Ca^{2+}) storing network of channels within the fibers, which bulges into the terminal cisternae and is invaginated by the transverse tubules [64].

Myofibrils are units within the fiber. Each myofibril consists of cylindrical segments called sarcomeres, which can be considered the contractile units of the fiber. Under a microscope, the muscle reveals a dark and light striation pattern in longitudinal sections [154]. This is due to the presence of thick (15-18nm [134]) filaments, which are mainly comprised of myosin, and thin (5-8nm [134]) filaments, consisting mainly of actin. The myosin filaments comprise a long tail and a globular head. The head is extended outwards and contains a binding site for actin and an enzymatic site for catalyzation of adenosine triphosphate (ATP) hydrolysis [102]. The thin actin filaments are wrapped in

the proteins troponin and tropomyosin. Troponin contains a binding site for Ca^{2+} and tropomyosin blocks the actin's binding site for the myosin head in a resting state.

A sarcomere is an arrangement of myosin and actin filaments between so called Z-disks, as shown in Figure 2.1b. The dark, anisotropic myosin filaments are referred to as A-band, the area of actin filaments with no myosin overlap is called I-band.

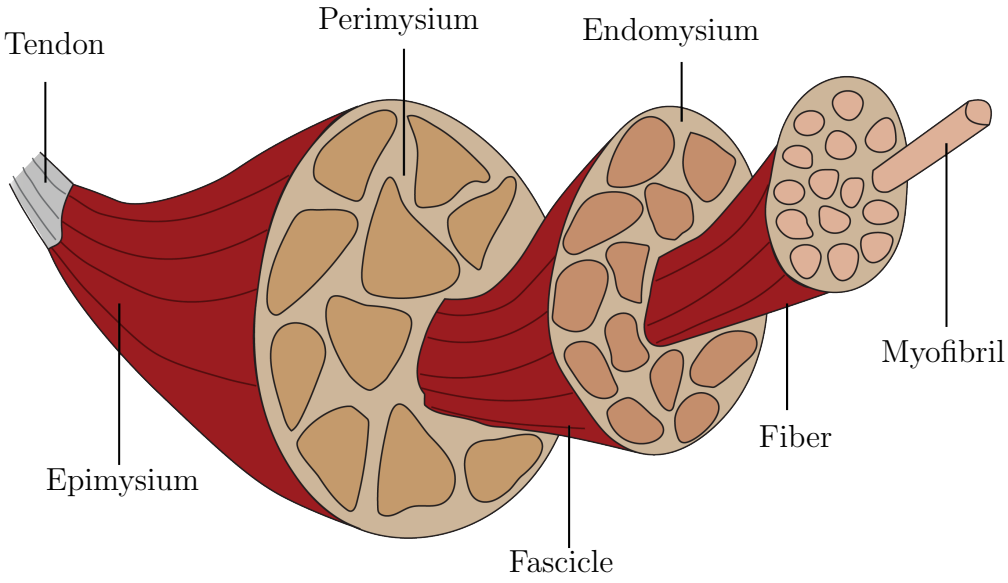

(a) Hierarchical organization of skeletal muscle.

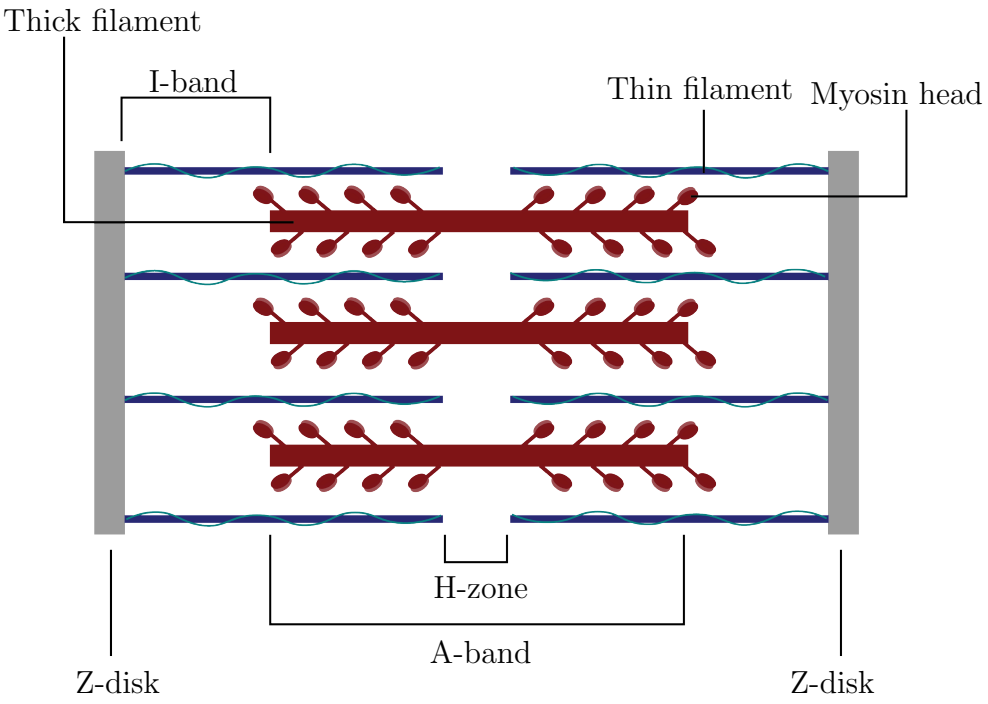

(b) Sarcomere.

Figure 2.1: (a) Hierarchical structure of a muscle from the whole muscle to the myofibril. A myofibril consists of various sarcomeres. (b) A sarcomere is an arrangement of myosin and actin filaments between so called Z-disks.

The H-Zone is the area without overlaps between myosin and actin filaments. The middle disk of the sarcomere is referred to as the M-disk, at which the myosin filaments are connected by a fine, filamentous structure. Each myosin filament is connected to the Z-disks via titin, another array stabilizing fine filaments, and surrounded by a hexagonal lattice of actin filaments [154].

2.2 Muscle Contraction

Through active contraction, skeletal muscles enable movement. Thus, they can be considered the functional unit for force generation. In order to contract, the muscle needs a signal, which it receives in the form of an action potential from the brain via the nerve pathways. Neurons innervating skeletal muscles are referred to as motor neurons. A motor unit is comprised of a motor neuron and the muscle fibers that are innervated by it. Motor units occur in different sizes, i.e., they innervate different numbers of fibers. Depending on the type of movement, either small motor units (for fine motor tasks) or large motor units (for force-intense tasks) are recruited. When a motor unit is stimulated, all fibers of the motor unit contract [102].

A distinction is made between different forms of muscle contractions. Isometric contractions are contractions in which the muscle is activated, but its length does not change. An isometric contraction can be, for example, holding an object at a certain position. A concentric contraction occurs when the muscle shortens during contraction. This occurs if the muscle is activated and lifting a load which is less than the muscle's maximum tetanic tension. Muscle lengthening during contraction is referred to as eccentric contraction.

Certain theories are employed to explain the contraction mechanism and contraction properties of skeletal muscles at the sarcomere level:

2.2.1 Excitation-Contraction Coupling

In 1954, Hugh Huxley [125] and Andrew Huxley [124] independently contributed in a major way to the understanding of muscle fiber contraction [155]. Using interference [124] and electron microscopes [125], it was observed that the A-band of the sarcomeres remains relatively constant in length during contraction, i.e., while sarcomere shortening. The I-band changed, however, its length along with the sarcomere. Through these observations, the sliding filament theory was proposed: The thin actin filaments slide past the intervening myosin filaments, when the muscle shortens. As the ends of the actin filaments come closer to each other, the H-zone gets narrower, while the A-band remains constant.

Filament sliding can be explained with a process called cross-bridge cycling: A contraction starts with an action potential traveling from the brain to the motor neuron. The action potential travels along the sarcolemma, through the transverse tubules into the SR and causes a release of Ca^{2+} from the terminal cisternae of the SR into the sarcoplasm surrounding the myofibrils. The released Ca^{2+} binds with troponin and leads to removal of the tropomyosin blockage, such that the myosin heads are able to bind with the actin filaments by building so-called cross-bridges. Through the binding, enough energy is provided such that the myosin heads pull the actin filaments towards the H-zone. This leads to the generation of force and is called power stroke, causing the sliding of the filaments

against each other. An ATP molecule binds to the myosin and enables a release of the cross-bridge, such that it can return to the original configuration. As long as there is Ca^{2+} present or there are incoming action potentials, the cross-bridge cycle is repeated.

2.2.2 Force-Length and Force-Velocity Relationship

Each cross-bridge can generate force independently. Therefore, the total force developed by the fiber during a contraction depends on the number of cross-bridge formations. Due to the cross-bridges being arranged in equal distance along the myosin filament, the amount of overlap between the thick and thin filaments defines the number of possible cross-bridge formations and thus also the amount of exerted force [102]. This indicates that there is an optimal fiber length at which the fiber can exert the maximum force.

In 1966, Gordon et al. [92] conducted experiments on isolated frog muscle fibers to establish the force-length relationship, as illustrated in Figure 2.2a. The plateau region in the mid part of the curve represents the part of a maximum number of cross-bridges formed. The plateau occurs because the thick filaments do not contain cross-bridges in the mid part, where the overlap of actin and myosin increases but the number of cross-bridges stays constant. If the fiber is stretched, the overlap decreases and thus the number of cross-bridges reduces until there are no more cross-bridge formations and therefore also no exerted force. During fiber shortening, the thin filaments start overlapping which leads to a reduction in overlap with the thick filaments, thus reducing the number of cross-bridges and the exerted force [149].

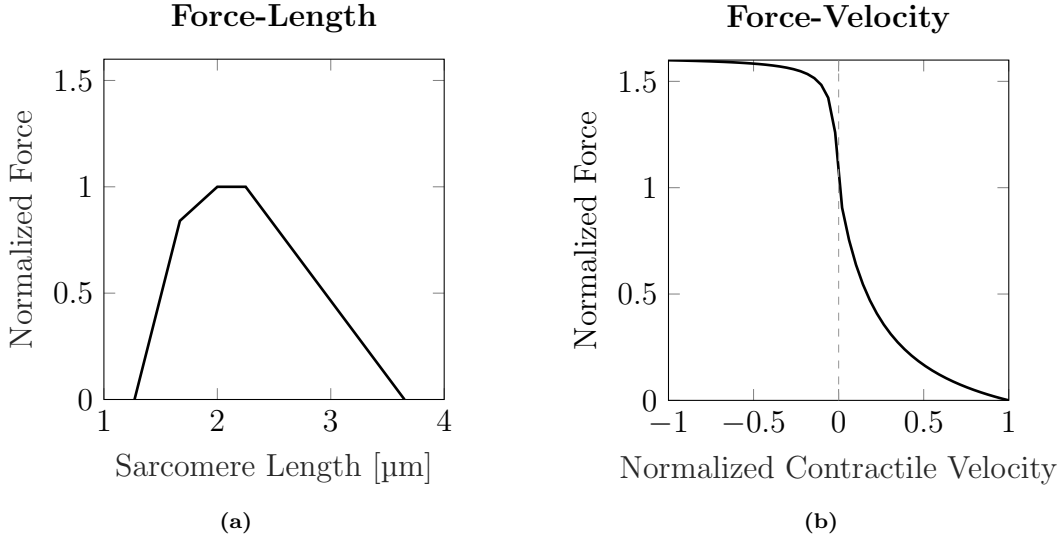

Figure 2.2: (a) Force-length relationship. Values from [92]. (b) Force-velocity relationship. Negative contraction velocities represent sarcomere lengthening, i.e. eccentric contractions. Values from [9, 103, 184].

The maximum force a muscle can exert depends on the shortening velocity of the fiber. An increased contraction velocity of the fiber leads to a reduced amount in force generation [103]. This can be explained by missed binding sites of the myosin and actin filaments as the sliding against each other speeds up, thus reducing the number of cross-bridge formations. Eccentric contractions (which is visualized as a negative velocity in

Figure 2.2b) lead to further stretching of sarcomeres which are only partially activated and thus increases the generated force [64]. The maximum cycling rate of the cross-bridges limits the maximum fiber shortening rate.

2.3 Skeletal Muscle Architecture

The large variety of muscle sizes and shapes does not only apply to the outer shape of a muscle, but also affects the inner arrangement of fibers relative to the muscle's axis of force generation. This arrangement is defined as muscle architecture [149] and has a strong effect on the muscle's functionality. In general, muscle architecture can be categorized into parallel, fusiform, pennate, as shown in Figure 2.3. Further, convergent and circular muscles exist.

For parallel and fusiform muscles, the fibers run straight from the muscle's origin to its insertion oriented in the direction of the muscle's longitudinal axis. In pennate muscles, the fibers insert to the tendon or an internal plane called aponeurosis at an angle, referred to as pennation angle. Early studies on muscle architecture determination were conducted by Gans et al. [82], who developed microdissection-based methods for enabling a measurement of the pennation angle. Fibers in pennate muscles are in general shorter than in fusiform or parallel muscles.

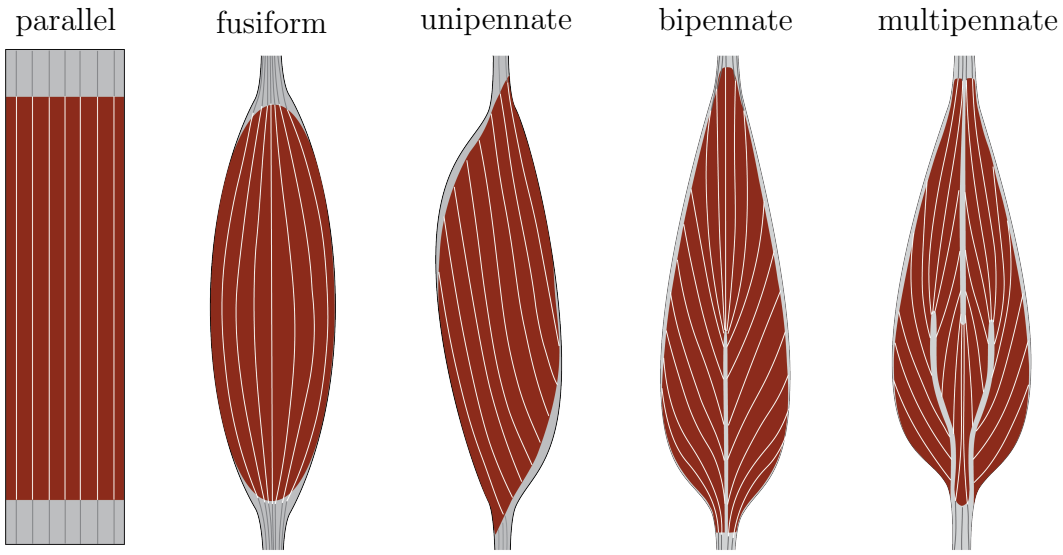

Figure 2.3: Examples for skeletal muscle architectures.

Due to different fascicle arrangements in skeletal muscles, one distinguishes between two different cross-sectional area definitions, as illustrated in Figure 2.4a: The anatomical physiological cross-sectional area (ACSA) denotes the cross-sectional area of the muscle perpendicular to the longitudinal axis of the muscle. The physiological cross-sectional area (PCSA) describes the cross-sectional area of the muscle perpendicular to the fibers at its largest point [172]. In a parallel or fusiform muscle, ACSA and PCSA coincide, but in pennate muscles, they differ.

A major difference in pennate muscles is that for the same volume, the pennate arrangement of muscle fibers allows a muscle to place significantly more fibers in the muscle

than a parallel or fusiform muscle, as illustrated in Figure 2.4b. Therefore, the larger number of fibers in pennate muscles enables the muscle to generate a higher amount of force. There exists a direct proportionality between maximum tetanic tension the muscle can generate and PCSA [150], yielding an important force-determining architectural characteristic of skeletal muscle.

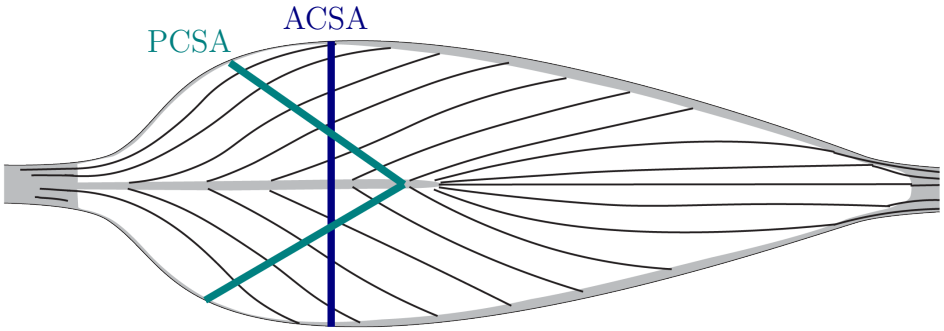

(a) Definition of physiological and anatomical cross-sectional area.

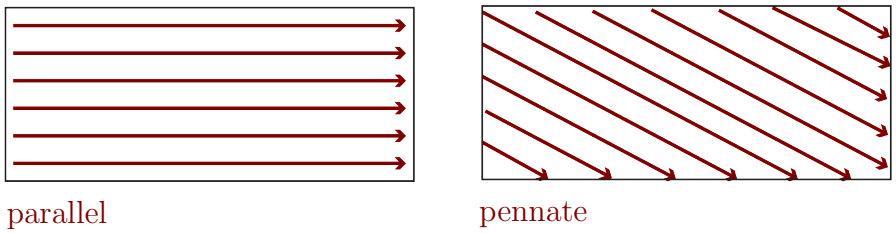

(b) Effect of packing more fibers into pennate muscles.

Figure 2.4: (a) PCSA and ACSA for an example bipennate muscle. (b) Cutout of a parallel and a pennate muscle illustrating the effect of packing more fibers into the same volume. The section of the parallel muscle contains six fibers, while the same sized cutout of the pennate muscle comprises 11 fibers.

2.4 Tibialis Anterior Muscle

The tibialis anterior (TA) muscle is a muscle in the anterior part of the lower leg, which arises "from the upper two thirds of the lateral surface of the tibia" [280] and inserts into the medial cuneiform bone and the first metatarsal bone [280]. The TA is responsible for dorsiflexion (see Figure 2.5b) and contributes to the inversion of the foot.

Architecturally, the TA is a bipennate muscle which is divided into a superficial and a deep compartment, as shown in Figure 2.5c. The compartments are divided by an internal aponeurosis, which merges with the muscle belly and the tibialis anterior tendon at the distal end. A recent study [162] found smaller values for muscle thickness and pennation angles in the superficial compartment than in the deep compartment, while it had previously been assumed to be symmetric [158].

For the investigations in this thesis, the TA was selected due to its superficial location and ease of detection using ultrasound imaging.

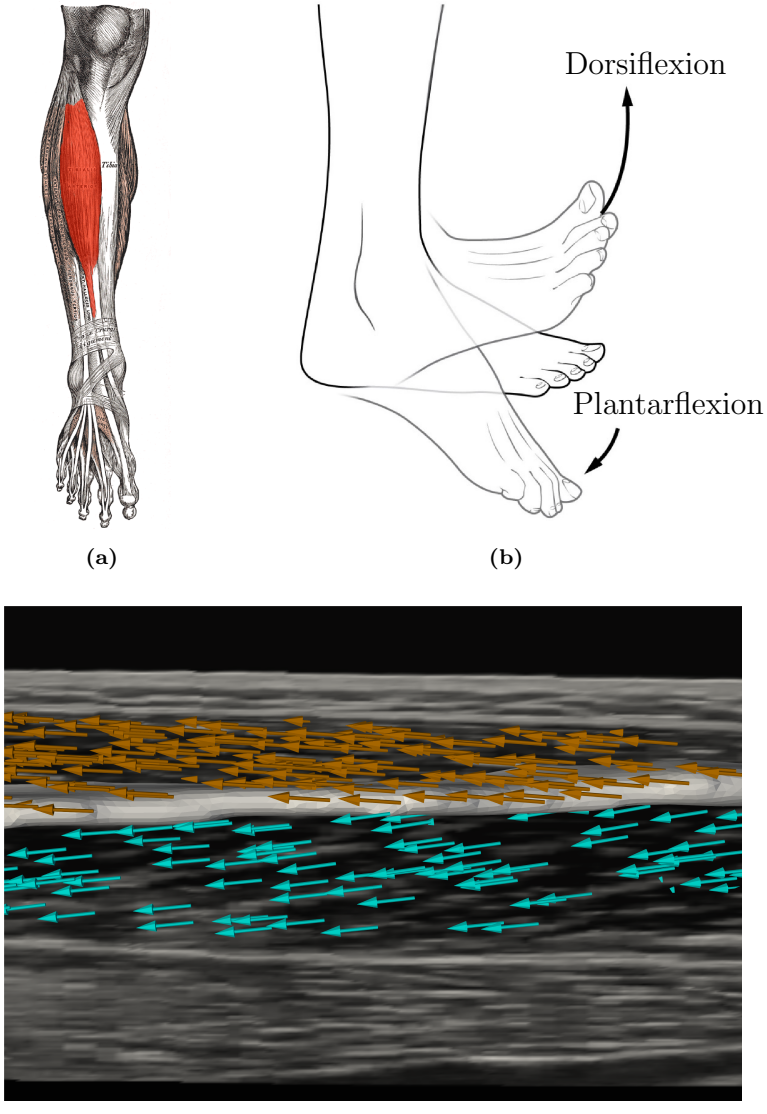

Figure 2.5: (a) Anterior view of the lower leg with the tibialis anterior muscle highlighted in red, image adapted from [4] (public domain). (b) Illustration of dorsiflexion (which the tibialis anterior is responsible for) and plantarflexion, image from [3] (licensed under CC BY 3.0). (c) Sagittal slice of reconstructed 3D ultrasound image of the tibialis anterior illustrating the superficial (orange) and deep (green) compartment.

3 Technological Background

In this thesis, 3D ultrasound-based methods are developed and presented. Due to the complexity of such technologies, this chapter presents the underlying principles. Section 3.1 explains the basic principles of medical ultrasound imaging techniques, which make the methods in this thesis work in the first place. In Section 3.2, a detailed description of the 3D ultrasound workflow, from data collection to reconstruction and visualization, is presented. Finally, a short overview of motion capture technologies is given, which are used for both 3D ultrasound methods and in the further course of this thesis (Section 3.3).

3.1 General Principles of Medical Ultrasound Imaging

Acoustic signals are longitudinal waves caused by local periodic compression of solid, liquid or gaseous material. Typically, the human ear can detect sound waves with a frequency in the range between 20Hz and 20kHz [20]. Frequencies below 20Hz are referred to as infrasound. Ultrasound waves are acoustic waves with frequencies above 20kHz [10, 177]. Figure 3.1 illustrates the sound wave spectrum.

Echolocation is a principle used by some mammals, such as bats or dolphins, which are able to sense ultrasound wave frequencies. Such animals determine the distance to objects by sending out ultrasound waves and receiving echoes. This principle is also used in medical ultrasound applications. Since the first ultrasound device in clinical use in 1958 [177], medical ultrasound has developed significantly. Nowadays, medical ultrasound imaging is a commonly employed tool for non-invasive imaging. Ultrasound imaging comes with advantages such as small size, comparably low cost (e.g., compared to MRI) and enabling acquisitions without harmful radiation (e.g., compared to CT). Common frequencies used for medical ultrasound are between 2 and 40MHz [177].

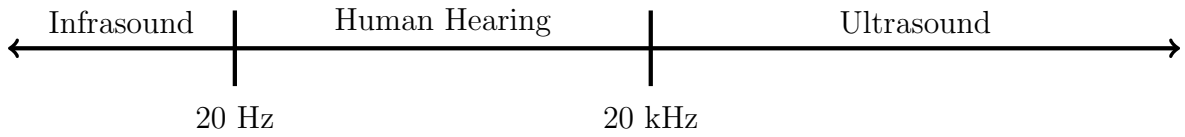

Figure 3.1: Sound wave spectrum.

3.1.1 Basic Physics of Ultrasound Imaging

The speed with which ultrasound waves travel through different types of media is called propagation speed. Its value depends on the material characteristics of the medium it travels through, especially on its density and stiffness. The propagation speed in human soft tissue is assumed to be approximately $1540\frac{\mathrm{m}}{\mathrm{s}}$ [10].

The acoustic impedance is a measure for describing the amount of resistance an ultrasound beam is exposed to once it travels through different types of tissue. The acoustic impedance is described as the product of the material's density and the speed of an ultrasound wave.

Interaction of Ultrasound Waves with Tissue

When an ultrasound beam enters the human body, various interaction types with tissue are possible, which all affect the resulting image. If the ultrasound beam reaches a boundary between two materials with different acoustic impedances, the beam is reflected and can be detected by the receiver. The magnitude of the difference in acoustic impedance is proportional to the signal strength of the echo. Therefore, if both materials have the same acoustic impedance, no echo will be produced. If they have a very large difference in acoustic impedance, the amount of reflection will be large, possibly up to total reflection. This would result in a clearly defined boundary in the ultrasound image and no visible contours behind it, see Figure 3.2. Table 3.1 shows the amount of reflection between different materials.

A beam with a perpendicular angle of incidence to the body surface will result in the largest reflection back to the transducer. If the beam has an oblique angle of incidence, then it will be reflected obliquely at an angle equal to the angle of incidence [10, 20].

Scatter appears at irregular surfaces [20] and describes a diffuse reflection of ultrasound waves in multiple directions.

As the beam travels through the tissue, it suffers from a reduction in intensity, called attenuation. As there is a dependency between frequency and attenuation, high-frequency beams will be attenuated more than low-frequency beams. In general, higher frequencies allow higher resolution, which in turn means that acquisitions of deeper tissue layers are accompanied by lower resolution [10, 105].

Boundaries	**Reflected**
Fat/Muscle	1 %
Fat/Kidney	0.6 %
Muscle/Blood	0.1 %
Soft Tissue/Water	0.25 %
Soft Tissue/Air	99.9 %

Table 3.1: Reflection of ultrasound waves at material boundaries in percent, values from [177]. Note the large amount of reflection at the soft tissue/air boundary, which can be explained by the large difference in acoustic impedance (of a magnitude of four [177]).

Echogenicity

As mentioned above, depending on the type of tissue, a certain amount of sound waves can be reflected or transmitted. The amount of reflected or transmitted waves can be characterized, which is referred to as echogenicity. It categorizes tissue into hyperechoic (visualized in white color on the ultrasound image), hypoechoic (visualized in gray color) and anechoic (visualized in black color) [126]. While fluid structures, such as blood vessels, are considered anechoic, soft tissues, such as muscles, are hypoechoic and displayed in

gray colors. Tissues such as bone are hyperechoic and result in a total reflection of the ultrasound beam. Figure 3.2 shows an example ultrasound image of the distal end of the lower limb in cross-sectional view, illustrating the echogenicity.

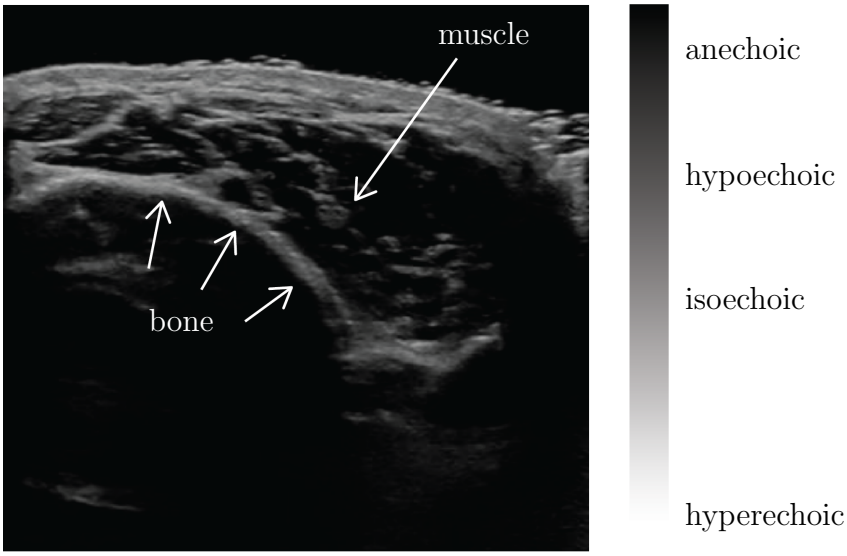

Figure 3.2: Cross-sectional B-Mode ultrasound image of the distal part of the lower leg. The prominent white area is the tibia where all sound waves are reflected. This results in a black space behind the bone boundary. The iso- and hypoechic part in the middle is the tibialis anterior muscle. The colorbar shows a reference for echogenicity classification.

3.1.2 Ultrasound Probe

An ultrasound beam is emitted from a device called transducer which can generate and detect ultrasound waves. It uses the piezoelectric effect to convert mechanical energy into electrical energy and vice versa: Piezoelectric materials change their electrical polarization and thereby produce an electric field when they are mechanically deformed. Conversely, an applied electric field (realized as a voltage pulse) causes a physical deformation of the piezoelectric material. In medical ultrasound transducers, common piezoelectric materials are lead zirconium titanate [105] and barium titanate [177].

The ultrasound probe is the device used in medical ultrasound investigations, which contains the transducer elements. Ultrasound waves can be generated by vibration of the piezoelectric transducer elements, which are disk-shaped and wrapped in thin metal [10]. Since the reflected echo causes a deformation of the piezoelectric element, an electrical signal determining the distance to the reflecting point of the echo will be generated. For ultrasound data acquisition, a mostly water-based transmission gel is used as a coupling medium to overcome the large amount of reflected ultrasound waves [10]. This is especially due to the large reflection at the air/tissue boundary (Table 3.1).

Novel technologies also exist that generate ultrasonic waves through semiconductors, covering a range of frequencies [20].

For visualization of anatomical structures as two- or three-dimensional images, ultrasound probes in medical imaging are commonly realized as an arrangement of many

transducers. Therefore, various ultrasound probe types exist for different applications, as illustrated in Figure 3.3:

Linear Probe In a linear probe, the transducer elements are arranged in a linear structure. The emitted ultrasound beams are parallel to each other. Therefore, the resulting image is rectangular-shaped. Linear probes are mainly high-frequency probes and enable high resolution imaging. Thus, they are suitable for imaging of shallow structures [177], such as the thyroid or musculoskeletal applications.

Convex Probe The transducer elements in a convex probe are arranged in a curved orientation. Convex probes have lower frequencies and enable a large field of view. Therefore, they are used for obstetrics and abdominal examinations [20]. The resulting image has a convex shape, i.e., like a truncated circular section.

Sector Probe Sector probes are smaller than linear and curvilinear probes and have a low frequency. The area of the probe touching the surface is small, such that the ultrasound beam can make its way through the intercostal space [20]. Therefore, sector probes are used for cardiac imaging. The resulting image is a circular sector.

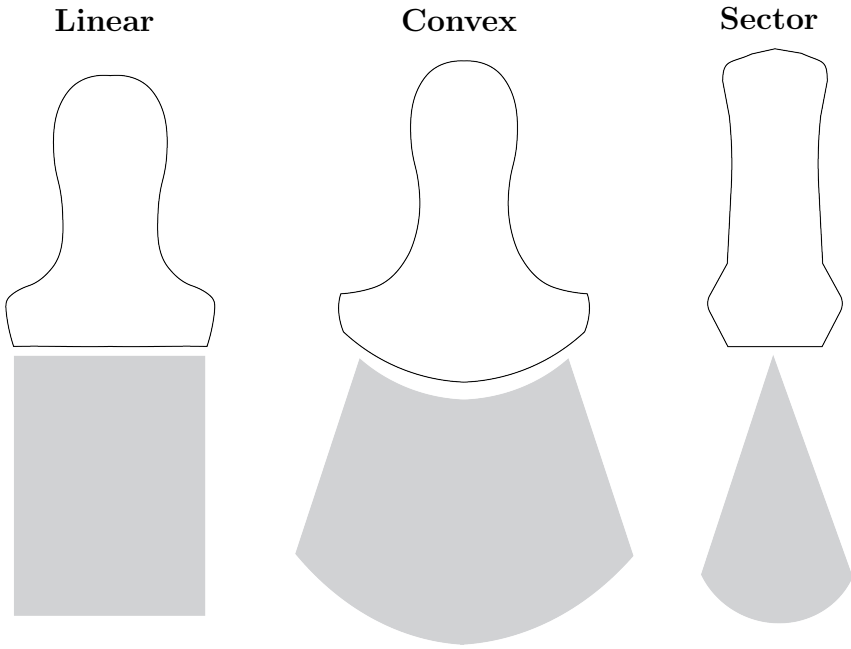

Figure 3.3: Different ultrasound probe types with the 2D image they produce, illustrated in gray.

3.1.3 Imaging Modes

Different ultrasound data acquisition modes exist, which are dependent on the type of application:

A-Mode The Amplitude-Mode or A-Mode generates a one-dimensional signal. The echo signals of a reflected sound wave are converted to voltage and are displayed as amplitudes.

B-Mode In Brightness-Mode or B-Mode, the A-Mode signals are combined into a 2D image. The amplitude of the A-Mode signal defines the intensity of an image pixel for generating a grayscale image. Therefore, various ultrasound beams are sent from the ultrasound probe. B-Mode imaging is the most commonly used ultrasound mode [177].

Doppler Mode Doppler ultrasound Mode makes use of the Doppler effect, i.e., the appearing change in frequency of a sound wave in relation to a moving observer or source. The Doppler Mode is used for visualizing blood flow. Since blood cells circulate within the vessels, frequency differences can be measured for computing blood flow velocities and directions [177].

Shear Wave Elastography Mode The Shear Wave Elastography Mode is used for the investigation of tissue elasticity. By sending out an acoustic radiation force, shear waves are induced, which lead to tissue displacement. Tissue stiffness can be measured by observing the propagation speed of the shear waves. Usually, the propagation speed of the waves is displayed as a colormap overlayed over the B-Mode image [247].

3.2 3D Ultrasound Imaging

The use of ultrasound systems for obtaining volumetric data sets began in the 1970s and the first commercially available 3D ultrasound scanner, the Kretz Combison 330, was presented in 1989 [68, 193]. In comparison to 2D ultrasound imaging, adding a third dimension for generating volumes is a promising method which comes with the following advantages [67, 68, 173, 193]:

3D Visualization of Anatomical Structures The reconstructed volume can be viewed in multiple planes or even as a surface volume, which is not possible with 2D scanning.

Decrease in Operator-Dependency The operator does not have to mentally integrate the 2D images into the anatomy. Therefore, 3D ultrasound imaging is a method with a decreased operator-dependency compared to 2D ultrasound. This may also lead to shorter image acquisition procedures. Further, for 2D scans, the operator manually controls the orientation of the image obtained. In a 3D volume, it is easier to relocate a 2D image at the exact location between scans as the operator can go through image slices.

More Accurate Volume Measurements Quantitative determinations of measurements in 3D, such as the volume of an organ, can be more accurate from 3D ultrasound data acquisition, compared to estimates obtained from 2D images.

3D Modality Fusion Volumetric ultrasound data sets instead of 2D images improve the integration into other 3D imaging modalities, such as MRI or CT.

In the following, the relevant steps for 3D ultrasound techniques are described in detail based on the common workflow, which consists of data acquisition, calibration, 3D reconstruction and visualization[1], see Figure 3.4.

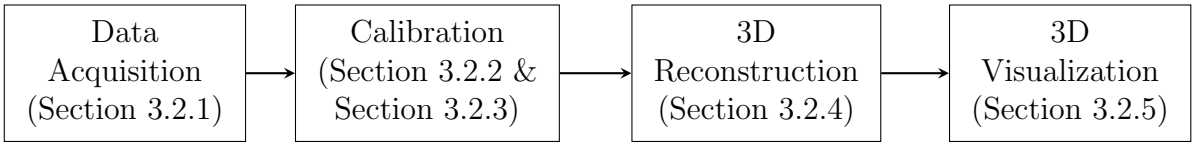

Figure 3.4: Workflow for 3D ultrasound, from data acquisition to calibration, 3D reconstruction and visualization.

3.2.1 3D Ultrasound Data Acquisition

A variety of 3D ultrasound data acquisition methods exist. They can be grouped as explained below [67, 120, 167, 173, 193]:

2D Array Transducers There are ultrasound probes with the integrated possibility for taking volumetric images. Such probes can be realized by 2D phased arrays, which generate 3D images, e.g., [15, 37, 60, 174, 263]. The beam orientation is electronically controlled, such that the beam forms a truncated pyramid as it diverges from the transducer. 2D array transducers allow data collection in real time, thus the collection of time-dependent 3D data is possible. 2D array transducers, however, come with several challenges such as the need of a large number of elements making the fabrication of these transducers rather difficult [120]. Therefore, the arrays in these transducers are relatively small which means they have a comparably small field of view [120]. 2D array transducers are mainly used for echocardiology, which requires dynamic 3D imaging of the heart and its valves, e.g., [17, 195, 223, 274].

Mechanical 3D Ultrasound Systems Mechanical 3D ultrasound systems include a mechanism which enables mechanical steering, while 2D images are continuously collected. The steering is mostly realized by a motor. The relative position and orientation of the images during sweeping are known due to the controlled movement. Thus, a 3D volume can be reconstructed from the position, orientation and the corresponding 2D images. According to their movement direction, the different types of mechanically swept 3D

[1] In this chapter, for the sake of completeness, different methods for 3D ultrasound data acquisition are presented. Not all of them require every step of this workflow, for example calibration. However, each step of the workflow is essential for the methods developed and applied in this thesis.

ultrasound can be divided into linear movement, tilting and rotation [67, 68, 120, 193]. Mechanical 3D ultrasound systems can be realized in two ways:

In mechanical 3D ultrasound probes, the scanning mechanism can be built into the probe housing. A built-in motor tilts the probe, such that so images are arranged like a fan [68]. Such 3D probes are mainly used for abdominal and obstetrical imaging, e.g., [91, 146]

In other mechanical 3D ultrasound systems, the mechanical scanning mechanism is externally attached to the probe's housing, often moved by a robot-assisted system. In linear mechanical 3D ultrasound systems, the probe is moved along a line trajectory. Such systems are often used for vascular imaging applications, e.g., [7, 143].

3D Freehand Ultrasound with Position Sensing In 3D freehand ultrasound with position sensing, the operator manually scans the body part which is to be examined. The principle of this technique is that the position and orientation of the probe are known. To achieve this, the probe is equipped with any kind of position sensor. Through the position and orientation tracking of the probe and the corresponding 2D images, 3D volumes can be reconstructed, see Figure 3.5. Benefits of 3D freehand ultrasound compared to 3D probes are the smaller size of the probe and lower cost [167]. Various methods using position tracking for 3D freehand scanning exist [58], with the most commonly used ones being optical sensors and magnetic sensors [193]. The tracking techniques are further described in Section 3.3.

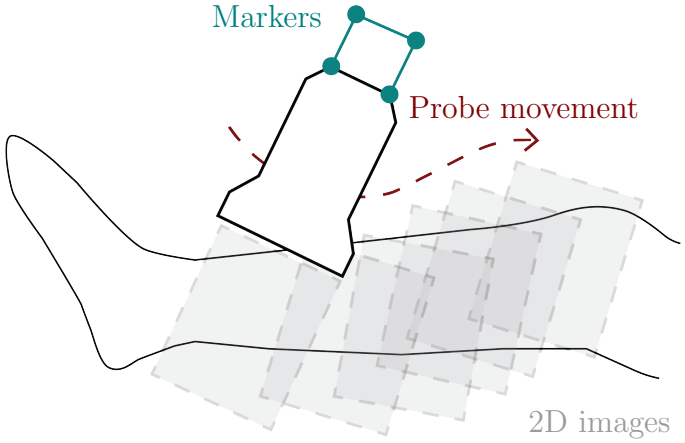

Figure 3.5: 3D freehand ultrasound with position sensing: here, as an example with reflective motion capture markers (green) applied on the lower limb.

3D Freehand Ultrasound without Position Sensing Another approach for 3D freehand ultrasound is image reconstruction without position sensing on the probe by analyzing image features, such as speckle, e.g., [84, 88, 147]. Speckle is an image artifact caused by interference of overlapping echoes [36, 55]. If two images are obtained the same way, i.e., at the same position and orientation, then the speckle will be the same. Thus, conclusions about the positions of the images can be made via the speckle decorrelation

of two images from different positions. However, accuracy of such approaches is reduced, compared to methods using position sensing [120, 173].

Further, recently presented approaches for 3D freehand reconstruction without position tracking used Machine Learning algorithms [196, 197] or tracking of skin features [244, 245].

Within the scope of this thesis, a method using the 3D freehand ultrasound technique with reflective optical markers, as well a method for mechanically and electrically moving the probe in a controlled manner are developed and presented.

3.2.2 Spatial Calibration

This thesis covers methods with mechanical and 3D freehand ultrasound systems. Both systems require the probe's position and orientation to be known. They are, however, not necessarily the same as the position and orientation of the 2D ultrasound image plane. For determining the image plane's position and orientation, a rigid-body coordinate transformation from the image plane to the ultrasound probe coordinate system is applied. The process of determining the transformation is referred to as spatial calibration, which is usually done using a phantom-based technique. The principle is that a phantom, i.e., an object with known geometry, is scanned. Then, the sought transformation matrix can be computed by correlating the position of phantom features on the image plane and on the actual phantom [167, 194]. Therefore, different coordinate systems exist, as illustrated in Figure 3.6.

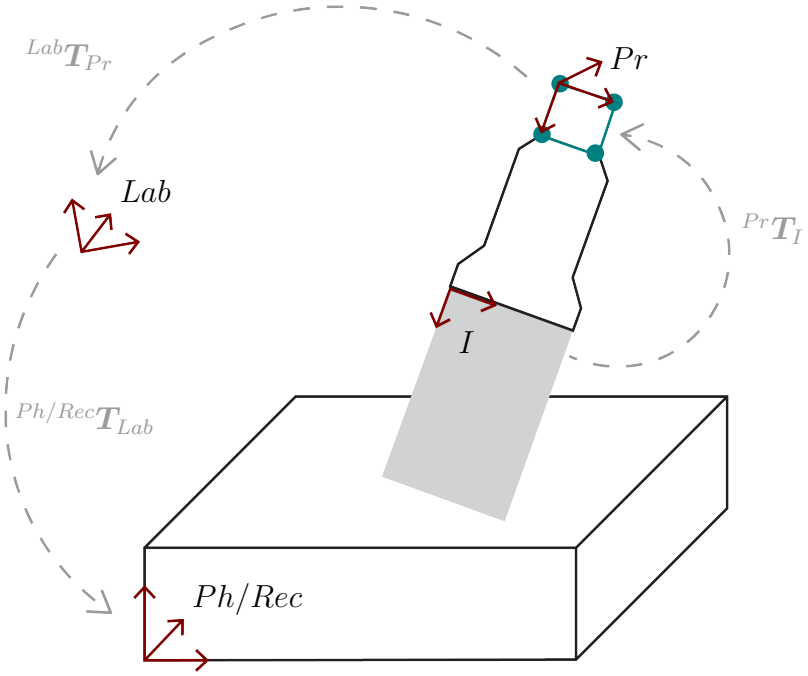

Figure 3.6: Coordinate systems and transformations of the 3D ultrasound system. *I*: Image pixel coordinate system. *Pr*: Probe coordinate system. *Lab*: Laboratory coordinate system. *Ph*: Phantom coordinate system. *Rec*: Reconstruction volume.

Each image point ${}^{I}\boldsymbol{x}$ can be mapped to the phantom's space by,

$$ {}^{Ph}\boldsymbol{x} = {}^{Ph}\boldsymbol{T}_{Lab}\,{}^{Lab}\boldsymbol{T}_{Pr}\,{}^{Pr}\boldsymbol{T}_{I}\,{}^{I}\boldsymbol{x}, \tag{3.1} $$

where Ph denotes the phantom space, Lab is the laboratory reference space, Pr describes the coordinate system of the probe and I is the 2D image space. Respectively, ${}^{Ph}\boldsymbol{T}_{Lab}$ describes the transformation from the laboratory reference space Lab to the phantom space Ph, ${}^{Lab}\boldsymbol{T}_{Pr}$ is the transformation from the probe space Pr to the laboratory reference space Lab and ${}^{Pr}\boldsymbol{T}_{I}$ denotes the transformation from the image space I to the probe coordinate system Pr.

${}^{Lab}\boldsymbol{T}_{Pr}$ can be determined directly from the position tracking mechanism attached to the probe and ${}^{Ph}\boldsymbol{T}_{Lab}$ is often known from the phantom geometry. ${}^{Pr}\boldsymbol{T}_{I}$ needs to be determined by spatial calibration. Therefore, Equation (3.1) must be solved for ${}^{Pr}\boldsymbol{T}_{I}$.

Each transformation matrix consists of three translations (x, y, z) and three rotations (α, β, γ). Prager et al. [194] defined the rotation scheme as "effected by first rotating through γ around the x-axis, then through β around the y-axis, and finally through α around the z-axis" [194]. Using this convention, each roto-translation matrix has the following form:

$$ {}^{Pr}\boldsymbol{T}_{I} = \begin{pmatrix} \cos\alpha\cos\beta & \cos\alpha\sin\beta\sin\gamma - \sin\alpha\cos\gamma & \cos\alpha\sin\beta\cos\gamma + \sin\alpha\sin\gamma & x \\ \sin\alpha\cos\beta & \sin\alpha\sin\beta\sin\gamma + \cos\alpha\cos\gamma & \sin\alpha\sin\beta\cos\gamma - \cos\alpha\sin\gamma & y \\ -\sin\beta & \cos\beta\sin\gamma & \cos\beta\cos\gamma & z \\ 0 & 0 & 0 & 1 \end{pmatrix}. \tag{3.2} $$

The fourth column of Equation (3.2) describes a translation. Since the coordinate system of the 2D ultrasound image is defined in pixels, it needs to be transformed to another metric unit for consistency with the other coordinate systems. This can be achieved by multiplication of ${}^{I}\boldsymbol{x}$ with pixel scaling factors s_x and s_y:

$$ {}^{I}\boldsymbol{x} = \begin{pmatrix} s_x u \\ s_y v \\ 0 \end{pmatrix}. \tag{3.3} $$

u and v are the column and row positions of the image pixel. Note that for calibration in a water bath, the speed of sound is dependent on the water temperature, which may lead to image distortions. For instance, for water in room temperature, the speed of sound is approximately $1485\frac{\mathrm{m}}{\mathrm{s}}$ [25, 167]. In order to solve this, a correction factor t can be multiplied by v, as described in [112]:

$$ t = \frac{\text{speed in measured water temperature}}{\text{speed in average soft tissue}} = \frac{\text{speed in cold water}}{1540\frac{\mathrm{m}}{\mathrm{s}}}. \tag{3.4} $$

Various speed of sound values in water at different temperatures can be found in [25].

Calibration Phantoms

Ultrasound calibration phantoms are usually part of or immersed in a container which is filled with an ultrasound coupling medium, e.g., water. These phantoms can vary greatly in shape and complexity. In the following, some of the commonly used calibration phantoms are presented. For the interested reader, a more detailed description of different calibration phantoms can be found in [113, 167, 194].

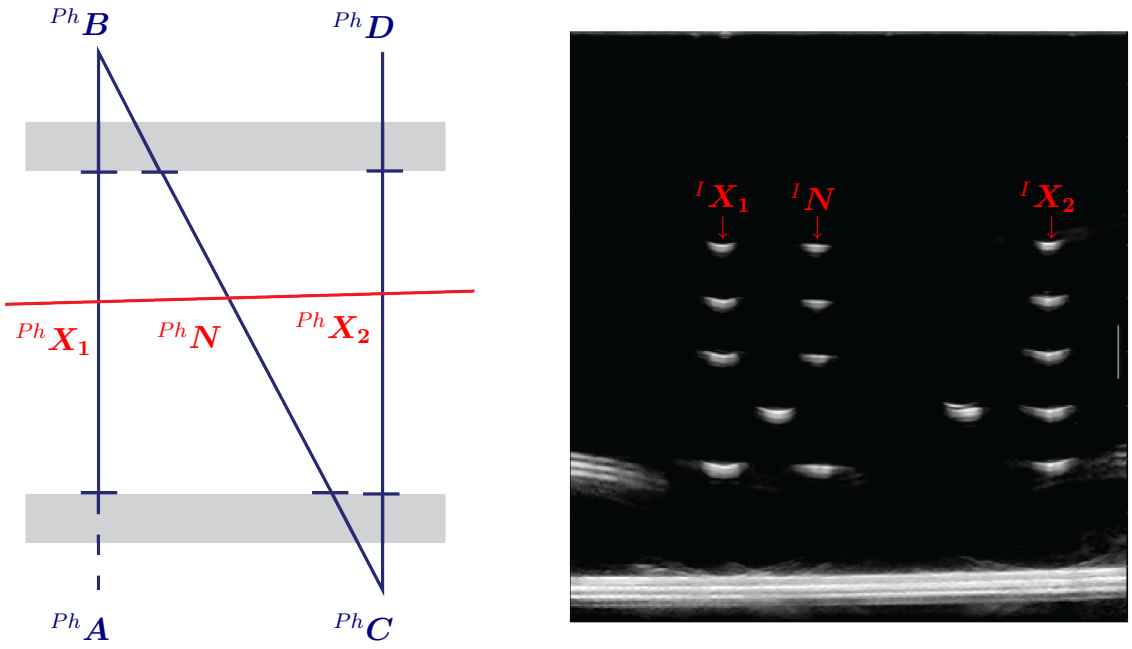

Figure 3.7: N-wire phantom. (a) Schematic view of the wires (blue) from above, the red line indicates a 2D image scan plane. The corresponding B-Mode image is shown in (b). The intersection points of the image plane with the wires are marked with red color. Note that the straight white line in the bottom part of the image refers to the bottom of the water tank.

Cross-Wire Phantom The cross-wire phantom, which was one of the first spatial calibration phantoms [113, 167, 256], is a phantom with low complexity. It consists of two wires crossing each other. The material of the wires can be nylon, for instance. When scanned with an ultrasound probe, the intersection of the wires is visible as a cross in the ultrasound image. The intersection is scanned from different directions and orientations. The position of the wires is known via a fixed phantom coordinate system relative to the wires. Therefore, the calibration matrix can be computed by solving Equation (3.1) for ${}^{Pr}\boldsymbol{T}_I$.

Single Wall Phantom The bottom of a water tank can serve as a calibration phantom itself, which is referred to as single wall phantom. It appears as a white straight line in the ultrasound image (see the bottom part of Figure 3.7b). Lines can be segmented automatically using various line detection algorithms, such as a random sample consensus (RANSAC) [70] algorithm or a Hough transform [111]. The probe is moved in different directions and orientations, such that ideally all possible translations and rotations are covered. Each detected line can be defined by two points. Therefore, two points per image can be identified to compute ${}^{Pr}\boldsymbol{T}_I$.

N-Wire Phantom N-wire phantoms were initially used for patient registration with preoperative CT scans [35] and are now commonly used for 3D ultrasound calibration. The wires are formed in an "N" or "Z" shape, which explains the naming, see Figure 3.7a. The endpoints of the wires are known by the geometry of the phantom. On the intersection plane of the ultrasound image, three points are visible on the ultrasound image for each

N-wire, as shown in Figure 3.7b.

Using geometric relations, a position $\boldsymbol{N}$ in the phantom can be determined [114] by,

$$^{Ph}\boldsymbol{N} = {}^{Ph}\boldsymbol{B} + \frac{|{}^{I}\boldsymbol{X_1} - {}^{I}\boldsymbol{N}|}{|{}^{I}\boldsymbol{X_1} - {}^{I}\boldsymbol{X_2}|}({}^{Ph}\boldsymbol{C} - {}^{Ph}\boldsymbol{B}), \tag{3.5}$$

where $|{}^{I}\boldsymbol{X_1} - {}^{I}\boldsymbol{N}|$ and $|{}^{I}\boldsymbol{X_1} - {}^{I}\boldsymbol{X_2}|$ are the distances between the respective image points[2]. They can be derived from the 2D ultrasound images.

Various further developments and improvements of N-wire phantoms have been proposed, e.g., [39, 44, 187].

Other 3D Ultrasound Calibration Phantoms Further spatial calibration techniques such as phantoms with different custom-designed geometries, e.g., [46, 230, 246], or image-based calibration methods, e.g., [268], have been proposed.

The principle of spatial calibration is that points on the images and the corresponding points in phantom space are obtained for setting up the equations to determine the calibration matrix. Since this mostly leads to more equations (from the features extracted on multiple images) than unknowns, an overdetermined system of equations arises. The system can be solved by either using iterative or closed-form methods [167]. For the closed-form solution, where a set of points is mapped to those of a phantom, a least-squares fitting method by Arun et. al [12] can be employed. Thus, the closed-form solution requires ${}^{Ph}\boldsymbol{T}_{Lab}$ to be known. The translations are determined by an alignment of two sets of points. The rotations are computed by using singular value decomposition [167]. For iterative methods, the Levenberg-Marquardt algorithm is most commonly used for 3D ultrasound calibration [167].

Calibration Evaluation

The spatial calibration can be evaluated in terms of precision and accuracy [39, 113]. Calibration reproducibility (CR) is a measure for reconstruction precision. After performing n calibration trials, CR is determined by mapping specific image points, i.e., the centroid and/or the image corners, into the probe coordinate system by multiplying them with the n computed calibration matrices. CR is computed as [39, 113],

$$CR = \frac{1}{n}\sum_{i=1}^{n}|{}^{Pr}\bar{\boldsymbol{x}} - {}^{Pr}\boldsymbol{T}_I\,{}^{I}\boldsymbol{x}|, \tag{3.6}$$

where ${}^{Pr}\bar{\boldsymbol{x}}$ is given as the centroid:

$${}^{Pr}\bar{\boldsymbol{x}} = \frac{1}{n}\sum_{i=1}^{n}{}^{Pr}\boldsymbol{T}_I\,{}^{I}\boldsymbol{x}. \tag{3.7}$$

Calibration reproducibility requires knowledge of the calibration matrix ${}^{Pr}\boldsymbol{T}_I$, but not the other transformation matrices. Therefore, it became the norm for measuring calibration precision [113].

[2] In this thesis, |...| refers to the Euclidean norm.

Point reconstruction accuracy (PRA) is a measure for spatial calibration accuracy. PRA is computed by scanning a point-like phantom (where ${}^{Ph}\boldsymbol{T}_{Lab}$ is known) n times and then transforming it to the phantom's reference coordinate system *Ref* using n different calibration matrices. PRA is computed as,

$$PRA = |{}^{Ref}\boldsymbol{x} - {}^{Ref}\boldsymbol{T}_{Lab}\,{}^{Lab}\boldsymbol{T}_{Pr}\,{}^{Pr}\boldsymbol{T}_{I}\,{}^{I}\boldsymbol{x}|, \tag{3.8}$$

where ${}^{Ref}\boldsymbol{x}$ is the position of the point in the point-like phantom's reference coordinate system *Ref*.

3.2.3 Temporal Calibration

Temporal calibration refers to the process of deriving the correct mapping of the 2D ultrasound images to the position and orientation information of the probe. This is required since the 2D images and the position data do not necessarily have the same timestamp and frame rate. The principle of temporal calibration is to scan a phantom while moving the probe in a controlled manner. Subsequently, the position of the extracted feature of the phantom and the position sensor on the ultrasound probe are compared. For example, a water bath can serve as a phantom. By moving the ultrasound probe up and down, the position of the bottom of the water bath (which is represented as a line in the image) can be correlated with the corresponding position information [253]. Similar to the spatial single wall calibration phantom, the lines on the resulting 2D images can be segmented automatically.

3.2.4 Volume Reconstruction

After collecting and synchronizing the images and position values, the data can be reconstructed as a 3D volume on a regular or irregular grid. Here, the images are mapped to the positional values corresponding to,

$${}^{Rec}\boldsymbol{x} = {}^{Rec}\boldsymbol{T}_{Lab}\,{}^{Lab}\boldsymbol{T}_{Pr}\,{}^{Pr}\boldsymbol{T}_{I}\,{}^{I}\boldsymbol{x}, \tag{3.9}$$

where *Rec* is the coordinate system of the reconstruction volume which needs to be determined and filled with image pixel values. Note that the equation is the same as Equation (3.1), except for the phantom space Ph, which is replaced with the reconstruction volume space *Rec*. In the following, the process of volume reconstruction of 3D ultrasound data is described, with a presentation of different methods.

3D Volume Determination

In theory, the 3D volume could be reconstructed in the laboratory coordinate system *Lab*. It is, however, likely that there is a large number of empty volume elements, so-called voxels, in *Lab*. This would result in unnecessary and possibly prohibitive computational overhead for filling *Lab* with image pixel values. Therefore, another coordinate system, the reconstruction volume *Rec*, is introduced. It contains all acquired images but aims to minimize the number of empty voxels. When setting up *Rec*, the orientation of the volume and the scaling of the voxels must be defined in three dimensions. The lower the

scale of the voxels, the higher the resolution of the 3D volume, but this also increases the computational effort.

One approach is to determine *Rec* by a bounding box method where a box is spanned around the maximum and minimum point of the coordinates in the laboratory space [270]. The origin of the bounding box volume is the minimum point. The dimensions of the volume can be determined by the pixel spacing [270]. More complex approaches use methods based on a principal component analysis (PCA) [132] to rotate the volume into the coordinate system defined by its principal axes.

Filling the Volume

After determination of *Rec*, image pixel values can be assigned to the internal voxel positions of the reconstruction volume. The algorithms for filling the 3D volume can be divided into the following three categories [238, 269]:

Pixel-Based Methods (PBM) In PBM, each pixel of the 2D ultrasound images is traversed and assigned to the voxels of the reconstruction volume *Rec*. PBM methods mostly consist of two steps called bin filling and hole filling. In the bin filling step, the pixels' values are assigned to voxels. Sometimes empty voxels remain after bin filling. The remaining empty voxels are filled in the hole filling step. One of the most popular methods for bin filling is pixel nearest neighbor (PNN) [212, 269], in which the nearest voxel neighbor for each image pixel position is defined and the voxel is assigned to the corresponding pixel value. Since the algorithm traverses through each pixel, multiple contributions to the same voxel are possible. In this case, various options are possible: at the occurring pixel values, one may take the average or maximum value of the so far occurring values for the current voxel, the most recent or the first pixel value. Other methods, such as kernel-based methods, spread the pixel value around a local neighborhood instead of assigning it to one voxel, e.g., [164].

As mentioned above, there might be empty voxels in *Rec* after the bin filling step, which can for example occur if the voxel size is relatively small compared to the distance between adjacent ultrasound images. Therefore, in the hole filling step, the volume filled within the bin filling step is traversed and attempted to be filled. This can be achieved by another nearest neighbor implementation, where the maximum or median value of filled voxels within a 3D neighborhood of the empty voxel is considered. Further, various approaches using different interpolation methods exist, e.g.,[59, 234, 261, 270].

Voxel-Based Methods (VBM) In VBM, all voxels of the reconstruction volume *Rec* are traversed. Voxel nearest neighbour (VNN) [231] is an algorithm where each voxel is filled with the nearest pixel value. The principle of VNN is used in the 3D freehand ultrasound acquisition and visualization system Stradx [192], which is the original version of Stradwin. Instead of generating a 3D volume, the software visualizes arbitrarily oriented 2D slices from the set of collected images, thereby achieving a fast reconstruction.

Rather than taking the value of one specific pixel for each voxel, other methods fill the voxel with an interpolation of more than one input pixel, e.g., [23, 51, 257]. A further method estimates the probe trajectory by using a virtual plane instead of the closed 2D images for each voxel [51].

Distance-weighted interpolation is a method which assigns weights to pixels within one specific region. The weight of each pixel is the inverse distance of the pixel to the voxel. Since the distance-weighted method is subject to blurring boundaries of small tissues [269], improvements have been proposed, e.g., [118, 123].

Function-Based Methods (FBM) FBMs use functions, for instance polynomial ones, for 3D ultrasound reconstruction which pass through the input pixels. By evaluating the functions at regular intervals, a resulting voxel array can be defined. Examples for FBMs are the radial basis function interpolation of Rohling et al. [212], which creates a spline approximation of the 3D volume, a Rayleigh reconstruction and interpolation with a Bayesian framework [222] or an interpolation using Bezier curves [116].

3.2.5 3D Visualization

Filling the 3D volume with pixel values generates a 3D volume. The visualization of such a volume can be especially important for diagnostic purposes. The visualization of the 3D ultrasound volume can be divided into three types referred to as multiplanar reformatting, volume rendering and surface rendering [67, 68]:

Multiplanar Reformatting In the multiplanar reformatting technique, individual 2D slices from the 3D image are displayed, which the operator can move and rotate to change the views on the tissue, see Figure 3.8a. The planes can be displayed orthogonally to each other or the 2D ultrasound images are displayed on a polyhedron.

Volume Rendering Instead of viewing single 2D planes, the volume can be rendered to view the whole 3D structure, see Figure 3.8b. Volume rendering works by casting rays through the data which intersect with the voxels of the 3D data and assigning properties to each voxel in terms of brightness, transparency and sometimes color [193]. Volume rendering is computationally expensive and does not display soft tissue details.

Surface Rendering If the volume of a particular organ or structure is to be computed, it must be delineated from the surrounding tissue. This is achieved by segmentation. By manually or (semi-) automatically contouring the boundaries of the relevant structure on the 2D images, these can be displayed as a surface representation, as in Figure 3.8c. Some algorithms only require the segmentation of several slices and can automatically compute a surface from them [254].

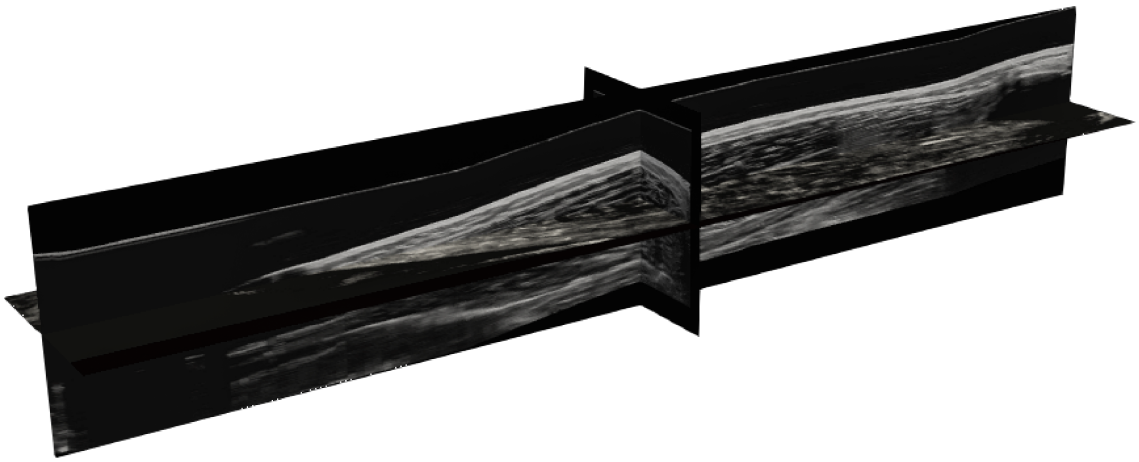

(a) Multiplanar reformatting.

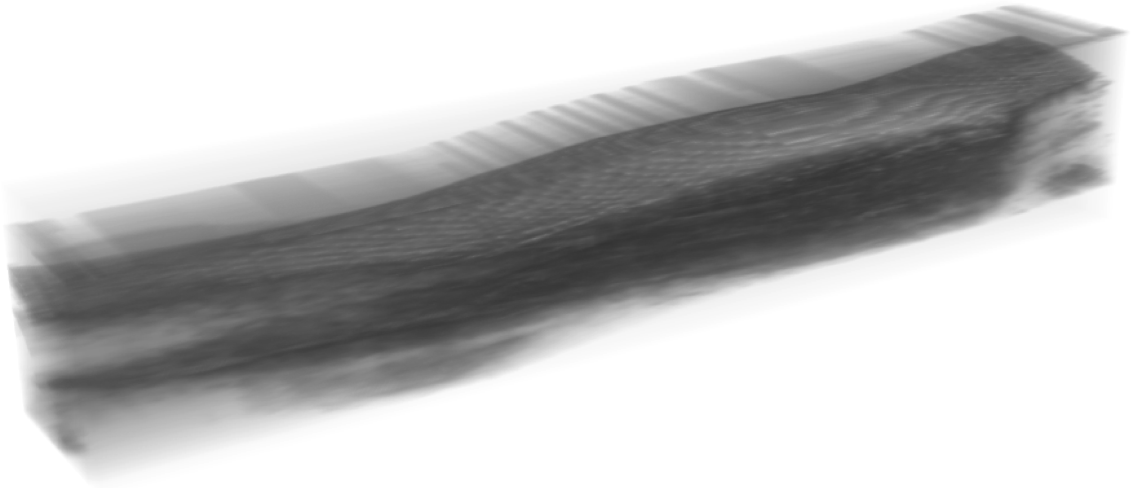

(b) Volume rendering.

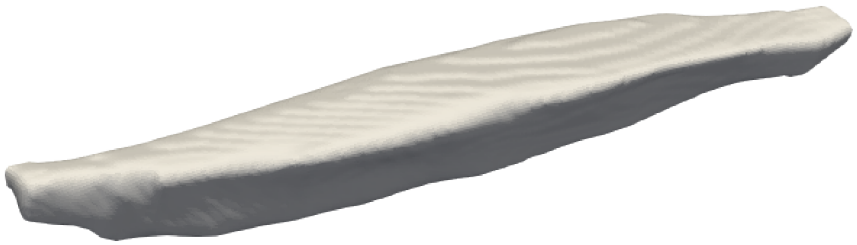

(c) Surface rendering.

Figure 3.8: Example visualizations of a 3D reconstruction of a human tibialis anterior muscle.

3.3 Motion Capture

The process of recording any kind of moving object is referred to as motion capture. The development of motion capture technology began with Eadweard Muybridge, who was able to detect a flight phase in a horse gallop in 1878 for the first time by sequentially triggering several cameras one after the other. Further, Étienne-Jules Marey developed a first high-speed camera in 1882 [272]. Since then, the technology for capturing movements has developed tremendously, with current applications in various fields such as biomechanics, gait analysis or video animation. Nowadays, a wide variety of motion capture systems with different complexities exist. The systems can be grouped into optical and non-optical methods.

Examples for non-optical methods make use of magnetic sensors and inertial measurement units. Magnetic sensors consist of a receiver and a transmitter. The strength of the magnetic field is measured by the receiver in three orthogonal directions from which the position and orientation of the object can be computed. While magnetic sensors do not need a clear line of sight between receiver and transmitter, they are sensitive to metal, especially ferromagnetic material. Inertial measurement units comprise accelerometers, gyroscopes and sometimes magnetometers. They work well for orientation estimation, but tend to suffer from location drift, so that maximum scanning time is limited [193].

In optical motion capture systems, various high speed infrared cameras are used to record markers attached to the tracked object. Such markers can be either active markers, i.e., light-emitting diodes (LEDs) or spherical passive markers consisting of or being surrounded by a retroreflective material which the infrared camera can capture. Figure 3.9 shows an ultrasound probe equipped with reflective markers for 3D freehand ultrasound imaging.

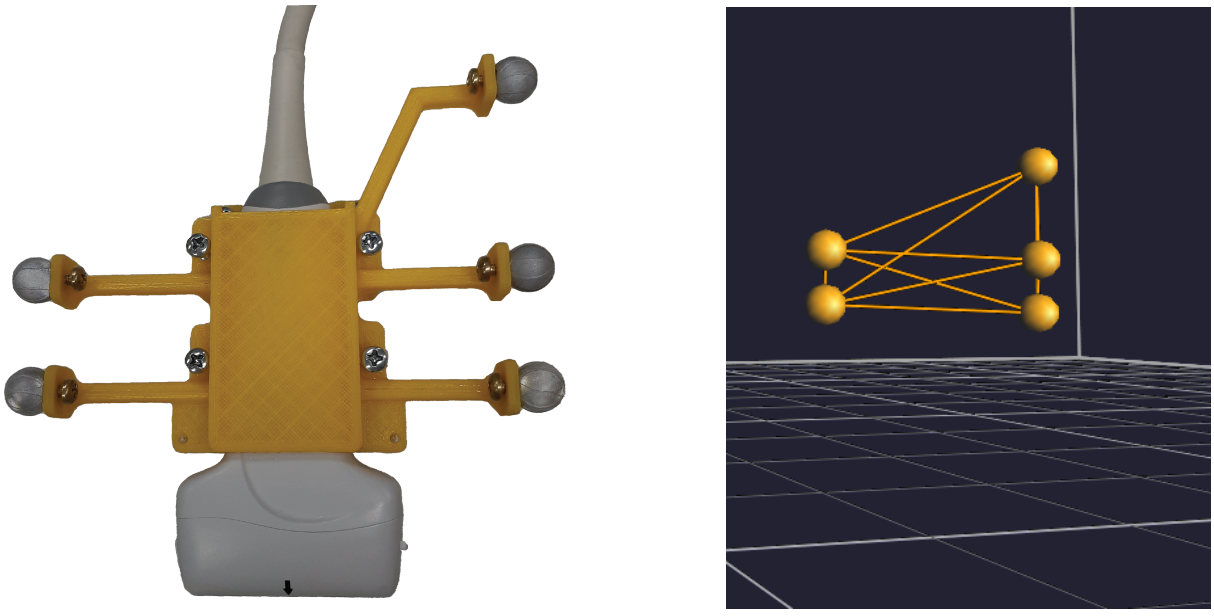

(a) (b)

Figure 3.9: (a) 3D printed ultrasound probe holder with reflective markers for freehand scanning. (b) The corresponding marker arrangement in 3D view in the motion capture software VICON Nexus (version 2.12.0).

In order to ensure that the reflective markers are recorded by the infrared cameras, it must be ensured that there is nothing between the camera and the marker hiding the marker. Optical sensors are not affected by metal parts and show high accuracy in locating 3D positions in space [193]. Through calibration of the cameras and determination of an origin of the current investigated volume, the 3D positions of the markers in the calibrated volume can be computed. Two or more cameras are needed for locating an object in a 3D coordinate system. For determination of an object's orientation, several markers are required [58] defining a segment as a rigid body. Since the aim of motion capture systems is to investigate movements of body segments, the markers are usually placed on bony landmarks of the subject for avoiding marker displacement due to soft tissue movement relative to the body segment movement.

Within the scope of this thesis, an optical motion capture system is employed.

Part II

The Automated 3D Ultrasound System

4 Development of an Automated 3D Ultrasound Workflow[1]

In 3D freehand ultrasound, manual movement of the ultrasound probe may be accompanied with variations in contact forces exerted by the operator. This might lead to inconsistent tissue deformation. Furthermore, scanning trajectories may vary between operators and between trials of the same operator, thereby reducing reproducibility in 3D freehand ultrasound investigations.

To overcome these challenges, a novel portable and automated 3D ultrasound is developed in this thesis. This chapter presents the system and a workflow for volumetric ultrasound data acquisition and volume reconstruction. The automated 3D ultrasound system, presented in Section 4.2, enables ultrasound imaging with controlled scanning trajectories by using motors which electrically move the probe. Due to integrated encoders, which provide information of the probe position, there is no need of a position sensor on the ultrasound probe. An included force control mechanism ensures a constant contact force to the skin. Some preparations and considerations in the laboratory environment, which are crucial for 3D ultrasound data acquisitions, are described in Section 4.1. Further, relevant 3D ultrasound data reconstruction methods are introduced in Section 4.3.

4.1 System Preparation

Before acquiring 3D ultrasound data, various aspects need to be considered. These include preparations and measurement options of the ultrasound system and the use of infrared cameras, e.g., when simultaneously recording of joint angles or the probe position. In this section, the essential preparation aspects for ultrasound data acquisition and the employed hardware are described.

4.1.1 Ultrasound

All ultrasound images in this thesis were acquired with a SuperSonic Aixplorer MACH30 ultrasound machine and a SuperLinear 18-5 ultrasound probe, which covers a frequency range of 5-18MHz. Linear ultrasound probes come with a higher resolution, compared to convex probes, and a larger field of view, in contrast to sector probes. Considering this, the employed linear ultrasound probe is suitable for musculoskeletal ultrasound investigations. The high resolution of the probe (below 250µm) facilitates visualization of muscle fascicles (see Section 2.1).

For 3D ultrasound imaging the tibialis anterior (TA) muscle, one needs to scan along the natural curvature of the lower limb with the linear shaped probe. Therefore, the

[1]Parts of this chapter are published in [217].

probe might not have skin contact at all points of the scanning trajectory, which allows the presence of air between the probe and the subject's skin. Since a large amount of reflection occurs at the air/tissue border (Table 3.1), the image would be entirely black beyond this border. A gel pad can be used to compensate for the curved shape of the lower leg and therefore avoid issues caused by the loss of skin contact. In this thesis, such a gel pad (Aquaflex, Parker Laboratories, Fairfield, USA) is used in Chapter 6 and Chapter 7. An image depth of 5.5cm and 4.5cm were identified as suitable for 3D ultrasound measurements of the TA, with and without using a gel pad, respectively. Figure 4.1 shows a cross-sectional ultrasound image of the TA in the distal part of the lower leg acquired without and with a gel pad.

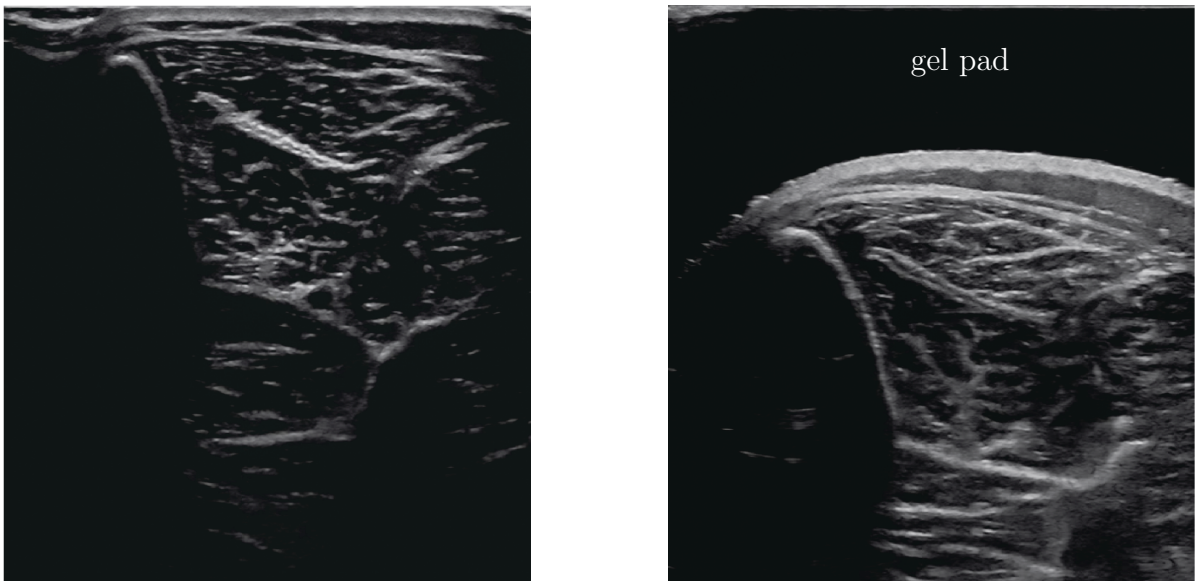

(a) Without gel pad.

(b) With gel pad.

Figure 4.1: B-mode image of a cross-section of the TA using (a) no gel pad and (b) a gel pad, image depth is 5.5cm for both. The upper black area in (b) represents the gel pad. The natural curvature of the lower leg surface is more clearly visible in (b) than in (a), where tissue deformation (e.g., flattening of the skin surface) is caused by the attempt of maintaining skin contact. Note the change in required imaging depth with the gel pad due to its own thickness.

4.1.2 Motion Capture

In this thesis, all studies using motion capture technology were conducted using a VICON system (VICON, Oxford, UK) with eight infrared cameras employing VICON Nexus software (version 2.12.0). For the system, a sensible camera alignment is essential. A main step in preparation of an experimental setup including optical motion capture systems is the correct positioning and orientation of the infrared cameras. A camera should ideally be able to detect a marker at all times. Thus, one needs to ensure that there are no objects covering the marker. However, due to its large size, the ultrasound machine may cause obstructions.

One approach is therefore to place some or all cameras on tripods, compared to a setting where the cameras are mounted at an elevated position on the laboratory walls. This is

employed for studies conducted within this thesis (Chapters 5, 6 and 7). Here, some of the cameras are placed on tripods, such that they can record markers from different perspectives, e.g., also from below the marker position, instead of only from above.

Another important aspect is avoiding the presence of other reflective objects, which can lead to erroneously detected markers. Therefore, care should be taken to eliminate or cover such reflective objects, e.g., by using tape. The automated 3D ultrasound system developed in this thesis (Section 4.2) consists of metal axes, thus they have been covered with non-reflective tape for simultaneously recording motion capture data.

4.2 The Automated 3D Ultrasound System

The previous section described the necessary preparations for 3D ultrasound data acquisition. In this section, the setup of the automated 3D ultrasound system and the underlying techniques and functionalities are introduced.

4.2.1 Functional Requirements

The aim of the automated 3D ultrasound system is to enable reproducible volumetric ultrasound acquisitions. Therefore, the automated 3D ultrasound system is designed to meet the following functional requirements:

Moveable Axes Since 3D ultrasound images are acquired by scanning along the muscle's longitudinal axis, it must be ensured that the probe can move along several degrees of freedom. Thus, the probe must be able to move along three different axes.

Cylindrical Design Since some surfaces of the human body are curved, it is crucial that the ultrasound probe can be placed not only perpendicular to the tissue, but also at oblique angles. Thus, one of the three axes should be circular. With this principle, the ultrasound probe can move around the body part, similar to a tomographic system.

Force Control Variations in contact force exerted by the operator may lead to varying levels of tissue deformation at different locations of the muscle. Consequently, the system needs to have an integrated force control mechanism which ensures a consistent contact force within one trial and across subsequent trials.

Position Sensing Optical motion capture is an expensive technology which mostly requires a laboratory environment. This makes 3D freehand ultrasound acquisitions using optical motion capture restricted in terms of portability. Thus, the automated 3D ultrasound system needs to integrate position sensing capabilities.

Size The first prototype of the automated 3D ultrasound system is developed for studies investigating the TA. Therefore, the device needs to be able to capture the entire volume and length of the muscle until the 90^{th} percentile of humans, as in ISO 7250 [5].

Expandability The first prototype is planned for investigations of the TA. These can mostly be conducted with acquisitions where only one ultrasound sweep is needed. Hence, the first prototype is planned with two axes, which are capable of moving automatically, and one axis, which is moved manually. For future applications, however, the system needs to have the possibility to automate the entire measurement workflow.

Safety Care must be taken to ensure that the system never injures the subject. Therefore, there must be an easily accessible mechanism which allows the system to be switched off immediately.

4.2.2 System Overview

The automated 3D ultrasound scanning system consists of the following components, as shown in Figure 4.2.

- the custom-designed device,
- an ultrasound machine (Aixplorer MACH30, SuperSonic Imagine) with a linear probe (L18-5), mounted on the custom-designed device,
- an industrial PC (CX2040, Beckhoff) embedded in a control cabinet to control the custom-designed device, which moves the ultrasound probe,
- a frame grabber or video capture device (USB3HDCAP, StarTech.com Ltd), connected to the ultrasound machine,
- a laptop for recording the ultrasound images (T470, Lenovo),
- an emergency stop button for ensuring that the system cannot be dangerous to the subject.

The custom-designed device is illustrated in Figure 4.3. It contains two custom-designed semicircular axes with a radius of 30cm, which are connected by a horizontal axis. In total, a scanning length of 40cm is possible. Therefore, for scans of the lower leg, the custom-designed device is capable of scanning a wide range of body sizes within the percentile range according to ISO 7250 [5].

Moreover, the size of the custom-designed device enables 3D acquisition of different muscles of the body, e.g., muscles of the back or abdominal muscles. For such a setup, the subject would lie underneath the semicircles. Here, a trade-off would be the depth of the tissue that can be imaged, or the resolution at the corresponding depth. Scanning other limb muscles, e.g., arm muscles is also enabled. Here, the subject needs to place the arm underneath the device. Furthermore, the components of the custom-designed device are very easily interchangeable and configurable. Thus, an extension of the measurement area can also be made possible. As a matter of course, for scans of larger body parts, it is also possible to exchange the horizontal axis with a longer one.

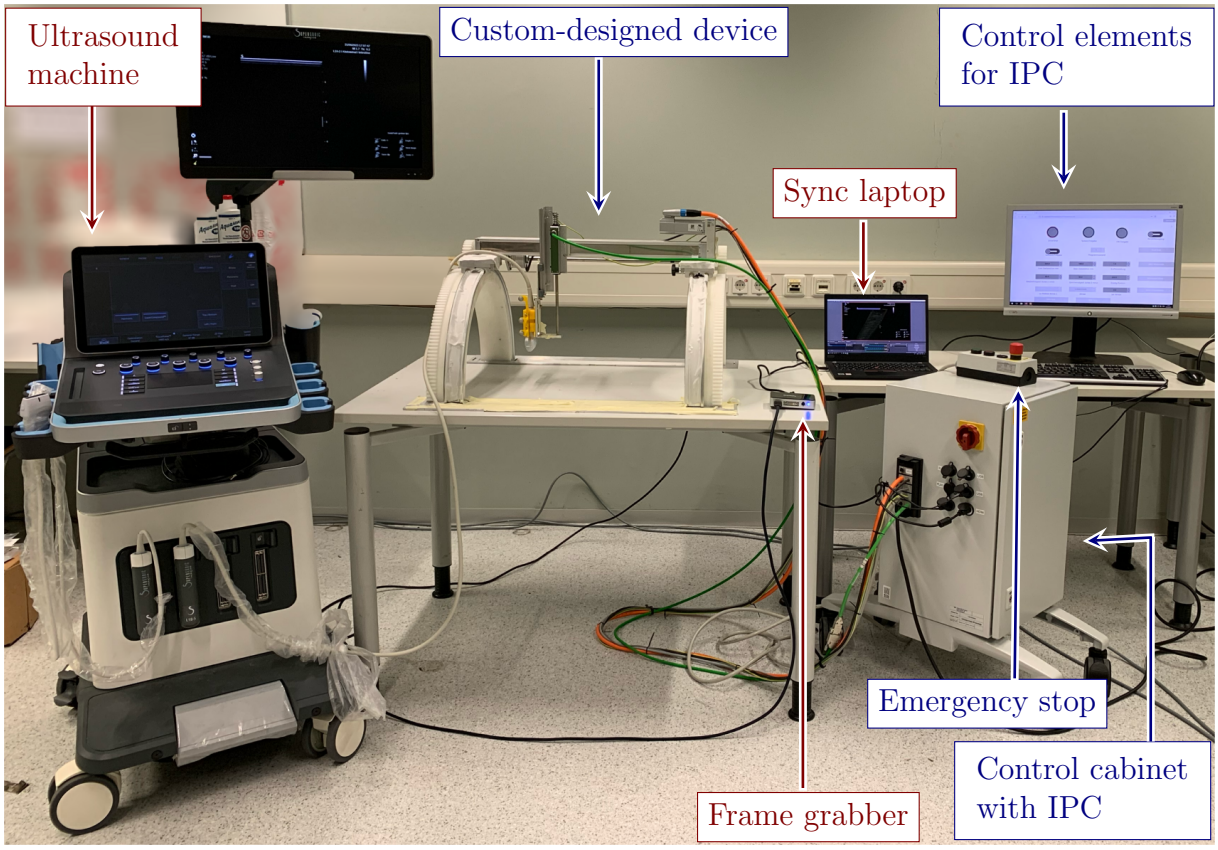

Figure 4.2: Setup of the automated 3D ultrasound system with the comprised components. Ultrasound-related components are shown in red, components of the custom-designed device are illustrated in blue. IPC: Industrial PC.

An expandable vertical axis is mounted on a moveable carriage on the horizontal axis. A 3D printed ultrasound probe holder[2] is rigidly attached to the vertical axis. The horizontal axis is moved manually on semicircles, and the design allows for 3D muscle data to be recorded within a single sweep. An extension to move the axis with a motor is possible, however, manual adjustment of the horizontal axis' position is easy and fast. Through the semicircular structure, scanning is possible from oblique angles, in both vertical and azimuthal directions. The semicircular axes are equipped with gears to ensure that the carriage will move simultaneously on both semicircles axes, and to prevent any bending due to different movements.

For moving the probe along the longitudinal axis of the muscle, the horizontal axis is realized as a spindle axis (ELGC-BS-KF-45-500-10P, Festo GmbH) which is driven by a servomotor (EMME-AS-40-S-LV-AMB, Festo GmbH). The vertical movement of the ultrasound probe is actuated by a direct linear motor with an integrated drive (NL080X-165-HR, NiLAB GmbH). The position of the probe within the device coordinate system is recorded by encoders in all axes: The horizontal and the vertical axes include linear

[2]The probe holder used within the scope of this thesis is also used for 3D freehand ultrasound imaging. Therefore, it contains placeholders for reflective markers. A detailed description of the probe holder is provided in Appendix B.

encoders measuring the position of the carriage. The angular position of the horizontal axis on the semicircles is recorded by a rotary encoder. The encoders of the horizontal and vertical axes scan the position every 2ms, while the rotary encoder operates in 10ms cycles.

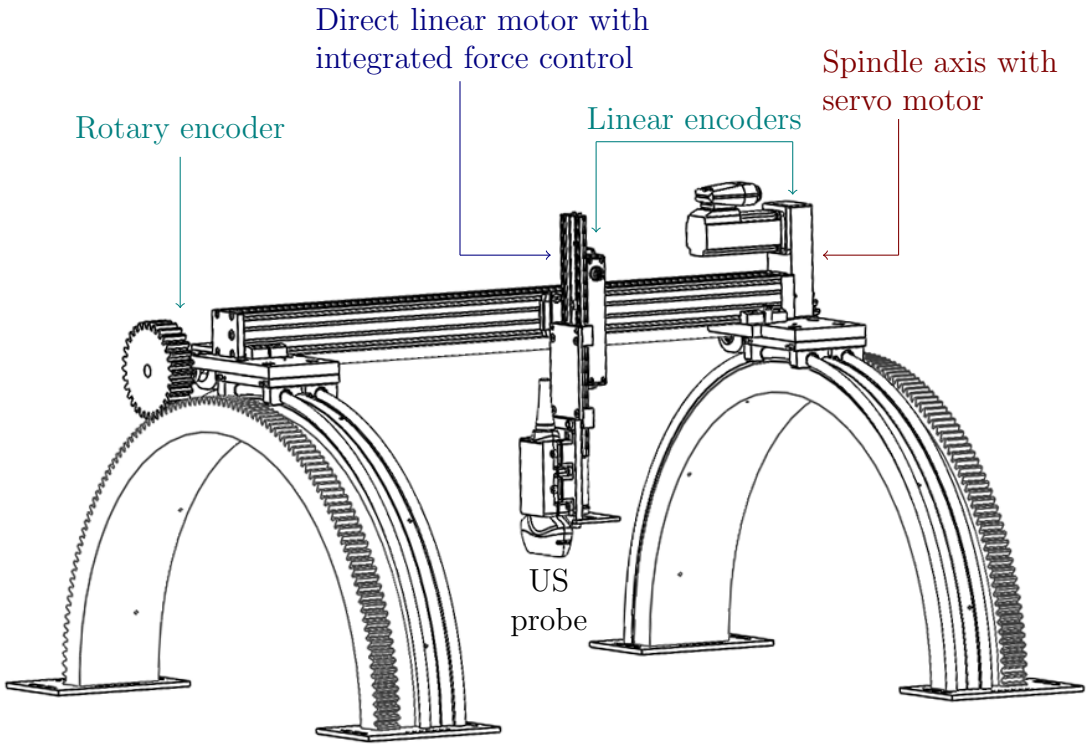

Figure 4.3: Custom-designed device with its components. The colors refer to: position sensing through encoders (green), integrated force control through the direct linear motor (blue) and horizontal movement direction through the spindle axis (red). US: Ultrasound

4.2.3 Force Control

The direct linear motor of the vertical axis of the custom-designed device has a built-in mechanism for force control applications by using voltage differences. The force control mechanism works via a cascade controller in the drive inverter, which sequentially controls position, speed and motor current with a combination of proportional-integral-derivative controllers. The motor current can be directly converted into applied force via the electromechanical properties of the motor. Thus, it is ensured that the ultrasound probe makes contact with the skin with a consistent contact force. Therefore, muscle deformation due to probe pressure is consistent. Different force settings in a range of 1 to 200 can be set by the operator through a graphical user interface on the industrial PC.

The corresponding force values in Newton have been determined experimentally with the ultrasound probe in a vertical direction, i.e., the horizontal axis positioned at the top of the semi-circle. The force values can be obtained from the curve fit in Figure 4.4. The experimentally determined force values are listed in Appendix A.

Variations in the azimuthal angle can lead to different applied forces. Within one sweep along the scanning length, the angle of the horizontal axis does not change. Hence,

the applied force does not vary within one sweep. Therefore, within one sweep, the tissue deformation over the scanning length will be consistent. For multiple sweep examinations, it is possible to adjust the force setting according to the current angle at the semi circles, as this can be computed using geometric relations.

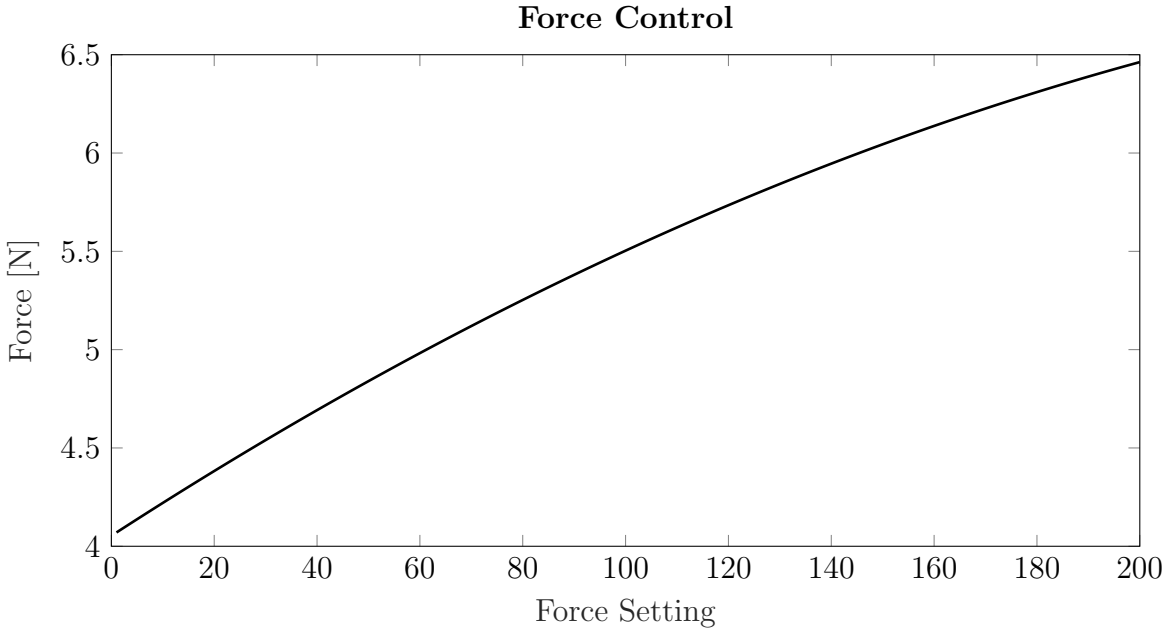

Figure 4.4: Force values and settings after curve fitting.

4.2.4 Device Control

The automated 3D ultrasound system is controlled via an industrial PC with a custom-written program in TWINCAT (version 3.1.4024.32) including four main movement modes, as illustrated in Figure 4.5. For all modes, position information of the encoders is saved during the recording and can be exported in CSV-format. Movement velocity of the axes can be set manually for all modes. For three of the modes, the operator can set a desired force setting as in Figure 4.4. The movement modes are possible with contact force on the scanned medium or within a liquid medium, e.g., water. The movement modes are as follows:

Vertical Movement The operator specifies an end point on the horizontal axis. The device moves the probe to the end point. The probe is then periodically moved upwards and downwards, until the operator stops the acquisition. The *Vertical Movement* mode is used for the temporal calibration. Therefore, it is mainly used in a liquid medium, e.g., a water bath.

Move to Target The *Move to Target* mode is intended for static measurements where the probe remains fixed in one place. The automated 3D ultrasound system moves to an operator defined point on the horizontal axis. Then, the vertical axis moves down and holds a position with constant force (if in contact with a surface) until the operator stops the acquisition.

Scanning Movement The device moves from a defined start point to a defined end point on the horizontal axis. This mode is used for 3D ultrasound measurements with one sweep, such as for the TA. As for the *Move to Target* mode, a desired force setting may be selected.

Pendulum Movement The pendulum mode works the same way as *Scanning Movement*, but does not stop after reaching the endpoint. Instead, it moves periodically between the start and endpoint until the operator stops the measurement via a stop button. A desired force setting can be selected, as for the *Move to Target* and *Scanning Movement* mode. This mode is primarily used for dynamic TA investigations, as described in Chapter 7.

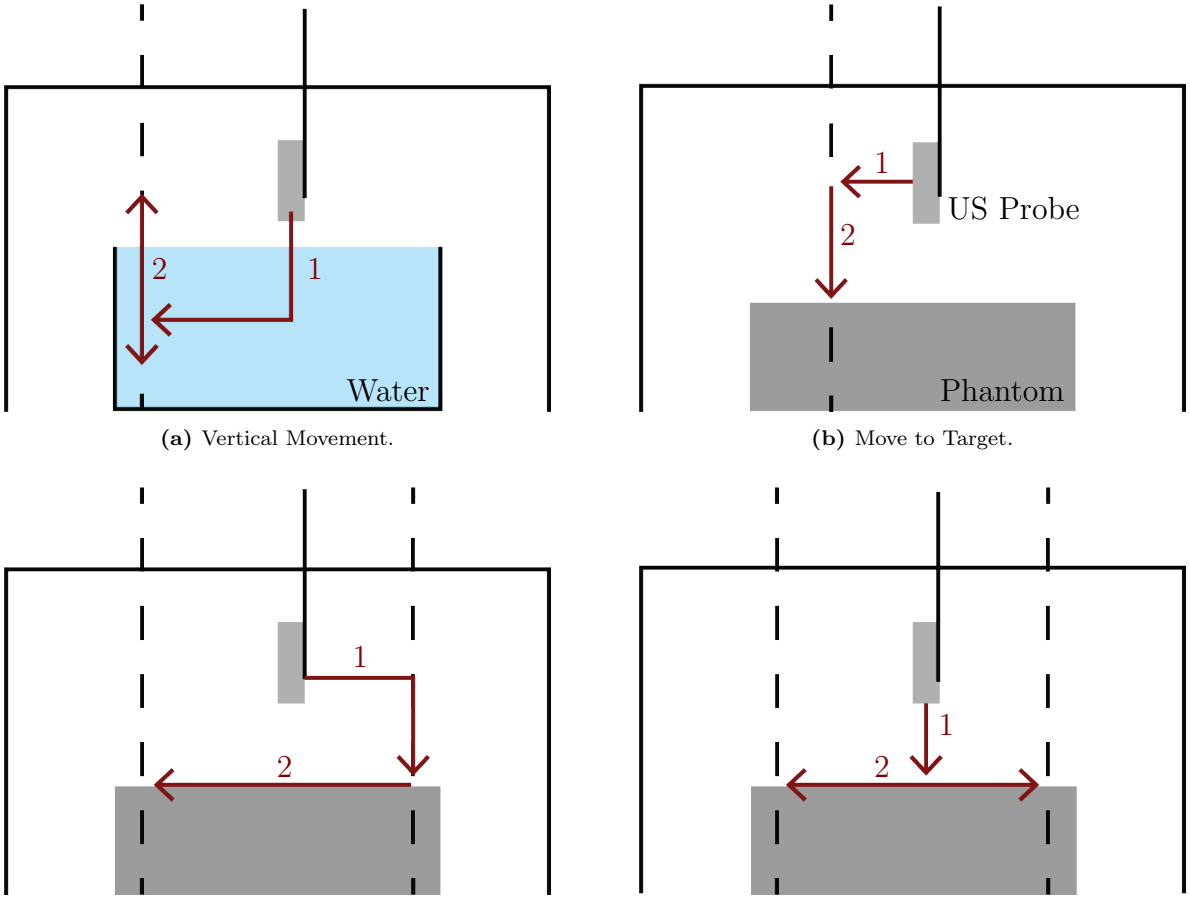

(a) Vertical Movement. **(b)** Move to Target. **(c)** Scanning Movement. **(d)** Pendulum Movement.

Figure 4.5: Device modes. (a) Vertical Movement (within a liquid medium, e.g. water). (b) Move to Target. (c) Scanning Movement. (d) Pendulum Movement. The numbered arrows illustrate the sequence of executed movements. US: Ultrasound.

4.2.5 Synchronization

To synchronize the recording of the ultrasound images and the positional encoder data, a trigger signal is activated each time the device starts or stops a movement, as illustrated in Figure 4.6. A custom-written Python script (Python 3.10.6) receives the signal and starts or stops a recording in OBS studio (version 27.2.4). It is also possible to synchronize the encoder data with the motion capture data. For this, the device sends a trigger signal (5V) to the motion capture acquisition board's trigger input and starts or stops a recording in the VICON Nexus software (version 2.12.0).

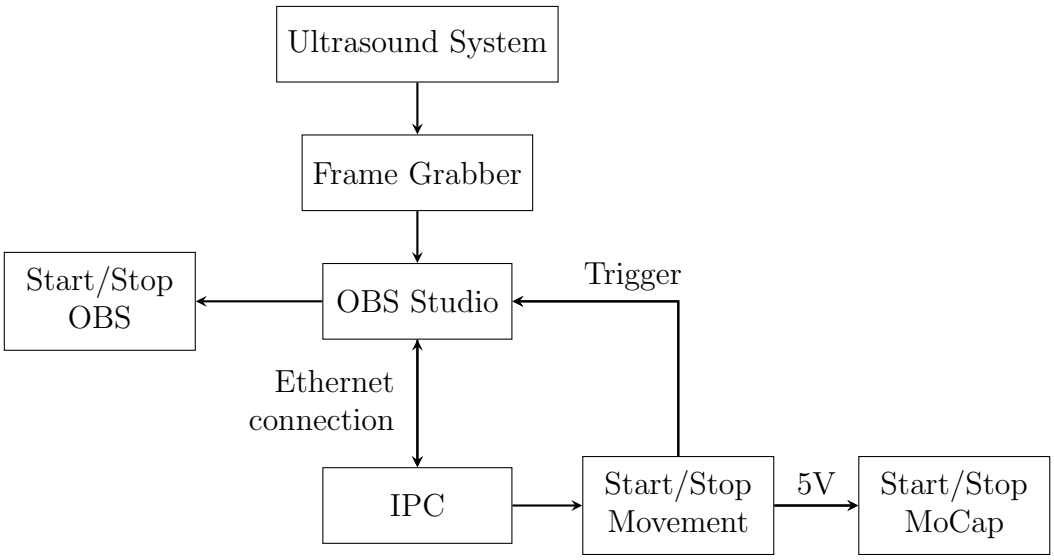

Figure 4.6: Synchronization: Once a movement of the custom-designed device is commenced using the industrial PC (IPC), it simultaneously sends a trigger to the laptop with OBS studio. The trigger further starts a video recording of the ultrasound images using the frame grabber until it receives a stop signal. If desired, it also triggers a recording of the motion capture (MoCap) data.

4.2.6 System Calibration

Spatial and temporal calibration are required for determining the image position and the temporal shift between the images and the position information, as explained in Sections 3.2.2 and 3.2.3. In the following, the implementation of the calibration methods is described.

Spatial Calibration

In this thesis, an N-wire phantom (fCal-2.0[3]) is used for spatial calibration, which is available at the Plus toolkit [144] website[4]. The phantom consists of four walls, two of which have holes with a diameter of 1mm. The wires can be spanned through the holes. The walls with the holes are 140mm long and have a thickness of 10mm, the distance between them is 90mm. The holes are arranged in a distance of 5mm from each other

[3]The fCal-2.0 phantom has been extended for 3D freehand ultrasound imaging in this thesis. A figure and further description of the extension can be found in Appendix B.

[4]https://plustoolkit.github.io/features

in the vertical and horizontal direction. In total, this leads to an arrangement of five rows and 17 columns of holes. Therefore, one can span five N-wires in the phantom. In addition, there are elevations on the outer sides of the walls to be able to fix the wires by means of rubber bands.

The intersection points of the wires of the N-wire phantom and the ultrasound image scan plane appear as points on the 2D ultrasound image, as illustrated in Figure 4.7a.

Automatic Wire Detection In this thesis, an algorithm for automatically detecting the N-wire points on the ultrasound images is developed and implemented. First, the outer edges of the image are set to zero in order to avoid false detection, such as the bottom of the water tank or reflections, see Figure 4.7b.

The algorithm for detecting the wire positions on the image works as follows:

1. First, the image is transformed to a grayscale image, such that all pixel values are within a range between zero and one.

2. A threshold value (typically between 0.3 and 0.4) is defined. Pixel values below the threshold value are set to zero (Figure 4.7c). This avoids interference effects caused by reflections, e.g., by the bottom wall of the water tank.

3. After thresholding, a label matrix is created, which gives labels to the connected components of the image. This is realized with the Matlab (R2020a) function *bwlabel*, which employs an algorithm that is further described in [97].

4. There are five wires in the existing N-wire Phantom, which means 15 visible points per image. Therefore, the 15 labels with the largest number of associated data points are determined. This step is done in order to avoid erroneous detection, such as reflections.

5. For each of these 15 largest point clusters, the position of the centroid is computed.

6. The positions of the centroids are the wire positions, see Figure 4.7d. In order to be able to assign the positions to the correct wires, they are sorted in rows and columns.

For measurements where the phantom is aligned vertically under the probe or to avoid minor false detections, two additions have been implemented to ensure that the wires are aligned with each other. With the extensions, the column position (x-coordinate of the image) and row position (y-coordinate of the image) can be set to the mean of the current considered column or row (Figure 4.7e and 4.7f).

Since the phantom matrix is unknown for automated scans, there are in total 12 unknowns (six translational and six rotational degrees of freedom) in the resulting system of equations. Over 10 calibration trials, the calibration reproducibility, as in Equation (3.6), using the Levenberg-Marquardt algorithm was determined as 0.651mm. This means that the variability in reconstructed point position on the images is 0.651mm [113].

The wire detection algorithm was implemented using Matlab (R2020a).

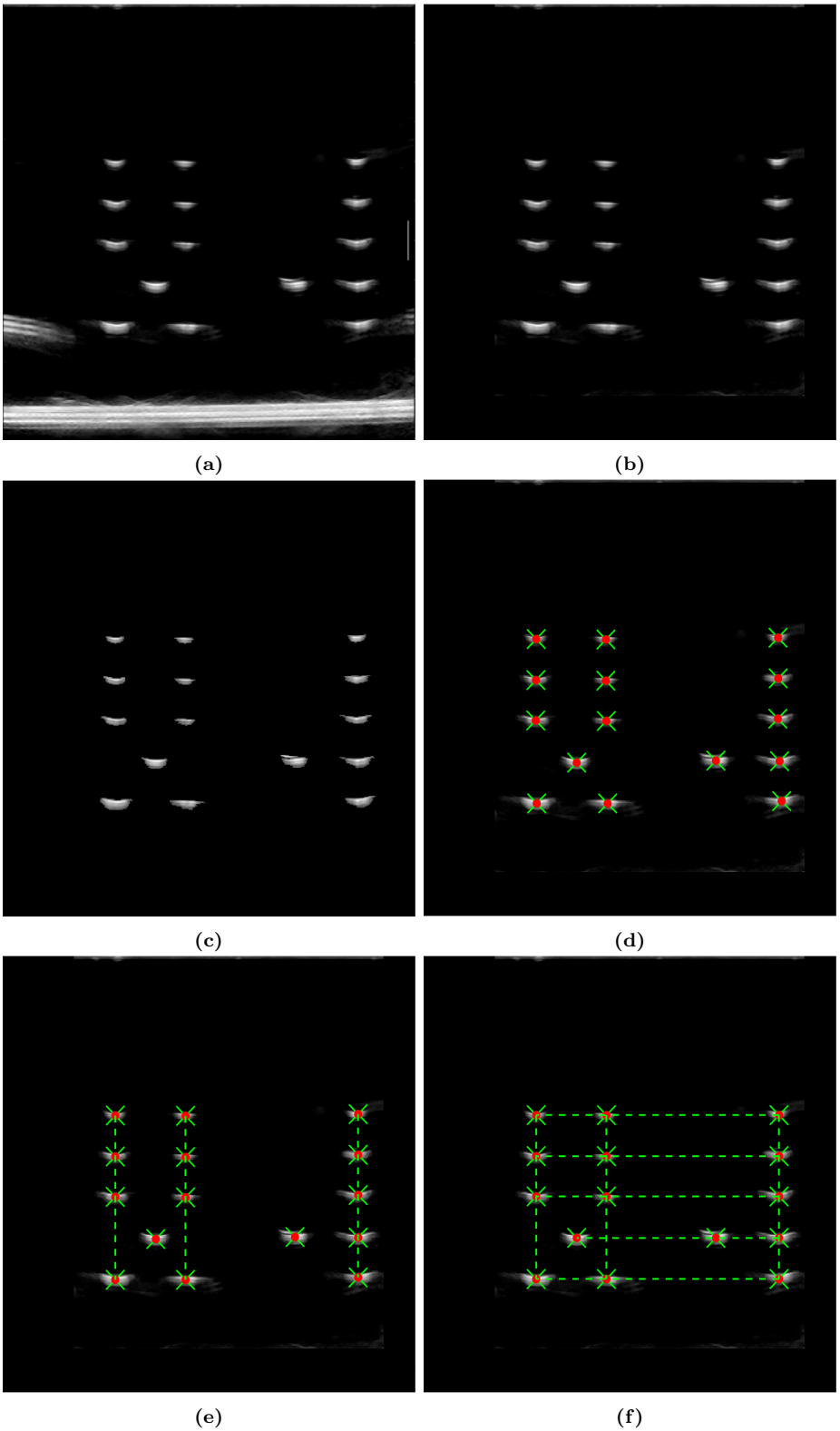

Figure 4.7: Wire detection algorithm for N-wire calibration. (a) Original image, the points correspond to the wires intersecting with the imaging plane. The line in the bottom corresponds to the bottom of the water tank. (b) Image after setting outer edges to zero. (c) Thresholding of the image. (d) Detected wires (red points, green crosses are for better visualization). (e) Column-wise stacking of detected wires. (f) Row- and column-wise stacking of detected wires.

Temporal Calibration

For determination of the temporal shift between the ultrasound images and the position information, a method from Treece et al. [253] is used, where the probe is periodically moved up and down in a water tank, realized by the *Vertical Movement* mode. The relative vertical movement of the bottom of the water tank is visible in the ultrasound images as a line moving up and down.

Automatic Line Detection For automatically detecting the line in the ultrasound image, a method from Prager et al. [194], who introduced a simplified approach from Clarke et al.'s method [48], is implemented:

A given number of vertical lines is extracted from the image. In this thesis, the number of vertical lines is selected as 24. The pixel values along each of such lines are filtered with a 2D Gaussian smoothing kernel. After the Gaussian filter, the numerical gradient of the lines is computed. High values of the gradient are caused by strong dark-to-light transitions. Therefore, in order to detect the first bright line in the image, the gradient lines are scanned from the top part of the image until they exceed a certain threshold value. This determines one pixel for each vertical line. However, due to the appearance of noise or poor ultrasound image quality, it is possible that points outside the searched plane are identified.

Since such points can be considered outliers, a random sample consensus (RANSAC) [70] algorithm is used for fitting the line to the pixel points. The RANSAC algorithm is an iterative method for estimating a mathematical model of a data set which contains outliers. The algorithm works as following:

1. First, a sample of a small subset of data points, which are treated as inliers, is taken.
2. A line is fit to the chosen data points from step 1.
3. A score is defined by counting the amount of inlier points where a high score indicates a high number of inliers.
4. Steps 1 to 3 are repeated n times.
5. The solution with the highest score is taken.

Figure 4.8 shows two example frames of a temporal calibration trial with detected lines and identified outliers.

After determination of the line position, the curves for line and marker position are normalized to a scale between zero and one, see Figure 4.9. The temporal offset can be determined via a cross-correlation. Encoder position data is collected with a higher frame rate, i.e., 500Hz, than the ultrasound images. In this thesis, the frame grabber collects images with a frame rate of 30Hz. Therefore, both image and position data are first resampled to 1000Hz for computing the temporal shift in milliseconds. The temporal resolution is restricted by the ultrasound's frame rate. For the automated 3D ultrasound system, the resulting shift between position data and ultrasound images, determined from temporal calibration, was 27.13±17.14ms. This is within the frame time of one ultrasound frame acquired with a frame rate of 30Hz, i.e., a frame time of 33.33ms.

The line detection algorithm was implemented using Matlab (R2020a).

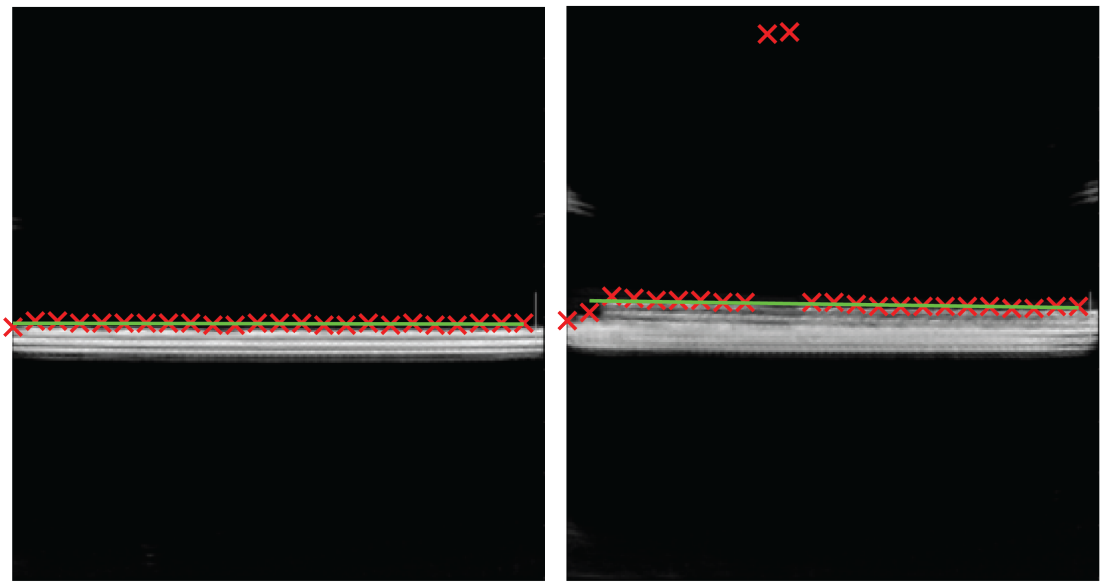

(a) (b)

Figure 4.8: Example frames after line detection. The red crosses indicate detected positions at the vertical lines and the line fit is shown in green. (a) Line fit without significant outliers. (b) Line fit that is not affected by significant outliers.

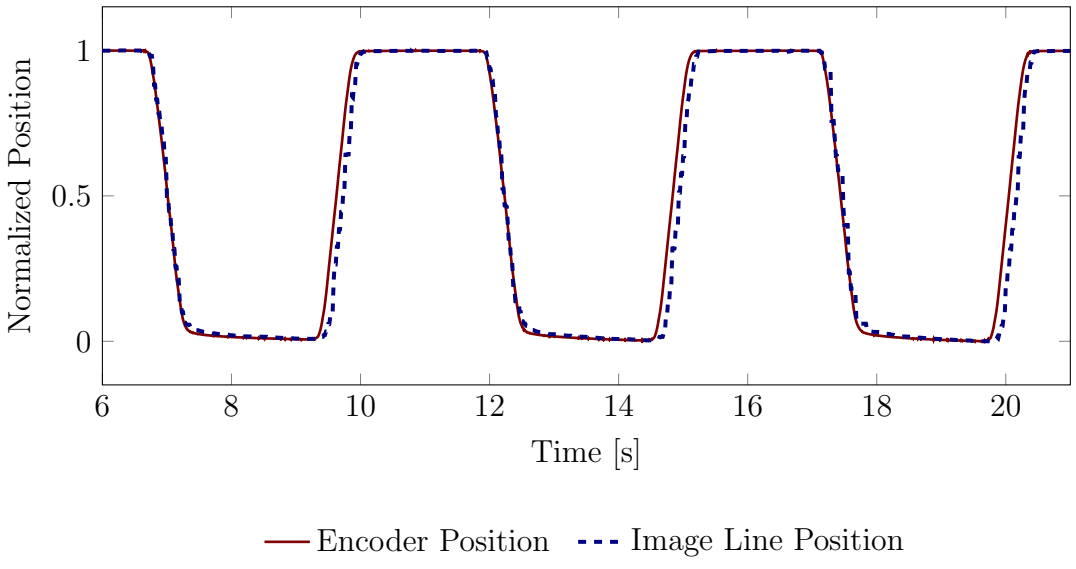

Figure 4.9: Temporal calibration for the automated 3D ultrasound system. The graph shows the line position in the ultrasound image and the vertical encoder position. Note the matching plateaus, similar to time intervals with negative slope. Only time intervals with positive slope show a slight shift, however, they do not accumulate over time.

4.2.7 Coordinate Transformations

For 3D reconstruction of the ultrasound images, the following sequence of transformations, similar to Equation (3.1), needs to be applied, see Figure 4.10:

$$ {}^{Rec}\boldsymbol{x} = {}^{Rec}\boldsymbol{T}_{Dev}\, {}^{Dev}\boldsymbol{T}_{Pr}\, {}^{Pr}\boldsymbol{T}_{I}\, {}^{I}\boldsymbol{x} \; . \tag{4.1} $$

Rec describes a given reconstruction volume, *Dev* is the device coordinate system, *I* refers to the ultrasound image plane. Therefore, ${}^{I}\boldsymbol{x}$ and ${}^{Rec}\boldsymbol{x}$ are the positions of each image pixel in image and reconstruction space, respectively. ${}^{Rec}\boldsymbol{T}_{Dev}$ is the transformation from the device coordinate system to the reconstruction volume space, ${}^{Dev}\boldsymbol{T}_{Pr}$ is the transformation from probe to device coordinates, ${}^{Pr}\boldsymbol{T}_{I}$ is the transformation from the image scan plane to the probe coordinate system, which is obtained from the calibration protocol. ${}^{Dev}\boldsymbol{T}_{Pr}$ can be obtained from the encoder data. The transformation consists of a translation $\boldsymbol{T}_t$ and a rotation $\boldsymbol{R}$. For the rotation around the horizontal z-axis, a rotation matrix is applied. The translation vector is composed of the z position which can be directly determined by the horizontal axis encoder. The y positions can be determined from the position information of the vertical and rotary encoders. The device coordinate system's origin is located in the center of the semicircle at $\varphi = 0°$. Further, the rotation and translation matrices are given as,

$$ \boldsymbol{R} = \begin{pmatrix} \cos\varphi & -\sin\varphi & 0 \\ \sin\varphi & \cos\varphi & 0 \\ 0 & 0 & 1 \end{pmatrix} \text{ and } \boldsymbol{T}_t = \begin{pmatrix} 0 \\ (r-v) \\ h \end{pmatrix}, \tag{4.2} $$

where φ is the angle from the rotary encoder in degrees, r the semicircle radius (300mm), y is the current location of the vertical axis in millimeter and z is the current location on the horizontal axis. Translation and rotation can be combined in a 4x4 roto-translation matrix:

$$ {}^{Dev}\boldsymbol{T}_{Pr} = \left(\begin{array}{ccc|c} & \boldsymbol{R} & & \boldsymbol{T}_t \\ \hline 0 & 0 & 0 & 1 \end{array}\right) = \begin{pmatrix} \cos\varphi & -\sin\varphi & 0 & 0 \\ \sin\varphi & \cos\varphi & 0 & (r-v) \\ 0 & 0 & 1 & h \\ 0 & 0 & 0 & 1 \end{pmatrix} . \tag{4.3} $$

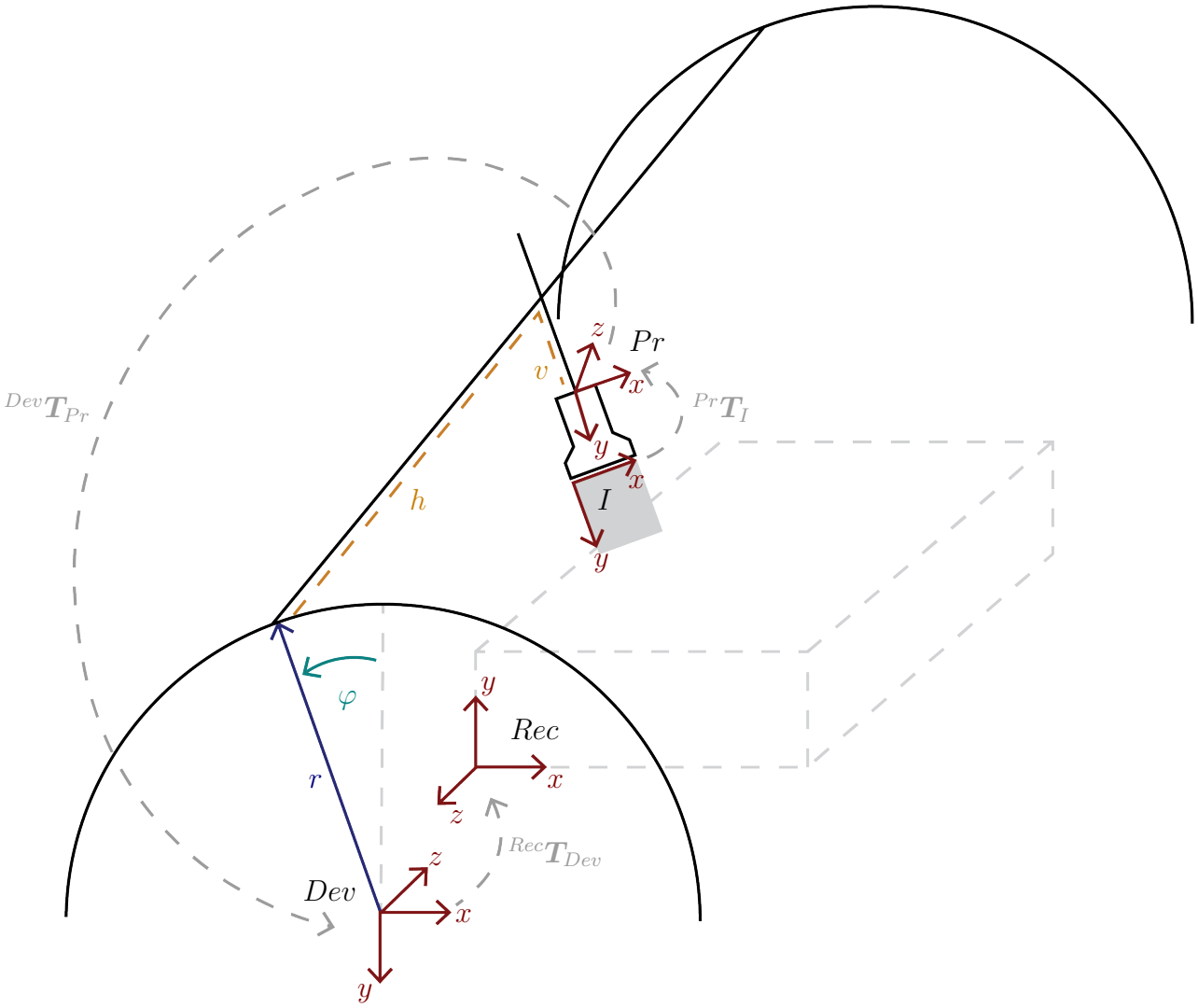

Figure 4.10: Coordinate systems and transformations of the 3D ultrasound system. *I*: Image Pixel Coordinate System, *Pr*: Probe Coordinate System, *Dev*: Device Coordinate System, *Rec*: Reconstruction Volume.

4.3 3D Reconstruction

In this thesis, two different methods for 3D reconstruction of ultrasound data are employed. Since this chapter is about the workflow of the automated 3D ultrasound system, the methods are presented for this system. However, the methods can be used for the 3D freehand ultrasound workflow in the same way.

This section presents a custom-written reconstruction method which allows to generate a volume as a 3D matrix array filled with image pixel values. The volume can be exported in several formats, e.g., VTK (see Section 4.3.3). This allows examinations of the internal structures of the 3D array. Thus, the method is used in Chapter 5 for validation and in Chapter 6 for investigating the internal fascicle architecture of the TA.

All of the described processing steps for the workflow are implemented with custom code written in Matlab (R2020a).

4.3.1 Reconstruction Volume Determination

The reconstruction volume *Rec* must first be defined. In order to determine the size and position of *Rec*, the image pixel positions of all acquired 2D images are transformed into the device space *Dev*, see Figure 4.11a:

$$^{Dev}\boldsymbol{x} = {}^{Dev}\boldsymbol{T}_{Pr}\,{}^{Pr}\boldsymbol{T}_{I}\,{}^{I}\boldsymbol{x} \; . \tag{4.4}$$

For determination of the orientation of the reconstruction volume *Rec*, a principal component analysis (PCA) is applied to the edges of the images rotated into the laboratory/device coordinate system, as shown in Figure 4.11b. The rotated volume is then shifted to the new origin, which is the minium point of x-, y- and z-coordinates. After rotation, the axes of the volume are aligned in a way that the x-axis corresponds to the left-right dimension of the 2D image, the y-axis is the up-down direction of the 2D image and the z-axis is the scanning direction.

Once the image stack is rotated and translated to the appropriate position, it is necessary to define the spatial resolution of *Rec*. This means that the scaling of the voxels in the reconstruction volume needs to be determined. The voxel spacing in the reconstruction volume is chosen as the pixel spacing in x- and y-direction. In z-direction (scanning direction), voxel spacing is the product of the actual length of the image stack and the inverse of number of images, as in [40].

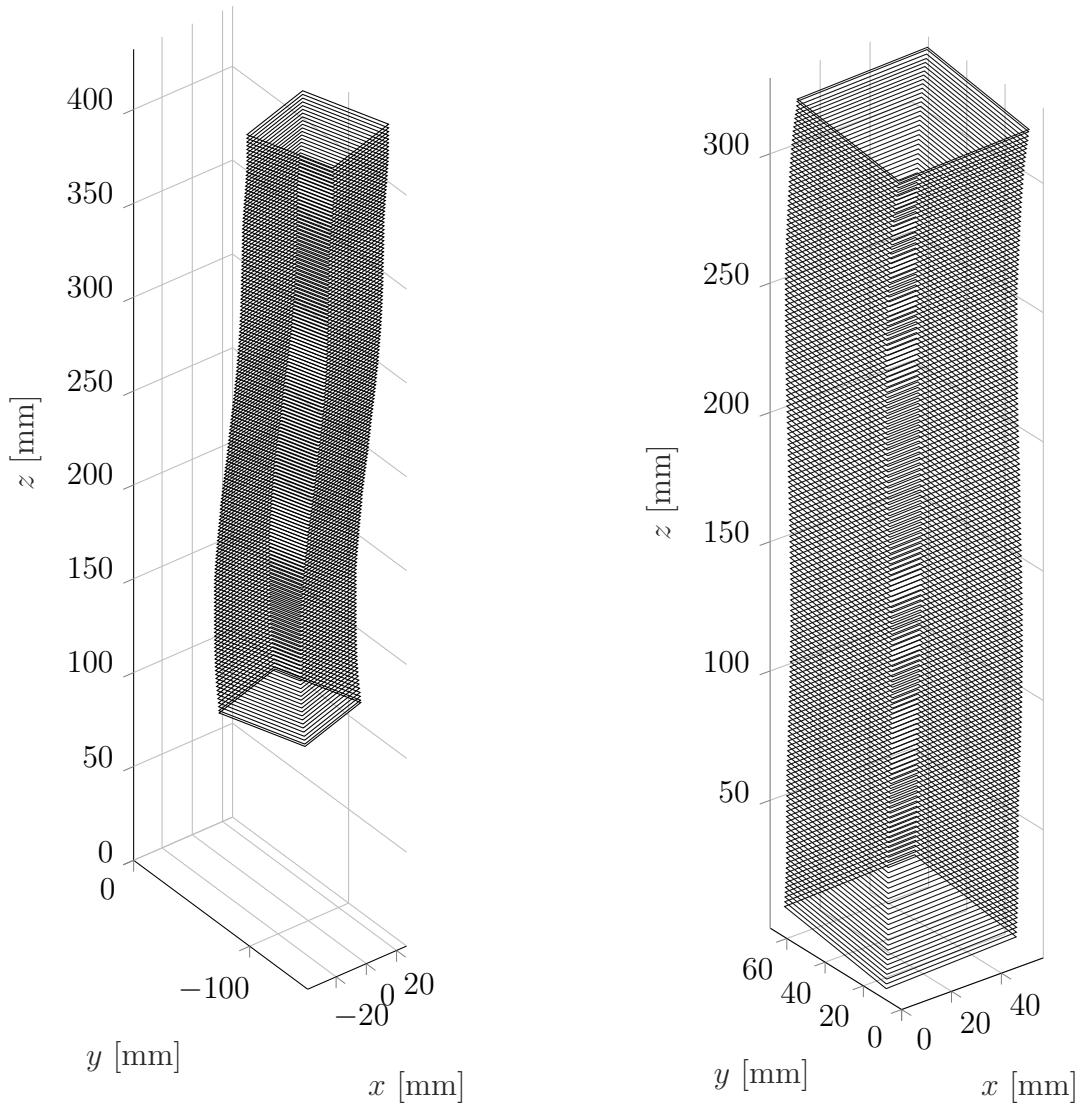

(a) Laboratory space.

(b) After PCA transformation.

Figure 4.11: Image stacks in laboratory reference space and reconstruction volume coordinate systems. (a) Laboratory reference coordinate system with a large amount of empty voxels. (b) Image stack after PCA rotation and origin shift.

4.3.2 Filling the Volume

In this thesis, a pixel-based method is implemented for filling *Rec* with image pixel values. Therefore, filling the volume is a two-step process consisting of bin filling and hole filling.

Bin Filling

Bin filling is the process of assigning image pixel values to positions in the reconstruction volume *Rec*. An algorithm adopted from Purnama et al. [199] is implemented. Once *Rec* has been defined, Equation (4.1) is applied to all image pixel positions. Thus, the image pixel positions ${}^{I}\boldsymbol{x}$ are transformed to ${}^{Rec}\boldsymbol{x}$ for all 2D images. In order to reduce the computation time, a bounding volume enveloping the transformed image pixel positions is created (using the Matlab (R2020a) function *alphaShape*). Therefore, only reconstruction volume points within the bounding volume are considered.

A nearest neighbor search is used to find the nearest reconstruction voxel position v_{ijk} of each transformed image pixel position ${}^{Rec}\boldsymbol{x}$. If the nearest voxel v_{ijk} of one specific pixel value is empty, i.e., has the value zero, the corresponding specific transformed pixel value of ${}^{Rec}\boldsymbol{x}$ is assigned to the voxel, i.e., p_{val}. Here, i, j, k refer to the indices of the reconstruction volume *Rec*. If v_{ijk} already has an assigned image pixel value, the mean of the already assigned value and the current nearest neighbor is taken, see Algorithm 1.

Algorithm 1 Bin Filling Algorithm

for all image pixels $l = 1, 2, \ldots$ **do**
  Find nearest neighbor v_{ijk}
  if v_{ijk} is empty **then**
    Assign $v_{ijk} = p_{val}({}^{Rec}\boldsymbol{x}_l)$
  else
    $v_{ijk} = \frac{n \cdot v_{ijk} + p_{val}({}^{Rec}\boldsymbol{x}_l)}{n+1}$, where n is the number of previous contributions to v_{ijk}

Hole Filling

Depending on the resolution of the reconstruction volume *Rec*, it is possible that there are empty voxels after the bin filling step. Hole filling is the step for interpolation of such empty voxels, which are voxels with a value of zero. First, all voxels are normalized to values between zero (black) and one (white). To avoid interpolation over true image values of zero, all initial image values of the grayscale image are initially incremented by 0.03. For all empty voxels within the bounding volume of the reconstruction volume, the seven nearest neighbor voxels within the bounding volume are defined. The empty voxels within the bounding area are then filled with the mean value of the seven nearest non-zero voxels within the bounding area. Afterwards, all pixel values are decreased by 0.03 again. Figure 4.12 shows a cross-sectional (axial) and a sagittal slice of a 3D reconstructed image after bin filling and hole filling.

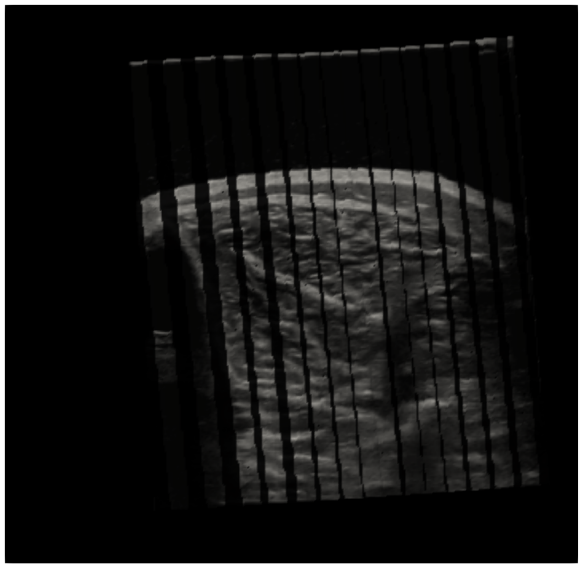

(a) Before hole filling.

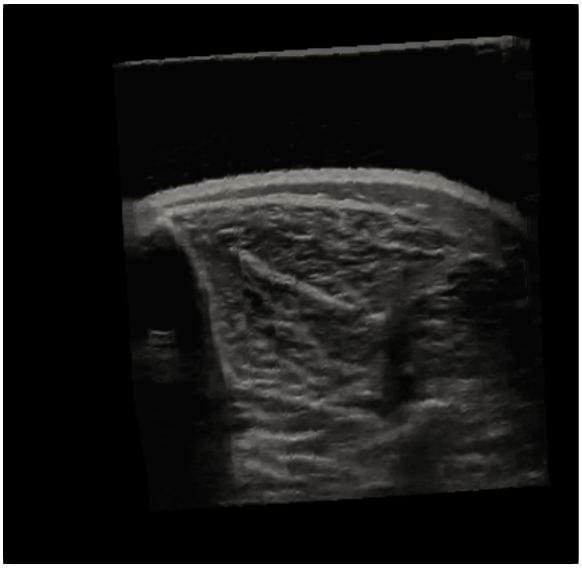

(b) After hole filling.

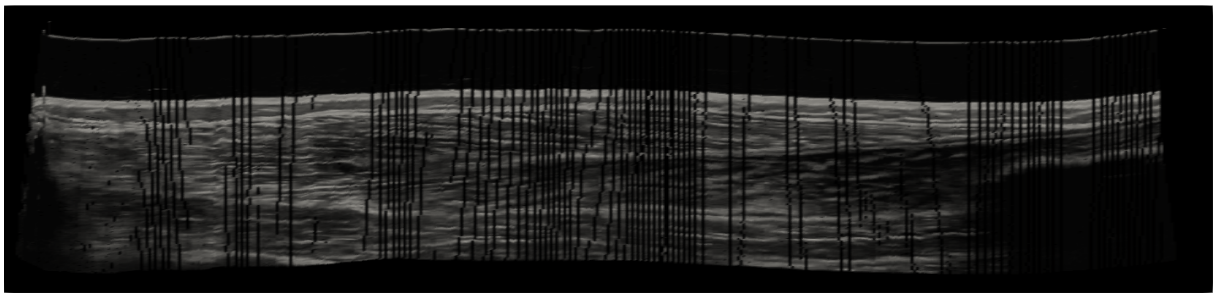

(c) Before hole filling.

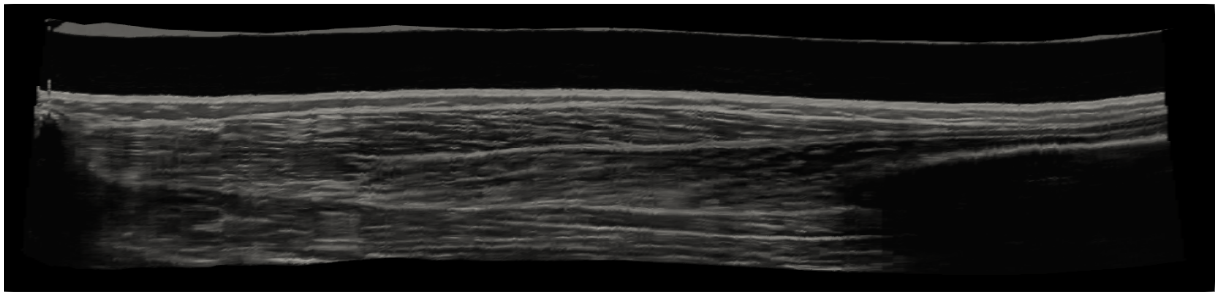

(d) After hole filling.

Figure 4.12: Slices of a reconstructed volume of the TA after bin filling in (a) axial and (c) sagittal view and the corresponding slices after hole filling in (b) axial and (d) sagittal view. The example data set is from a 3D freehand ultrasound trial to demonstrate the effects of hole filling, since 3D freehand ultrasound usually results in more empty voxels after bin filling.

4.3.3 Data Export

The reconstructed and filled volumes can be exported in the Visualization Toolkit (VTK)[5] format [227]. The files involve a 3D matrix array containing the filled volume and information on the voxel spacing. VTK is an open-source toolkit for several visualization applications such as image processing, volume rendering or 3D computer graphics and further applications [227]. VTK files can be imported for visualization using ParaView[6], which is an open-source engine, used in this thesis for visualizing different types of data.

4.3.4 Segmentation

After generating a 3D matrix array of the acquired 2D images at the corresponding positions, i.e., a 3D volumetric array of voxels assigned with grayscale values, segmentation is a necessary step to enable determination of specific measures, such as muscle volume. The Medical Imaging Interaction Toolkit (MITK, v2021-02)[7] [273] is used for segmentation in the custom-written 3D reconstruction workflow. It enables different manual and semi-manual image segmentation methods. By either manually outlining several slices and using an automatic method, which interpolates between a number of segmented slices, binary segmentation masks are created. MITK contains further automatic segmentation methods such as thresholding, Otsu's method [183] or a watershed transform. The segmentation masks can be exported in different file formats, e.g., NifTI[8]. A direct polygon or smoothed polygon generation from the segmentation mask is possible, which can be exported in various surface mesh formats, such as PLY or STL.

4.4 3D Reconstruction using Stradwin

The second 3D reconstruction method uses Stradwin[9] [192]. Stradwin is a freely available software tool developed by the Machine Intelligence Laboratory at the Cambridge University's Engineering Department. The program was developed mainly for data acquisition and visualization of 3D freehand ultrasound applications. Stradwin requires two different input files: a binary image file (.sxi) containing the collected images and a text file (.sw) comprising pixel scaling information for each image and associated position and orientation data. After generating the necessary files from the images and position data, the files can be imported into Stradwin. In the program, the 2D images are automatically positioned according to the position and orientation data in the sw file. Stradwin contains different windows for control and visualization purposes. In the "Reslice" or "Pressure" window, viewing of different planes is possible. In the "Draw" window, the geometry can be segmented where either all slices can be segmented individually, or, similar to MITK, it is possible to interpolate over individual segmented slices [252]. The segmented slices can be transformed into a 3D surface geometry [251] by the program. An algorithm for estimating volumes is further implemented in Stradwin [254]. The surface geometries in Stradwin can be exported in different formats, such as VRML files.

[5] https://vtk.org/
[6] https://www.paraview.org/
[7] https://www.mitk.org/wiki/The_Medical_Imaging Interaction_Toolkit_(MITK)
[8] https://nifti.nimh.nih.gov/
[9] http://mi.eng.cam.ac.uk/Main/StradWin

The Stradwin reconstruction is faster than the custom-written one (in the range of seconds compared to approximately 3-6 minutes). However, this method is more restricted for the export of 3D arrays, e.g. regarding the formats. Therefore, the Stradwin reconstruction method is employed in Chapter 7, where mainly surface geometries of the TA are investigated.

The generation of Stradwin files was implemented using Matlab (R202a).

4.5 Volume Analysis

The binary segmentation mask including voxel scaling information can be analyzed in terms of volume, length, cross-sectional area and thickness of the examined geometry. Alternatively, it is possible to generate binary masks from the surface geometries. In this thesis, as proposed in the study of Raiteri et al. [200], a weighted PCA is applied initially to rotate the geometry into the coordinate system of its principal component axes.

Volume is defined as the sum of the segmented voxels multiplied by their resolution in each dimension. Length is the euclidean distance from the centroids of the first and last segmented slice, e.g., the most proximal and most distal point for TA measurements. Volume and length of geometries, such as muscles, are computed in Chapters 5-7.

For each segmentation slice, the cross-sectional area (CSA) is computed by the sum of pixels multiplied by the pixel spacing, see Figure 4.13a. The CSA is investigated in Chapters 6 and 7. Per definition, thickness is the maximum vertical distance in the cross-section. For each segmentation slice, a Sobel edge detector is applied for detecting the mask boundaries, as shown in Figure 4.13b. This is realized with the Matlab (R2020a) function *edge* All opposite edges and their distance from each other are determined. By detecting the maximum values of the distances in the vertical direction, the height of the respective slice of the geometry is defined, see Figure 4.13c. Thickness is investigated in Chapter 5.

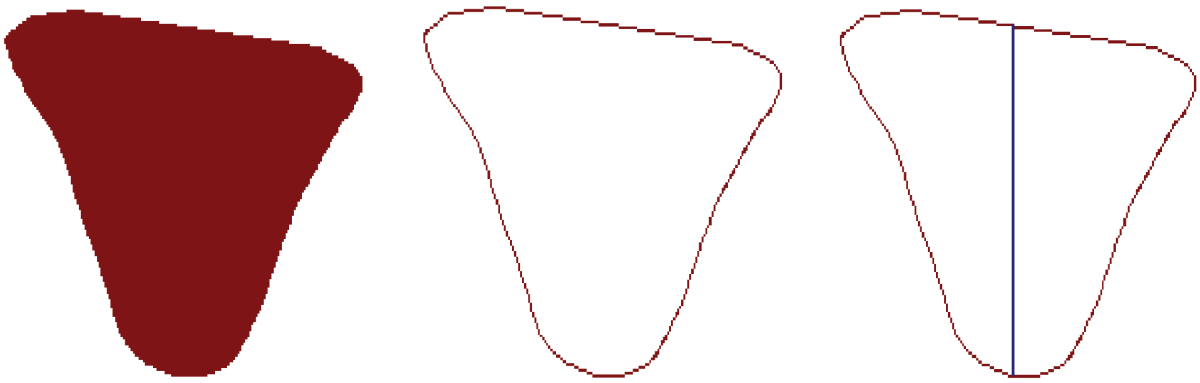

(a) Binary segmentation mask. **(b)** Sobel edge detector. **(c)** Thickness.

Figure 4.13: Determination of tibialis anterior thickness, demonstrated on an example image slice.

5 Validation and Application of the Automated 3D Ultrasound System[1]

Chapter 4 described the methods used for 3D ultrasound data acquisition and reconstruction. In this chapter, a validation study of the automated 3D ultrasound system is presented, which includes a comparison with the freehand ultrasound technique. Two custom-designed phantoms[2], as described in Section 5.1, are used for validation. In addition to employing the data acquisition workflow on phantom data, it is also applied on the human tibialis anterior (TA) muscle. Furthermore, the reconstructions of data sets acquired by automated and freehand ultrasound are evaluated with respect to accuracy and reproducibility (Section 5.3).

Appendix B provides a description of the setup of the freehand workflow.

5.1 Ultrasound Phantoms

Two ultrasound phantoms, cast in custom-designed 3D printed molds are employed. The phantoms consist of a mixture of distilled water, evaporated milk, n-propanol in a 2% agarose concentration, benzoic acid for conservation, and silicon dioxide powder for soft tissue-like scattering of ultrasound waves. The phantom recipes are adopted from Madsen et al. [157] and Menikou and Damianou [166]. Both phantoms are placed in a cuboid mold. The mold surrounding the phantom is filled with a material consisting of a 4% agarose mixture, similar to the phantom material. In contrast to the phantom material, the surrounding material does not contain scattering powder. Due to the cuboid shape of the phantoms' molds, the surface of the phantoms over which the ultrasound probe moves is planar. Table 5.1 shows the ingredients for manufacturing one liter of phantom and surrounding material.

The custom-designed phantoms differ in shape, see Figure 5.1: The cylindrical phantom is a cylinder with a length of 170mm and a diameter of 20mm. Its volume can be computed from geometric relations. The muscle-like phantom has an idealized belly-like shape of a muscle. It is realized as a cylinder with narrow ends and a muscle belly with a larger cross-section. In addition, the phantom is cut along its longitudinal axis. The volume of the muscle-like phantom was determined by water displacement as 35.5ml.

[1] Parts of this chapter published in [217].

[2] The custom-designed phantoms for validating the 3D ultrasound workflows have been developed and evaluated within the student research thesis of Dimitra Stanigloudi [240].

	Surrounding Material	Phantom Material
Distilled Water [ml]	644	736
Propanol [ml]	56	64
Agarose [g]	28	16
Evaporated Milk [ml]	500	400
Benzoic Acid [g]	1	0.8
Silicon Dioxide Powder [g]	-	21

Table 5.1: Phantom ingredients for one liter of each material.

(a) Cylindrical phantom.

(b) Muscle-like phantom.

Figure 5.1: Custom-designed phantoms before filling the cuboid molds with the surrounding material. (a) Cylindrical phantom. (b) Muscle-like phantom.

5.2 Methods

In this chapter, a study is conducted to evaluate the accuracy and reproducibility of the methods developed in Chapter 4. This section depicts the experimental setup of the validation study. Further, the methods for post-processing of the acquired data, i.e., volume reconstruction and analysis, are described.

5.2.1 Experimental Setup

The experimental trials using the automated 3D ultrasound system and the freehand technique have two major aims: The first aim is to validate the automated 3D ultrasound workflow. The second aim is to compare the automated 3D ultrasound system with the 3D freehand ultrasound technique methods regarding reproducibility.

Phantom Trials

The experimental protocol was designed as follows: First, the muscle-like phantom was scanned eight times using the automated 3D ultrasound system with force setting 25, which corresponds to 4.5N (see Figure 4.4). The phantom cuboid blocks were placed on a table for conducting the measurements. For avoiding that the phantom can slide, screw clamps were used to attach wooden boards on the table. The wooden boards touched the phantom sidewalls, thereby holding the phantom blocks in place.

Moreover, the automated 3D ultrasound system scanned the cylindrical phantom in three different force settings: low, moderate and high (force settings 1, 100 and 200, corresponding to 4.1N, 5.5N and 6.5N). Each scan was repeated eight times for each contact force. In the following, these trials are referred to as *automated*. The duration for each scan for the automated trials was 15 seconds for the phantom trials.

Further, 3D freehand ultrasound trials were conducted. Here, two different operators manually scanned the cylindrical phantom with four different contact force modes: (1) the operators were not told to scan with any specific contact force, just so that scanning felt comfortable for the operator. In the following, this is referred to as *individual force*. The operators were then told to apply (2) low contact force, (3) moderate contact force, and (4) high contact force. Each scan of the contact forces was repeated eight times. The duration time for freehand trials ranged from 9-20 seconds for phantom trials.

For both manual and automated scans, sufficient amounts of ultrasound transmission gel were used on the phantom to ensure an appropriate acoustic coupling.

Muscle Trials on a Human Subject

Data was collected from a human TA of a healthy 22 year old female subject (height: 166cm, weight: 57kg, body mass index: $20.7\frac{\text{kg}}{\text{m}^2}$)[3]. The automated 3D ultrasound system scanned the TA of the same subject with two different force settings (1 and 200). In addition, one operator conducted freehand ultrasound scans with an individual force level. The duration time for one TA scan was 17 seconds for automated trials and 11-19 seconds for freehand trials. In both the manual and the automated TA scanning protocol, the measurement was repeated 10 times.

For both manual and automated scans, sufficient amounts of ultrasound transmission gel were applied to the TA to ensure an appropriate acoustic coupling.

5.2.2 3D Reconstruction and Image Segmentation

The custom-written 3D reconstruction, as described in Section 4.3, was employed. For segmentation of the phantom data, a Watershed transformation for segmenting the phantom's cross-sectional area was applied. Inaccurate automatically segmented slices were corrected manually.

For muscle data, several slices were segmented manually and the built-in algorithm of the program for interpolation between the slices was used. Phantom and TA thickness were computed as described in Section 4.5. Figure 5.2 shows segmentations of the phantom

[3]The experimental procedures involving human subjects described in this chapter were approved by the University of Stuttgart's Committee on Responsibility in Research (number: Az. 21-011).

and TA, and the thickness definition. A smoothed polygon was created using MITK to generate 3D volumes of the segmented slices.

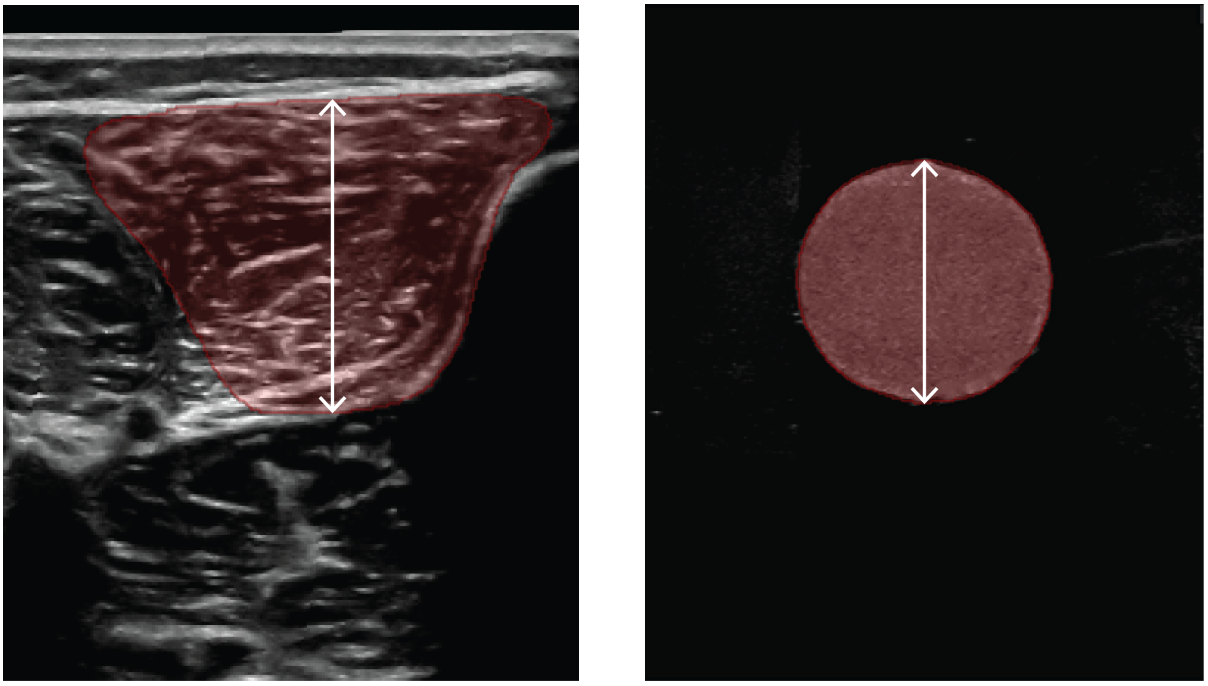

(a) Tibialis anterior. **(b)** Phantom.

Figure 5.2: Segmentation (red) and thickness definition (white) for (a) TA and (b) phantom volume slices.

5.2.3 Statistical Analysis

A Shapiro-Wilk test was used for testing of normal distribution. For statistical analysis, analyses of variance (ANOVAs) were used for normally defined distributed data. Kruskal-Wallis tests were used for non-normally distributed data to test for examining significant differences. Significance was defined as a P-value $P<0.05$. As a measure of statistical dispersion, the mean coefficient of variation (CoV) was computed for movement trajectories and thickness computations.

5.3 Results

Figure 5.3a and Figure 5.3b show exemplary reconstructions of the cylindrical and muscle-like phantom from the automated trials. The shapes of the reconstructed volumes are visually aligned with the original phantoms (Figure 5.1). Figure 5.3c demonstrates a reconstructed volume (from the automated trials) of the TA measurement in multiplanar reformatting view. In addition, the segmented muscle is visualized. Figure 5.3d illustrates a plane of the reconstruction volume in sagittal direction, which reveals the central aponeurosis and fascicle orientations within the plane.

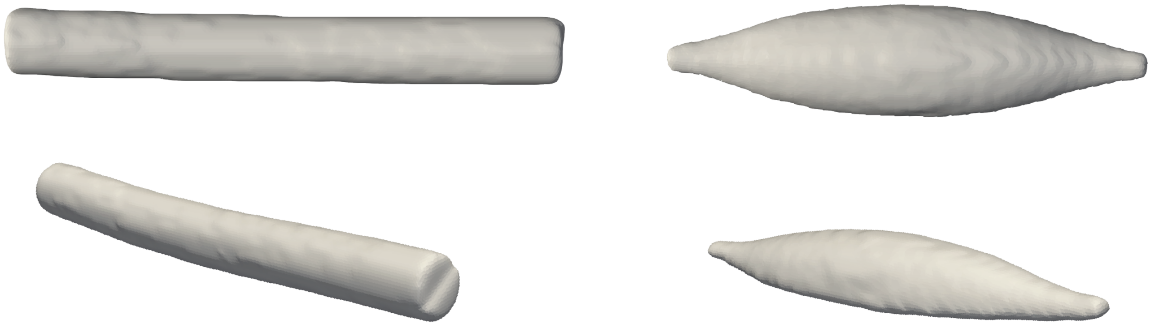

(a) Cylindrical phantom.

(b) Muscle-like phantom.

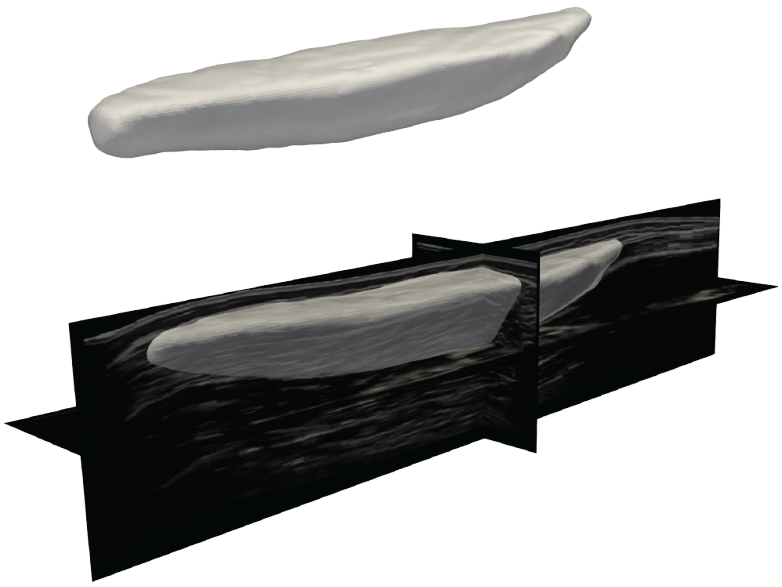

(c) Tibialis anterior.

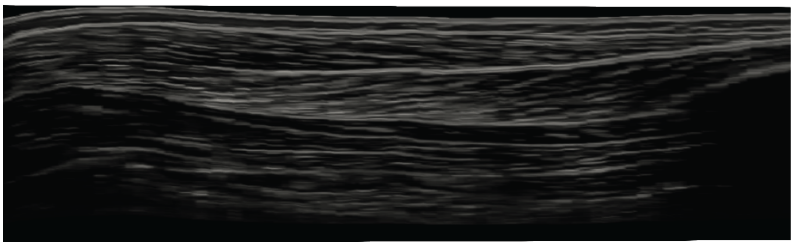

(d) Sagittal plane of the tibialis anterior volume reconstruction.

Figure 5.3: Phantom reconstruction using the automated 3D ultrasound system. (a) Cylindrical phantom. (b) Muscle-like phantom. (c) Tibialis anterior volume in multiplanar reformatting view. (d) Sagittal view of the tibialis anterior revealing the fascicle architecture.

5.3.1 Volume and Length

Table 5.2 lists volume and length measurements and mean errors for the muscle-like phantom, which are obtained using the automated 3D ultrasound system. The mean error was 0.94mm (0.23%) for length and 0.08ml (0.23%) for volume. This indicates a high accuracy of the reconstructions.

	Volume	Length
True Value	35.5ml	140mm
Measurement	35.58±0.07ml	140.35±1.06mm
Absolute Error	0.08±0.07ml	0.94±0.51mm
Percent Error	0.23±0.20%	0.67±0.36%

Table 5.2: Mean volume and length for the muscle-like phantom for data acquired with the automated 3D ultrasound system. Both volume and length errors are small for the automated trials, indicating a high accuracy.

Table 5.3 illustrates a volume and length analysis for the cylindrical phantom for automated and freehand trials with different operators. For length measurements, both freehand scans show a higher mean error than the automated scans. Yet, for volume measurements, operator 2 has a slightly smaller mean error than the automated scans. Both freehand and automated scans tend to underestimate the phantom volume for the cylindrical phantom, whereas for phantom length, the freehand scans slightly overestimate the trials. The automated trials slightly underestimate phantom length. Overall, errors for the muscle-like phantom are smaller for volume and length than for the cylindrical phantom.

For the TA, volume results were 64.91±1.21ml for automated and 66.13±3.16ml for freehand trials. Length measurements were 193.19±0.62mm for automated and 191.62±1.24mm for freehand trials. TA volume did not differ significantly between automated and freehand trials. There were, however, significant differences in muscle length between freehand and automated trials for both applied force levels.

		Volume	Length
	True Value	53.41ml	170mm
Automated	Measurement	51.46±0.40ml	169.06±1.34mm
	Absolute Error	1.94±0.40ml	1.25±1.05mm
	Percent Error	3.64±0.74%	0.73±0.62%
Operator 1	Measurement	50.57±1.54ml	172.43±2.92mm
	Absolute Error	2.84±1.54ml	2.87±2.47mm
	Percent Error	5.32±2.88%	1.68±1.46 %
Operator 2	Measurement	51.83±0.92ml	173.11±2.20mm
	Absolute Error	1.64±0.81ml	3.11±2.20mm
	Percent Error	3.07±1.51 %	1.83±1.30%

Table 5.3: Mean volume and length for the cylindrical phantom for automated and freehand (operator 1 and 2) trials. Length errors are smaller for the automated trials.

5.3.2 Reproducibility

In order to make sure that the validity of the proposed method is independent of movement variability, it was ensured to minimize the inter-trial variability by enforcing a rather reproducible trajectory of the limb. Figure 5.4 shows the image stack in the reconstructed volume for an automated and two different freehand TA muscle trials. The marker coordinates of the freehand scans were transformed into the probe coordinate system. Figure 5.5 illustrates a comparison of the scanning trajectories. From visual inspection, it could be observed that the freehand trajectories show sliding movements in the left-right and up-down movement. The automated trajectories, however, reveal a properly lined up image stack. A mean CoV of 36% in x-direction (left-right), 71% in y-direction (up-down) and 12.63% in z-direction (forward-backward) was found for the freehand scans. This indicates a variation in movements when repeatedly conducting freehand scans compared to automated scans. A dispersion in movement trajectories in freehand scans for the phantom trials was observed.

The muscle and phantom thickness were computed to determine the deformation over the muscle and phantom length for automated and freehand trials. Deformation was defined as the difference of the original thickness of the known geometry (20mm) and the computed mean thickness from 20 to 80% of the phantom length, as illustrated in the top part of Figure 5.6. In general, higher deformation values can be assumed with a higher contact force. Deformation values differ between automated and freehand scans and between the two operators, although force settings were similar. This indicates operator-dependent exerted contact forces. For automated scans, the deformation increases relatively constant from low to high force setting. The mid and bottom part of Figure 5.6 show the volume and length errors for the different force settings for automated and freehand. For automated scans, volume and length errors are overall small. According to Figure 5.6, larger volume errors can be observed at higher deformations, i.e., stronger contact forces, whereas this does not apply for length errors. The length errors are in general smaller for automated scans than for freehand scans.

The left part of Figure 5.7 reveals a variation in thickness values for both operators and the automated scans for phantom trials. Thickness values for moderate, high and individual force levels are significantly different between the operators ($P<0.001$ for moderate and high force level, $P=0.001$ for individual force level). This indicates an operator-dependency in the applied forces. Interestingly, for operator 1 all force levels besides the low and the individual levels differ significantly ($P<0.001$). However, for operator 2, all force levels besides the moderate and the individual force level differ significantly ($P=0.03$ for low and moderate force level, $P<0.001$ for the other force levels). The shaded areas in the right part of Figure 5.7 show the standard deviation of the thickness over the phantom length for two force levels, i.e. the dispersion. For the automated trials, the dispersion is smaller than for the freehand trials indicating a lower variation between trials. For quantitative analysis, the mean CoV for all trials, see Table 5.4, was computed and higher CoVs were found for the freehand trials than for the automated trials.

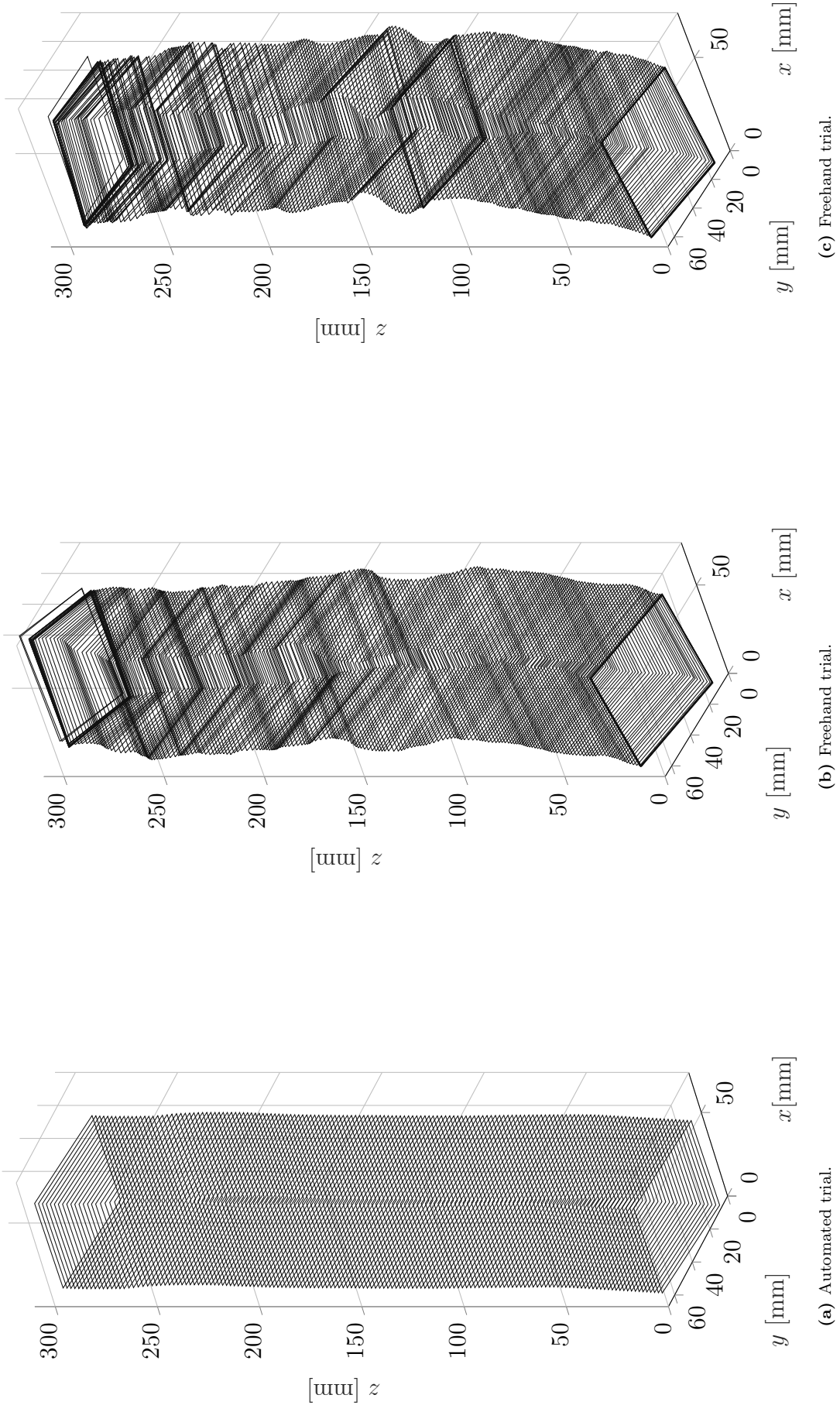

(a) Automated trial. **(b)** Freehand trial. **(c)** Freehand trial.

Figure 5.4: Image corner coordinates transformed in the reconstruction volume for (a) automated and (b) and (c) two different freehand trials, employed on the tibialis anterior muscle. In contrast to the freehand trials, the images of the reconstruction based on the automated trials are properly lined up.

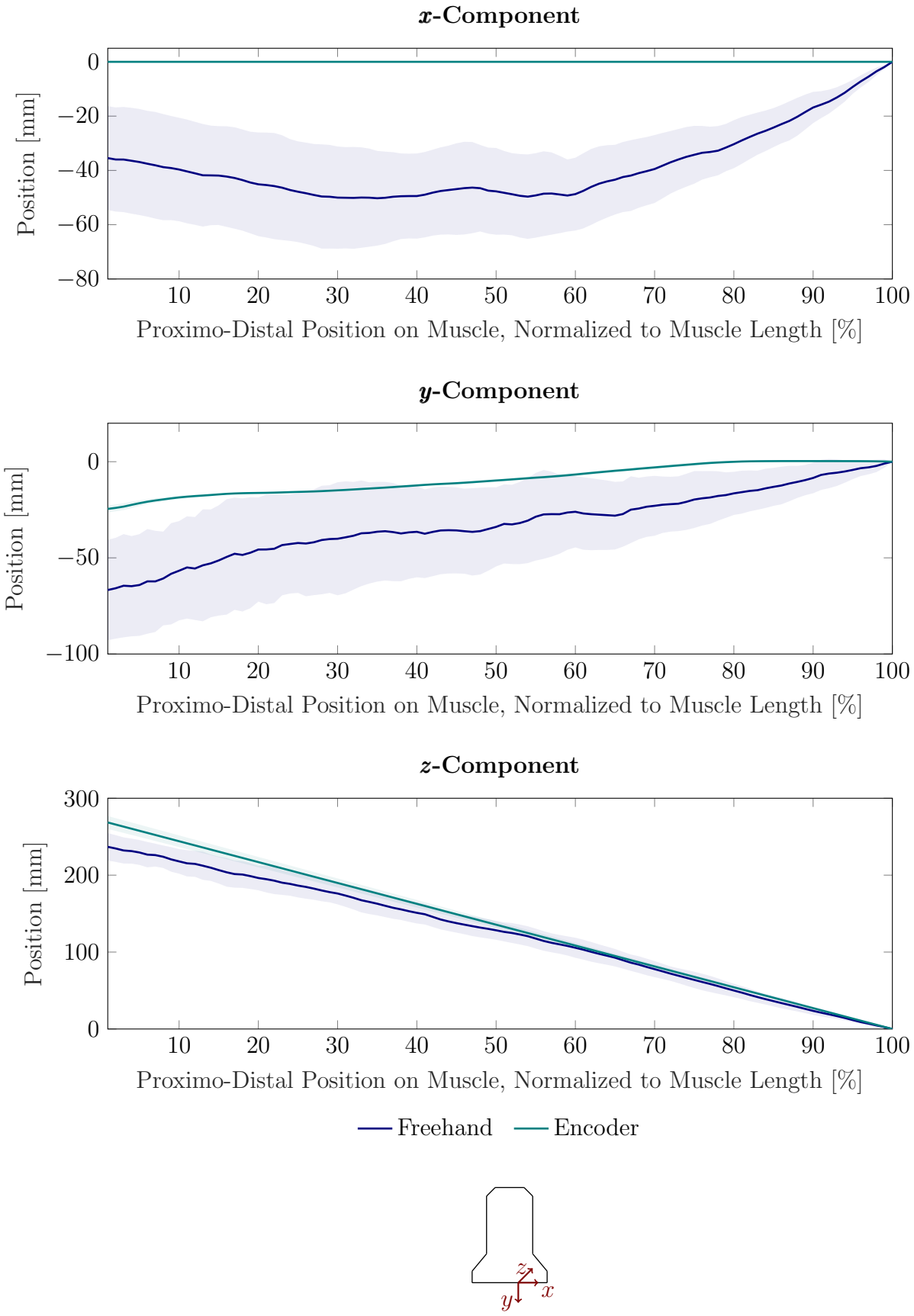

Figure 5.5: Marker and encoder trajectories for tibialis anterior trials in probe space. x-direction is left-right, y-direction is up-down and z-direction is forward-backward. The freehand trials show a higher variation in the ultrasound probe position, especially for the x-direction and y-direction.

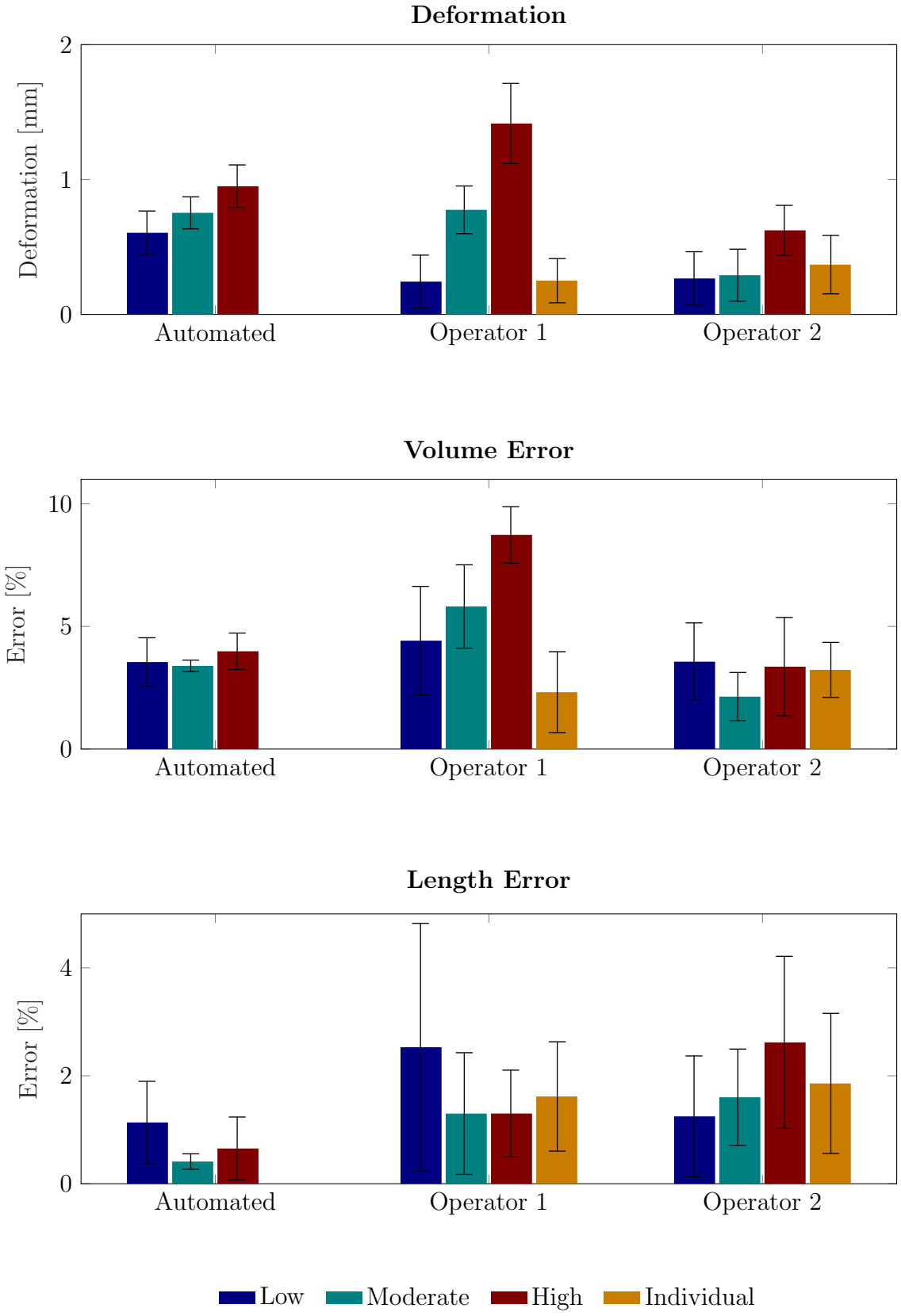

Figure 5.6: Mean deformation, volume and length error for automated and freehand scans and different force values for the cylindrical phantom trials. Error bars indicate standard deviations. The automated trials show small volume and length errors and overall small standard deviations.

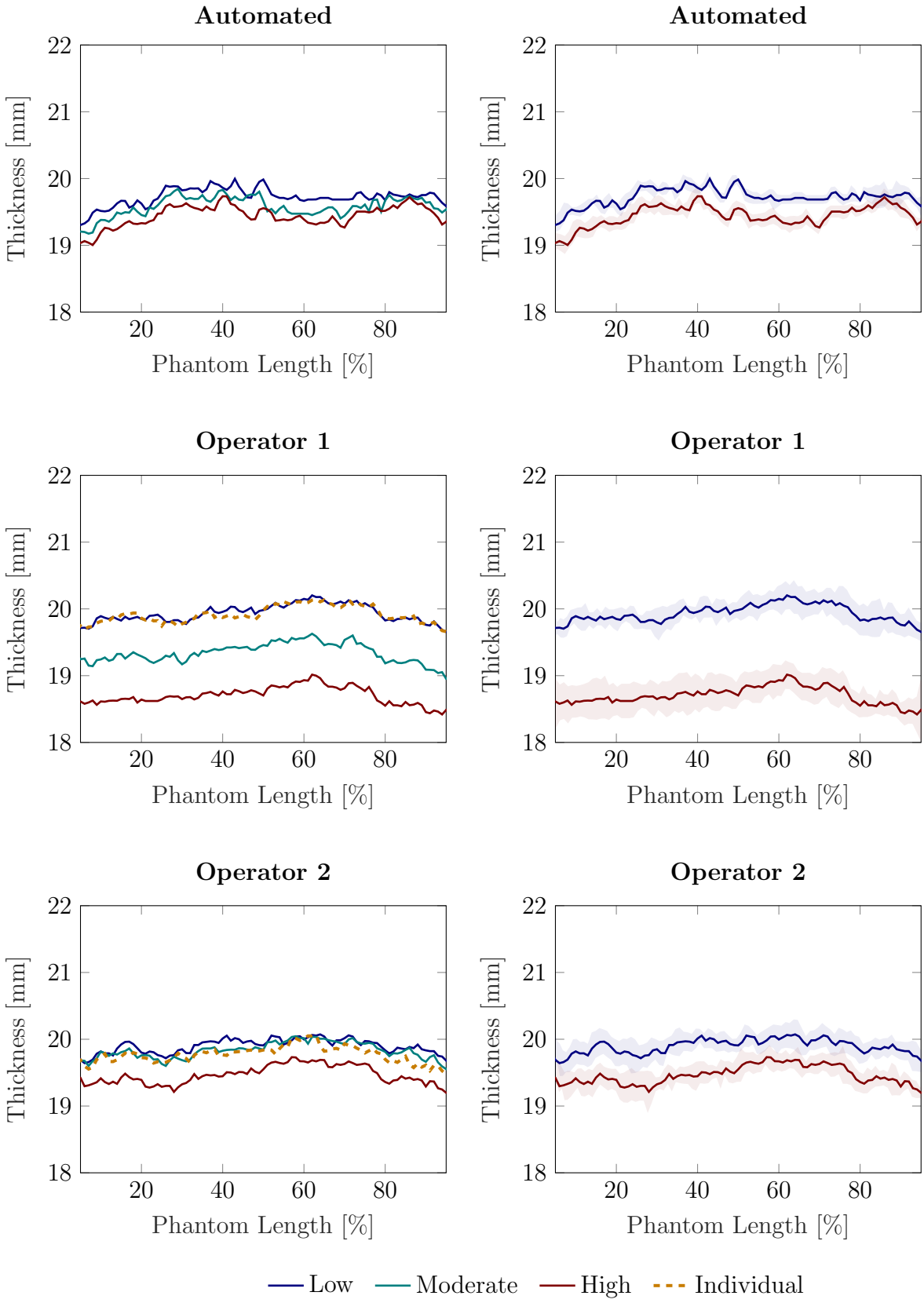

Figure 5.7: Left: Mean thickness values over phantom length for automated scans and two operators. Note that the absolute forces may differ for low, medium, and high settings between operators and automated 3D ultrasound system, which explains inter-operator differences in thickness. Right: The shaded areas illustrate the standard deviations. For better readability, the moderate and individual force are not displayed.

The thickness of the TA over the muscle length, as shown in Figure 5.8, was computed for automated and freehand scans. The CoVs for muscle thickness were lower for the automated scans, as listed in Table 5.5. No significant differences were found in mean thickness over muscle length between automated and freehand scans. Muscle thickness did not differ significantly for automated scans with high and low pressure settings.

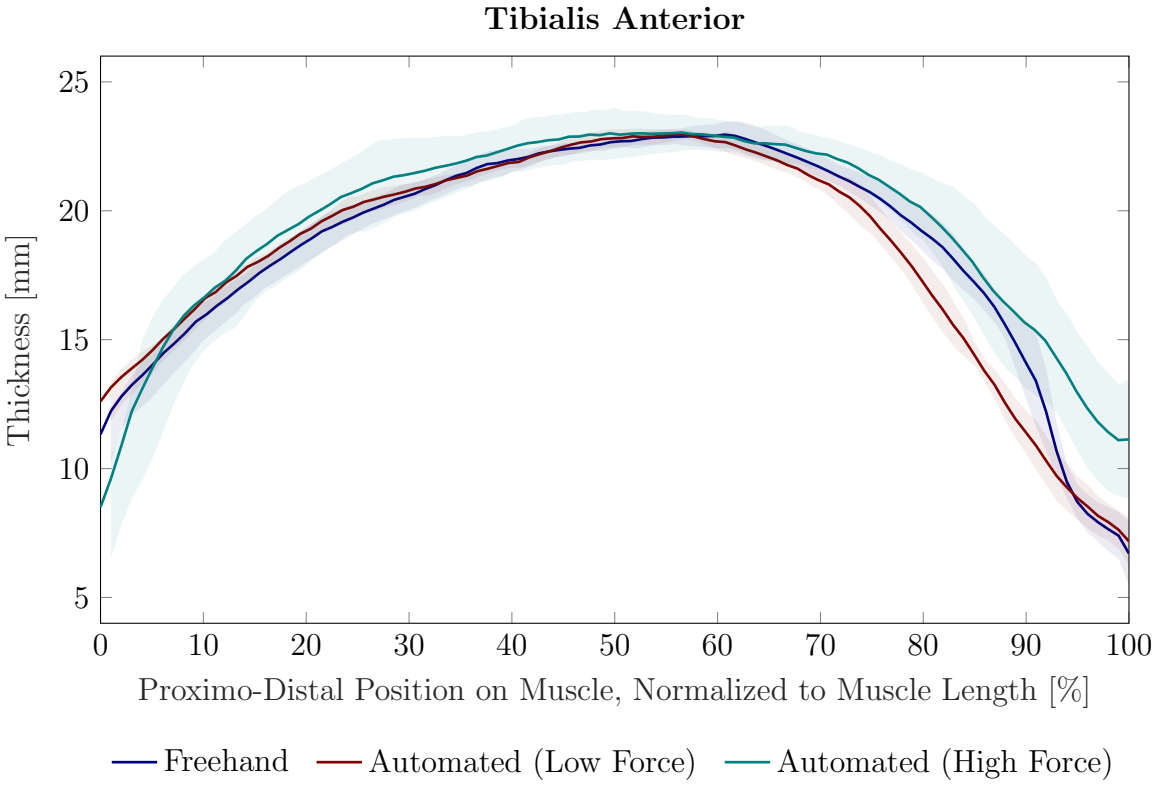

Figure 5.8: TA thickness for automated and freehand data. Muscle thickness does not differ significantly between automated and freehand trials, also not between different force levels of the automated trials.

A L	A M	A H	O1 L	O1 M	O1 H	O1 I	O2 L	O2 M	O2 H	O2 I
0.472	0.329	0.547	0.860	0.850	1.277	0.830	0.854	0.812	0.846	1.023

Table 5.4: Coefficient of variation for thickness values of the cylindrical phantom [%]. The automated trials show smaller CoVs in muscle thickness than the freehand trials, i.e., a smaller dispersion in computed phantom thickness. A: Automated, O1: Operator 1 (freehand), O2: Operator 2 (freehand), L: Low force, M: Moderate force, H: High force, I: "Individual" force.

Automated (L)	Automated (H)	Freehand
3.372	2.802	7.292

Table 5.5: Coefficient of variation for thickness values of the TA [%]. CoVs in muscle thickness are larger for freehand trials than for automated trials. L: Low force, H: High force.

5.4 Discussion

In this chapter, the automated 3D ultrasound system for enabling controlled 3D ultrasound measurements has been evaluated and compared to the freehand technique. The automated 3D ultrasound system can be employed with any ultrasound machine. Thus, the current large ultrasound machine (Aixplorer MACH 30) can easily be exchanged with a portable one. Consequently, due to the currently relatively small size of the proposed automated 3D ultrasound system, it is a portable system and can be moved freely between rooms or institutions with different available ultrasound machines. In comparison with other medical imaging modalities, such as MRI, this enables more flexible 3D examinations. Furthermore, with the automated 3D ultrasound system, there is no need for a laboratory environment with an optical motion capture system due to the integrated encoders. Hence, the operator also does not need to ensure that no markers are hidden during measurements. This is particularly advantageous for complex experimental configurations. Therefore, the automated 3D ultrasound system can be used for clinical research for obtaining volumetric information of skeletal muscles. With the possibility to add another motor (see Section 4.2.2) and conduct automated multiple sweep studies, the automated 3D ultrasound system is also capable of acquiring volumes of larger muscles. Thus, the automated 3D ultrasound system presents a less complex and more portable alternative to other imaging techniques, such as MRI, which are commonly used for such examinations.

A high accuracy in reconstructing the 3D volume of both the cylindrical and the muscle-like phantom was found for volume and length measurements. Furthermore, standard deviations for these parameters were smaller for the automated trials than for freehand trials. This indicates a more reproducible reconstruction of the scanned volumes when using the automated 3D ultrasound system.

5.4.1 Operator Dependency

Effects on tissue deformation due to probe pressure have been found in previous studies [31, 90]. The higher CoVs for thickness for freehand scans demonstrate that the operators' applied force values also vary between scans. Furthermore, the operators applied a different amount of force when they were told to scan the phantoms without considering the amount of applied force. This suggests an operator-dependency in applied force during 3D freehand ultrasound acquisitions. This may lead to errors of quantitative morphological measurements of skeletal muscle. Studies have developed hand-held or robot-assisted force control mechanisms to attach to an ultrasound probe [21, 90, 117, 262] to overcome such issues.

Previous studies [62, 135], however, demonstrated, effects of probe orientation on measurements of muscle thickness and pennation angle. The trajectories for freehand TA scans in this chapter show large dispersions also indicating probe tilt and rotation. The proposed automated 3D ultrasound system ensures consistent trajectories for repeated measurements and a stable orientation of the probe during the scan. This renders it a more accurate and reproducible 3D ultrasound data acquisition tool in comparison to conventional ultrasound, even if robot-assisted.

5.4.2 Combination with Additional Techniques

Furthermore, the implemented pendulum movement mode allows scanning periodically along the horizontal axis. When simultaneously enabling a controlled movement of the foot or another body part, the automated 3D ultrasound system can be used in future studies for advanced automated and controlled 3D dynamic investigations of skeletal muscle [216]. This can provide completely new insights into the muscle's dynamic contraction behavior. In Chapter 7, a study on such dynamic movements is conducted.

Moreover, since the automated 3D ultrasound system can conduct measurements with ultrasound gel and is not designed for use in a water bath, data from other investigation methods such as electromyography (EMG) can be collected simultaneously, e.g., with ultrasound transparent electrodes [33]. This can reveal novel information of the relation between muscle deformation and electrical activation.

5.4.3 Safety

The custom-designed device is an electrically driven ultrasound probe holder, which is constructed for the purpose of 3D ultrasound imaging. This can be beneficial, since the safety of the examined subject is ensured through the intrinsic construction. Therefore, if different subjects or body parts are to be examined, only minor settings have to be adjusted, such as the start and end positions of the scanning trajectory. Similar adjustments can be more complex for robot arms, which are configured for 3D ultrasound imaging. In comparison to other compact non-commercial systems that do not use a robot arm, e.g., [119, 121, 122], the automated 3D ultrasound system enables scanning from oblique angles. This is relevant for scanning the curved surfaces of the human body.

Other automated 2D ultrasound systems, however, enable scanning from oblique angles and make use of passive mechanisms for ensuring a contact force on the skin [128, 258, 259]. These systems are well-designed for 2D ultrasound examinations in the field of focused assessment with ultrasound for trauma [128], fetal ultrasound [259], and lung ultrasound [258]. Here, the passive force mechanism is realized by a spring, which ensures contact between the skin and the probe. However, the spring applies a specific force only in a vertical downwards direction, and the force may vary for other probe angles [259]. This suggests that the passive spring mechanism may deform tissues inconsistently along the scanning path, whereas consistent tissue deformation would be preferable for 3D ultrasound examinations. Thus, an active force control mechanism, as realized in this chapter, can be considered to be more suitable for 3D ultrasound examinations of skeletal muscle. In addition, [128, 258, 259] are designed for 2D ultrasound examinations and therefore do not include a position sensing mechanism. This means that the acquisition of the ultrasound probe position may rely on optical motion capture markers, which can lead to occlusion problems. Furthermore, [128] and [259] would require an extended scan range to capture the TA or multiple other lower extremity muscles.

Therefore, the automated 3D ultrasound system enables force controlled scanning from oblique angles, in a safe setup with low complexity.

5.4.4 Contact Force

As mentioned in Section 1.2.2, previous studies observed that the applied force for ultrasound examinations is in a range of 5-20N [89, 237]. Lee et al. [145] found significant differences on TA thickness for inward probe pressures in the range of 1-4N. Ishida and Watanabe [127] detected significant changes in thickness of the transversus abdominis muscle for small forces below 2N. The studies are in contrast to this chapter's findings on mean TA thickness which did not change significantly between low and high force level. One possible explanation is the force range covered by the experiments, i.e., 4.1N and 6.5N. Thus, low force values, as employed by Ishida and Watanabe [127], could not be examined for observing thickness changes. For further development, the range can be extended for larger and smaller force values. The current lower limit of 4.1N exists because of the gravitational force, which is due to the weight of the components attached to the vertical axis. By changing the materials of the components from metal to more lightweight materials such as plastics, the weight can be reduced. Therefore, this can decrease the lower force limit. With this, the effects of lower forces on the TA can be examined in future studies.

5.4.5 Limitations

One limitation is that the segmentation masks from the semi-manual segmentation of the reconstruction volumes were used. Therefore, volume and length are dependent on the quality of the image segmentation. Even though standard deviations for computed volumes and lengths were low for both freehand and automated scans, small changes in segmentation may result in errors in volume and length measurements. In addition, segmentation inconsistencies may lead to changes in thickness distribution over length. This can also explain the spikes in the phantom thickness curve for the automated scans (Figure 5.7). To be consistent with segmentation, all trials in our study were segmented by the same operator. A fully automatic segmentation algorithm can, however, lead to an improvement in segmentation consistency and thus also increase volume and length computation accuracy.

5.5 Conclusion

In conclusion, the automated 3D ultrasound system allows accurate and reproducible measurements. The small size makes the automated 3D ultrasound system portable and therefore enables fast and flexible acquisition of 3D volumes of skeletal muscles. In future studies, the automated 3D ultrasound system can be used for static and dynamic investigations of healthy and pathological muscles. It can also be combined with data collection using other techniques such as EMG. To further increase reproducibility, accurate positioning of the subject may be important. For future studies, it is therefore useful to ensure that the subjects are clearly positioned relative to the device. This can be achieved by means of a design which is attached to the device and includes a fixture for the leg, or respectively the examined body part.

Part III

Determining Skeletal Muscle Parameters in Static and Dynamic Conditions

6 Fascicle Detection from 3D Ultrasound Imaging[1]

There is a direct relationship between the force a muscle can generate and the physiological cross-sectional area (PCSA) [150], which is calculated via the muscle fiber architecture. Therefore, accurate knowledge of the alignment and orientation of the fascicles is essential for understanding the muscle's function. The architecture plays a key role in the generation of computational models of skeletal muscles. So far, the *in vivo* methods used for obtaining information of the fascicle architecture of skeletal muscles, such as ultrasound, mainly focuses on 2D information [110, 141]. Another MRI-based method is diffusion tensor imaging (DTI), which requires longer acquisition times and is thus difficult to implement with higher muscle activations or contractions.

In this chapter, a workflow for determination of 3D fascicle architecture from volumetric ultrasound images is developed and introduced. Chapter 5 demonstrated a validation and an evaluation of the methods in Chapter 4. The methods developed and validated in the previous chapters are used for reconstructing volumes of the tibialis anterior (TA) muscle. A protocol with a short acquisition time is used, such that imaging of a whole muscle takes approximately 15-20 seconds. From the 3D images, muscle volume and pennation angle are determined. Additionally, an image-processing-based algorithm is developed which enables detection of fascicle orientations in 3D, as presented in Section 6.1.4. The algorithm is validated on a custom-designed phantom (Section 6.1.1) and applied on the TA of 10 human subjects.

6.1 Methods

This section describes the methods used for the fascicle determination workflow. The methods include the design of the custom-designed wire phantom, the experimental procedures for obtaining 3D ultrasound data, methods for reconstruction and the novel algorithm for 3D fascicle recognition.

6.1.1 Fascicle Phantom

A phantom for investigating ultrasound-based orientations in a controlled manner has been designed for this study, as shown in Figure 6.1. The fascicle phantom consists of four walls arranged in a square. The walls are 100mm high and each side is 200mm wide. Three walls are 5mm thick, one wall has a thickness of 12mm. Two walls parallel to each other include 1680 holes (56 along its length and 30 along its height). The diameter of the holes is 1mm. The distance between adjacent holes (in vertical and horizontal

[1]Parts of this chapter are published [219].

direction) is 2.5mm. The value of 2.5mm has proven to be effective in achieving both a small distance between holes and precise production. Two wire groups are spanned from the holes of one wall to the holes in the parallel wall. In order to keep the wires tight, button-like elevations are attached to the outer sides of the phantom walls, to which the wires can be attached with rubber bands. The elevations are similar to those of the Plus toolkit calibration phantom [144]. The phantom walls were designed using SolidWorks (Premium 2021 SP3.0) and 3D printed from polylactic acid filament.

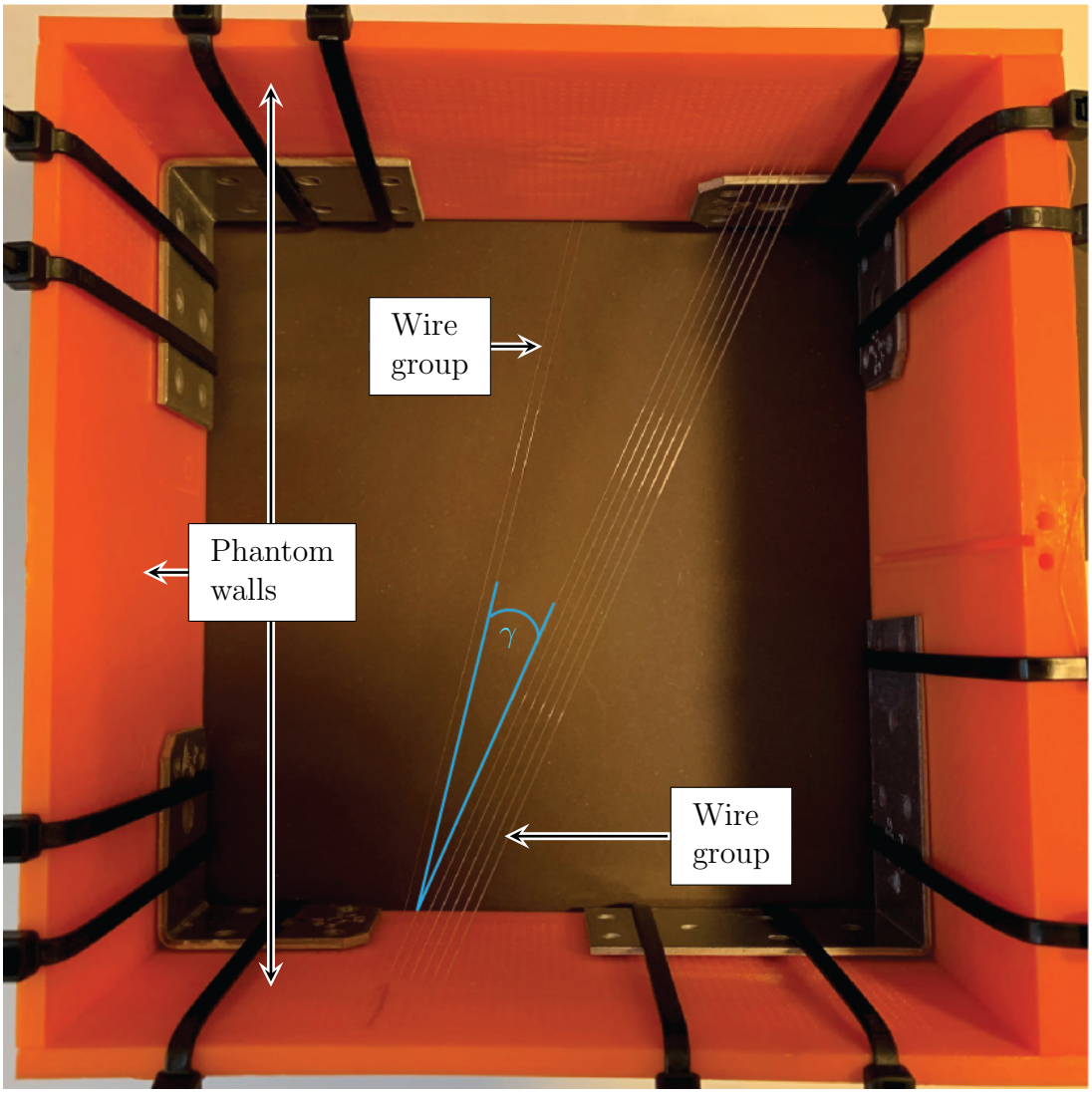

Figure 6.1: Fascicle phantom with 0.1mm nylon wires. The angle γ=10.78° between the wire groups is displayed in blue.

The wires are nylon threads with a diameter of 0.1mm, which is close to the size of thick muscle fibers [64]. One wire group is arranged in six horizontal and three vertical wire lines, using 18 holes on each opposite phantom wall. The other wire group consists of two parallel wires (horizontal), resulting in two holes on each opposite phantom wall. Thus, a total of 40 holes are used (2·18 + 2·2). Due to the known geometry of the phantom and its hole positions from the CAD model, the wire orientations and therefore also the angle between the wire groups are known. The angle is 10.78°.

For ensuring a sufficient acoustic signal during ultrasound scanning, the phantom was immersed in a water tank.

6.1.2 Experimental Setup

Data was collected from 10 healthy subjects[2] (six male, four female). Table 6.1 lists the anthropometric characteristics of the subjects.

Age	Height	Weight	BMI
30±4 years	177±8cm	69.3±11.7kg	22.04±1.98 $\frac{\text{kg}}{\text{m}^2}$

Table 6.1: Anthropometric characteristics of the subjects (mean and standard deviation). BMI: Body mass index.

The automated 3D ultrasound system, as presented in Chapter 4, was used for obtaining volumetric ultrasound data sets in this chapter, with a low force level, which refers to a force of 4.1N (see Appendix A). For phantom trials, 11 trials of the fascicle phantom were recorded by scanning along the wires. For muscle trials, 3D ultrasound images of the TA muscle of the right leg were obtained. Three ankle joint angles were examined.

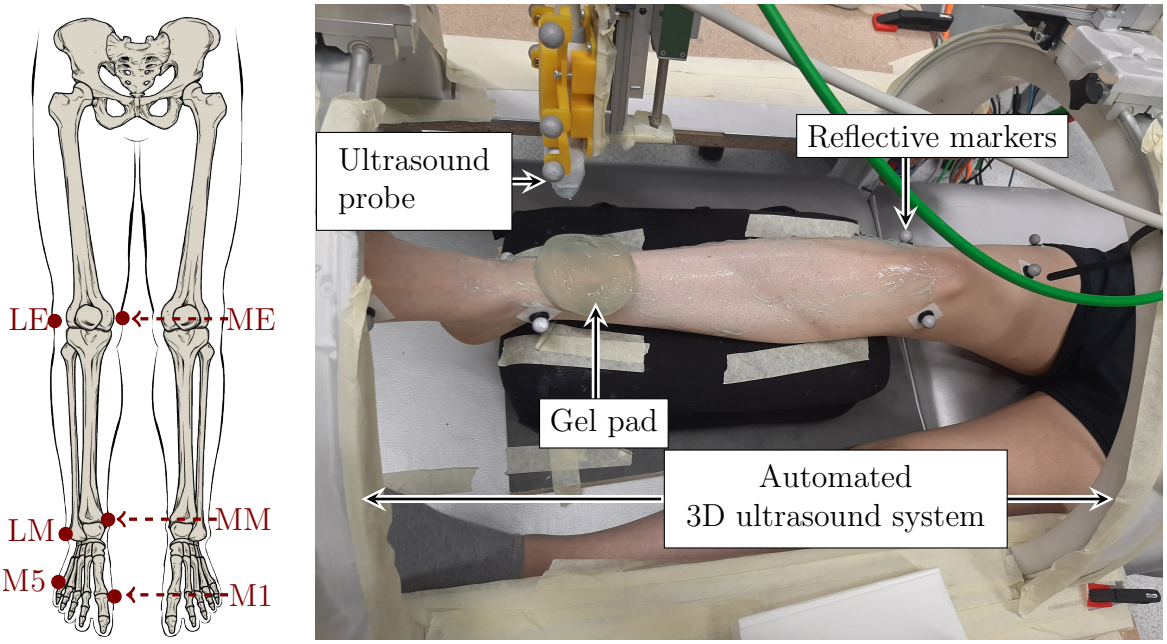

(a) (b)

Figure 6.2: (a) Marker placement. LE: Lateral epicondyle, ME: Medial epicondyle, LM: Lateral malleolus, MM: Medial malleolus, M1: First metatarsal head, M5: Fifth metatarsal head. Image adapted from [24] (licensed under CC BY 4.0) (b) Subject setup with the automated 3D ultrasound system. The figure illustrates the resting position.

Here, the subjects were asked to bring the foot into (1) maximum plantar flexion and (2) to a foot position corresponding to the ankle joint angle for neutral standing position (111±2°). One additional foot position (3) was examined, where the foot was in

[2]The experimental procedures involving human subjects described in this chapter were approved by the University of Stuttgart's Committee on Responsibility in Research (number: Az. 21-011).

a resting position, as illustrated in Figure 6.2b. The selection of the neutral position as the foot position with the smallest ankle joint angle was due to the leg positioning, where the calf muscle was placed on a cushion and the foot and ankle are not supported. This setup restricted maximum dorsiflexion to the defined neutral position.

To avoid a loss of skin contact due to the natural curvature of the lower leg, a gel pad (Aquaflex, Parker Laboratories, Fairfield, USA) and ultrasound gel were used during scanning. The gel pad was moved manually along the leg while scanning.

To record ankle joint angle positions, reflective motion capture markers were placed on the lateral and medial knee epicondyle, lateral and medial malleolus, first and fifth metatarsal, see Figure 6.2a. The markers were recorded by eight infrared cameras (VICON). The ankle joint angle was computed as the angle between the vector from lateral knee epicondyle to lateral malleolus and the vector from lateral malleolus to fifth metatarsal. The mean joint angles for plantarflexion, resting position and neutral position were 157±7°, 145±6°, and 109±7°, respectively.

Each scan of the automated 3D ultrasound system took approximately 15 seconds. A total of three measurements were performed per subject (one for plantarflexion, resting position and neutral position, respectively).

6.1.3 3D Reconstruction and Image Segmentation

The custom-written 3D reconstruction, as described in Section 4.3, was employed and MITK was used for segmentation. The voxel sizes of the reconstruction volume are 0.17x0.17x0.66mm and 0.14x0.14x0.37mm. This means the distances between two consecutive images in the reconstruction volume are 0.66mm and 0.37mm for muscle and phantom data, respectively. For phantom data, both wire compartments were segmented separately. For muscle data, the whole TA was segmented. In addition, the superficial and deep compartments of the TA were segmented separately. Geometries of the muscle from the segmentation masks were created. MITK's drawing tool was used for segmenting the aponeurosis. Cross-sectional area (CSA) and muscle volume were computed as described in Section 4.5. A smoothed polygon was created using MITK to generate 3D volumes of the segmented slices.

6.1.4 Fascicle Detection Algorithm

The segmentation masks served for masking the 3D reconstructed images, see Figure 6.3b. The aponeurosis mask was used to avoid detection of aponeurosis directions as fascicle directions. All image values within the aponeurosis mask were set to zero. For muscle data, a principal component analysis (PCA) was applied on the cartesian coordinates of the geometry of the whole muscle. The three principal axes directions were taken to establish a muscle coordinate system. The masked reconstructed volume was rotated, such that it is aligned with the muscle coordinate system. This means that the sagittal plane of the 3D volume is aligned with the sagittal plane of the muscle coordinate system.

A multiscale vessel enhancement filter (MVEF) [73, 138, 161] was applied on the 2D sagittal images (yz-plane for muscle, xz-plane for phantom data, see Figure 6.3c). The MVEF applies a Gaussian filter (σ=2 for muscle data and 3.5 for phantom data) to the image and computes the Hessian Matrix and their eigenvalues and eigenvectors to enhance

the white lines on the images. As sensitivity threshold values [73], the function's default values β=0.5 and c=15 are selected. The filter settings were constant over all subjects. In this step of the algorithm, the purpose of employing the MVEF is to determine the voxel positions of the enhanced lines, i.e., the positions of the perimysium. The 3D fascicle orientations are computed at a later stage of the algorithm.

After applying the MVEF on the 2D sagittal images, the filtered 2D image slices were re-stitched to a 3D volume. The masked MVEF output was filtered with a Gaussian kernel and the Hessian matrix of the Gaussian filtered volume was computed. The eigenvalues and eigenvectors of the filtered Hessian matrix were determined. The eigenvector of the smallest eigenvalue defines the 3D fascicle direction for each voxel, which means that each voxel contains a direction vector consisting of three components.

For determining the positions of the detected fascicles, the re-stitched MVEF output volume was transformed to a binary matrix array. This was done by setting all voxels with a smaller value than 10% of the maximum voxel value to zero. All voxel values above were set to one. The binary image is then used as a mask for the direction fields, see Figure 6.3d. To determine this threshold of 10%, the histogram of the voxel values was utilized for determining a value in the range of the most frequently occurring voxel values. Thus, voxels with values below the threshold are defined as erroneously detected fascicles. For muscle data, the mask of the compartment was shrunk after MVEF in order to avoid detecting directions of the muscle's surrounding epimysium. The shrunk mask was applied to the filtered volume, as illustrated in Figure 6.3e. The size of shrinking was adjusted for each subject and muscle compartment, where the average shrinking size was 10 pixels. In general, the shrinking size was higher for the superficial than for the deep compartment. The direction components were multiplied by the scaling factors, i.e. voxel sizes, of the volume in x-, y-, and z-direction.

In order to consider only the major orientations, vectors with a length smaller than 50% of the maximum direction vector length were removed. This threshold was achieved by manually testing the impact of different thresholds and selecting the one which visually smoothed the directions.

The detected directions at the end of the lines are detected in different orientations around a sphere, as the algorithm detects tube- or blob-like structures. Therefore, all directions with less than 18 non-empty neighbors were deleted in order to remove the end points of detected lines.

A fast, unsupervised and robust discretized spline smoother [85–87] was applied on the detected directions to smooth the vector field, with the smoothing parameter set to 35. The smoother applies a penalized least square method. By using weights, the method is capable of working with missing values (NaNs). Thus, the smoother can be employed for inter- and extrapolation of the direction data. In order to fill the whole muscle volume with directions, a linear interpolation was employed on the gridded vector field for muscle data. For extrapolating over the whole muscle volume, due to the earlier shrinking of the mask, the spline smoother was applied again with a small smoothing parameter of 0.5.

The computed fascicle directions can be exported as a 3D vector field including position information in VTK format [227] after applying the fascicle detection algorithm. In this chapter, different filters of Paraview (version 5.8.0) are used to visualize fascicle tracts and directions. The *Streamline tracer* filter allows the generation of stream lines from the imported vector field. With the *Glyph* filter, it is possible to visualize the directions

of the imported vector field with arrows. Importing the volume of the 3D ultrasound reconstruction and applying the *Slice* filter enables an illustration of image slices. These can be overlayed with the computed fascicle orientations and visualized tracts.

6.1.5 Angle Determination

This section describes the methods employed for computing the phantom wire angle and the TA pennation angle.

Phantom Study

The directions at the detected positions after applying the fascicle detection algorithm were computed for the two phantom compartments. From the directions, the angle was computed using the dot product formula. The angle was computed as the angle between each direction vector of one compartment and each direction vector of the other compartment.

Muscle Data

For computation of the pennation angle, a PCA was applied on the points within the aponeurosis geometry. The aponeurosis direction was defined as the largest principal component axis. The pennation angle was defined as the angle between the aponeurosis direction and the direction vector at each voxel (determined by the fascicle detection algorithm). The mean pennation angle over all volume elements of the muscle compartments was computed at the three ankle joint angle positions (plantarflexion, resting position, neutral position). To reduce the amount of data of the volume elements for easier computation and statistical analysis, the angles of the individual volume elements were resampled (from a magnitude of about $1{\cdot}10^7$) to 5000 per compartment.

All postprocessing of data, such as fascicle detection and 3D reconstruction, was done using Matlab (R2020a).

6.1.6 Statistical Analysis

Shapiro-Wilk tests were used for testing data for normal distribution. For examining significant differences between two different groups (differences between superficial and deep compartment), a Wilcoxon signed-rank test was used, as the data were not normally distributed. For examining significant differences between more than two different groups (differences between plantarflexion, resting position and neutral position), one way repeated measures analyses of variance (ANOVAs) were applied for normally distributed data. Friedman tests were used for non-normally distributed data. The level of significance was set to a P-value $P<0.05$. The effect sizes were classified as small ($r=0.1$), medium ($r=0.3$), and strong ($r=0.5$) [50].

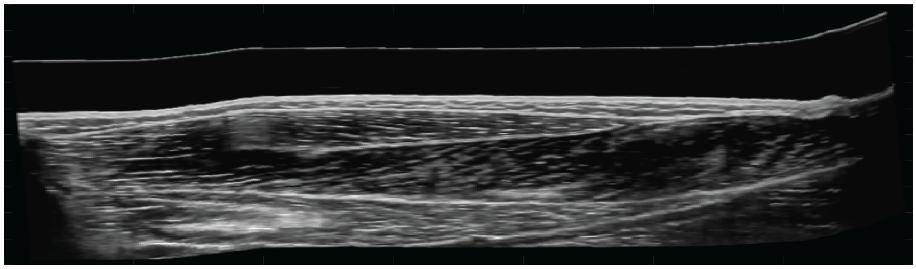

(a) Sagittal image slice of the reconstructed volume, rotated into muscle coordinate system.

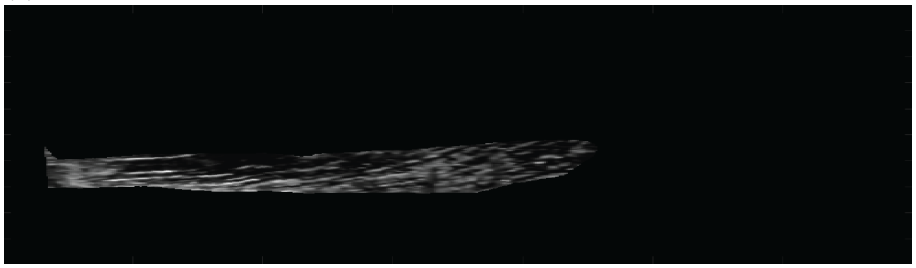

(b) Masking of the muscle compartment.

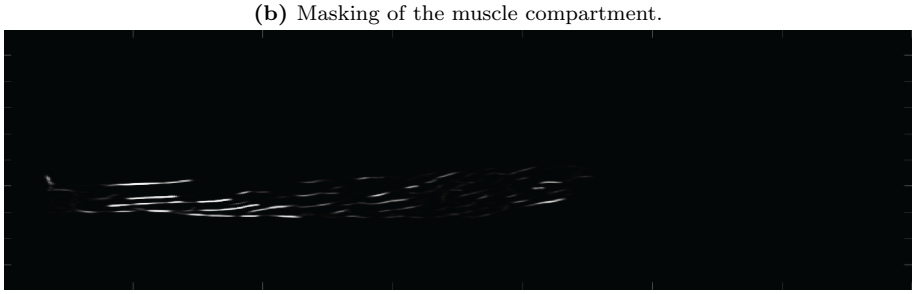

(c) After applying the MVEF.

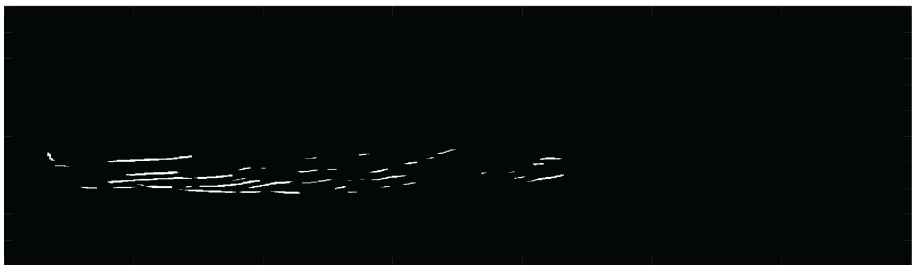

(d) Binarizing the filtered image.

(e) Shrunk mask.

Figure 6.3: Workflow for fascicle detection from 3D ultrasound images, as described in Section 6.1.4. (a) Sagittal image slice of the reconstructed volume, rotated into muscle coordinate system. (b) Masking of the muscle compartment. (c) After applying the MVEF. (d) Binarizing the filtered image and (e) shrunk mask.

6.2 Results

In this section, the results of the data acquisition and fascicle detection are presented. The fascicle detection algorithm is validated using the phantom data. The muscle data are evaluated in terms of volume and pennation angle computation.

6.2.1 Phantom Study

Figure 6.4 shows two different planes of the reconstructed fascicle phantom volume. The view from above (Figure 6.4a) shows the directions of the two wire groups, similar to the actual phantom wires (Figure 6.1). In the axial plane, which was used for image segmentation, both wire compartments are visible.

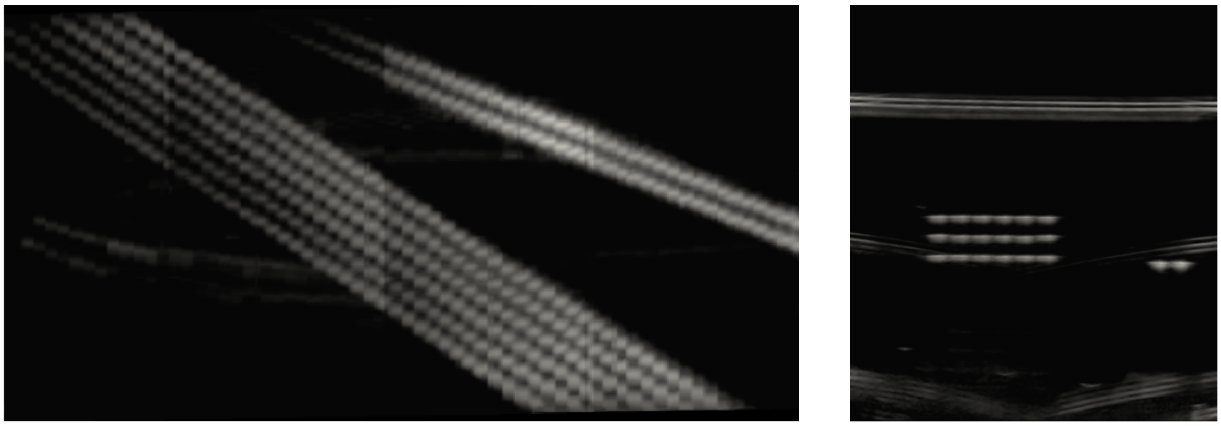

(a) View from above. **(b)** Axial view.

Figure 6.4: Image planes of the reconstructed volume of the fascicle phantom. (a) Longitudinal view, similar to the view from above in Figure 6.1, where the wires are arranged the same way. (b) Axial view, where the two wire groups are visible.

Figure 6.5 shows a histogram of the angle for each direction vector of one compartment with each direction vector of the other compartment. For comparing all directions, a mean absolute error of 0.92±0.59° and a mean relative error of 0.80±0.74° was observed.

The mean direction for both compartments was defined as the normalized sum of vectors. Here, a mean angle of 10.10±0.35° and a mean absolute error of 0.68±0.35° could be observed.

6.2.2 Muscle Volume Reconstruction

The computed mean muscle volume of the TA across all subjects was 91.2±23.5cm^3. Muscle volume did not differ significantly across the three ankle joint angles. Muscle volumes at plantarflexion and neutral position were larger by 2.4±6.0% and 1.6±6.0%, respectively, compared to the resting position.

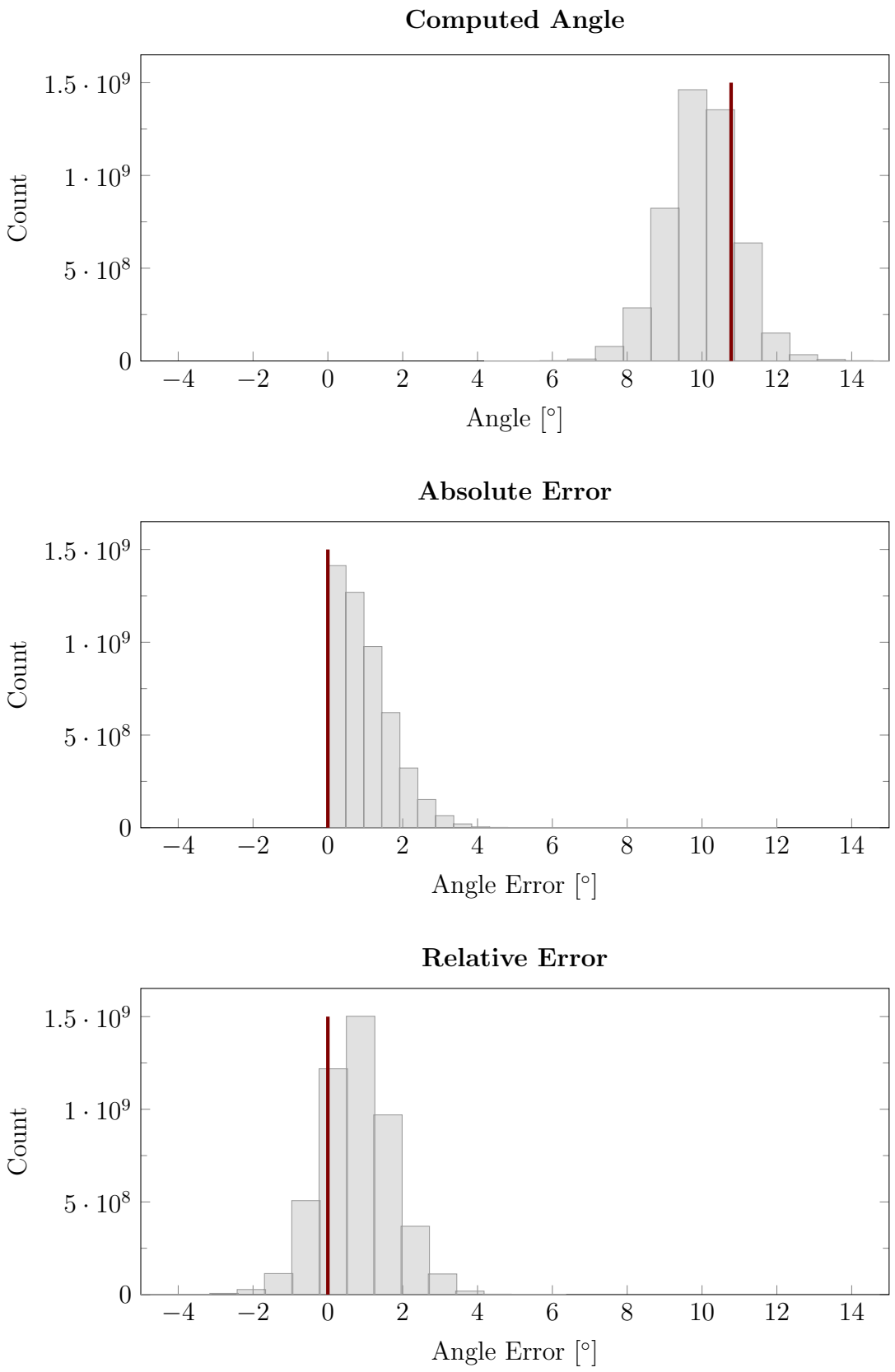

Figure 6.5: Computed wire phantom angles and absolute and relative errors. The phantom angle of 10.78° between the wire groups and the 0° reference for errors are shown as a vertical red line in the histograms.

6.2.3 Muscle Fascicle Reconstruction

The 3D volume of the TA and its central aponeurosis obtained from segmentation and surface creation using MITK is illustrated for one representative subject in Figure 6.6a.

Figure 6.6b shows a visualization of the TA fascicle reconstructions after tractography (using Paraview) in resting foot position, where superficial and deep compartment are illustrated in orange and green, the aponeurosis geometry is colored in gray. The figure shows that the fascicles for the two compartments run in different directions from the central aponeurosis. Figure 6.6c illustrates the exported vector field from the fascicle detection algorithm, visualized as arrows. Figure 6.6d displays an overlay of the arrows with a sagittal image slice of the reconstructed 3D ultrasound image. Here, the perimysium is shown as light gray or white lines between the black or dark gray colored muscle fascicles.

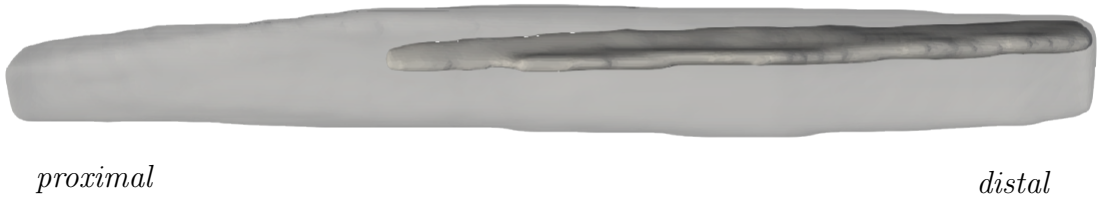

(a) TA volume with the internal aponeurosis.

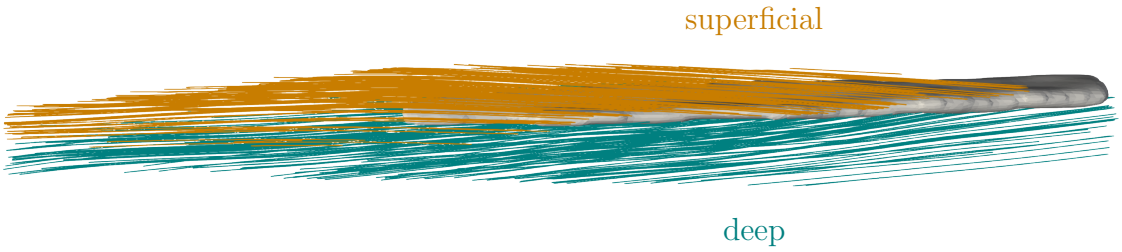

(b) Fascicle lines of the whole muscle using the *Streamline tracer* filter.

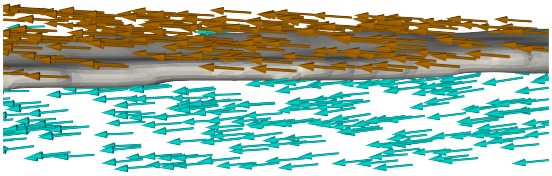

(c) Fascicle directions in both compartments illustrated as arrows using the *Glyph* filter.

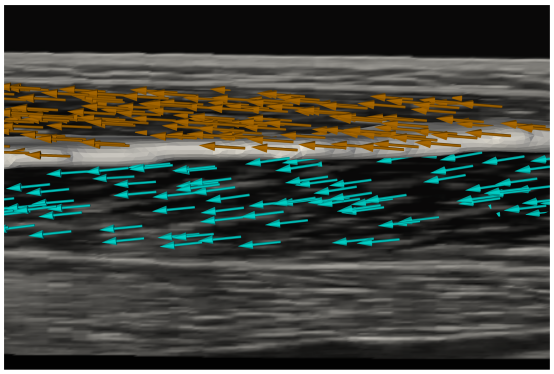

(d) Overlay of a 2D sagittal image with the reconstructed fascicle directions, which are visually aligned.

Figure 6.6: Fascicle reconstruction of the TA for one representative subject using Paraview. The superficial compartment is visualized in orange and the deep compartment in green.

From visual inspection, the computed directions are aligned with the perimysium. Since the perimysium is parallel to the fascicles, this indicates that the computed directions are also aligned with the fascicles on the 3D volume image slice.

Figure 6.7 shows the distribution of the cross-sectional area (CSA) and pennation angle for both compartments over the resting position muscle length L_{Rest} for the same representative subject as in Figure 6.6. L_{Rest} is defined as 100% and the muscle lengths for plantarflexion and neutral position are computed relative to L_{Rest}. In the TA, the superficial compartment does not cover the whole muscle length, in contrast to the deep compartment. The angle distribution is visualized over the whole resting position muscle length, thus ending at approximately 80-90% of the resting position muscle length for the superficial compartment. The shaded areas represent standard deviations. For this subject, the maximum CSA is shifted towards the proximal part of the muscle for neutral position. The computed angles for the superficial compartment show greater variation and a slight increase of pennation angle in neutral position, compared to resting position and plantarflexion. The distribution of the angle for the deep compartment shows, however, a more noticeable increase for the neutral position, especially in the distal region of the muscle. Only minor differences between plantarflexion and resting position are evident in both compartments. An illustration of the distribution of the pennation angle in superficial and deep compartment for each subject can be found in Appendix C. Here, as for the example subject, similar variations and a trend in increasing pennation angles for the neutral position can be observed, more evident for the deep compartment.

In Figure 6.8, the pennation angle for each voxel is displayed color-coded according to the magnitude of the angle for both compartments for plantarflexion, resting position and neutral position, for the same subject as in Figure 6.6. For the superficial compartment, the pennation angle increases for the neutral position can be mainly observed in the distal and mid part of the muscle. For the deep compartment, pennation angle increases can be found in the distal part on the lateral side of the muscle. This is in accordance with Figure 6.7, where the angles in the superficial compartment for the neutral position are increased in the distal part of the muscle. Similar, for the deep compartment, pennation angle increases can be observed in the distal part on the lateral side of the muscle, which is also consistent with Figure 6.7.

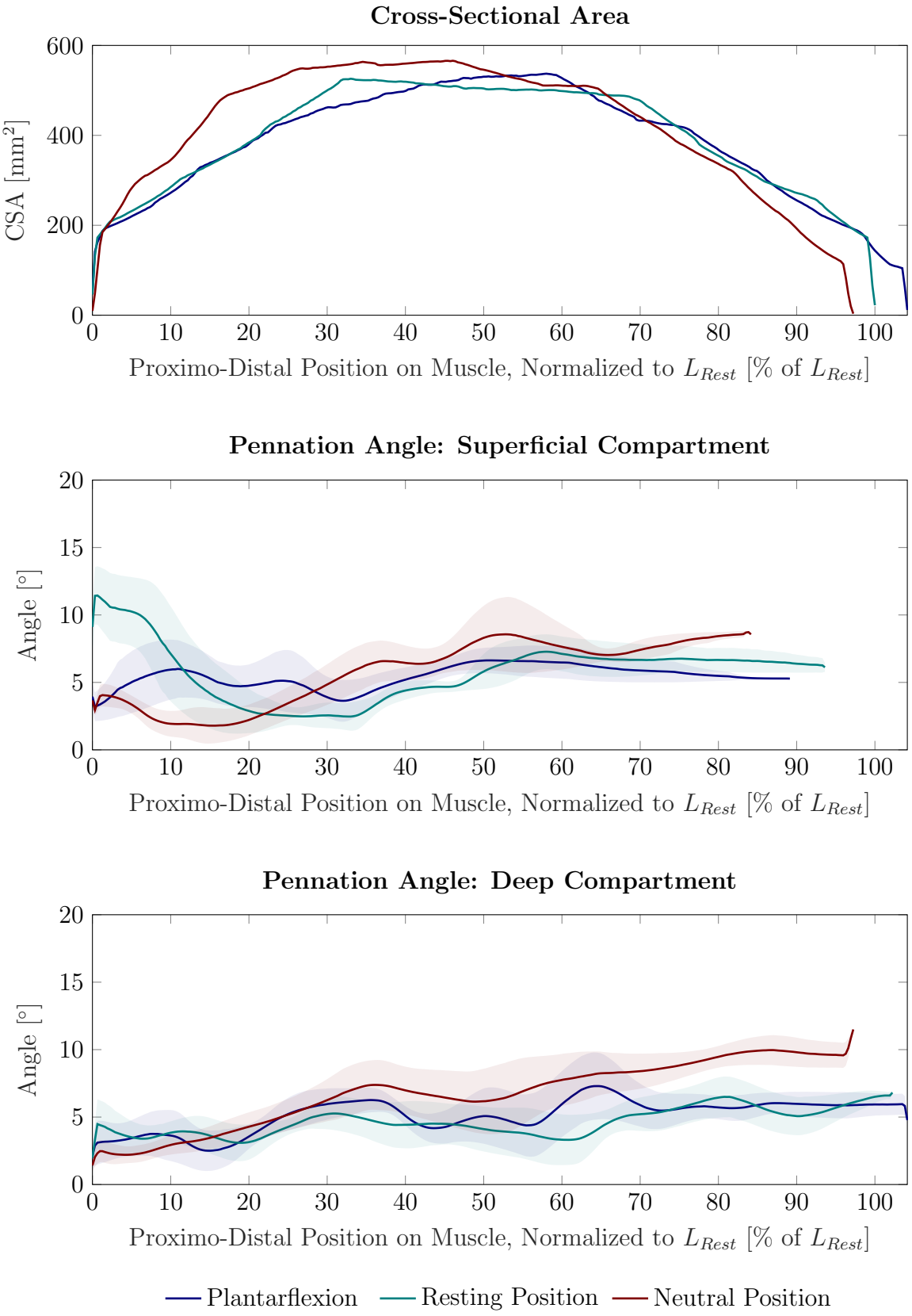

Figure 6.7: CSA and pennation angle for superficial and deep compartment relative to the resting position muscle length L_{Rest} for one representative subject (the same as in Figure 6.6 and Figure 6.8). The pennation angle is decreased for plantarflexion and the resting position, compared to the neutral position, which is more evident for the deep compartment than for the superficial one.

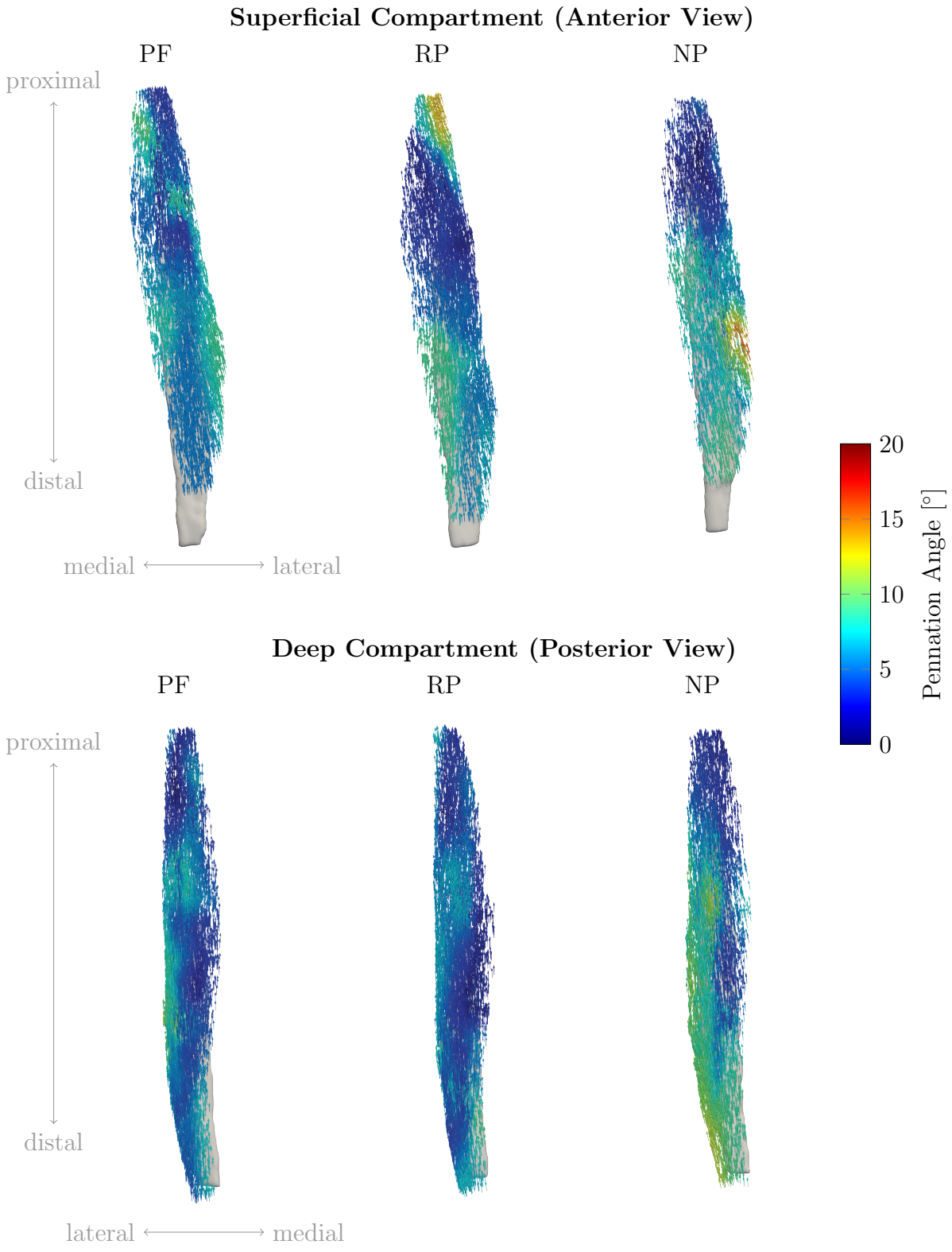

Figure 6.8: Pennation angle distribution of one representative subject (the same as in Figure 6.6 and Figure 6.7) for the superficial and deep compartments in plantarflexion, resting position and neutral position. The directions are color-coded according to the computed pennation angle. The gray surface illustrates the aponeurosis in the corresponding position. For the neutral position, an increase in pennation angle can be observed especially in the distal part of the TA. PF: Plantarflexion, RP: Resting position, NP: Neutral position.

Considering the mean pennation angles over all subjects, in both compartments, the differences between plantarflexion and resting position are relatively small (about 1°, see Figure 6.9). For the superficial compartment, pennation angles are significantly increased for the neutral position, compared to the resting position and plantarflexion ($P<0.001$ and effect size $r=0.0037$ and $r=0.0033$, respectively), whereas the resting position and plantarflexion do not show significant differences. For the deep compartment, the pennation angles for the neutral position are significantly larger than for the resting position and plantarflexion ($P<0.001$ and effect size $r=0.0072$ and $r=0.008$, respectively). In addition, the resting position and plantarflexion show significant differences ($P<0.001$ and effect size $r=0.0017$). Overall, mean pennation angles are significantly smaller for the superficial compartment, compared to the deep compartment ($P<0.001$ and strong effect size $r=0.67$).

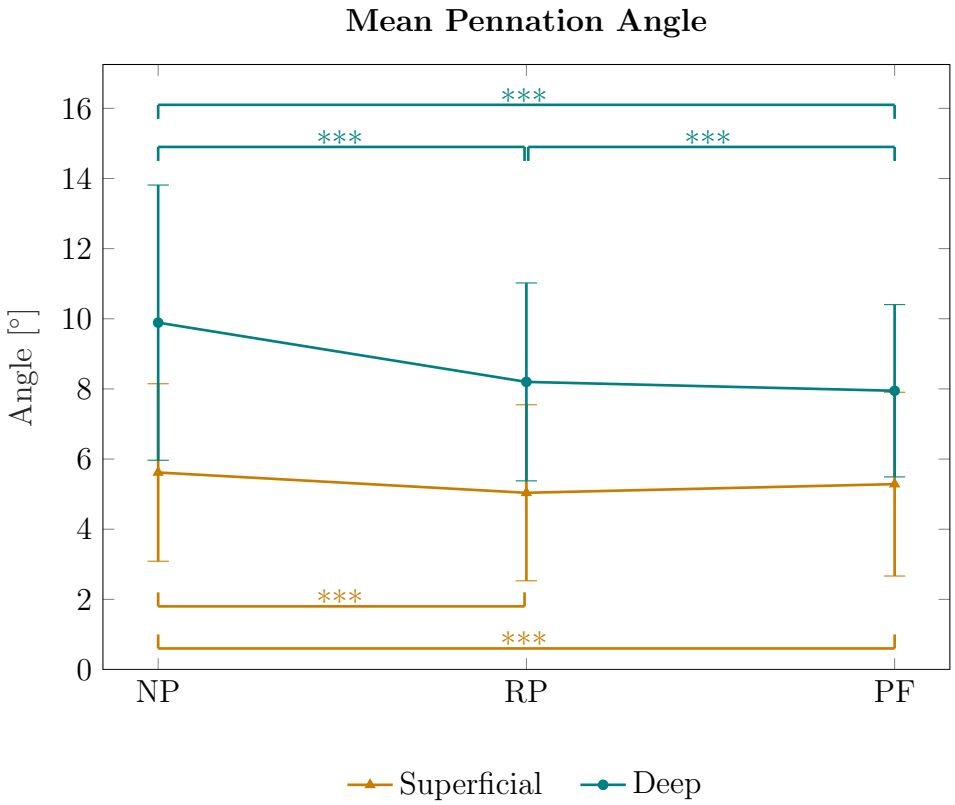

Figure 6.9: Average pennation angle for all subjects for superficial and deep compartment of the TA. The mean angles are increased for neutral position position compared to resting position and plantarflexion. Mean angles for the deep compartment are significantly increased compared to the superficial compartment (*** indicates significant differences). PF: Plantarflexion, RP: Resting position, NP: Neutral position.

Figure 6.10 shows the mean distribution of pennation angles for all subjects over the corresponding resting muscle length L_{Rest}. In the deep compartment, mean pennation angles are increased for the neutral position compared to the resting position and plantarflexion. For the superficial compartment, mean neutral position angles are slightly increased in the mid-part of the muscle. Plantarflexion and resting position do not show large differences for both compartments. For the deep compartment, an overall increase of the angle in the distal part of the muscle can be observed.

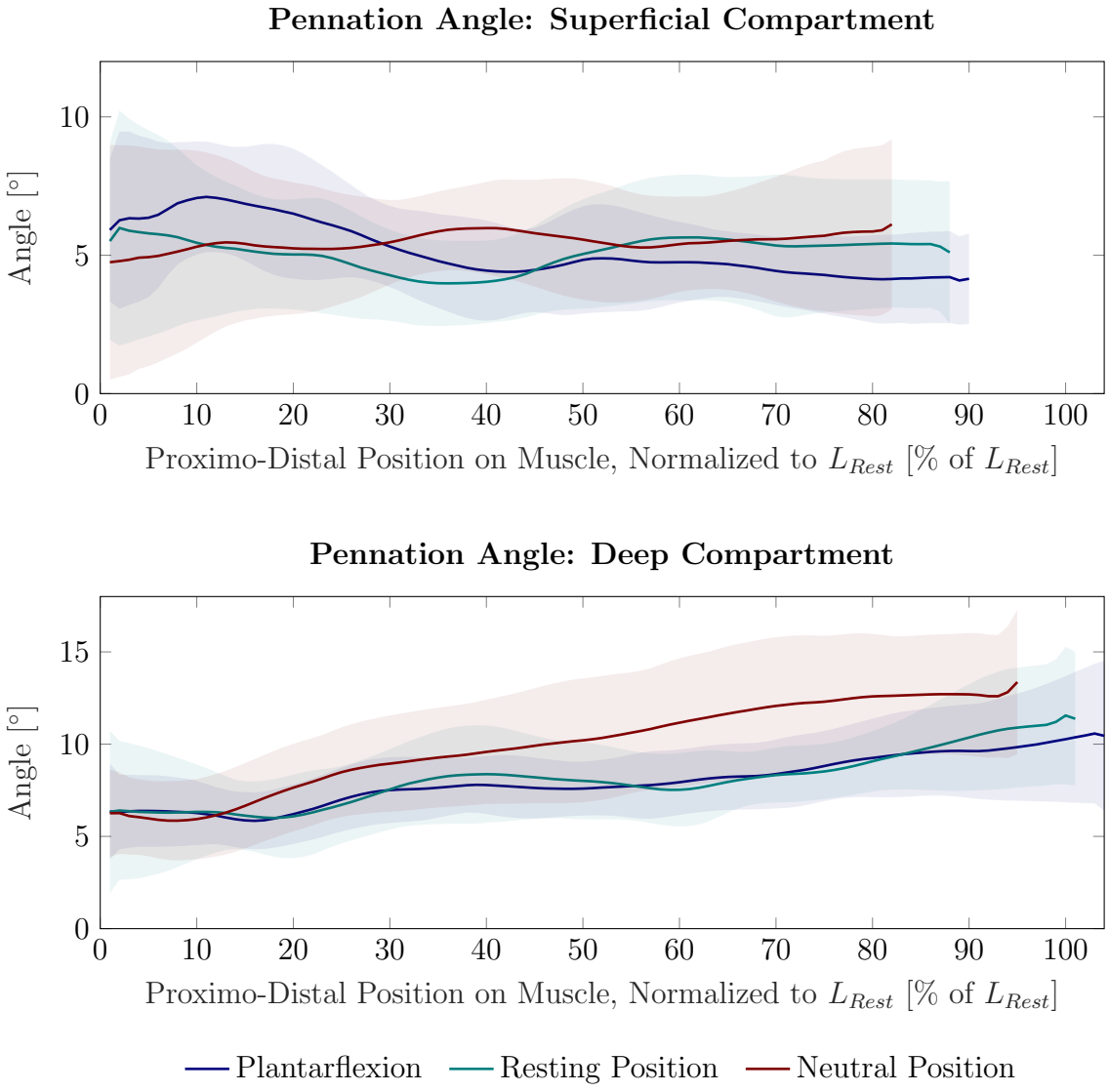

Figure 6.10: Average pennation angle distribution for all subjects over the resting position muscle length L_{Rest}. The deep compartment shows increases in pennation angle for the dorsiflexion position.

6.3 Discussion

In this chapter, a method for 3D fascicle investigations of skeletal muscle has been presented. This study demonstrates that it is possible to determine fascicle orientations with the automated 3D ultrasound scanning system. In a first step, the method has been validated on a custom-designed phantom with known wire orientations. The results of the phantom validation indicate a high accuracy of the proposed method. In a second step, the method was applied to 3D fascicle detection on a human TA.

6.3.1 Muscle Volume

The reproducibility of muscle volume measurements for different muscle lengths, corresponding to the three ankle joint angles, indicates the applicability of the method for capturing 3D muscle geometry [38]. In this study, a mean TA muscle volume of $91.2\pm23.5\text{cm}^3$ was observed for healthy subjects. This result is consistent with previous studies of healthy subjects [130]. Table 6.2 shows TA volume determinations from previous studies. Results of some cadaver studies show smaller TA volumes [74, 239, 266, 271]. For [266] and [239], this can be explained by the fact that the subjects had a very high age, i.e., more than 50 years higher than the average age of this chapter's subject group. Other previous studies found, however, larger TA volumes [43, 65, 80, 159, 200, 203]. The differences in TA volume of the individual studies can have a variety of reasons. Muscle volume can differ depending on the amount of movement, the type of sport and the training condition of the subject [96]. Moreover, in segmentation-based volume determinations, e.g., [19, 41, 77, 78, 200, 218, 226, 267], as used in most imaging methods, the calculated volume heavily depends on the segmentation quality and the segmenting operator. In order to maximize consistency and avoid differences in segmentations due to different operators, all segmentations in our study were done by the same operator. In addition, in manual segmentation a clear demarcation of adjacent muscles is not always possible [80].

6.3.2 Pennation Angle

In this chapter, the determined pennation angles of the TA are relatively small, with angles of about 4° to 8° at neutral ankle joint angle (Figure 6.9), which is slightly lower compared to literature data (e.g., 7° [151], 8° [45], 10° [93], 11° [160], 9-11° [201]). This could be due to the constant, controlled contact force of the ultrasound probe of the automated 3D ultrasound system. The contact force depends on the ultrasound probe weight and the components it is attached to. The action of external forces transverse to the muscle surface can lead to a change in the pennation angle. Wakeling et al. [264] demonstrated that compression of the human medial gastrocnemius muscle with elastic bands leads to a reduction of the pennation angle. Similarly, it has been shown that increasing transverse contact force of an ultrasound sensor results in a reduction of the pennation angle [214, 243]. The applied contact force in this study was 4.1N. In a previous study [145] investigating contact forces on the TA muscle, significant differences in muscle thickness have been found for applied force levels of 1-4N. Furthermore, significant changes in muscle thickness have been found for the transversus abdominis for forces below 2N [127] (see also Chapter 4). Both studies revealed changes in muscle thickness for force values below the force level employed in this study.

	Volume [cm^3]	Subjects	Age [Years]	Height [cm]	Weight [kg]	Condition	Method
This Chapter	91.2±23.5	10	30±4	177±8	69.3±11.7	Healthy	3D Ultrasound
Charles et al. [43]	129±22	10	27±4	174.7±9.91	76±12	Healthy	MRI
Esformes et al.[*1] [65]	131.8±18	6	23±3	175±8	70±6	Healthy	MRI
	133.6±20						Ultrasound
	132.8±21						Ultrasound
Friederich and Brand[*2] [74]	130	2	37	183	91	*ex vivo*	Dissection
	58		63	168	59	*ex vivo*	Dissection
Fukunaga et al. [80]	142.5±27.7	12	32.6±8.2	176.4±6.2	73.5±9.4	Healthy	MRI
Jensen et al. [130]	86.5±18.7	12	26±2			Healthy	MRI
Maganaris et al. [159]	152.7±9	6	28±4	175±8	75±7	Healthy	MRI
Raiteri et al. [200]	142-284	12	24±2	175±7	69±10	Healthy	3D Ultrasound
Ramsay et al. [203]	111.5±34.8[*3]	10	61±10	175.9±6.4	86.4±11.8	Poststroke	MRI
	112±25.8[*4]					Poststroke	MRI
Sopher et al. [239]	65±5	8	80±5	173±1		*ex vivo*	Dissection
Ward et al. [266]	75.9±25.2[*5]	21	83±9	168.4±9.3	82.7±15.3	*ex vivo*	Dissection
Wickiewicz et al.[*6] [271]	74.8[*5]	3				*ex vivo*	Dissection
	68.8[*5]					*ex vivo*	Dissection
	43.1[*5]					*ex vivo*	Dissection

[*1] The study computed the muscle volume both using MRI and ultrasound. For the two ultrasound trials which were conducted, cross-sectional images were recorded, such that volume could be computed from them.
[*2] The study dissected the legs of two cadavers. Here, the values for both of them are given.
[*3] Paretic side.
[*4] Non paretic side.
[*5] This value is derived from the given muscle mass m as $V = \frac{m}{\rho}$, where $\rho = 1.056 \frac{\mathrm{g}}{\mathrm{cm}^3}$ [150] is the muscle density.
[*6] The study dissected the legs of three cadavers. Here, the values for all of them are given.

Table 6.2: Tibialis anterior muscle volume determined in previous studies.

Consequently, these changes in muscle thickness might result in a decrease of pennation angle. Possibly, the influencing factor could be prevented by measurement of muscle architecture with a reduction in contact force. For investigating this effect more in detail, future studies could examine if there are differences between low forces and no contact force at all by using a water tank.

Furthermore, the nature of the method for determining the fascicle orientation might be another reason for smaller pennation angles than in previous literature. In a study by [204], fascicle orientations of the vastus lateralis muscle were determined from 2D ultrasound images using a wavelet transform, Radon transform and manual digitization. The determined pennation angles were found to be smaller for the wavelet transform than for the Radon transform or manual digitization in some images. The authors justified this by stating that manual determination of fascicle directions is more likely to be based on prominent, longer fibers (the Radon transform is similar). However, the wavelet transform considers the mean of local orientations within a defined kernel size, which is also relevant for investigating the fascicle curvature [206]. Considering this, the method of this chapter also incorporates more local orientations through voxel-wise eigenvalue decomposition, rather than relying on prominent lines as in manual determination (and in the aforementioned studies with larger average angles).

A large number of studies show a decrease in pennation angles with muscle lengthening from neutral position to plantarflexion (pennation angle decrease from: 8°-6°, with 45° range of motion [151], 10°-7°, with 30° range of motion [115], 12°-9°, with 30° range of motion [158], 10°-8°, with 30° (0.52 rad) range of motion [210] 10°-9°, with 15° range of motion [201]). The studies typically measured the 2D pennation angles of some representative fascicles in the middle region of the muscle or their compartments. With the proposed 3D characterization, a significant decrease in the pennation angle for the deep TA region with muscle lengthening from neutral position over resting position to plantarflexion has been found (Figure 6.9). The superficial region shows smaller changes in the pennation angle with muscle lengthening, which becomes significant only between the neutral position and resting position, as well as between neutral position and plantarflexion.

The low effect sizes and the comparatively large standard deviations of the pennation angles might be attributed to methodological differences between this study and conventional 2D ultrasound studies. 3D characterization with much higher spatial resolution compared to local pennation data from 2D ultrasound lead to comparably large variability of the pennation angles within the muscle (Figure 6.9). Nevertheless, studies agree that there are only small changes in pennation angle with muscle lengthening in the TA. This can be explained by a geometrical model of Eng et al. [63], in which, depending on the muscle deformation during muscle lengthening, there is no or negligible change in the pennation angle. In addition, significantly higher pennation angles in the deep compared to the superficial compartment could be observed. This is in agreement with measurements on the TA of women (n=45), but is in contrast to men (n=64) [162]. In this chapter, due to the small number of participants (six male, four female), such differences could not be examined statistically. However, this may be investigated in future studies.

For the example subject, the pennation angle over the muscle length (Figure 6.7) shows alterations in angle magnitude over the muscle length. Yet, such variations along the scanning direction are small in absolute terms (approximately 2°). Thus, they can be explained by measurement uncertainty as well. Another possible explanation is that this

could be caused by involuntary shifts of the leg during the scan. Since the leg was not fixed during the measurement, it is further possible that the pressure of the ultrasound probe caused the muscles to shift.

6.3.3 Limitations/Outlook

The lack of fixture of the leg is a limitation of the study. For future studies, it could be beneficial to restrict the movement of the foot, such that the same ankle joint angles are compared between subjects.

In this chapter, the subjects were told to move their foot to positions such as plantarflexion. Since no force resistance was included, it can be assumed that muscle contraction levels were relatively low. It would therefore be valuable to incorporate EMG electrodes for determining the muscular activity and a dynamometer for force resistance to study changes in 3D muscle architecture during higher contraction levels.

So far, the method has been validated using phantom data. For future studies, it would be useful to also obtain a DTI data set from the same subjects and compare the computed pennation angles to the 3D ultrasound-based ones. Another possible validation method for future applications could be an *ex vivo* study, where the 3D ultrasound imaging method is applied and afterwards a muscle, e.g. a piece of meat, is dissected manually or perhaps digitized.

Using advanced tractography algorithms similar to the ones employed for processing DTI data sets, the course of the fascicles can be tracked from ultrasound images as well. Thus, future applications should investigate such methods as well for determining not only the pennation angle, but also other characteristics, such as the fascicle length or the curvature of the fascicles.

6.4 Conclusion

In conclusion, a method has been presented that allows reconstruction of 3D muscle architecture and volumes. Validation of the method on phantom data indicates a high accuracy of the method. Compared to other imaging modalities, such as MRI, a less complex method was introduced for investigating 3D fascicle architecture, which also allows imaging at higher contraction levels. Thus, the method can be used in a variety of clinical and scientific settings. This can help obtaining a better understanding of differences between healthy muscles and musculoskeletal disorders, such as cerebral palsy, which could promote new therapy approaches. Further, the fascicle distribution and orientations obtained from the proposed method can provide better input and reference data for of computational models of skeletal muscles increasing the potential to address current and future research questions. This can increase the understanding of a muscle's mechanical behavior with various muscle architectures.

7 Dynamic 3D Ultrasound Imaging of the Tibialis Anterior[1]

In a systematic review, van Hooren et al. [110] showed the feasibility of 2D ultrasound for investigating fascicle length and pennation angle during dynamic contraction. However, with such examinations, 3D information is missing which may provide relevant information on the muscle's characteristics. In contrast, previous studies which investigated volumetric muscle data using 3D ultrasound mainly focused on isometric contractions or resting states, i.e., static imaging conditions, e.g., [41, 200, 267]. Since isometric conditions account for only a small part of movements in everyday life, it is important to investigate the muscle volume and shape in dynamic conditions as well. Understanding how a skeletal muscle deforms during dynamic movement can provide additional valuable knowledge on the muscle's dynamic contraction behavior. This may lead to the achievement of useful input information for computational models.

This chapter presents a novel approach for determining the deformation of the tibialis anterior (TA) muscle during dynamic movement by acquiring a series of 2D ultrasound images. By using motion capture and encoder data, the probe position and ankle joint angle are recorded simultaneously. Through defining ankle joint angle intervals, a reconstruction of ultrasound images during movement is made possible.

7.1 Methods

This section describes the experimental methods for obtaining 3D ultrasound images in dynamic conditions, i.e., while the subject actively moves the foot in controlled conditions. Further, the algorithm for reconstructing 3D volumes of the TA during motion is presented, which groups ankle joint angles into intervals of 1°.

7.1.1 Experimental Setup

The automated 3D ultrasound system, which is described in Chapter 4, was used for acquisition of 3D ultrasound data. Simultaneously, eight infrared cameras (VICON) recorded positional data from reflective markers at a frame rate of 100Hz. For computation of the ankle joint angle, the markers were placed at the following locations: lateral and medial epicondyle, lateral and medial malleolus, first and fifth metatarsal (the same positions as in Chapter 6, see Figure 6.2a). The subject's lower limb was placed on a hard cushion. The positioning allowed movement of the foot and visibility of the reflective markers. Encoder positions, motion capture data and 2D ultrasound images from the frame grabber were synchronized using the method described in Appendix B.

[1]Parts of this chapter are published in [220] and [216] (licensed under CC BY 4.0).

3D ultrasound images of the TA of the right leg of five subjects[2] (two male, three female) were obtained. The anthropometric characteristics of the subjects are listed in Table 7.1.

Age	Height	Weight	BMI
27.8±3.1 years	177.2±7.9cm	68±10.9kg	21.52±1.93 $\frac{kg}{m^2}$

Table 7.1: Anthropometric characteristics of the subjects (mean and standard deviation). BMI: Body mass index.

As a first part of the study, for reference, the participants were told to actively move their foot to two different positions: (1) plantarflexion and (2) neutral foot position, which is defined as the neutral standing position (see also Chapter 6). One scan of each position was conducted per subject with an average scan time of 15-20 seconds.

For the second part of the study, i.e., the dynamic trials, the subject periodically moved the foot with a constant velocity from the neutral position to plantarflexion and vice-versa. Average joint angles for plantarflexion and the neutral position were 156.7±6.4° and 112.5±9.42°, respectively.

A metronome was used for visual and audio feedback for the subject to control their foot velocity. Moving velocity was set on the metronome to 45 and 100 beats per minute, which is referred to as *slow* and *fast*, respectively. This means that the foot was in plantarflexion on every second beat, and in the neutral position on each beat in between.

Simultaneously, the automated 3D ultrasound system moved the probe periodically from the proximal to the distal end of the TA and vice-versa (along the horizontal axis).

The principle of the data acquisition method is illustrated in Figure 7.1. Since the repetitive foot movement is a monotonous task, it can be demanding in terms of coordination and concentration. Therefore, each subject's trial for a given velocity (which totaled 9 minutes) was split into four separate smaller trials of 2 minutes and 15 seconds each, in order to ensure a constant concentration level for the subjects during the measurements. To avoid loss of skin contact, a gel pad (Aquaflex, Parker Laboratories, Fairfield, USA) and ultrasound gel were used. The gel pad was moved manually along the leg while scanning.

[2]The experimental procedures involving human subjects described in this paper were approved by the University of Stuttgart's Committee on Responsibility in Research (number: Az. 21-011).

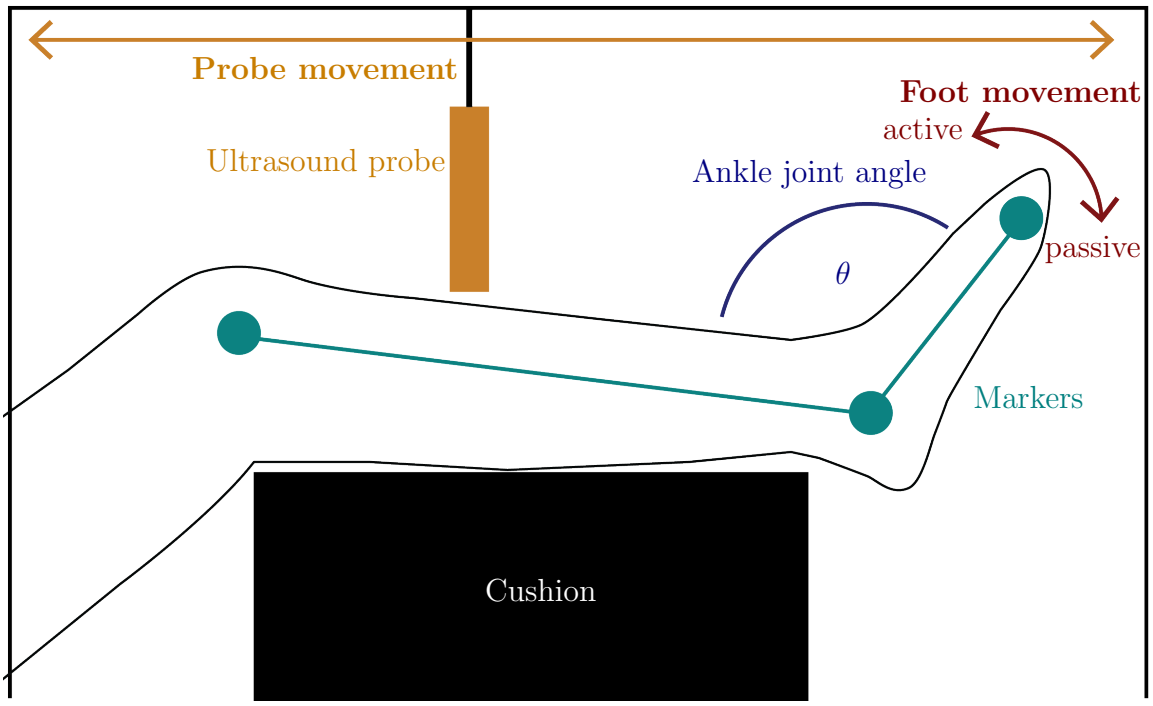

(a)

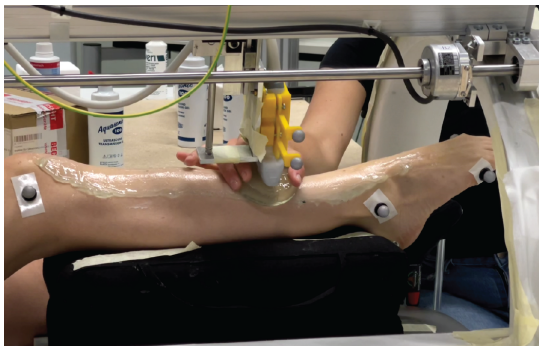

(b)

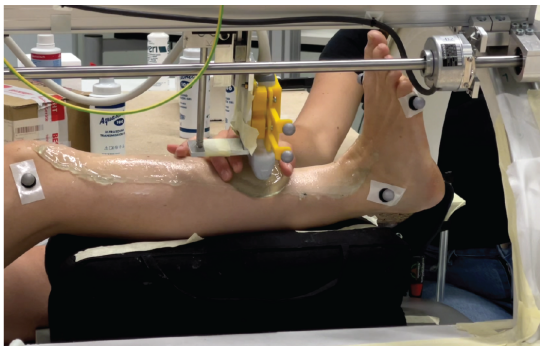

(c)

Figure 7.1: Experimental setup for dynamic imaging. (a) The lower leg is elevated and equipped with reflective markers (green) from which the ankle joint angle θ (blue) can be computed. While the foot moves periodically from plantarflexion to neutral position (red arrow) and vice-versa, the ultrasound probe moves back and forth (orange arrow) from the distal to the proximal end of the TA. As the dorsiflexion movement direction is generated by TA contraction, it is defined as an *active* movement whereas the opposite plantarflexion is defined as a *passive* movement. (b) and (c) show images of the setup with one subject during dynamic imaging at two different ankle joint angle positions. Here, the gel pad is moved alongside to ensure sufficient image quality.

7.1.2 Angle Intervals

After recording, encoder positions and motion capture data were sampled to the ultrasound frame rate. Four trials of one velocity were stitched for obtaining a sufficient number of 2D images within one joint angle interval for reconstruction. The ankle joint angle θ was computed as the angle between the vector from lateral knee epicondyle to lateral malleolus and the vector from lateral malleolus to fifth metatarsal (see Figure 7.1a).

Ultrasound measurements for a given ankle joint angle were binned into intervals of 1°, which means $\theta - 0.5° \leq \theta < \theta + 0.5°$.

Furthermore, it was determined if the slope on the ankle joint angle curve was negative or positive. This was done for defining the direction of the foot movement, i.e., if it is a dorsiflexion (negative slope) or plantarflexion (positive slope) movement. Since 3D ultrasound images of the TA were acquired, the dorsiflexion movement direction, induced by contraction of the TA, is referred to as *active* and the opposite plantarflexion movement direction is referred to as *passive* in the following. All frames and encoder positions belonging to one specific angle interval and movement direction were extracted.

Figure 7.2 shows one example trial with *slow* velocity with computed ankle joint angles and the corresponding encoder position. Figure 7.3 illustrates a cutout of Figure 7.2 (of approximately 15 seconds) as an example with three extracted frames for *active* movements.

If the distance between two images within one interval was smaller than 0.8mm, the average of those images and corresponding position values was taken. The image stack and the corresponding encoder positions were exported to Matlab (R2020a) if they met the following criteria: 1) a minimum of 40 images are within the image stack of the interval with one movement position and 2) the maximum distance between two images within the stack is less than 25mm. A Stradwin file was generated from the Matlab file containing all 2D images and position information for a given θ interval.

Since there are four different conditions (*slow active*, *slow passive*, *fast active*, *fast passive*), the maximum and minimum available θ meeting the inclusion criteria was determined for each condition. Range of motion (ROM) was defined as the range from the larger value of the smallest available θ value for *active* and *passive* movement to the smaller value of the largest available θ value for *active* and *passive* movement. For each of the four conditions, the volume was reconstructed in 10% intervals of ROM. The ROM intervals correspond to the muscle elongation caused by extension of the foot for plantarflexion, i.e., the 0% of ROM means the shortest TA muscle length and 100% of ROM refers to the longest one.

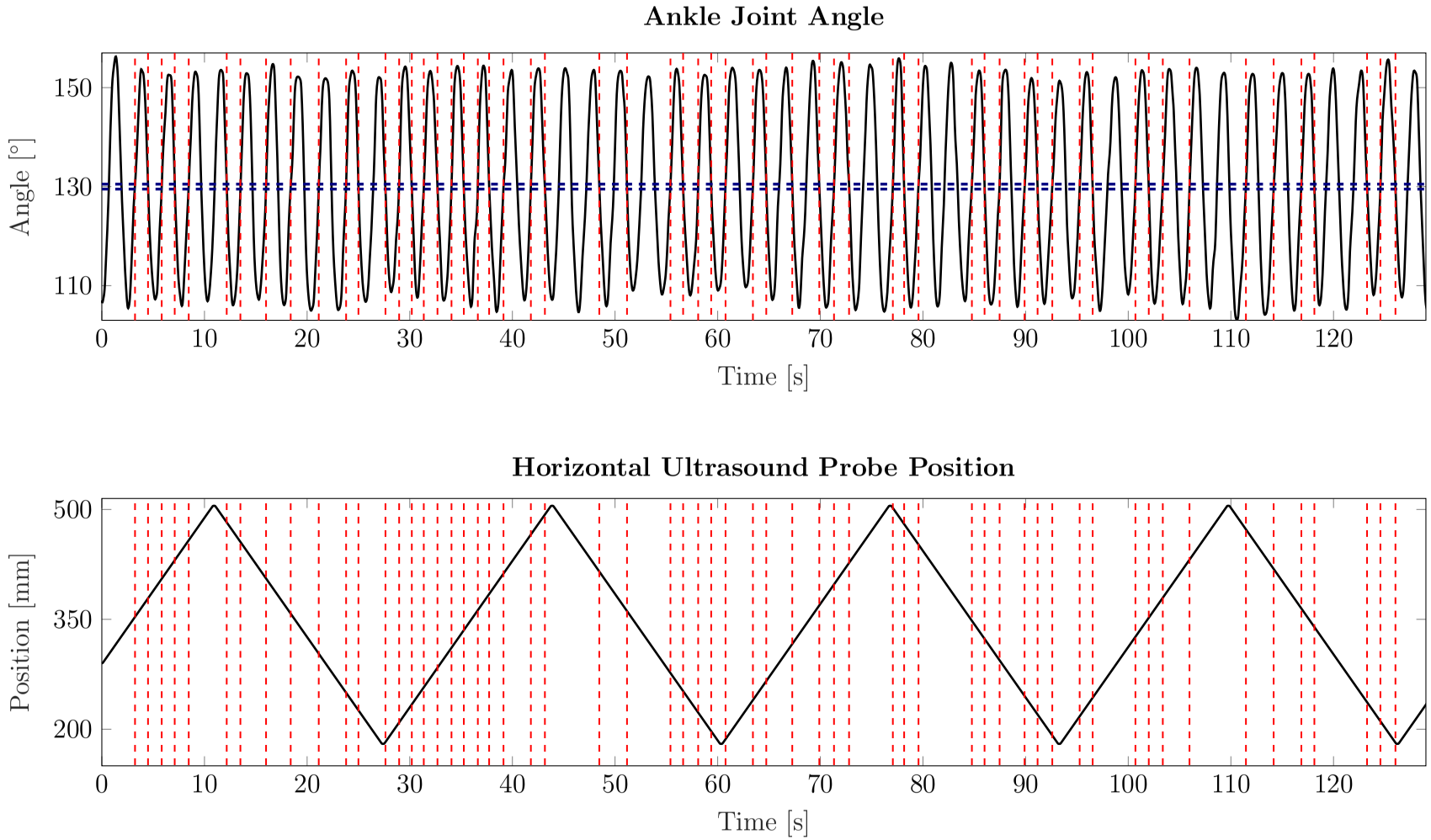

Figure 7.2: Joint angle interval definitions. The top part of the image shows the ankle joint angle (*slow* velocity), the bottom part illustrates the ultrasound probe's position along the horizontal axis. The blue line is one representative angle interval of 130° and the red lines show the corresponding position tags.

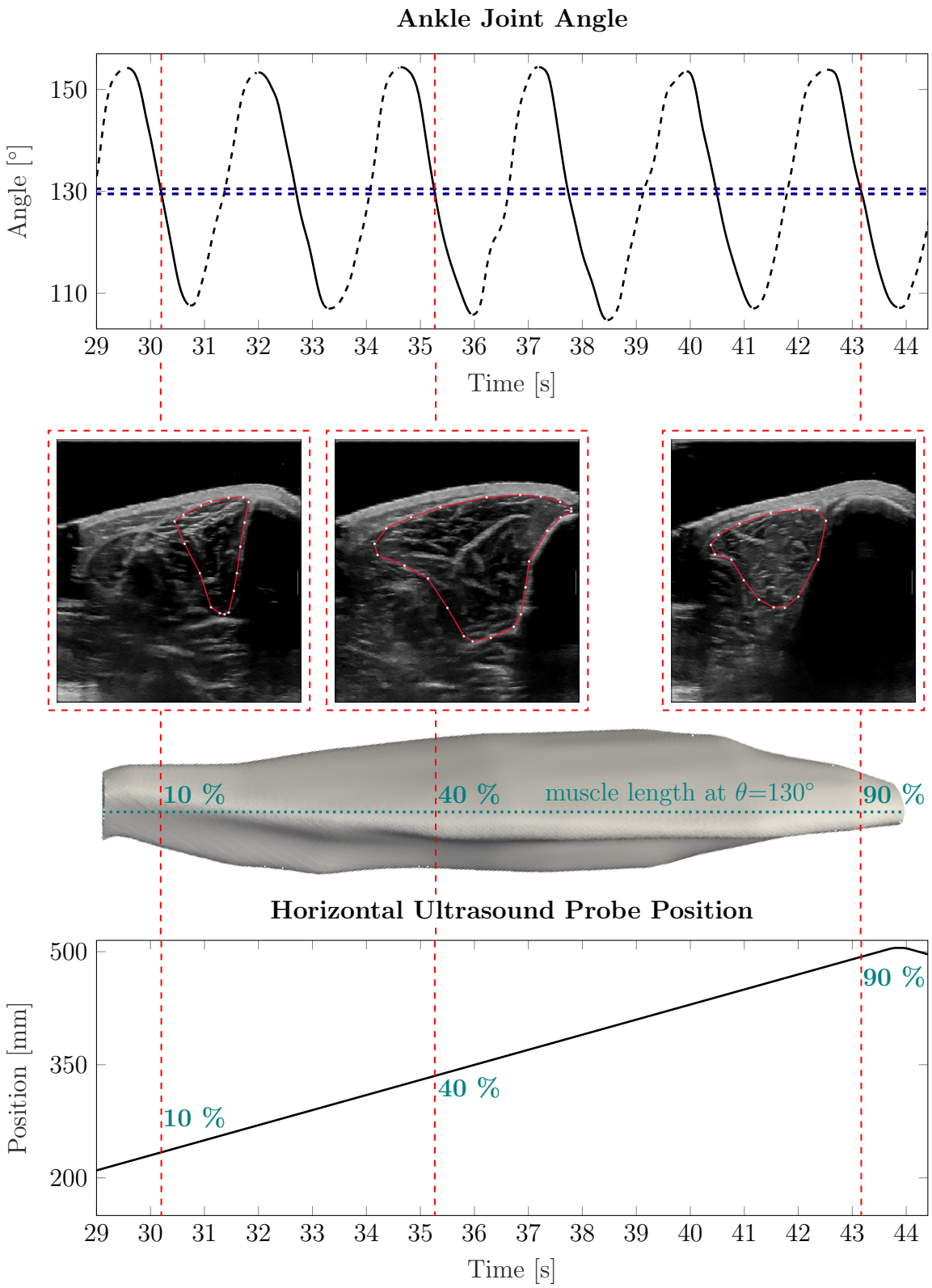

Figure 7.3: A cutout of Figure 7.2 (*slow* velocity) which illustrates the angular interval binning more in detail. The top part of the figure shows a 15 second sequence of measured ankle joint angle during a cyclic *slow* velocity trail. Here, it is distinguished between *active* (solid lines) and *passive* (dashed lines) movement. A 1° interval at an ankle joint angle of 130° is illustrated in blue, the red lines show three example image frames, which are extracted. Below, the corresponding 2D B-Mode ultrasound images and the corresponding position on the muscle are shown. The bottom part displays the ultrasound probe's position along the horizontal axis of the device.

7.1.3 3D Reconstruction and Image Segmentation

For this study, Stradwin was used for 3D reconstruction of the TA (see Section 4.4). The segmentation was done by manually outlining the muscle on 15-20 slices at approximately equidistant frames along the muscle's longitudinal axis. The process is illustrated in Figure 7.5. From the manually outlined slices, Stradwin interpolates a surface through the segmented image slices and creates a 3D volume [252, 254]. Surface creation settings in Stradwin were set to *low resolution* and *high smoothing* strength. After generating a surface geometry of the TA in Stradwin, the method for computation of the volume, length and cross-sectional area (CSA) was used, as described in Section 4.5.

7.1.4 Ellipsoid Prediction

An ellipsoid can be considered a highly simplified shape of a muscle, which has been shown to allow reproduction of muscle shapes and gearing ratios [235]. For later comparison with experimental TA data, the equation for the volume of an ellipsoid was used for computing its CSA:

$$V = \frac{4}{3}\pi abc. \tag{7.1}$$

Here, a, b, c are the lengths of the semi-axes of the ellipsoid, as shown in Figure 7.4. The parameter c is defined as the longitudinal semi-axis of the ellipsoid,

$$c = \frac{1}{2}L_{Muscle}, \tag{7.2}$$

where L_{Muscle} is the muscle length at the corresponding θ interval. The maximum CSA of an ellipsoid can be defined as:

$$CSA_{Ellipsoid} = \pi ab. \tag{7.3}$$

Muscle volume was assumed to stay constant, while c was considered to elongate as the muscle would be lengthened by moving the foot from neutral position to plantarflexion. Using the experimentally determined CSA values, $CSA_{Ellipsoid}$ can be determined as:

$$CSA_{Ellipsoid} = \frac{3}{4}\frac{V_{muscle}}{c}. \tag{7.4}$$

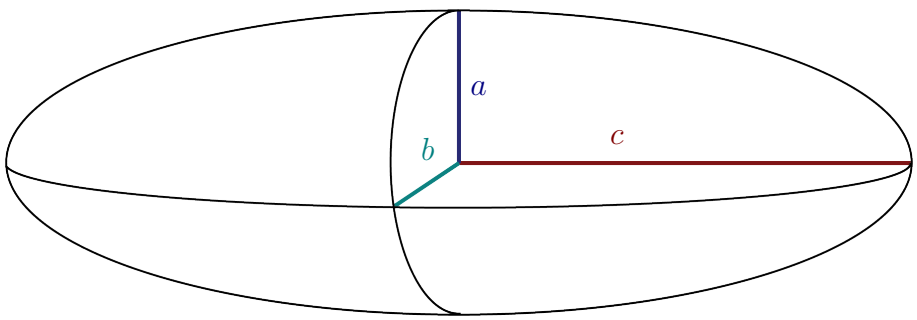

Figure 7.4: Ellipsoid with semi-axes.

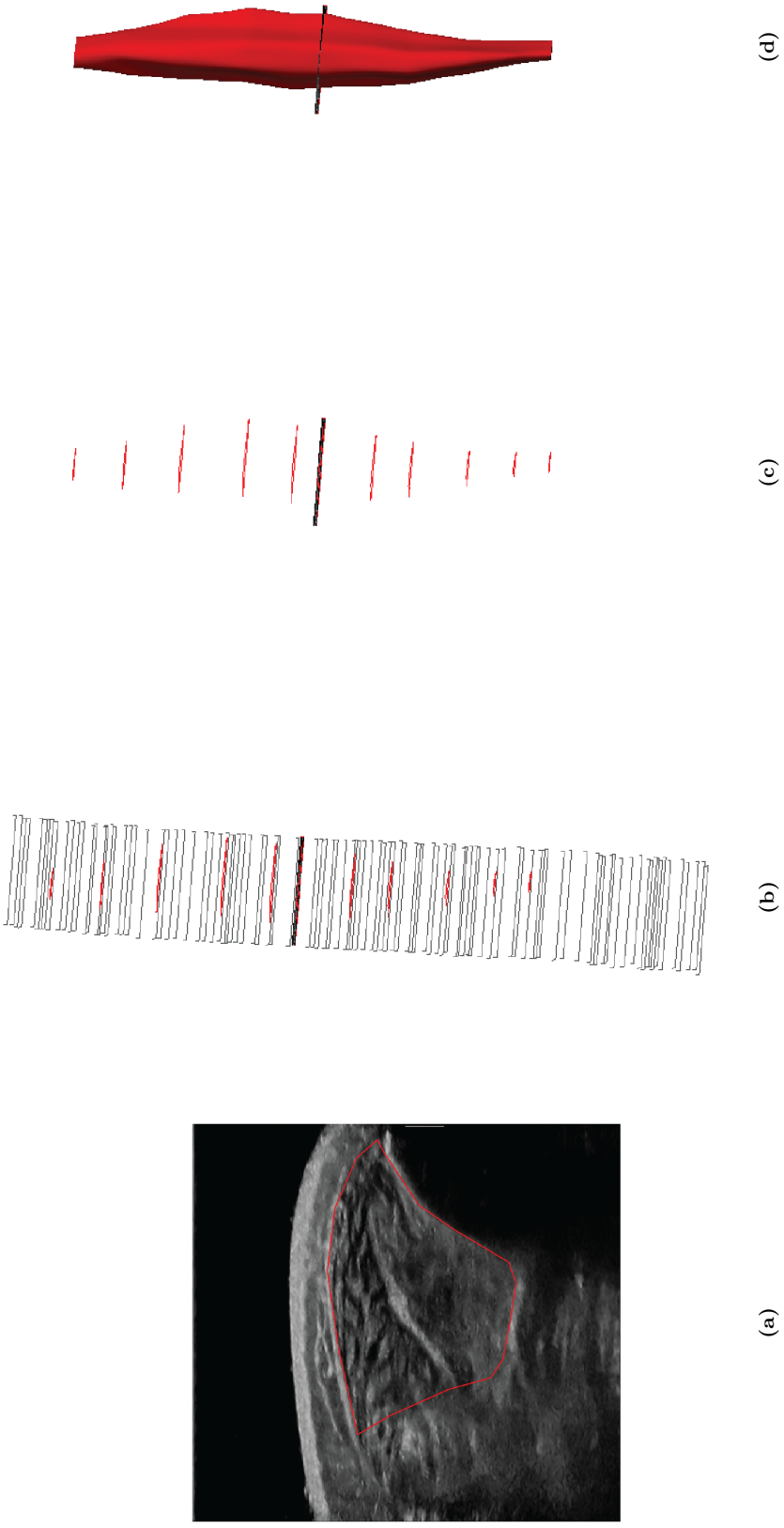

Figure 7.5: Segmentation and volume reconstruction using Stradwin. (a) Segmentation of one example slice. (b) Frames within one ankle joint angle interval with segmented slices highlighted in red. (c) Segmented slices from which (d) the surface geometry is reconstructed.

7.1.5 Statistical Analysis

Shapiro-Wilk tests were used for testing the data for normal distribution. For comparison between groups, one way repeated analyses of variance (ANOVAs) were used for normally distributed data and Friedman tests were applied for non-normally distributed data. Analyses of covariance were employed for comparison between regression lines. The level of significance was set to a P-value $P<0.05$.

7.2 Results

Figure 7.6 and Figure 7.7 show examples of 3D reconstructions for one representative subject for all 11 intervals of ROM, for *active* TA shortening and *passive* TA lengthening, respectively. From visual inspection, it can be observed that muscle length increases with an increase in the ankle joint angle, i.e., an increase in ROM. This leads to a stretch of the muscle while elongating, i.e., the muscle gets thinner.

7.2.1 Muscle Volume and Length

The mean computed muscle volume of the five subjects for the static trials was $88.96\pm28.11\text{cm}^3$. For these trials, muscle volumes did not differ significantly between neutral position and plantarflexion. For the dynamic trials, the determined mean muscle volume was $89.22\pm26.43\text{cm}^3$. Muscle volume did not differ significantly between the different ROM intervals. Also, no significant differences between the muscle volumes obtained from dynamic and static trials could be observed. Averaged over all subjects, the maximum differences of normalized muscle volume between different ROM intervals for dynamic trials were in a 2% range. The mean change in muscle length from neutral position to plantarflexion was 19.95 ± 3.69mm (9.61% increase) for static trials and 22.51 ± 8.49mm (11.21% increase) for dynamic trials.

7.2.2 Cross-Sectional Area

The shortest muscle length, corresponding to the smallest ankle joint angle and 0% of ROM, was defined as 100% of the reference muscle length L_0. Muscle lengths of other ROM intervals were computed with regard to L_0. Thus, by increasing the ROM intervals to 100% of ROM, the maximum muscle length is 111.21% of L_0, corresponding to a mean stretch of 11.21%.

Figure 7.8 illustrates the mean normalized CSA value for the whole muscle for the four conditions (*slow active*, *slow passive*, *fast active*, *fast passive*) and the predicted ellipsoid CSA value $CSA_{Ellipsoid}$. Here, $CSA_{Ellipsoid}$ shows a straight line with a negative slope, i.e., a decrease in CSA for elongation of the ellipsoid. The experimentally determined CSA shows a similar trend for decrease in CSA for increasing L_0, which can be observed for all conditions. Significant differences in mean CSA between different muscle lengths, i.e. different ROM intervals, were found for *slow active* ($P=0.004$), *slow passive* ($P<0.001$) and *fast active* ($P<0.001$), and no significant differences for *fast passive* ($P=0.111$). Mean CSA was significantly different between *slow active* and *fast active* ($P=0.003$) and *fast active* and *fast passive* ($P=0.001$).

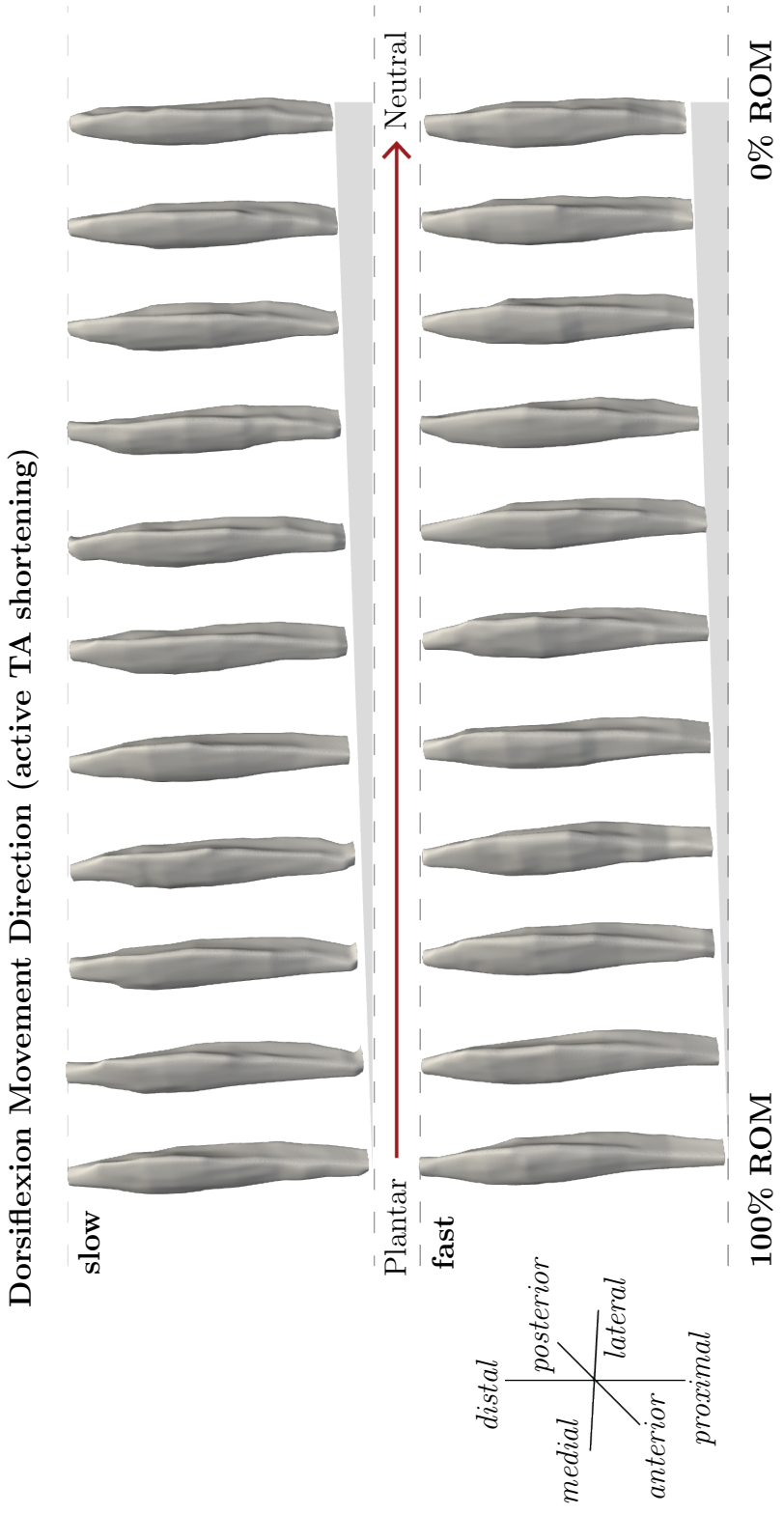

Figure 7.6: Example reconstruction for 10% intervals of ROM for *active* movement with *slow* and *fast* velocity. Muscle shortening towards the neutral position can be observed.

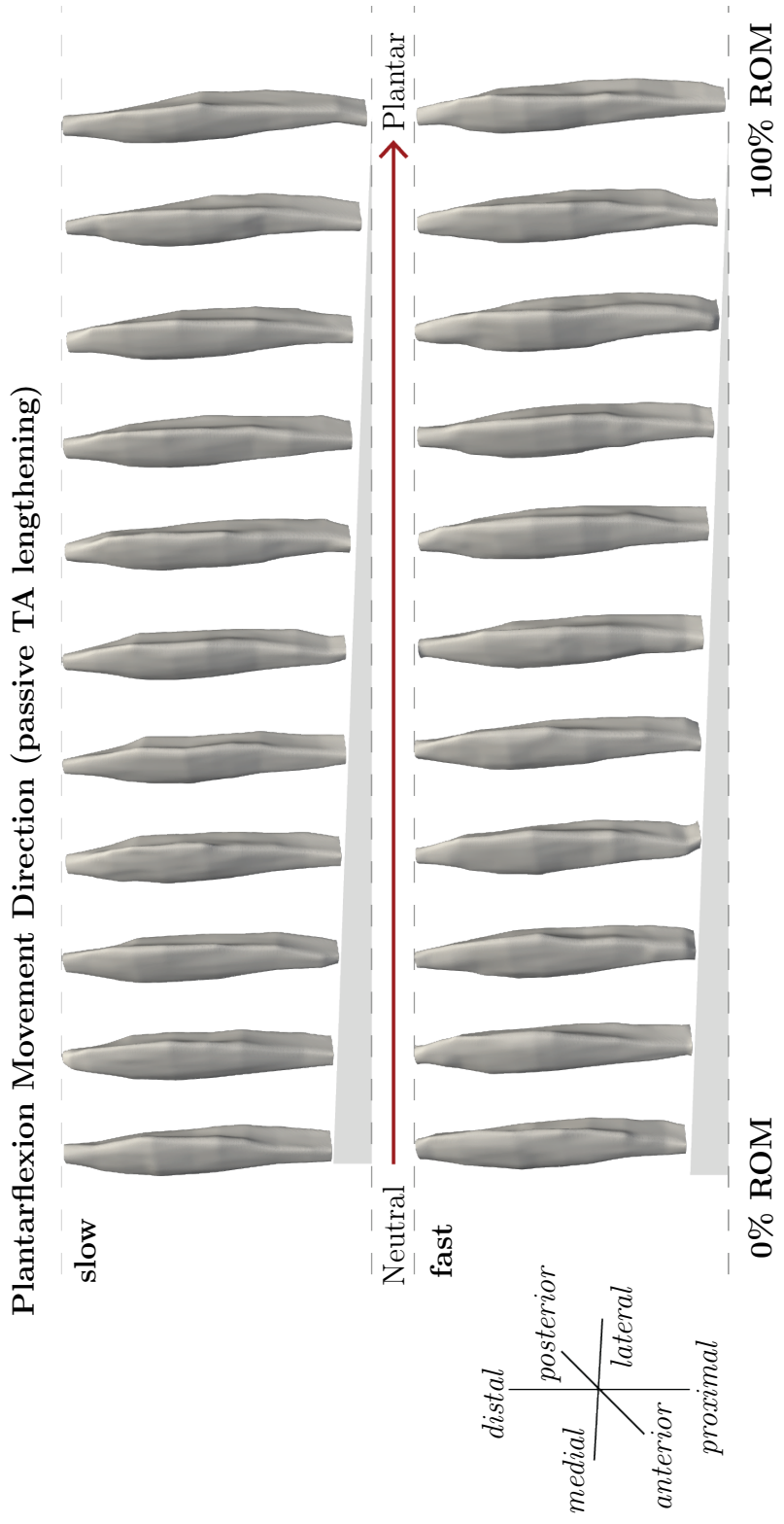

Figure 7.7: Example reconstruction for 10% intervals of ROM for *passive* movement with *slow* and *fast* velocity. Muscle lengthening and stretching towards the plantarflexion position are visible.

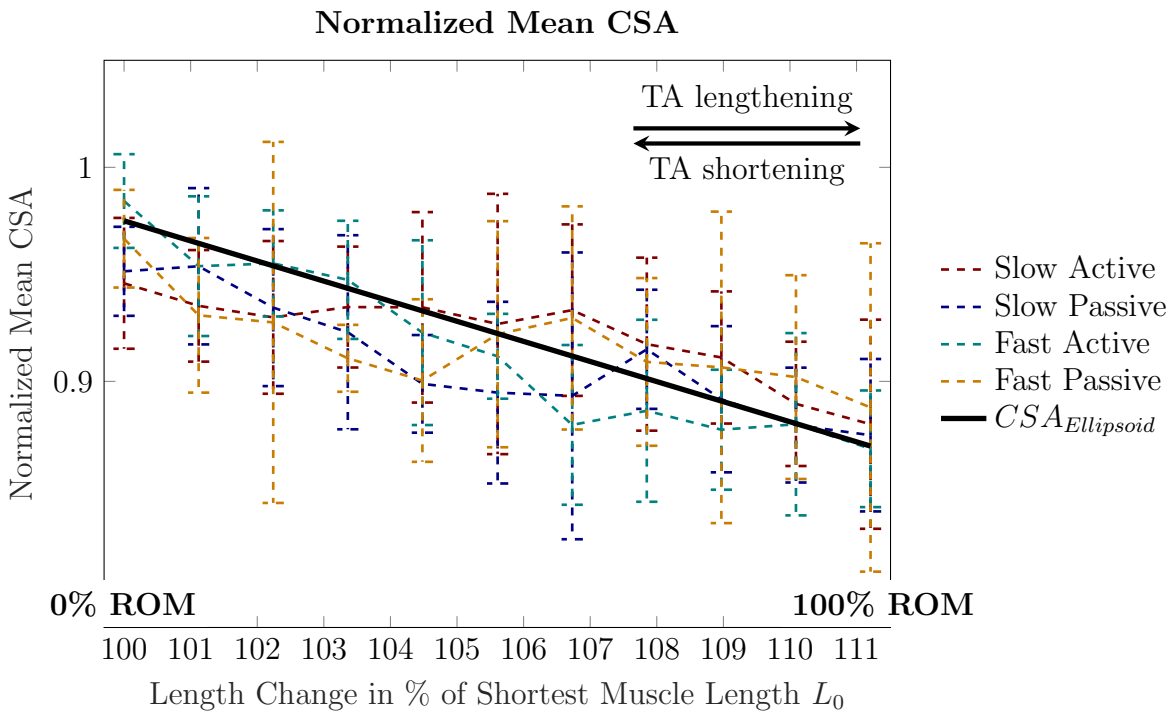

Figure 7.8: Mean normalized CSA (for the whole muscle) for the four conditions and different muscle lengths. The normalized volume value for the ellipsoid, which is defined as constant for all muscle lengths, was set to 1.3. In general, the normalized mean CSA decreases for increasing muscle length.

Figure 7.9 illustrates the mean normalized CSA of all subjects for the four different conditions, plotted over the shortest muscle length L_0 for the dynamic trials. The curves are color-coded according to L_0, i.e., from red (minimum muscle length, corresponding to 0% ROM) to blue (maximum muscle length, corresponding to 100% ROM). For better visualization, they are illustrated with alternating solid and dashed lines. For all four conditions, the curves show an increase in CSA in the middle region of the muscle, while they narrow towards the proximal and distal ends. This can be explained by the spindle-like shape of the muscle, i.e., the muscle belly is located in the middle part of the muscle and narrows towards the tendons at the proximal and distal part of the muscle. It can be observed that the maximum value of the CSA for the *fast active* movement is shifted in the left direction on the x-axis, i.e., towards the proximal side, for decreasing muscle length. In particular, this is visible for the *fast active* condition (see Figure 7.9c). Thus, for the more proximal part of the muscle, the red curve (0% ROM) is above the blue curve (100% ROM). In the distal part of the muscle, the red curve is below the blue one. During *fast active* contractions (see Figure 7.9c) there is a noticeable increase in the maximum CSA (blue line, representing 100% ROM to red line, representing 0% ROM) as the muscle shortens.

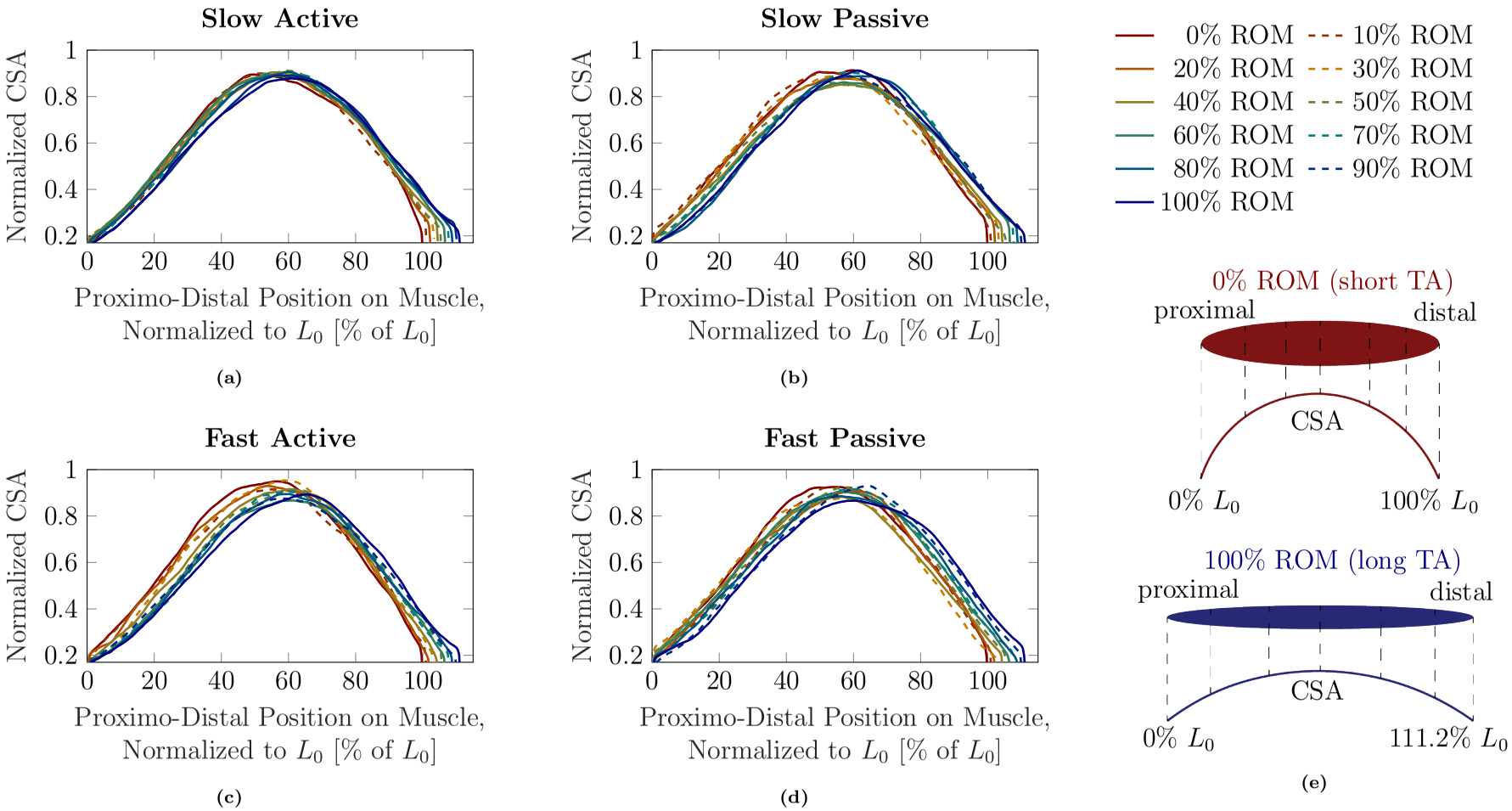

Figure 7.9: CSA over muscle length normalized to the shortest muscle length L_0 for the four conditions. Different muscle lengths corresponding to different ROM values (0% to 100% ROM) are visualized with different line types and colors. (a) *slow active*, (b) *slow passive*, (c) *fast active*, (d) *fast passive*. As schematically shown in (e), 0% ROM and 100% ROM refer to the shortest and longest TA length, respectively. The muscle CSA (exemplary broken vertical lines in (e) is plotted from the proximal to the distal end of the muscle, which corresponds to 111.2% L_0 for the longest muscle.

Assessment of the three other conditions (*slow active*, *slow passive*, *fast passive*) is difficult due to slight fluctuations in the curves, which may be caused by movement and evaluation artifacts. To achieve a better understanding of the changes in maximum CSA and its position on the longitudinal axis of the muscle, the curves were smoothed by fitting them with a second degree polynomial function. For testing of correlation between the curves and the polynomial fit, a Pearson correlation was applied and a mean correlation coefficient R=0.981 (ranging from 0.967 to 0.989) was found. Thus, the polynomial fit can be considered a reliable approximation of the CSA curves.

The pale colored lines in Figure 7.10 illustrate the resulting maximum CSA values and their corresponding positions on the muscle's longitudinal axis for the four conditions. For muscle shortening, the CSA seems to increase by approximately 5% and its position seems to shift from approximately 60% of L_0 to 55% of L_0, i.e. in the proximal direction on the longitudinal muscle axis. To confirm these statements statistically and to examine the differences between the four conditions, an analysis of covariance, which makes use of linear regressions, was employed (thick colored lines in Figure 7.10). Based on the analysis of covariance, it can be concluded that a reduction in the maximum CSA for muscle stretching can be observed in all four conditions. Maximum CSA is significantly different between *slow active* and *fast active* (P=0.005), *slow passive* and *fast active* (P=0.028) and *fast active* and *fast passive* (P=0.0014). The position of the maximum CSA shifts to the proximal part for shorter muscle lengths for all four conditions. The position of the maximum CSA does not significantly differ between the four conditions.

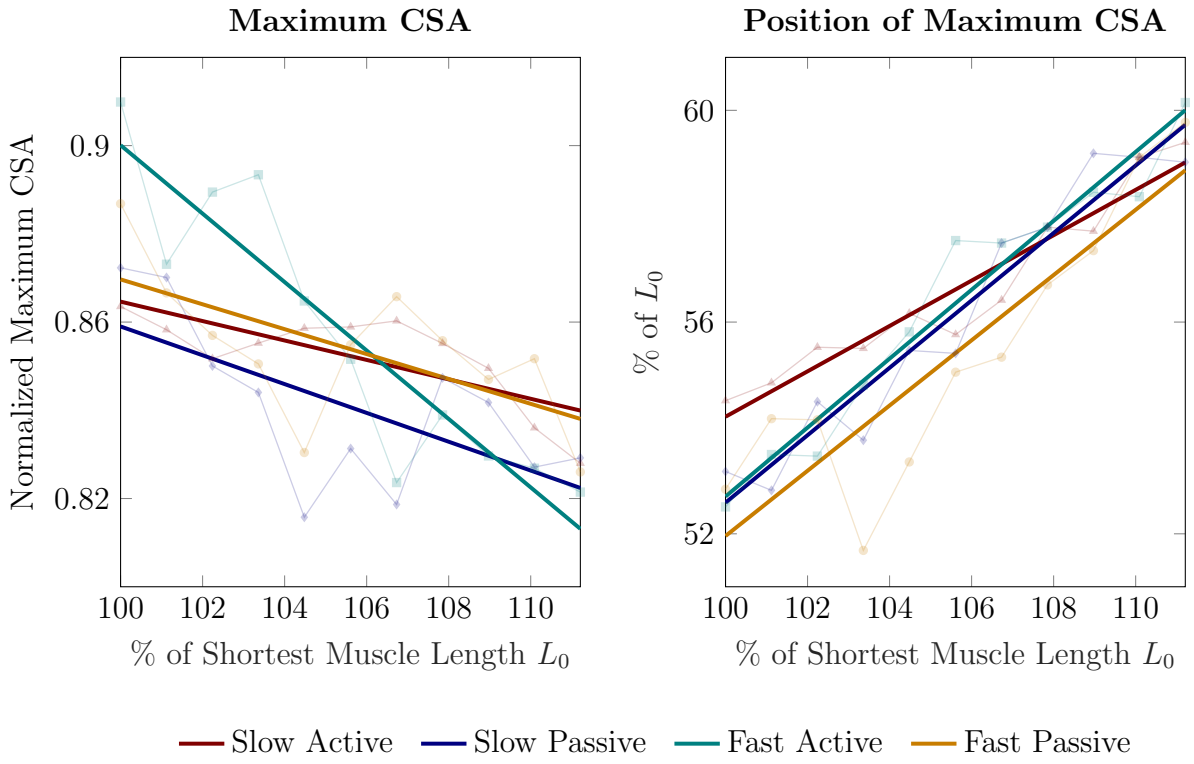

Figure 7.10: Maximum CSA value and position for the four conditions and different muscle lengths. The maximum CSA decreases for increasing muscle length and its position shifts towards the distal part for increasing muscle length.

7.3 Discussion

In this chapter, a novel approach for obtaining 3D volumes of the TA during movement has been introduced. In both static and dynamic conditions, the muscle volume stayed constant while muscle lengthening was observed due to an increase of ROM. This is consistent with previous literature [19, 76] and may indicate a low error of the new method for determining muscle shape and volume under dynamic conditions. So far, 3D freehand ultrasound imaging studies on skeletal muscles mainly focused on isometric contractions, i.e., static conditions, for obtaining 3D volumes [19, 41, 267]. With the proposed method, 3D reconstructions of the TA during periodic movements are possible. This may provide entirely new means to investigate the muscle's dynamic contraction behavior.

7.3.1 Comparison with a Simple Ellipsoidal Muscle Model

When the ankle joint angle decreases, the TA muscle shortens and the maximum CSA shifts towards the proximal origin of the muscle. Since the muscle volume stays constant, it has to redistribute along the shorter length of the muscle. The comparison of the CSA prediction by an ellipsoidal muscle model with experimentally obtained data shows a similar trend in decrease of CSA for increase in muscle length (see Figure 7.8). This demonstrates that the proposed method can serve as a suitable tool for determining 3D muscle deformations during dynamic contractions.

Although an ellipsoid is a highly simplified shape of a skeletal muscle, it has been shown to be an appropriate geometric body for predicting muscle shape and contraction behavior [235]. Yet, the suitability for the ellipsoid as a representative muscle shape [14] may vary between different muscles. This applies particularly to non-spindle-shaped muscles with more complex muscle geometries, such as the back and shoulder muscles [241, 250]. Thus, the proposed method enables the generation of more sophisticated input geometries for modeling skeletal muscle, compared to a simplified shape, such as an ellipsoid.

7.3.2 Comparison of 2D and 3D Ultrasound

Franchi et al. [71] found positive correlations between muscle thickness measured from 2D ultrasound images and anatomical CSA obtained from MRI. Investigating the TA by using 2D ultrasound, Maganaris et al. [158] and Reeves et al. [210] did not find significant changes in TA muscle thickness at different ankle joint angles. Their results applied to resting conditions and maximum voluntary contraction (MVC). In this chapter, an increase of the mean CSA (Figure 7.8) and maximum CSA (Figure 7.10) has been found with a decrease of the ankle joint angle in both *passive* and *active* conditions. In terms of the relationship between the anatomical CSA and muscle thickness [71], this would not be consistent with the findings of Maganaris et al. [158] and Reeves et al. [210]. Hu et al. [115] found, however, significant differences between muscle thickness for dorsiflexion and plantarflexion angles and Choi et al. [45] observed increases in muscle thickness during contraction.

Such differences in findings may be explained by the different methods used in the mentioned studies or differences in TA architecture of the examined subject groups. The TA has a complex bipennate architecture and exhibits sexual dimorphisms in humans [162]. Furthermore, the TA presents morphological asymmetries between its superficial and deep

unipennate regions. For example, the superficial and deep TA regions differ in thickness and pennation angle [162]. Dependent on their architecture, muscles and muscle compartments can deform differently in their width and thickness when shortened [63]. Observed muscle deformations via 2D ultrasound may therefore depend on the positioning and orientation of the ultrasound probe.

Hence, the existing differences in findings on 2D thickness indicate the need of a method for obtaining 3D volumes of muscles revealing deformation patterns during dynamic contractions, of which the proposed method is capable.

7.3.3 Impact of Movement Condition on CSA

Significant differences in mean CSA were observed for different muscle lengths for the *slow active*, *slow passive* and *fast active* condition but not for the *fast passive* one (see Figure 7.8). This could be explained by two factors: First, moving the foot quickly in a controlled manner was more strenuous for the subjects in terms of coordination than performing the same movement slowly. Therefore, there may have been greater variations in the execution of the movement. Secondly, increasing the movement velocity during contractions against equal loads (in our case the inertia of the foot) requires higher muscle activations. Thus, it can be expected that the *fast passive* TA movements required a higher activation of the antagonistic plantar flexors (i.e., the gastrocnemius muscles and the soleus muscle) compared to *slow passive* TA movements. In previous studies on the human lateral gastrocnemius, a gradual increase in muscle activation from 10% to 100% resulted in different muscle thicknesses [133]. This is due to activation and force-dependent changes in the internal muscle architecture, especially the pennation angle. At higher contraction velocity, there is greater muscle fiber rotation, i.e., change in pennation angle [16, 63]. This can also lead to movement velocity dependent differences in CSA. Since the lower leg rested on the plantar flexors in the experimental setup (Figure 7.1), their higher *active* deformation at increased cycle frequencies (100 beats per minute) led to a greater vertical movement of the lower leg and the ultrasound probe. Thus, artifacts in the ultrasound TA images may occur. Consequently, such vertical movement may induce the larger standard deviations in the computed CSA observed, as in Figure 7.8 (yellow broken line). Hence, the scatter of the data for the *fast passive* condition is larger, which is probably why statistically significant deviations do not occur.

The results showed significantly different maximum CSA values between the *fast active* and all other conditions. The observed differences are explainable and to be expected because the muscle shape differs between *active* and *passive* muscles with the same length [38]. The linear regression of the maximum CSA curve (see Figure 7.10) shows the steepest slope for the *fast active* condition, where the highest TA muscle activation can be expected. This indicates a greater bulging of the muscle for the *fast active* condition. The findings are in agreement with those of Raiteri et al. [200], who measured CSA changes of the TA during isometric contractions with different activation levels using 3D freehand ultrasound. For low activation levels in a range of 5-10% MVC, the change in CSA compared to a resting state was in a range of 2-4%, which is relatively small. Larger increases in CSA were observed for 25% and 50% MVC.

The increase in CSA for higher velocities can be related to the variable contraction behavior of a muscle and the architectural gearing ratio (AGR) [34]. The AGR is defined

as the relation of the muscle shortening velocity to the fiber shortening velocity. When a muscle contracts, variable shape changes of the muscle can occur [63], i.e., the thickness can increase, decrease or stay constant. This is caused by the architectural changes in the muscle during dynamic contraction, as muscle fibers can both shorten and rotate. The combination of shortening and rotation enables changes in the pennation. Thus, changes in pennation angle enable the muscle belly to shorten faster than the fibers, which refers to an AGR greater than one. In this chapter, the increase in CSA for faster velocities may therefore be caused by a higher AGR.

7.3.4 Limitations

One limitation of the proposed method is that the leg of the subject was not fixed during scanning. Therefore, it was not possible to enable a fully controlled movement of the leg. This means that side movements of the foot while *active* or *passive* movement were possible. Further, some participants felt a moderate discomfort and needed to shift the leg's position between trials, even though the movement was relatively small, since the subjects stayed in the lying position and did not stand up in between. Thus, the stitched trials might not always be recorded at the exact same leg position. Moreover, the movement velocity of the foot was based on the metronome. This does not ensure that all movements were exerted with the exact same velocity. Therefore, in order to ensure more controlled conditions in terms of movement direction and velocity, future studies should include a fixture of the leg which only enables plantarflexion and dorsiflexion movements. The fixation of the leg and the kinematic control of a reproducible cyclic joint movement may be realized by using an isokinetic measurement system, such as an ISOMED [109]. Through the possibility of more controlled measurements with less movement artifacts, the deformation gradient of the muscle may be computed. This means that 3D deformation changes can be determined between different muscle lengths during dynamic movements.

Furthermore, the activation level of the muscle was not measured. Since the subjects moved their feet without any resistance, it can be assumed that the activation level of the TA was in a low range, probably around 5-10% of MVC. Therefore, differences in CSA between *active* and *passive*, and *slow* and *fast* velocities were comparably small. It would therefore be beneficial to include a force resistance and measurement of muscle activity, to also study effects of the CSA during higher muscle contraction levels. Thus, future studies should contain a mechanism, such that the foot moves against a controlled resistance, e.g., a dynamometer, and EMG electrodes.

7.4 Conclusion

In summary, a method for determining muscle shape deformation during dynamic contraction has been proposed in this chapter. Constant muscle volumes during contraction show the reliability of the method. Moreover, the method is able to determine realistic changes in 3D muscle shape, such as the proximal shift in maximum CSA. Thus, an improved understanding of muscle contraction behavior, especially during dynamic movements, can be achieved with the proposed method. Since the acquisition of 3D deformation of skeletal muscle during dynamic movement is highly restricted with the current existing imaging

methods, the method proposed in this chapter contributes significantly to the research area.

Data on changes in muscle shape during contraction are needed for the validation of 3D muscle models [228]. Therefore, the proposed method may help to enhance input data for existing computational models and to answer new research questions. In addition, new insights into the muscle geometry in dynamic conditions may help to establish new means to investigate skeletal muscles in healthy and pathological conditions. As such, further extensions may enable the development of new therapy approaches.

8 Discussion & Outlook

In this thesis, a system for automated 3D ultrasound measurements has been developed. The system has been validated using custom-designed phantoms [240] and compared to freehand ultrasound measurements. Furthermore, two different methods for reconstruction of ultrasound and position data have been implemented. The workflow for generating volumetric data using the automated 3D ultrasound system has been applied in two different studies. In one of them, a workflow for 3D fascicle reconstructions has been presented. The other study established a method for generating volumetric data during dynamic movements. Thus, the major contributions of this thesis can be summarized as follows:

- The development of an automated 3D ultrasound system, which is portable and enables the controlled and reproducible acquisition of volumetric data sets.
- A workflow for fast 3D ultrasound data acquisition and reconstruction, which enables studies in conditions that are limited in other imaging modalities such as MRI.
- A method for determining 3D muscle characteristics from ultrasound data sets, including volume, length and fascicle orientation, which enables data investigation of architectural muscle characteristics in 3D and generation of input data for patient-specific computational models.
- A method for acquisition and reconstruction of the tibialis anterior (TA) muscle during dynamic, periodic movements, through which the volume deformation can be investigated in dynamic conditions.

Considering the contributions in their entirety, workflows for fast acquisition of both muscle geometry and its internal structure have been presented, for static and dynamic conditions. Thus, the fundamentals for the generation of patient-specific computational models have been established in this thesis.

Chapters 5, 6 and 7 already discussed the corresponding results in a separate discussion and gave an outlook with respect to the specific methods in the chapters. Therefore, in this chapter an overall discussion of the developed methods is given. Here, the focus is set more on the interaction and combination of the presented methods. Potentials, challenges and future applications of the overall big picture are discussed.

8.1 Potentials and Challenges

One major aim of this thesis is to enable acquisition of data which can be used for generating patient-specific models, i.e., models considering the patient's individual body

shape and constitution. The workflow for 3D ultrasound data acquisition, reconstruction and muscle segmentation (Chapter 4) demonstrates a method for generating surface or volume models. Such models can serve as a realistic input geometry for computational models of muscles, e.g. Finite Element (FE) models. Often, the models are based on simplified geometries. Employing experimentally obtained ultrasound-based geometries may therefore lead to improvements in model predictions.

For FE models, both knowledge of the geometry and the material description are crucial. In Chapter 6, TA geometries for different ankle joint angles, i.e., different muscle lengths, could be obtained. Therefore, the 3D deformation of the muscle, i.e., the geometry, is given. Since the muscle is an anisotropic medium, the orientation of the fibers is important for the material description. The data obtained in Chapter 6 contains the corresponding fascicle direction at each volume element of the 3D reconstructed volume. Therefore, the geometry and fascicle information can be transferred into a computational model of the muscle, e.g. [27, 28, 69, 100, 101, 275]. Figure 8.1 illustrates a preliminary example TA geometry of the measurements in Chapter 6, which is transferred into an FE geometry including fascicle directions. By adding material properties to the muscles, different quantities can be predicted including internal and external forces or changes in muscle architecture and shape, as well as internal muscle activation.

Furthermore, such realistic input geometries including the internal fascicle architecture are not only important for FE models, but also for, e.g., electrophysiological models, such as [136, 169], which, for instance predict the propagation of action potentials.

The geometry and fascicle information models enable *in silico* studies, i.e. simulation studies, where conditions can be investigated that are difficult or even impossible to investigate experimentally. Here, various initial conditions can be tested or disease patterns and progressions can be simulated.

With the data already collected from the group of 10 subjects (Chapter 6), as well as data to be collected in future studies, one may create an FE model database. Such a database may represent some diversity, e.g., in terms of age, height, or gender, and may contain muscle volumes in different ankle joint angle positions. The database can be used for generation of statistical shape models of muscles.

With the data acquisition method applied in Chapters 6 and 7, TA shape models were generated for different ankle joint angles, i.e., different muscle lengths. Therefore, in contrast to employing the experimentally obtained data sets only for generation of FE models, they can also be used to validate the computational models. For example, one could simulate muscle shape and 3D architectural changes during muscle shortening and compare it to the experimentally obtained data set.

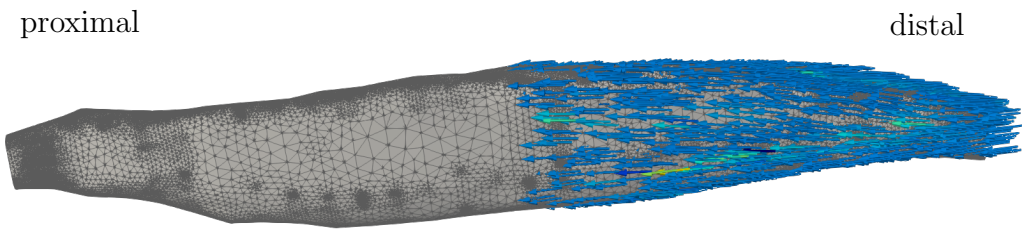

Figure 8.1: 3D ultrasound-based geometry of a TA transferred into an FE model. The model incorporates fascicle directions, illustrated in the distal part of the TA.

As mentioned above, in this thesis a method for determination of 3D muscle architecture and a method for acquisition and reconstruction of volumetric ultrasound data sets during dynamic movements were established. Ideally, a future application could combine the developed methods and investigate both the changes in 3D muscle architecture and the muscle deformation during dynamic movements. With this, both the 3D deformation gradient, and internal structural changes may be determined within one data set. The combination of 3D fascicle architecture and deformation during dynamic movements has not been studied before - neither with MRI-based techniques nor with ultrasound. In the current setup of the experimental methods, some challenges arise. They can be grouped into two major aspects:

First, in the dynamic study, an algorithm was developed which grouped all 2D images and position information into a corresponding ankle joint angle interval. In total, four trials of 2 minutes 15 seconds were stitched for each subject. The number of images within one ankle joint angle interval was sufficient for segmentation and determination of muscle volume. The reason for this is that for a static trial, one usually segments a number of images and interpolates in between. For 3D fascicle reconstruction one needs, however, a high spatial image resolution in scanning direction, i.e., one needs a large number of image frames and only little space between them. This means that for the dynamic trials, the average distance between two images, which defines the image's spatial resolution in scanning direction, is comparably large. The first challenge is therefore to ensure that there are enough ultrasound frames within each ankle joint angle interval for sufficiently resolved fascicle detection. Figure 8.2 shows an example image stack of images collected in a static trial and one with all images corresponding to one ankle joint angle interval, illustrating the difference in space between consecutive images.

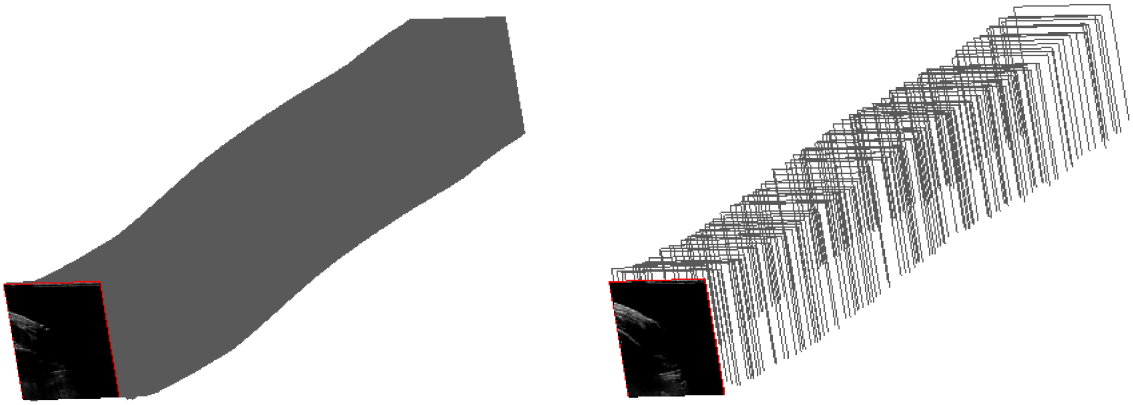

(a) Static trial. **(b)** Ankle joint angle interval.

Figure 8.2: Number of image frames in (a) static trial and (b) one ankle joint angle interval during dynamic imaging. Note how close the frames are to each other in the static trial and how much space there is between two consecutive frames in the dynamic trial.

The number of image frames within one ankle joint angle interval may be enhanced by simply increasing the ankle joint angle interval, which was 1° in the study conducted in Chapter 7. However, this would raise motion artifacts, thus such solution is not recommended. For the participating subjects, the manual movement of the foot was demanding in terms of coordination and therefore limited in time. Hence, the trial length of 2 minutes 15 seconds should not be extended as well. An alternative would be to record more

trials for collecting more data. More recorded data facilitate that an increased number of image frames is contained within one interval. This is possible but requires a lot of time for image processing and segmentation. Thus, the option of increasing the number of recorded trials should consider automated segmentation methods.

Currently, the employed ultrasound device displays images at a frame rate of 30-50Hz, depending on the depth and image settings. If it is possible to collect ultrasound images with a higher frame rate, more images would be available for each ankle joint angle interval. For this, the current ultrasound system would need to be exchanged with an advanced one. This could be even one which is capable of ultrafast ultrasound [248]. Ultrafast ultrasound imaging is a technique where the ultrasound beam is directly formed as a plane instead of line by line as with conventional ultrasound probes. The technique is computationally more expensive but enables ultrasound frame rates of more than 1000Hz.

Additionally, one could mount a second ultrasound probe to the automated 3D ultrasound system that moves at an offset, such that each probe scans half of the TA, thus doubling the resolution.

The second challenge in 3D fascicle reconstruction from the obtained dynamic 3D ultrasound data set is that there was a significant amount of unwanted movement of the subject's leg during the trials. In addition, subjects sometimes slightly changed the position of the leg between trials because of discomfort. The movements may lead to image artifacts or to the information on two subsequent images being shifted sideways. In the reconstruction or segmentation, this has shown up as jagged edges or bumps in the geometries. This would result in erroneous detection of fascicle directions. Most probably, the sagittal slice would show the fascicles not as straight lines, but more as wave-like structures.

The challenge of unwanted movement or change in leg position can be addressed by fixing the leg to disable side movements or alterations in the position between trials. One may use certain straps or design a special rig which only allows foot movement in one degree of freedom without any additional foot rotation. An overall more controllable realization would employ an isokinetic measurement system, e.g. a Biodex or ISOMED. Here, the limbs can be fixed and the movement range can be restricted to the desired range.

Combining an isokinetic system with the developed dynamic imaging method can facilitate further advantages as well: Since such systems include dynamometers, it is possible to include an external force in the measurement setup, such that the foot moves against a resistance. Therefore, higher activation levels can be investigated in stronger contraction scenarios. Future studies should therefore employ the dynamic 3D ultrasound imaging method together with an isokinetic measurement system. This is possible with slight adjustment of the custom-designed device to the dimensions of the dynamometer. Through implementation of the mentioned extensions, information on 3D fascicle architecture during dynamic deformation can be obtained. Due to the long acquisition times, such dynamic investigations are not possible with MRI-based techniques. Thus, this would be a major contribution to the field of musculoskeletal biomechanics and modelling.

8.2 Outlook

As discussed in the previous section, one aim of future applications is to combine the method for 3D fascicle detection with the method for dynamic data collection and reconstruction. The challenges of this combination and how to address them have been discussed. There are further applications in which the methods developed in this thesis can be employed, which are explained in the following.

Application on More Skeletal Muscles

The methods developed in this thesis were applied to the TA for demonstration purposes. The way the device is designed, it is possible to use it on other muscles. Further, the fascicle detection algorithm can be applied to 3D ultrasound data of other skeletal muscles without much additional effort. For this, the corresponding compartments have to be segmented individually, depending on the muscle's architecture. Therefore, future applications of these methods should also investigate the 3D fascicle architectures of other skeletal muscles. For the dynamic case, it would be necessary to build an appropriate device that would allow a corresponding movement in the direction of loading of the muscle to be examined. Alternatively, a system such as an ISOMED or Biodex can be used for this purpose, restricting the movement range of the examined body part.

Combination with EMG

In order to determine the electrical muscle activation, typically electromyography (EMG) electrodes are employed. In an experimental setup, this can be used for controlling the percentage of the maximum voluntary contraction (MVC), i.e., the level of contraction intensity. High density (HD) EMG is a technique where multiple of such electrodes are used to additionally obtain spatial information on the muscle activation. A useful application is therefore to use HD EMG electrodes in combination with the automated 3D ultrasound system. With such a setup, one can investigate relations between deformation, changes in fascicle architecture and spatial activation of the muscle. Investigating such relations is relevant in both static and dynamic conditions, i.e., in isometric and concentric or eccentric contractions. The information of muscular activation, additional to deformation and fascicle orientations, can enhance computational models of skeletal muscle.

Conventional EMG electrodes can disturb the B-Mode ultrasound image. There exist, however, custom-designed ultrasound transparent EMG electrodes [33]. With such electrodes, 3D ultrasound and HD EMG measurement could be combined. Therefore, the spatial distribution of muscle activation can be determined, e.g., it can be determined if there is a partial activation in dynamic contractions which might be different to the muscle activation in isometric contractions.

Extension of the Ultrasound Capabilities

The methods developed in this thesis enable determination of 3D muscle fascicle architecture and muscle shape changes, i.e., deformation during various contractions. As mentioned above, these are characteristics which are valuable for the generation of patient-specific computational models, since they provide information on the muscle's force-

generating capacities. In future studies, in addition to obtaining 3D ultrasound-based volume and fascicle architecture, further ultrasound-based technologies can be used for increasing the range of obtained information. For instance, one can additionally employ Shear Wave Elastography (SWE) ultrasound, which determines the stiffness of tissue. This could therefore provide additional information on the mechanical properties of muscles, which can be important for computational models.

Another interesting additional ultrasound-based technique is super-resolution ultrasound (SRU) [47], where moving particles in blood vessels are tracked. The particles are mainly injected as contrast agents. Through post-processing algorithms, SRU allows to obtain images of the blood vessels in a resolution of up to 5µm [47]. Therefore, not only large veins or arteries, but also capillaries can be visualized.

The SRU and SWE techniques could therefore provide additional information on the effects of muscle stiffness and blood perfusion.

System as a Wearable

Further developments of the current automated 3D ultrasound system may focus on significantly reducing the overall size of the system. A future application may convert the custom-designed device of the automated 3D ultrasound system into a wearable system. This can be realized by exchanging the components to smaller and more flexible ones. The components are downsized, such that one can attach the device to the body part which is scanned. In case of examining the TA, the wearable is attached to the shin. It may be a setup where an ultrasound probe can move up and down along the TA taking cross-sectional images, while the subject is free to move around the room. Further, circular movements around the leg can be enabled as well. The smaller version of the custom-designed device may be attached to the leg with straps, for example. One may conduct a measurement similar to the method presented in Chapter 7, where the subjects extended and flexed their foot periodically. The difference with a wearable device is, that it would be possible to conduct such measurements during a more natural movement such as gait. Such a measurement can be conducted, e.g., on a treadmill where one can control parameters, such as the walking speed. Using markers, e.g., reflective ones, the ankle joint angle can be determined for each frame and volumes of the muscle during gait can be generated. Assuming gait as a periodic movement, the method of Chapter 7 can be used for reconstruction of the data. Investigating the muscle during an everyday movement such as gait can improve our understanding of the muscle's contraction behavior during actual everyday movements. This can further help understanding and predicting the progression of neuromuscular diseases and advance new therapy approaches.

A Experimentally Determined Force Values

Table A.1 shows the experimentally determined force values for the automated 3D ultrasound system. The values were fit to a second degree polynomial function (fit: $f(x) = -2.456 \cdot 10^{-5}x^2 + 0.01696x + 4.053$), as shown in Figure A.1.

Force Setting	Measured Force Values [N]									Mean Force Value [N]
1	3.9	4.0	4.2	4.1	4.0	4.3	4.1	4.2	3.9	4.1
25	4.3	4.7	4.3	4.6	4.5					4.5
50	4.7	4.7	4.8	4.9	4.9					4.8
75	5.0	5.2	5.1	5.1	5.2	5.3				5.2
100	5.4	5.4	5.5	5.8	5.6					5.5
125	5.6	5.9	5.8	5.9	6.0	5.4	5.9			5.8
150	5.9	6.1	6.0	6.0	6.7	6.3	5.7			6.1
175	6.1	6.3	6.2	6.2	6.2	6.3				6.2
200	6.2	6.7	6.5	6.5	6.3	6.6				6.5

Table A.1: Experimentally determined force values for the automated 3D ultrasound system.

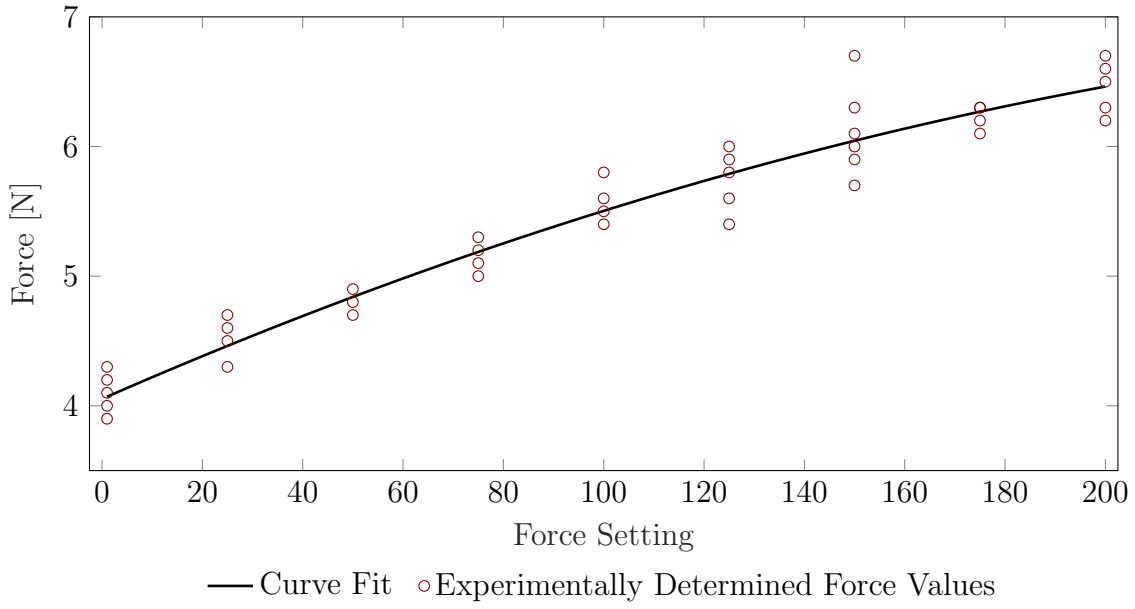

Figure A.1: Experimentally determined force values and curve fit.

B Setup of a 3D Freehand Ultrasound Workflow

In this thesis, an automated 3D ultrasound system is developed. Since the system is compared to a freehand ultrasound system, a workflow for 3D freehand ultrasound data acquisition is also established.

Measurement Preparations

In case of 3D freehand ultrasound, as in all experimental setups with optical motion capture, care must be taken to ensure that no markers are covered. Potential covering objects are the operators themselves. The ultrasound machine itself is a large machine which can cover reflective markers. Thus, when planning the measurement setup, one needs to consider the location of the operator, who moves the probe, and the ultrasound machine as possible covering objects. Therefore, cameras need to be placed appropriately around such objects.

Marker Holder

For 3D freehand ultrasound, the probe needs to be equipped with reflective markers. Such markers define a coordinate system, which is assumed as fix on the probe. This means there is no change of rotation or translation relative to the probe during the scan. Therefore, for an accurate 3D reconstruction of the images it is necessary that the markers on the probe will not move relative to each other or relative to the probe. To solve this, a probe holder with placeholders for optical markers, manufactured by VICON, has been designed, see Figure B.1. The reflective markers can be rigidly attached to the holder using screw connections. Inside, the shape of the probe holder is the negative of the probe shape, such that the respective transducer fits into the holder. The holder is designed using SolidWorks (Premium 2021 SP3.0) and 3D printed from polylactic acid filament.

Synchronization

For conducting 3D freehand trials, it is necessary to synchronize the recording of the ultrasound images with the motion capture system. In order to achieve simultaneous recording of the ultrasound images and motion capture marker data, an HD frame grabber (USB3HDCAP, StarTech.com Ltd) is connected with the ultrasound machine and the laboratory computer via an HDMI cable. The laboratory computer also controls the

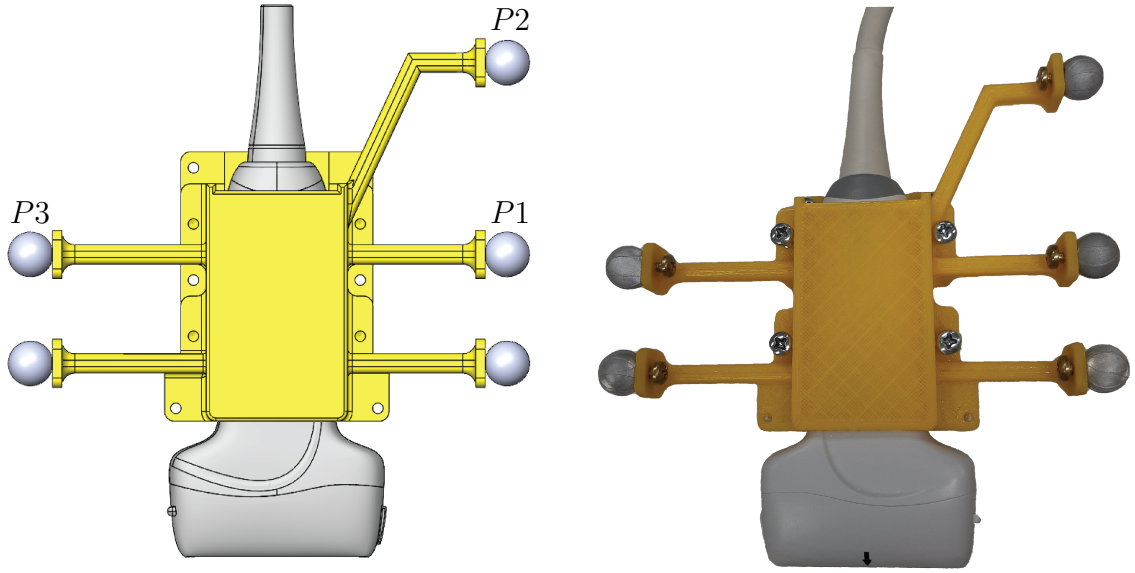

(a) CAD model. **(b)** 3D printed model.

Figure B.1: Custom-designed probe holder for reflective markers.

motion capture system. The motion capture system can send a User Datagram Protocol (UDP) message to a receiver containing relevant information if a recording starts or stops. By defining the right port and IP address, the UDP message can be used as a trigger module. A custom-written LabVIEW (version 2021.0) program, running on the laboratory computer, acts as the receiver for the UDP port. By decoding the message and setting the frame grabber input as an external webcam, it triggers a webcam recording. When active, the LabVIEW program is in a waiting mode for a UDP message and correspondingly starts or stops a recording of the ultrasound images as a video file, once the operator starts or stops a recording in the VICON Nexus software (version 2.12.0).

Calibration

This section explains the spatial and temporal calibration methods employed for the 3D freehand ultrasound workflow.

Spatial Calibration

The same N-Wire phantom from [144] is used for 3D freehand ultrasound, as it was used for the automated workflow. In order to determine the positions of the phantom in the laboratory coordinate system and the positions of the wires in the phantom coordinate system, the CAD model of the phantom was modified, such that a holder with a marker cluster can be attached via a screw connection, see Figure B.2. The modifications to the CAD model were made in SolidWorks (Premium 2021 SP3.0). Over seven calibration trials, a calibration reproducibility of 2.58mm was calculated, according to Equation (3.6), using the least-squares fitting of Arun et al. [12]. This means that the variability in reconstructed point position on the images is 2.58mm [113].

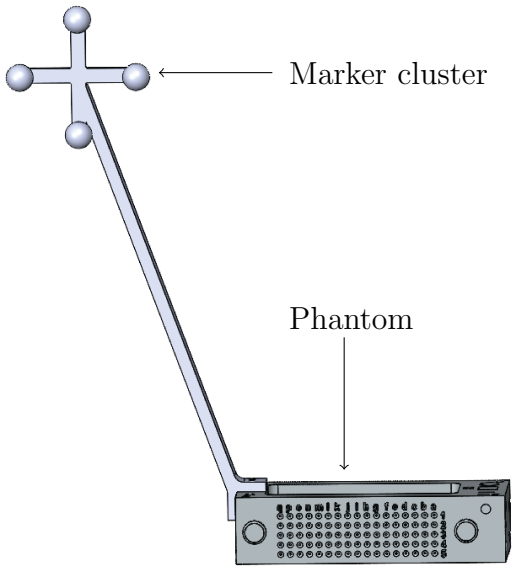

Figure B.2: CAD model of the N-wire Phantom with attached marker cluster.

Temporal Calibration

The procedure for temporal calibration is the same for freehand acquisition as for the automated workflow, with the only difference, that the probe is moved manually ("freehand") up and down in the water tank. Since marker data is usually collected with around 100-500Hz and, in this thesis, the frame grabber collects images with a frame rate of 30Hz, the systems are first resampled to a frequency of 1000Hz for determining the temporal shift in milliseconds, see Figure B.3.

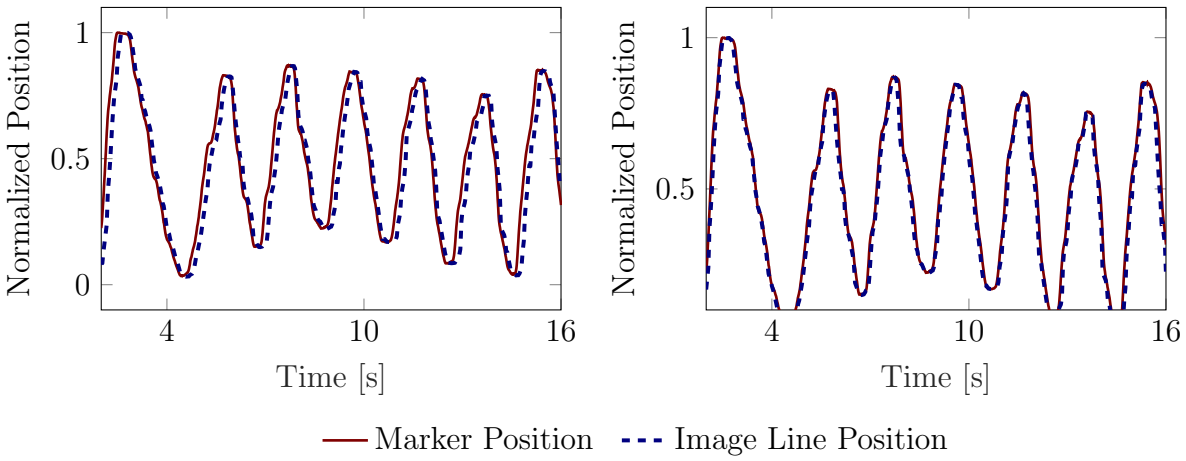

Figure B.3: Temporal calibration for 3D freehand ultrasound. The left graph shows the z-coordinate of a marker and the vertical position of the line in the ultrasound image, in the right image the temporal offset is fixed so that both curves are time synchronous.

As for the automated 3D ultrasound system, the temporal resolution is restricted by the ultrasound system's frame rate. Averaged over 10 temporal calibration trials, the temporal shift between the image line position and the marker position was 82.0±26.7ms. This corresponds to a shift of 2-3 ultrasound images, i.e. the temporal uncertainty is one

ultrasound frame which corresponds to 33.3ms.

Coordinate Transformations

For 3D reconstruction of the 2D images acquired with 3D freehand ultrasound imaging, the transformations as described in Equation (3.1) are necessary. With three markers ($P1$, $P2$, $P3$) on the marker holder, see Figure B.1a, the transformation matrix ${}^{Lab}\boldsymbol{T}_{Pr}$, i.e., the transformation from the probe coordinate system Pr to the laboratory coordinate system Lab, can be determined for each frame. This can be done as following [40, 168]: The three 3x1 direction vectors of the coordinate system can be determined using the cross product:

$$\boldsymbol{e}_x = \frac{P1 - P2}{|P1 - P2|}, \tag{B.1}$$

$$\boldsymbol{e}_z = \boldsymbol{e}_x \times \frac{P3 - P2}{|P3 - P2|}, \tag{B.2}$$

$$\boldsymbol{e}_y = \frac{\boldsymbol{e}_z \times \boldsymbol{e}_x}{|\boldsymbol{e}_z \times \boldsymbol{e}_x|}. \tag{B.3}$$

One marker represents the origin of the coordinate system, e.g., $P2$. Thus, the 4x4 roto-translation matrix ${}^{Lab}\boldsymbol{T}_{Pr}$ is defined as:

$${}^{Lab}\boldsymbol{T}_{Pr} = \begin{pmatrix} e_{x1} & e_{y1} & e_{z1} & P2_1 \\ e_{x2} & e_{y2} & e_{z2} & P2_2 \\ e_{x3} & e_{y3} & e_{z3} & P2_3 \\ 0 & 0 & 0 & 1 \end{pmatrix}, \tag{B.4}$$

where e_{x1}, e_{x2}, e_{x3} are the three components of $\boldsymbol{e}_x$ and so forth. This principle is also used to define the phantom coordinate system from its attached marker cluster.

C Pennation Angles over Resting Position Muscle Length L_{Rest}

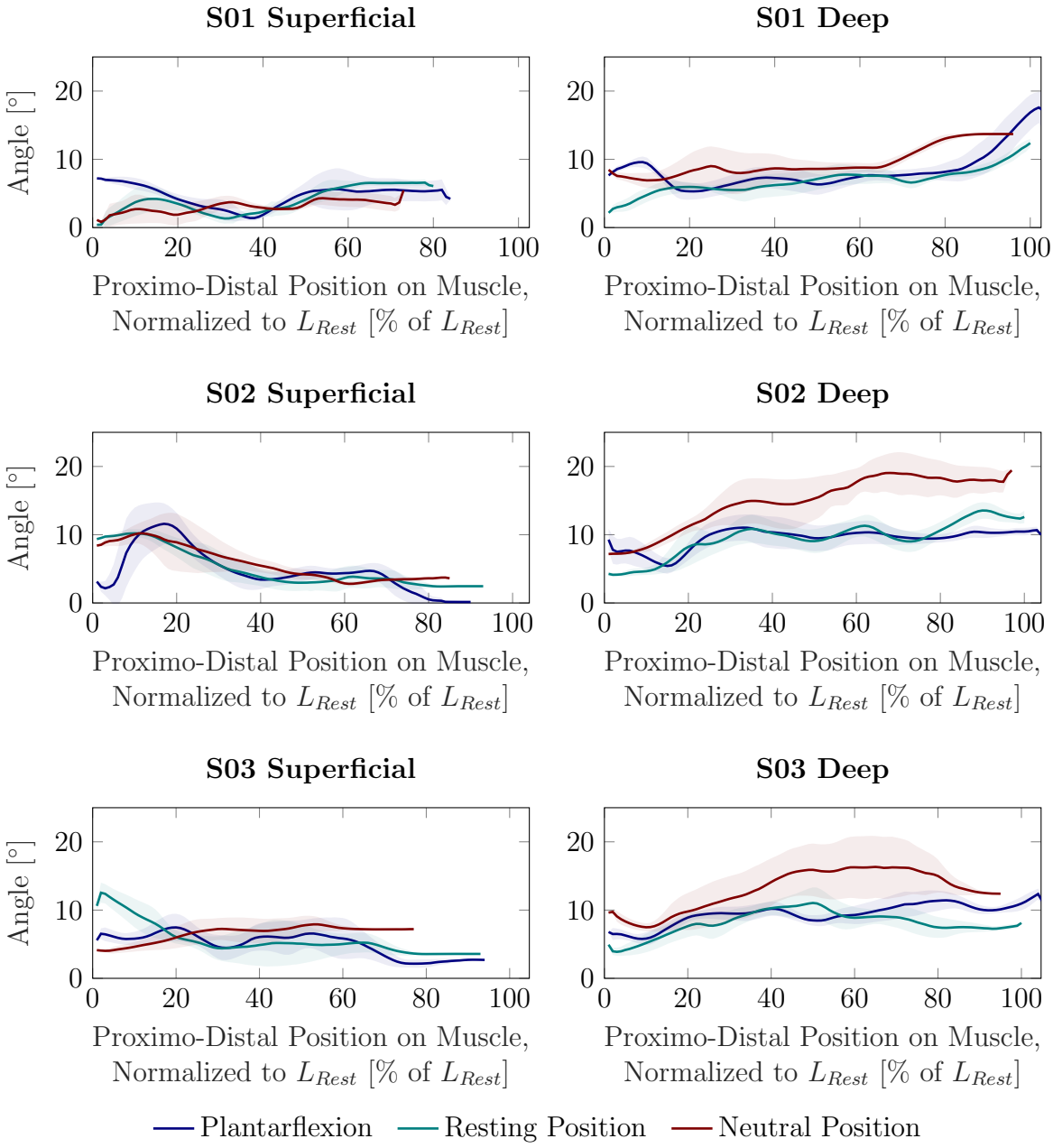

Figure C.1: TA pennation angle distribution over the resting position muscle length L_{Rest} for different subjects for the superficial and deep compartments. S01: Subject 1, S02: Subject 2, S03: Subject 3.

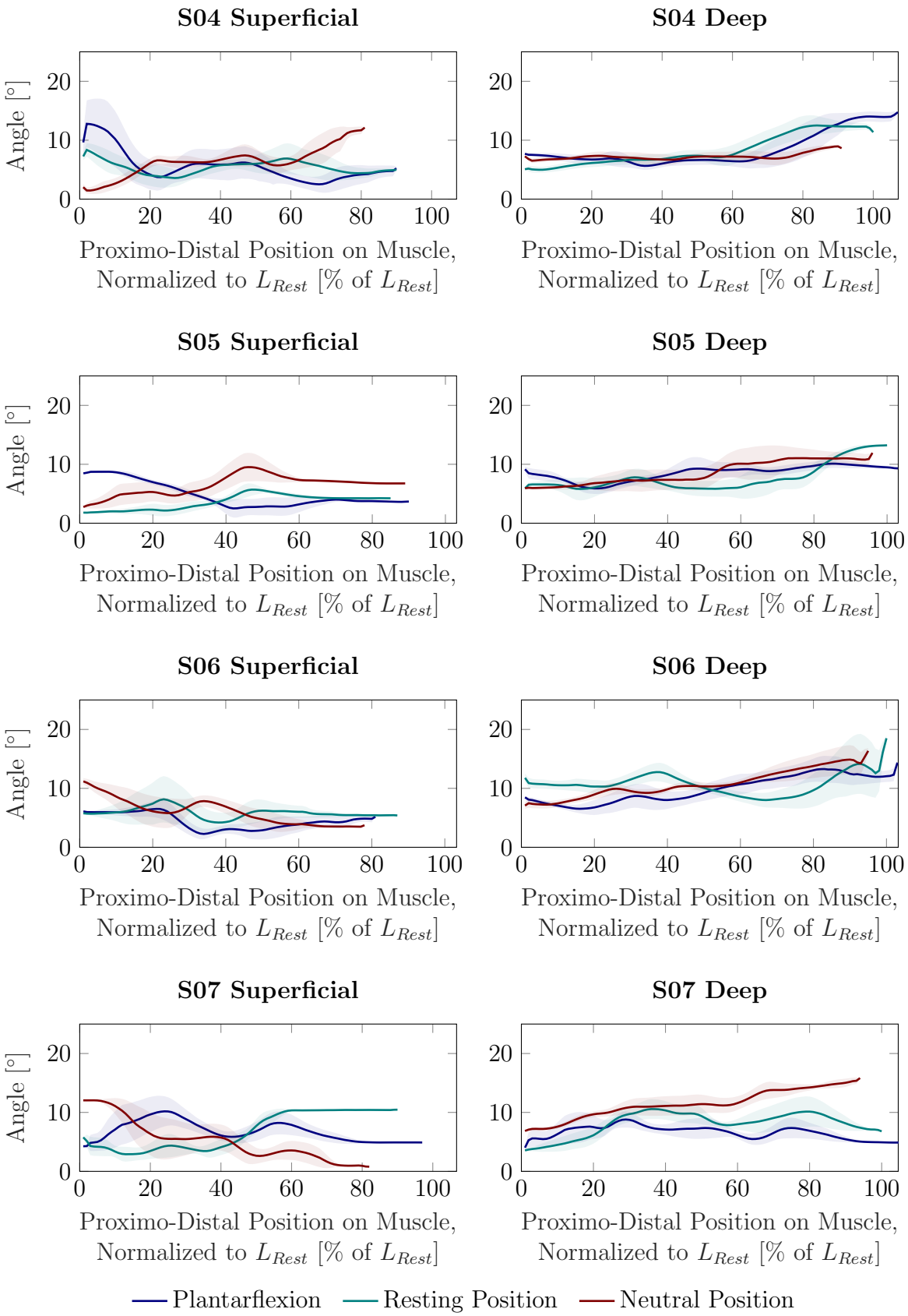

Figure C.2: TA pennation angle distribution over the resting position muscle length L_{Rest} for different subjects for the superficial and deep compartments. S04: Subject 4, S05: Subject 5, S06: Subject 6, S07: Subject 7.

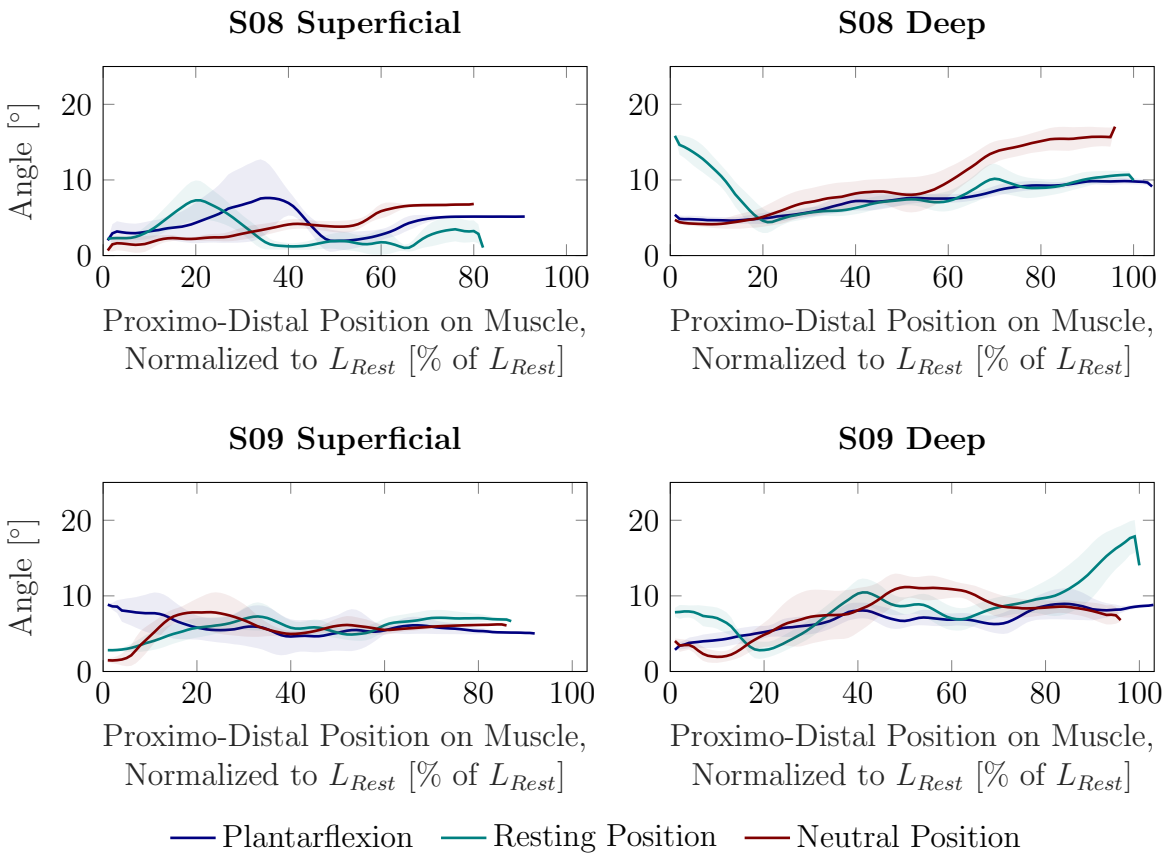

Figure C.3: TA pennation angle distribution over the resting position muscle length L_{Rest} for different subjects for the superficial and deep compartments. S08: Subject 8, S09: Subject 9.

Bibliography

[1] Anatomical planes. https://commons.wikimedia.org/wiki/File:Anatomical_Planes.svg. Accessed: 2023-08-17.

[2] Directional terms. https://commons.wikimedia.org/wiki/File:Directional_Terms.jpg. Accessed: 2023-08-17.

[3] Dorsiplantar. https://commons.wikimedia.org/wiki/File:Dorsiplantar.jpg. Accessed: 2023-08-18.

[4] Tibialis anterior. https://commons.wikimedia.org/wiki/File:Tibialis_anterior_2.png. Accessed: 2023-08-07.

[5] Basic human body measurements for technological design - part 3: Worldwide and regional design ranges for use in product standards, 2015.

[6] A. M. Agur, V. Ng-Thow-Hing, K. A. Ball, E. Fiume, and N. H. McKee. Documentation and three-dimensional modelling of human soleus muscle architecture. *Clinical Anatomy*, 16(4):285–293, jun 2003.

[7] C. D. Ainsworth, C. C. Blake, A. Tamayo, V. Beletsky, A. Fenster, and J. D. Spence. 3d ultrasound measurement of change in carotid plaque volume. *Stroke*, 36(9):1904–1909, sep 2005.

[8] H. Akima, J. ichi Ushiyama, J. Kubo, H. Fukuoka, H. Kanehisa, and T. Fukunaga. Effect of unloading on muscle volume with and without resistance training. *Acta Astronautica*, 60(8-9):728–736, apr 2007.

[9] J. Alcazar, R. Csapo, I. Ara, and L. M. Alegre. On the shape of the force-velocity relationship in skeletal muscles: The linear, the hyperbolic, and the double-hyperbolic. *Frontiers in Physiology*, 10, jun 2019.

[10] J. E. Aldrich. Basic physics of ultrasound imaging. *Critical Care Medicine*, 35(Suppl):S131–S137, may 2007.

[11] M. Alipour, K. Mithraratne, and J. Fernandez. A diffusion-weighted imaging informed continuum model of the rabbit triceps surae complex. *Biomechanics and Modeling in Mechanobiology*, 16(5):1729–1741, may 2017.

[12] K. S. Arun, T. S. Huang, and S. D. Blostein. Least-squares fitting of two 3-d point sets. *IEEE Transactions on Pattern Analysis and Machine Intelligence*, PAMI-9(5):698–700, sep 1987.

[13] D. S. Asakawa, S. S. Blemker, G. E. Gold, and S. L. Delp. In vivo motion of the rectus femoris muscle after tendon transfer surgery. *Journal of Biomechanics*, 35(8):1029–1037, aug 2002.

[14] A. Aubel and D. Thalmann. MuscleBuilder: A modeling tool for human anatomy. *Journal of Computer Science and Technology*, 19(5):585–595, sep 2004.

[15] A. Austeng and S. Holm. Sparse 2-d arrays for 3-d phased array imaging - experimental validation. *IEEE Transactions on Ultrasonics, Ferroelectrics and Frequency Control*, 49(8):1087–1093, aug 2002.

[16] E. Azizi, E. L. Brainerd, and T. J. Roberts. Variable gearing in pennate muscles. *Proceedings of the National Academy of Sciences*, 105(5):1745–1750, feb 2008.

[17] L. Balestrini, C. Fleishman, L. Lanzoni, J. Kisslo, A. Bengur, S. P. Sanders, and J. S. Li. Real-time 3-dimensional echocardiography evaluation of congenital heart disease. *Journal of the American Society of Echocardiography*, 13(3):171–176, mar 2000.

[18] L. Barber, C. Alexander, P. Shipman, R. Boyd, S. Reid, and C. Elliott. Validity and reliability of a freehand 3d ultrasound system for the determination of triceps surae muscle volume in children with cerebral palsy. *Journal of Anatomy*, 234(3):384–391, dec 2018.

[19] L. Barber, R. Barrett, and G. Lichtwark. Validation of a freehand 3d ultrasound system for morphological measures of the medial gastrocnemius muscle. *Journal of Biomechanics*, 42(9):1313–1319, jun 2009.

[20] F. E. Bell and R. Haddad. The basics of ultrasound physics. In *Understanding Physiology with Ultrasound*, pages 11–57. Springer US, 2022.

[21] M. A. L. Bell, H. T. Sen, I. Iordachita, and P. Kazanzides. Force-controlled ultrasound robot for consistent tissue pre-loading: Implications for acoustic radiation force elasticity imaging. In *5th IEEE RAS/EMBS International Conference on Biomedical Robotics and Biomechatronics*. IEEE, aug 2014.

[22] M. R. Bénard, J. G. Becher, J. Harlaar, P. A. Huijing, and R. T. Jaspers. Anatomical information is needed in ultrasound imaging of muscle to avoid potentially substantial errors in measurement of muscle geometry. *Muscle & Nerve*, 39(5):652–665, may 2009.

[23] S. Berg, H. Torp, D. Martens, E. Steen, S. Samstad, I. Høivik, and B. Olstad. Dynamic three-dimensional freehand echocardiography using raw digital ultrasound data. *Ultrasound in Medicine & Biology*, 25(5):745–753, jun 1999.

[24] J. G. Betts, K. A. Young, J. A. Wise, E. Johnson, B. Poe, D. H. Kruse, O. Korol, J. E. Johnson, M. Womble, and P. DeSaix. *Anatomy and Physiology 2e*. OpenStax, Apr. 2022.

[25] N. Bilaniuk and G. S. K. Wong. Speed of sound in pure water as a function of temperature. *The Journal of the Acoustical Society of America*, 93(3):1609–1612, mar 1993.

[26] D. C. Bland, L. A. Prosser, L. A. Bellini, K. E. Alter, and D. L. Damiano. Tibialis anterior architecture, strength, and gait in individuals with cerebral palsy. *Muscle & Nerve*, 44(4):509–517, jul 2011.

[27] C. Bleiler, P. P. Castañeda, and O. Röhrle. A microstructurally-based, multi-scale, continuum-mechanical model for the passive behaviour of skeletal muscle tissue. *Journal of the Mechanical Behavior of Biomedical Materials*, 97:171–186, sep 2019.

[28] S. S. Blemker, P. M. Pinsky, and S. L. Delp. A 3d model of muscle reveals the causes

of nonuniform strains in the biceps brachii. *Journal of Biomechanics*, 38(4):657–665, Apr. 2005.

[29] B. Bolsterlee, T. Finni, A. D'Souza, J. Eguchi, E. C. Clarke, and R. D. Herbert. Three-dimensional architecture of the whole human soleus muscle in vivo. *PeerJ*, 6:e4610, apr 2018.

[30] B. Bolsterlee, S. C. Gandevia, and R. D. Herbert. Effect of transducer orientation on errors in ultrasound image-based measurements of human medial gastrocnemius muscle fascicle length and pennation. *PLOS ONE*, 11(6):e0157273, jun 2016.

[31] B. Bolsterlee, H. D. Veeger, F. C. van der Helm, S. C. Gandevia, and R. D. Herbert. Comparison of measurements of medial gastrocnemius architectural parameters from ultrasound and diffusion tensor images. *Journal of Biomechanics*, 48(6):1133–1140, apr 2015.

[32] B. Borotikar, M. Lempereur, M. Lelievre, V. Burdin, D. B. Salem, and S. Brochard. Dynamic MRI to quantify musculoskeletal motion: A systematic review of concurrent validity and reliability, and perspectives for evaluation of musculoskeletal disorders. *PLOS ONE*, 12(12):e0189587, dec 2017.

[33] A. Botter, T. M. M. Vieira, I. D. Loram, R. Merletti, and E. F. Hodson-Tole. A novel system of electrodes transparent to ultrasound for simultaneous detection of myoelectric activity and b-mode ultrasound images of skeletal muscles. *Journal of Applied Physiology*, 115(8):1203–1214, oct 2013.

[34] E. L. Brainerd and E. Azizi. Muscle fiber angle, segment bulging and architectural gear ratio in segmented musculature. *Journal of Experimental Biology*, 208(17):3249–3261, sep 2005.

[35] R. A. Brown. A stereotactic head frame for use with ct body scanners. *Investigative radiology*, 14(4):300–304, 1979.

[36] C. B. Burckhardt. Speckle in ultrasound b-mode scans. *IEEE Transactions on Sonics and Ultrasonics*, 25(1):1–6, jan 1978.

[37] J.-M. Bureau, W. Steichen, and G. Lebail. A two-dimensional transducer array for real-time 3d medical ultrasound imaging. In *1998 IEEE Ultrasonics Symposium. Proceedings*. IEEE.

[38] M. Böl, K. Leichsenring, C. Weichert, M. Sturmat, P. Schenk, R. Blickhan, and T. Siebert. Three-dimensional surface geometries of the rabbit soleus muscle during contraction: input for biomechanical modelling and its validation. *Biomechanics and Modeling in Mechanobiology*, 12(6):1205–1220, feb 2013.

[39] G. Carbajal, A. Lasso, Á. Gómez, and G. Fichtinger. Improving n-wire phantom-based freehand ultrasound calibration. *International Journal of Computer Assisted Radiology and Surgery*, 8(6):1063–1072, jul 2013.

[40] F. Cenni, D. Monari, K. Desloovere, E. Aertbeliën, S.-H. Schless, and H. Bruyninckx. The reliability and validity of a clinical 3d freehand ultrasound system. *Computer Methods and Programs in Biomedicine*, 136:179–187, nov 2016.

[41] F. Cenni, S.-H. Schless, L. Bar-On, E. Aertbeliën, H. Bruyninckx, B. Hanssen, and K. Desloovere. Reliability of a clinical 3d freehand ultrasound technique: Anal-

yses on healthy and pathological muscles. *Computer Methods and Programs in Biomedicine*, 156:97–103, mar 2018.

[42] F. Cenni, S.-H. Schless, D. Monari, L. Bar-On, E. Aertbeliën, H. Bruyninckx, B. Hanssen, and K. Desloovere. An innovative solution to reduce muscle deformation during ultrasonography data collection. *Journal of Biomechanics*, 77:194–200, aug 2018.

[43] J. P. Charles, F. Suntaxi, and W. J. Anderst. In vivo human lower limb muscle architecture dataset obtained using diffusion tensor imaging. *PLOS ONE*, 14(10):e0223531, oct 2019.

[44] M. Chatrasingh and J. Suthakorn. A novel design of n-fiducial phantom for automatic ultrasound calibration. *Journal of Medical Physics*, 44(3):191, 2019.

[45] M.-S. Choi, J.-H. Shin, H.-K. Park, and W.-H. Lee. Reliability and validity of rehabilitative ultrasound images obtained using a hands-free fixed probe in measuring the muscle structures of the tibialis anterior and the gastrocnemius. *Physical Therapy Rehabilitation Science*, 8(4):194–201, dec 2019.

[46] B. Choroba, B. Pycinski, M. Krecichwost, D. Spinczyk, and E. Pietka. Novel geometric technique of ultrasound probe calibration. In *Advances in Intelligent Systems and Computing*, pages 182–193. Springer International Publishing, jun 2018.

[47] K. Christensen-Jeffries, O. Couture, P. A. Dayton, Y. C. Eldar, K. Hynynen, F. Kiessling, M. O'Reilly, G. F. Pinton, G. Schmitz, M.-X. Tang, M. Tanter, and R. J. van Sloun. Super-resolution ultrasound imaging. *Ultrasound in Medicine & Biology*, 46(4):865–891, apr 2020.

[48] J. Clarke, S. Carlsson, and A. Zisserman. Detecting and tracking linear features efficiently. In *Procedings of the British Machine Vision Conference 1996*. British Machine Vision Association, 1996.

[49] N. Cobetto, C.-E. Aubin, and S. Parent. Surgical planning and follow-up of anterior vertebral body growth modulation in pediatric idiopathic scoliosis using a patient-specific finite element model integrating growth modulation. *Spine Deformity*, 6(4):344–350, jul 2018.

[50] J. Cohen. *Statistical Power Analysis for the Behavioral Sciences*. Taylor & Francis, 1988.

[51] P. Coupé, P. Hellier, N. Azzabou, and C. Barillot. 3d freehand ultrasound reconstruction based on probe trajectory. In *Lecture Notes in Computer Science*, pages 597–604. Springer Berlin Heidelberg, 2005.

[52] R. Cunningham, P. Harding, and I. Loram. Deep residual networks for quantification of muscle fiber orientation and curvature from ultrasound images. In *Communications in Computer and Information Science*, pages 63–73. Springer International Publishing, 2017.

[53] J.-L. Daire, J.-P. Jacob, J.-N. Hyacinthe, P. Croisille, K. Montet-Abou, S. Richter, D. Botsikas, M. Lepetit-Coiffé, D. Morel, and J.-P. Vallée. Cine and tagged cardiovascular magnetic resonance imaging in normal rat at 1.5 t: a rest and stress study. *Journal of Cardiovascular Magnetic Resonance*, 10(1), nov 2008.

[54] B. M. Damon, Z. Ding, A. W. Anderson, A. S. Freyer, and J. C. Gore. Validation of diffusion tensor MRI-based muscle fiber tracking. *Magnetic Resonance in Medicine*, 48(1):97–104, jun 2002.

[55] R. G. Dantas, E. T. Costa, and S. Leeman. Ultrasound speckle and equivalent scatterers. *Ultrasonics*, 43(6):405–420, may 2005.

[56] J. Darby, B. Li, N. Costen, I. Loram, and E. Hodson-Tole. Estimating skeletal muscle fascicle curvature from b-mode ultrasound image sequences. *IEEE Transactions on Biomedical Engineering*, 60(7):1935–1945, jul 2013.

[57] D. Devaprakash, D. G. Lloyd, R. S. Barrett, S. J. Obst, B. Kennedy, K. L. Adams, A. Hunter, N. Vlahovich, D. L. Pease, and C. Pizzolato. Magnetic resonance imaging and freehand 3-d ultrasound provide similar estimates of free achilles tendon shape and 3-d geometry. *Ultrasound in Medicine & Biology*, 45(11):2898–2905, nov 2019.

[58] D. E. O. Dewi, M. M. Fadzil, A. A. M. Faudzi, E. Supriyanto, and K. W. Lai. Position tracking systems for ultrasound imaging: A survey. In *Lecture Notes in Bioengineering*, pages 57–89. Springer Singapore, 2015.

[59] D. E. O. Dewi, T. L. R. Mengko, I. K. E. Purnama, A. G. Veldhuizen, and M. H. F. Wilkinson. An improved olympic hole-filling method for ultrasound volume reconstruction of human spine. *International Journal of E-Health and Medical Communications*, 1(3):28–40, jul 2010.

[60] A. Dhanantwari, S. Stergiopoulos, L. Song, C. Parodi, F. Bertora, P. Pellegretti, and A. Questa. An efficient 3d beamformer implementation for real-time 4d ultrasound systems deploying planar array probes. In *IEEE Ultrasonics Symposium, 2004.* IEEE.

[61] M. Dhyani, S. C. Roll, M. W. Gilbertson, M. Orlowski, A. Anvari, Q. Li, B. Anthony, and A. E. Samir. A pilot study to precisely quantify forces applied by sonographers while scanning: A step toward reducing ergonomic injury. *Work*, 58(2):241–247, oct 2017.

[62] A.-C. Dupont, E. E. Sauerbrei, P. V. Fenton, P. C. Shragge, G. E. Loeb, and F. J. R. Richmond. Real-time sonography to estimate muscle thickness: Comparison with MRI and CT. *Journal of Clinical Ultrasound*, 29(4):230–236, 2001.

[63] C. M. Eng, E. Azizi, and T. J. Roberts. Structural determinants of muscle gearing during dynamic contractions. *Integrative and Comparative Biology*, 58(2):207–218, jun 2018.

[64] R. M. Enoka. *Neuromechanics of Human Movement*, chapter 6: Muscle and Motor Units, pages 205–248. Human Kinetics, 4 edition, 2008.

[65] J. I. Esformes, M. V. Narici, and C. N. Maganaris. Measurement of human muscle volume using ultrasonography. *European Journal of Applied Physiology*, 87(1):90–92, mar 2002.

[66] M. Farrow, J. Biglands, S. F. Tanner, A. Clegg, L. Brown, E. M. A. Hensor, P. O'Connor, P. Emery, and A. L. Tan. The effect of ageing on skeletal muscle as assessed by quantitative MR imaging: an association with frailty and muscle strength. *Aging Clinical and Experimental Research*, 33(2):291–301, mar 2020.

[67] A. Fenster and D. B. Downey. Three-dimensional ultrasound imaging. *Annual Review of Biomedical Engineering*, 2(1):457–475, aug 2000.

[68] A. Fenster, G. Parraga, and J. Bax. Three-dimensional ultrasound scanning. *Interface Focus*, 1(4):503–519, jun 2011.

[69] J. Fernandez, M. Buist, D. Nickerson, and P. Hunter. Modelling the passive and nerve activated response of the rectus femoris muscle to a flexion loading: A finite element framework. *Medical Engineering & Physics*, 27(10):862–870, Dec. 2005.

[70] M. A. Fischler and R. C. Bolles. Random sample consensus: a paradigm for model fitting with applications to image analysis and automated cartography. *Communications of the ACM*, 24(6):381–395, 1981.

[71] M. V. Franchi, S. Longo, J. Mallinson, J. I. Quinlan, T. Taylor, P. L. Greenhaff, and M. V. Narici. Muscle thickness correlates to muscle cross-sectional area in the assessment of strength training-induced hypertrophy. *Scandinavian Journal of Medicine & Science in Sports*, 28(3):846–853, sep 2017.

[72] M. V. Franchi, B. J. Raiteri, S. Longo, S. Sinha, M. V. Narici, and R. Csapo. Muscle architecture assessment: Strengths, shortcomings and new frontiers of in vivo imaging techniques. *Ultrasound in Medicine & Biology*, 44(12):2492–2504, dec 2018.

[73] A. F. Frangi, W. J. Niessen, K. L. Vincken, and M. A. Viergever. Multiscale vessel enhancement filtering. In *Medical Image Computing and Computer-Assisted Intervention — MICCAI'98*, pages 130–137. Springer Berlin Heidelberg, 1998.

[74] J. A. Friederich and R. A. Brand. Muscle fiber architecture in the human lower limb. *Journal of Biomechanics*, 23(1):91–95, jan 1990.

[75] W. R. Frontera and J. Ochala. Skeletal muscle: A brief review of structure and function. *Calcified Tissue International*, 96(3):183–195, oct 2014.

[76] N. Fry, C. Childs, L. Eve, M. Gough, R. Robinson, and A. Shortland. Accurate measurement of muscle belly length in the motion analysis laboratory: potential for the assessment of contracture. *Gait & Posture*, 17(2):119–124, apr 2003.

[77] N. Fry, M. Gough, and A. Shortland. Three-dimensional realisation of muscle morphology and architecture using ultrasound. *Gait & Posture*, 20(2):177–182, oct 2004.

[78] T. Fukunaga, Y. Ichinose, M. Ito, Y. Kawakami, and S. Fukashiro. Determination of fascicle length and pennation in a contracting human muscle in vivo. *Journal of Applied Physiology*, 82(1):354–358, jan 1997.

[79] T. Fukunaga, M. Miyatani, M. Tachi, M. Kouzaki, Y. Kawakami, and H. Kanehisa. Muscle volume is a major determinant of joint torque in humans. *Acta Physiologica Scandinavica*, 172(4):249–255, aug 2001.

[80] T. Fukunaga, R. R. Roy, F. G. Shellock, J. A. Hodgson, M. K. Day, P. L. Lee, H. Kwong-Fu, and V. R. Edgerton. Physiological cross-sectional area of human leg muscles based on magnetic resonance imaging. *Journal of Orthopaedic Research*, 10(6):926–934, nov 1992.

[81] Y. Fung. *Biomechanics: Mechanical Properties of Living Tissues*, chapter 9: Skeletal Muscle, pages 392–426. Springer, 1993.

[82] C. Gans and W. Bock. The functional significance of muscle architecture–a theoretical analysis. *Ergebnisse der Anatomie und Entwicklungsgeschichte*, 38:115–142, 1965.

[83] F. Gao, T. H. Grant, E. J. Roth, and L.-Q. Zhang. Changes in passive mechanical properties of the gastrocnemius muscle at the muscle fascicle and joint levels in stroke survivors. *Archives of Physical Medicine and Rehabilitation*, 90(5):819–826, may 2009.

[84] H. Gao, Q. Huang, X. Xu, and X. Li. Wireless and sensorless 3d ultrasound imaging. *Neurocomputing*, 195:159–171, jun 2016.

[85] D. Garcia. A fast all-in-one method for automated post-processing of PIV data. *Experiments in Fluids*, 50(5):1247–1259, oct 2010.

[86] D. Garcia. Robust smoothing of gridded data in one and higher dimensions with missing values. *Computational Statistics & Data Analysis*, 54(4):1167–1178, apr 2010.

[87] D. Garcia. smoothn. MATLAB Central File Exchange, 2023.

[88] A. H. Gee, R. J. Housden, P. Hassenpflug, G. M. Treece, and R. W. Prager. Sensorless freehand 3d ultrasound in real tissue: Speckle decorrelation without fully developed speckle. *Medical Image Analysis*, 10(2):137–149, apr 2006.

[89] M. W. Gilbertson and B. W. Anthony. An ergonomic, instrumented ultrasound probe for 6-axis force/torque measurement. In *2013 35th Annual International Conference of the IEEE Engineering in Medicine and Biology Society (EMBC)*. IEEE, jul 2013.

[90] M. W. Gilbertson and B. W. Anthony. Force and position control system for freehand ultrasound. *IEEE Transactions on Robotics*, 31(4):835–849, aug 2015.

[91] L. F. Gonçalves, W. Lee, J. Espinoza, and R. Romero. Three- and 4-dimensional ultrasound in obstetric practice. *Journal of Ultrasound in Medicine*, 24(12):1599–1624, dec 2005.

[92] A. M. Gordon, A. F. Huxley, and F. J. Julian. The variation in isometric tension with sarcomere length in vertebrate muscle fibres. *The Journal of Physiology*, 184(1):170–192, may 1966.

[93] I. Hagoort, T. Hortobágyi, N. Vuillerme, C. J. C. Lamoth, and A. Murgia. Age- and muscle-specific reliability of muscle architecture measurements assessed by two-dimensional panoramic ultrasound. *BioMedical Engineering OnLine*, 21(1), feb 2022.

[94] G. G. Handsfield, B. Bolsterlee, J. M. Inouye, R. D. Herbert, T. F. Besier, and J. W. Fernandez. Determining skeletal muscle architecture with laplacian simulations: a comparison with diffusion tensor imaging. *Biomechanics and Modeling in Mechanobiology*, 16(6):1845–1855, jun 2017.

[95] G. G. Handsfield, C. H. Meyer, M. F. Abel, and S. S. Blemker. Heterogeneity of

muscle sizes in the lower limbs of children with cerebral palsy. *Muscle & Nerve*, 53(6):933–945, feb 2016.

[96] E. D. Hanson, S. R. Srivatsan, S. Agrawal, K. S. Menon, M. J. Delmonico, M. Q. Wang, and B. F. Hurley. Effects of strength training on physical function: Influence of power, strength, and body composition. *Journal of Strength and Conditioning Research*, 23(9):2627–2637, dec 2009.

[97] R. M. Haralick and L. G. Shapiro. Computer and robot vision. 1:28–48, 1992.

[98] M. O. Harris-Love, C. Ismail, R. Monfaredi, H. J. Hernandez, D. Pennington, P. Woletz, V. McIntosh, B. Adams, and M. R. Blackman. Interrater reliability of quantitative ultrasound using force feedback among examiners with varied levels of experience. *PeerJ*, 4:e2146, jun 2016.

[99] A. M. Heemskerk, T. K. Sinha, K. J. Wilson, Z. Ding, and B. M. Damon. Repeatability of DTI-based skeletal muscle fiber tracking. *NMR in Biomedicine*, 23(3):294–303, jan 2010.

[100] T. Heidlauf, T. Klotz, C. Rode, E. Altan, C. Bleiler, T. Siebert, and O. Röhrle. A multi-scale continuum model of skeletal muscle mechanics predicting force enhancement based on actin–titin interaction. *Biomechanics and Modeling in Mechanobiology*, 15(6):1423–1437, mar 2016.

[101] T. Heidlauf and O. Röhrle. A multiscale chemo-electro-mechanical skeletal muscle model to analyze muscle contraction and force generation for different muscle fiber arrangements. *Frontiers in Physiology*, 5, dec 2014.

[102] W. Herzog. *Biomechanics of the Musculo-Skeletal System*, chapter 2.7 Muscle, pages 169–225. John Wiley & Sons Ltd., 3 edition, 2006.

[103] A. V. Hill. The heat of shortening and the dynamic constants of muscle. *Proceedings of the Royal Society of London. Series B - Biological Sciences*, 126(843):136–195, oct 1938.

[104] A. V. Hill. The pressure developed in muscle during contraction. *The Journal of Physiology*, 107(4):518–526, sep 1948.

[105] R. K. Hobbie and B. J. Roth. Sound and ultrasound. In *Intermediate Physics for Medicine and Biology*, pages 363–379. Springer International Publishing, 2015.

[106] P. Hodges, L. Pengel, R. Herbert, and S. Gandevia. Measurement of muscle contraction with ultrasound imaging. *Muscle & Nerve*, 27(6):682–692, may 2003.

[107] J.-Y. Hogrel, Y. Barnouin, N. Azzabou, G. Butler-Browne, T. Voit, A. Moraux, G. Leroux, A. Behin, J. S. McPhee, and P. G. Carlier. NMR imaging estimates of muscle volume and intramuscular fat infiltration in the thigh: variations with muscle, gender, and age. *AGE*, 37(3), jun 2015.

[108] K. R. Holzbaur, S. L. Delp, G. E. Gold, and W. M. Murray. Moment-generating capacity of upper limb muscles in healthy adults. *Journal of Biomechanics*, 40(11):2442–2449, 2007.

[109] D. Holzer, M. Millard, D. Hahn, T. Siebert, A. Schwirtz, and W. Seiberl. Tendon compliance and preload must be considered when determining the in vivo

force–velocity relationship from the torque–angular velocity relation. *Scientific Reports*, 13(1), apr 2023.

[110] B. V. Hooren, P. Teratsias, and E. F. Hodson-Tole. Ultrasound imaging to assess skeletal muscle architecture during movements: a systematic review of methods, reliability, and challenges. *Journal of Applied Physiology*, 128(4):978–999, apr 2020.

[111] P. V. Hough. Method and means for recognizing complex patterns, Dec. 18 1962. US Patent 3,069,654.

[112] P.-W. Hsu, R. W. Prager, A. H. Gee, and G. M. Treece. Rapid, easy and reliable calibration for freehand 3d ultrasound. Technical Report CUED/F-INFENG/TR 534, Cambridge University Department of Engineering, Aug. 2005.

[113] P.-W. Hsu, R. W. Prager, A. H. Gee, and G. M. Treece. Freehand 3d ultrasound calibration: a review. Technical Report CUED/F-INFENG/TR 584, Cambridge University Department of Engineering, Dec. 2007.

[114] P.-W. Hsu, R. W. Prager, A. H. Gee, and G. M. Treece. Real-time freehand 3d ultrasound calibration. In S. Y. Emelianov and S. A. McAleavey, editors, *Medical Imaging 2007: Ultrasonic Imaging and Signal Processing*. SPIE, mar 2007.

[115] C. Hu, H. Hu, X. Mai, W. L. A. Lo, and L. Li. Correlation between muscle structures and electrical properties of the tibialis anterior in subacute stroke survivors: A pilot study. *Frontiers in Neuroscience*, 13, nov 2019.

[116] Q. Huang, Y. Huang, W. Hu, and X. Li. Bezier interpolation for 3-d freehand ultrasound. *IEEE Transactions on Human-Machine Systems*, 45(3):385–392, jun 2015.

[117] Q. Huang, J. Lan, and X. Li. Robotic arm based automatic ultrasound scanning for three-dimensional imaging. *IEEE Transactions on Industrial Informatics*, 15(2):1173–1182, feb 2019.

[118] Q. Huang, M. Lu, Y. Zheng, and Z. Chi. Speckle suppression and contrast enhancement in reconstruction of freehand 3d ultrasound images using an adaptive distance-weighted method. *Applied Acoustics*, 70(1):21–30, jan 2009.

[119] Q. Huang, B. Wu, J. Lan, and X. Li. Fully automatic three-dimensional ultrasound imaging based on conventional b-scan. *IEEE Transactions on Biomedical Circuits and Systems*, 12(2):426–436, apr 2018.

[120] Q. Huang and Z. Zeng. A review on real-time 3d ultrasound imaging technology. *BioMed Research International*, 2017:1–20, 2017.

[121] Q. Huang, Y. Zheng, M. Lu, and Z. Chi. Development of a portable 3d ultrasound imaging system for musculoskeletal tissues. *Ultrasonics*, 43(3):153–163, jan 2005.

[122] Q.-H. Huang, Z. Yang, W. Hu, L.-W. Jin, G. Wei, and X. Li. Linear tracking for 3-d medical ultrasound imaging. *IEEE Transactions on Cybernetics*, 43(6):1747–1754, dec 2013.

[123] Q.-H. Huang and Y.-P. Zheng. An adaptive squared-distance-weighted interpolation for volume reconstruction in 3d freehand ultrasound. *Ultrasonics*, 44:e73–e77, dec 2006.

[124] A. F. Huxely and R. Niedergerke. Structural changes in muscle during contraction: Interference microscopy of living muscle fibres. *Nature*, 173(4412):971–973, may 1954.

[125] H. Huxley and J. Hanson. Changes in the cross-striations of muscle during contraction and stretch and their structural interpretation. *Nature*, 173(4412):973–976, may 1954.

[126] B. Ihnatsenka and A. Boezaart. Ultrasound: Basic understanding and learning the language. *International Journal of Shoulder Surgery*, 4(3):55, 2010.

[127] H. Ishida and S. Watanabe. Influence of inward pressure of the transducer on lateral abdominal muscle thickness during ultrasound imaging. *Journal of Orthopaedic & Sports Physical Therapy*, 42(9):815–818, sep 2012.

[128] K. Ito, S. Sugano, and H. Iwata. Portable and attachable tele-echography robot system: Fastele. In *2010 Annual International Conference of the IEEE Engineering in Medicine and Biology*. IEEE, Aug. 2010.

[129] M. Jansen, N. van Alfen, M. W. N. van der Sanden, J. P. van Dijk, S. Pillen, and I. J. de Groot. Quantitative muscle ultrasound is a promising longitudinal follow-up tool in duchenne muscular dystrophy. *Neuromuscular Disorders*, 22(4):306–317, apr 2012.

[130] E. R. Jensen, D. A. Morrow, J. P. Felmlee, N. S. Murthy, and K. R. Kaufman. Characterization of three dimensional volumetric strain distribution during passive tension of the human tibialis anterior using cine phase contrast MRI. *Journal of Biomechanics*, 49(14):3430–3436, oct 2016.

[131] Z. Jiang, S. E. Salcudean, and N. Navab. Robotic ultrasound imaging: State-of-the-art and future perspectives, 2023.

[132] R. S. José-Estépar, M. Martín-Fernández, P. Caballero-Martínez, C. Alberola-López, and J. Ruiz-Alzola. A theoretical framework to three-dimensional ultrasound reconstruction from irregularly sampled data. *Ultrasound in Medicine & Biology*, 29(2):255–269, feb 2003.

[133] N. Y. Kelp, C. J. Clemente, K. Tucker, F. Hug, S. Pinel, and T. J. M. Dick. Influence of internal muscle properties on muscle shape change and gearing in the human gastrocnemii. *Journal of Applied Physiology*, 134(6):1520–1529, jun 2023.

[134] W. Kilarski. Functional morphology of the striated muscle. In *Muscle and Exercise Physiology*, pages 27–38. Elsevier, 2019.

[135] M. Klimstra, J. Dowling, J. L. Durkin, and M. MacDonald. The effect of ultrasound probe orientation on muscle architecture measurement. *Journal of Electromyography and Kinesiology*, 17(4):504–514, aug 2007.

[136] T. Klotz, L. Gizzi, U. Ş. Yavuz, and O. Röhrle. Modelling the electrical activity of skeletal muscle tissue using a multi-domain approach. *Biomechanics and Modeling in Mechanobiology*, 19(1):335–349, sep 2019.

[137] R. J. Korthuis. *Skeletal Muscle Circulation*, chapter 2: Anatomy of Skeletal Muscle and Its Vascular Supply. San Rafael (CA): Morgan & Claypool Life Sciences, 2011.

[138] D.-J. Kroon. Hessian based frangi vesselness filter. MATLAB Central File Exchange, 2021.

[139] K. Kubo, T. Ikebukuro, and H. Yata. Effects of squat training with different depths on lower limb muscle volumes. *European Journal of Applied Physiology*, 119(9):1933–1942, jun 2019.

[140] T. Kurihara, T. Oda, K. Chino, H. Kanehisa, T. Fukunaga, and Y. Kawakami. Use of three-dimensional ultrasonography for the analysis of the fascicle length of human gastrocnemius muscle during contractions. *International Journal of Sport and Health Science*, 3(Special_Issue_2):226–234, 2005.

[141] L. K. Kwah, R. Z. Pinto, J. Diong, and R. D. Herbert. Reliability and validity of ultrasound measurements of muscle fascicle length and pennation in humans: a systematic review. *Journal of Applied Physiology*, 114(6):761–769, mar 2013.

[142] C. Körting, M. Schlippe, S. Petersson, G. V. Pennati, O. Tarassova, A. Arndt, T. Finni, K. Zhao, and R. Wang. In vivo muscle morphology comparison in post-stroke survivors using ultrasonography and diffusion tensor imaging. *Scientific Reports*, 9(1), aug 2019.

[143] A. Landry, J. D. Spence, and A. Fenster. Measurement of carotid plaque volume by 3-dimensional ultrasound. *Stroke*, 35(4):864–869, apr 2004.

[144] A. Lasso, T. Heffter, A. Rankin, C. Pinter, T. Ungi, and G. Fichtinger. PLUS: Open-source toolkit for ultrasound-guided intervention systems. *IEEE Transactions on Biomedical Engineering*, 61(10):2527–2537, oct 2014.

[145] S.-J. Lee, J. Y. Lim, C.-H. Lee, and D.-S. Park. Intra- and inter-rater reliability of muscle thickness measurement of the tibialis anterior using different inward pressures. *Physical Therapy Rehabilitation Science*, 8(4):218–224, dec 2019.

[146] K.-Y. Leung. Applications of advanced ultrasound technology in obstetrics. *Diagnostics*, 11(7):1217, jul 2021.

[147] P.-C. Li, C.-Y. Li, and W.-C. Yeh. Tissue motion and elevational speckle decorrelation in freehand 3d ultrasound. *Ultrasonic Imaging*, 24(1):1–12, jan 2002.

[148] G. A. Lichtwark, D. J. Farris, X. Chen, P. W. Hodges, and S. L. Delp. Microendoscopy reveals positive correlation in multiscale length changes and variable sarcomere lengths across different regions of human muscle. *Journal of Applied Physiology*, 125(6):1812–1820, dec 2018.

[149] R. L. Lieber. *Skeletal muscle structure, function, and plasticity: the physiological basis of rehabilitation*, chapter 2: Skeletal Muscle Physiology, pages 41–92. Wolters Kulver Lippincot Williams & Wilkins, 3 edition, 2010.

[150] R. L. Lieber and J. Friden. Functional and clinical significance of skeletal muscle architecture. *Muscle & Nerve*, 23(11):1647–1666, 2000.

[151] P. Liu, Y. Wang, H. Hu, Y. Mao, D. Huang, and L. Li. Change of muscle architecture following body weight support treadmill training for persons after subacute stroke: Evidence from ultrasonography. *BioMed Research International*, 2014:1–11, 2014.

[152] Z. Liu, S.-C. Chan, S. Zhang, Z. Zhang, and X. Chen. Automatic muscle fiber

orientation tracking in ultrasound images using a new adaptive fading bayesian kalman smoother. *IEEE Transactions on Image Processing*, 28(8):3714–3727, aug 2019.

[153] T. J. MacGillivray, E. Ross, H. A. Simpson, and C. A. Greig. 3d freehand ultrasound for in vivo determination of human skeletal muscle volume. *Ultrasound in Medicine & Biology*, 35(6):928–935, jun 2009.

[154] B. R. MacIntosh. *Skeletal muscle : form and function*, chapter 1: Muscle Architecture and Muscle Fiber Anatomy, pages 3–21. Human Kinetics, Champaign, Ill. ;, 2nd ed. edition, 2006.

[155] B. R. MacIntosh. *Skeletal muscle : form and function*, chapter 11: Muscle Contraction, pages 151–174. Human Kinetics, Champaign, Ill. ;, 2nd ed. edition, 2006.

[156] T. M. Maden-Wilkinson, J. S. McPhee, J. Rittweger, D. A. Jones, and H. Degens. Thigh muscle volume in relation to age, sex and femur volume. *AGE*, 36(1):383–393, aug 2013.

[157] E. L. Madsen, G. R. Frank, and F. Dong. Liquid or solid ultrasonically tissue-mimicking materials with very low scatter. *Ultrasound in Medicine & Biology*, 24(4):535–542, may 1998.

[158] C. N. Maganaris and V. Baltzopoulos. Predictability of in vivo changes in pennation angle of human tibialis anterior muscle from rest to maximum isometric dorsiflexion. *European Journal of Applied Physiology*, 79(3):294–297, jan 1999.

[159] C. N. Maganaris, V. Baltzopoulos, D. Ball, and A. J. Sargeant. In vivo specific tension of human skeletal muscle. *Journal of Applied Physiology*, 90(3):865–872, mar 2001.

[160] C. N. Maganaris, V. Baltzopoulos, and A. J. Sargeant. In vivo measurements of the triceps surae complex architecture in man: implications for muscle function. *The Journal of Physiology*, 512(2):603–614, oct 1998.

[161] R. Manniesing and W. Niessen. Multiscale vessel enhancing diffusion in CT angiography noise filtering. In *Lecture Notes in Computer Science*, pages 138–149. Springer Berlin Heidelberg, 2005.

[162] S. Martin-Rodriguez, J. J. Gonzalez-Henriquez, V. Galvan-Alvarez, S. Cruz-Ramírez, J. A. Calbet, and J. Sanchis-Moysi. Architectural anatomy of the human tibialis anterior presents morphological asymmetries between superficial and deep unipennate regions. *Journal of Anatomy*, mar 2023.

[163] V. Mazzoli, L. M. Gottwald, E. S. Peper, M. Froeling, B. F. Coolen, N. Verdonschot, A. M. Sprengers, P. Ooij, G. J. Strijkers, and A. J. Nederveen. Accelerated 4d phase contrast mri in skeletal muscle contraction. *Magnetic Resonance in Medicine*, 80(5):1799–1811, mar 2018.

[164] S. Meairs, J. Beyer, and M. Hennerici. Reconstruction and visualization of irregularly sampled three- and four-dimensional ultrasound data for cerebrovascular applications. *Ultrasound in Medicine & Biology*, 26(2):263–272, feb 2000.

[165] R.-M. Menchón-Lara, F. Simmross-Wattenberg, P. C. de-la Higuera, M. Martín-Fernández, and C. Alberola-López. Reconstruction techniques for cardiac cine MRI.

Insights into Imaging, 10(1), sep 2019.

[166] G. Menikou and C. Damianou. Acoustic and thermal characterization of agar based phantoms used for evaluating focused ultrasound exposures. *Journal of Therapeutic Ultrasound*, 5(1), jun 2017.

[167] L. Mercier, T. Langø, F. Lindseth, and L. D. Collins. A review of calibration techniques for freehand 3-d ultrasound systems. *Ultrasound in Medicine & Biology*, 31(2):143–165, feb 2005.

[168] D. Monari, F. Cenni, E. Aertbeliën, and K. Desloovere. Py3dfreehandus: a library for voxel-array reconstruction using ultrasonography and attitude sensors, 2014.

[169] M. Mordhorst, T. Heidlauf, and O. Röhrle. Predicting electromyographic signals under realistic conditions using a multiscale chemo-electro-mechanical finite element model. *Interface Focus*, 5(2):20140076, apr 2015.

[170] R. H. Morris and C. Sale. Imaging skeletal muscle by magnetic resonance imaging (MRI). In *Neuromethods*, pages 29–64. Springer US, 2023.

[171] C. I. Morse, J. M. Thom, M. G. Davis, K. R. Fox, K. M. Birch, and M. V. Narici. Reduced plantarflexor specific torque in the elderly is associated with a lower activation capacity. *European Journal of Applied Physiology*, 92(1-2):219–226, jun 2004.

[172] C. I. Morse, J. M. Thom, N. D. Reeves, K. M. Birch, and M. V. Narici. In vivo physiological cross-sectional area and specific force are reduced in the gastrocnemius of elderly men. *Journal of Applied Physiology*, 99(3):1050–1055, sep 2005.

[173] M. H. Mozaffari and W.-S. Lee. Freehand 3-d ultrasound imaging: A systematic review. *Ultrasound in Medicine & Biology*, 43(10):2099–2124, oct 2017.

[174] M. Mozaffarzadeh, M. Soozande, F. Fool, M. A. P. Pertijs, H. J. Vos, M. D. Verweij, J. G. Bosch, and N. de Jong. Receive/transmit aperture selection for 3d ultrasound imaging with a 2d matrix transducer. *Applied Sciences*, 10(15):5300, jul 2020.

[175] R. Nakadate, Y. Tokunaga, J. Solis, A. Takanishi, E. Minagawa, M. Sugawara, K. Niki, and A. Saito. Development of robot assisted measurement system for abdominal ultrasound diagnosis. In *2010 3rd IEEE RAS &EMBS International Conference on Biomedical Robotics and Biomechatronics*. IEEE, sep 2010.

[176] H. Neshat, D. W. Cool, K. Barker, L. Gardi, N. Kakani, and A. Fenster. A 3d ultrasound scanning system for image guided liver interventions. *Medical Physics*, 40(11):112903, oct 2013.

[177] D. Neumann and E. Kollorz. Ultrasound. In *Medical Imaging Systems*, pages 237–249. Springer International Publishing, 2018.

[178] A. Ng and J. Swanevelder. Resolution in ultrasound imaging. *Continuing Education in Anaesthesia Critical Care & Pain*, 11(5):186–192, oct 2011.

[179] J. J. Noble, N. R. Fry, A. P. Lewis, S. F. Keevil, M. Gough, and A. P. Shortland. Lower limb muscle volumes in bilateral spastic cerebral palsy. *Brain and Development*, 36(4):294–300, apr 2014.

[180] Y. Noh, R. J. Housden, A. Gomez, C. Knight, F. Garcia, H. Liu, R. Razavi,

K. Rhode, and K. Althoefer. An ergonomic handheld ultrasound probe providing contact forces and pose information. In *2015 37th Annual International Conference of the IEEE Engineering in Medicine and Biology Society (EMBC)*. IEEE, aug 2015.

[181] M. Noorkoiv, N. Theis, and G. Lavelle. A comparison of 3d ultrasound to MRI for the measurement and estimation of gastrocnemius muscle volume in adults and young people with and without cerebral palsy. *Clinical Anatomy*, 32(3):319–327, jan 2019.

[182] S. J. Obst, R. Newsham-West, and R. S. Barrett. In vivo measurement of human achilles tendon morphology using freehand 3-d ultrasound. *Ultrasound in Medicine & Biology*, 40(1):62–70, jan 2014.

[183] N. Otsu. A threshold selection method from gray-level histograms. *IEEE Transactions on Systems, Man, and Cybernetics*, 9(1):62–66, jan 1979.

[184] E. Otten. A myocybernetic model of the jaw system of the rat. *Journal of Neuroscience Methods*, 21(2-4):287–302, oct 1987.

[185] H. Ozaki, M. Sakamaki, T. Yasuda, S. Fujita, R. Ogasawara, M. Sugaya, T. Nakajima, and T. Abe. Increases in thigh muscle volume and strength by walk training with leg blood flow reduction in older participants. *The Journals of Gerontology Series A: Biological Sciences and Medical Sciences*, 66A(3):257–263, oct 2010.

[186] P. A. Patlan-Rosales and A. Krupa. A robotic control framework for 3-d quantitative ultrasound elastography. In *2017 IEEE International Conference on Robotics and Automation (ICRA)*. IEEE, may 2017.

[187] M. Peterhans, S. Anderegg, P. Gaillard, T. Oliveira-Santos, and S. Weber. A fully automatic calibration framework for navigated ultrasound imaging. In *2010 Annual International Conference of the IEEE Engineering in Medicine and Biology*. IEEE, aug 2010.

[188] M. P. Pfeiffer and R. W. Biederman. Cardiac MRI. *Medical Clinics of North America*, 99(4):849–861, jul 2015.

[189] A. J. Pigula, J. S. Wu, M. W. Gilbertson, B. T. Darras, S. B. Rutkove, and B. W. Anthony. Force-controlled ultrasound to measure passive mechanical properties of muscle in duchenne muscular dystrophy. In *2016 38th Annual International Conference of the IEEE Engineering in Medicine and Biology Society (EMBC)*. IEEE, aug 2016.

[190] C. Pons, B. Borotikar, M. Garetier, V. Burdin, D. B. Salem, M. Lempereur, and S. Brochard. Quantifying skeletal muscle volume and shape in humans using MRI: A systematic review of validity and reliability. *PLOS ONE*, 13(11):e0207847, nov 2018.

[191] S. Portnoy, G. Yarnitzky, Z. Yizhar, A. Kristal, U. Oppenheim, I. Siev-Ner, and A. Gefen. Real-time patient-specific finite element analysis of internal stresses in the soft tissues of a residual limb: A new tool for prosthetic fitting. *Annals of Biomedical Engineering*, 35(1):120–135, oct 2006.

[192] R. W. Prager, A. Gee, and L. Berman. Stradx: real-time acquisition and visualization of freehand three-dimensional ultrasound. *Medical Image Analysis*, 3(2):129–

140, jun 1999.

[193] R. W. Prager, U. Z. Ijaz, A. H. Gee, and G. M. Treece. Three-dimensional ultrasound imaging. *Proceedings of the Institution of Mechanical Engineers, Part H: Journal of Engineering in Medicine*, 224(2):193–223, feb 2010.

[194] R. W. Prager, R. N. Rohling, A. H. Gee, and L. Berman. Rapid calibration for 3-d freehand ultrasound. *Ultrasound in Medicine & Biology*, 24(6):855–869, jul 1998.

[195] K. R. Prakasa, D. Dalal, J. Wang, C. Bomma, H. Tandri, J. Dong, C. James, C. Tichnell, S. D. Russell, P. Spevak, M. Corretti, D. A. Bluemke, H. Calkins, and T. P. Abraham. Feasibility and variability of three dimensional echocardiography in arrhythmogenic right ventricular dysplasia/cardiomyopathy. *The American Journal of Cardiology*, 97(5):703–709, mar 2006.

[196] R. Prevost, M. Salehi, S. Jagoda, N. Kumar, J. Sprung, A. Ladikos, R. Bauer, O. Zettinig, and W. Wein. 3d freehand ultrasound without external tracking using deep learning. *Medical Image Analysis*, 48:187–202, aug 2018.

[197] R. Prevost, M. Salehi, J. Sprung, A. Ladikos, R. Bauer, and W. Wein. Deep learning for sensorless 3d freehand ultrasound imaging. In *Lecture Notes in Computer Science*, pages 628–636. Springer International Publishing, 2017.

[198] A. Priester, S. Natarajan, and M. Culjat. Robotic ultrasound systems in medicine. *IEEE Transactions on Ultrasonics, Ferroelectrics and Frequency Control*, 60(3):507–523, mar 2013.

[199] K. E. Purnama, M. H. F. Wilkinson, A. G. Veldhuizen, P. M. A. van Ooijen, J. Lubbers, J. G. Burgerhof, T. A. Sardjono, and G. J. Verkerke. A framework for human spine imaging using a freehand 3d ultrasound system. *Technology and Health Care*, 18(1):1–17, feb 2010.

[200] B. J. Raiteri, A. G. Cresswell, and G. A. Lichtwark. Three-dimensional geometrical changes of the human tibialis anterior muscle and its central aponeurosis measured with three-dimensional ultrasound during isometric contractions. *PeerJ*, 4:e2260, jul 2016.

[201] B. J. Raiteri, A. G. Cresswell, and G. A. Lichtwark. Muscle-tendon length and force affect human tibialis anterior central aponeurosis stiffness in vivo. *Proceedings of the National Academy of Sciences*, 115(14), mar 2018.

[202] E. Ramasamy, O. Avci, B. Dorow, S.-Y. Chong, L. Gizzi, G. Steidle, F. Schick, and O. Röhrle. An efficient modelling-simulation-analysis workflow to investigate stump-socket interaction using patient-specific, three-dimensional, continuum-mechanical, finite element residual limb models. *Frontiers in Bioengineering and Biotechnology*, 6, sep 2018.

[203] J. W. Ramsay, M. A. Wessel, T. S. Buchanan, and J. S. Higginson. Poststroke muscle architectural parameters of the tibialis anterior and the potential implications for rehabilitation of foot drop. *Stroke Research and Treatment*, 2014:1–5, 2014.

[204] M. Rana, G. Hamarneh, and J. M. Wakeling. Automated tracking of muscle fascicle orientation in b-mode ultrasound images. *Journal of Biomechanics*, 42(13):2068–2073, sep 2009.

[205] M. Rana, G. Hamarneh, and J. M. Wakeling. 3d fascicle orientations in triceps surae. *Journal of Applied Physiology*, 115(1):116–125, jul 2013.

[206] M. Rana, G. Hamarneh, and J. M. Wakeling. 3d curvature of muscle fascicles in triceps surae. *Journal of Applied Physiology*, 117(11):1388–1397, dec 2014.

[207] M. Rana and J. M. Wakeling. In-vivo determination of 3d muscle architecture of human muscle using free hand ultrasound. *Journal of Biomechanics*, 44(11):2129–2135, jul 2011.

[208] B. J. Ranger, M. Feigin, H. M. Herr, and B. W. Anthony. Image registration in a tomographic ultrasound system: Comparison between camera-tracking and image-based motion compensation. In *2017 IEEE International Ultrasonics Symposium (IUS)*. IEEE, sep 2017.

[209] B. J. Ranger, M. Feigin, X. Zhang, K. M. Moerman, H. Herr, and B. W. Anthony. 3d ultrasound imaging of residual limbs with camera-based motion compensation. *IEEE Transactions on Neural Systems and Rehabilitation Engineering*, 27(2):207–217, feb 2019.

[210] N. D. Reeves and M. V. Narici. Behavior of human muscle fascicles during shortening and lengthening contractions in vivo. *Journal of Applied Physiology*, 95(3):1090–1096, sep 2003.

[211] S. L. Reid, C. A. Pitcher, S. A. Williams, M. K. Licari, J. P. Valentine, P. J. Shipman, and C. M. Elliott. Does muscle size matter? the relationship between muscle size and strength in children with cerebral palsy. *Disability and Rehabilitation*, 37(7):579–584, jul 2014.

[212] R. Rohling, A. Gee, and L. Berman. A comparison of freehand three-dimensional ultrasound reconstruction techniques. *Medical Image Analysis*, 3(4):339–359, dec 1999.

[213] D. S. Ryan, N. Stutzig, A. Helmer, T. Siebert, and J. M. Wakeling. The effect of multidirectional loading on contractions of the m. medial gastrocnemius. *Frontiers in Physiology*, 11, jan 2021.

[214] D. S. Ryan, N. Stutzig, T. Siebert, and J. M. Wakeling. Passive and dynamic muscle architecture during transverse loading for gastrocnemius medialis in man. *Journal of Biomechanics*, 86:160–166, mar 2019.

[215] O. Röhrle, J. B. Davidson, and A. J. Pullan. Bridging scales: A three-dimensional electromechanical finite element model of skeletal muscle. *SIAM Journal on Scientific Computing*, 30(6):2882–2904, jan 2008.

[216] A. S. Sahrmann, L. Gizzi, A. Zanker, G. G. Handsfield, and O. Röhrle. Dynamic 3d ultrasound imaging of the tibialis anterior muscle. In *2022 44th Annual International Conference of the IEEE Engineering in Medicine& Biology Society (EMBC)*. IEEE, jul 2022.

[217] A. S. Sahrmann, G. G. Handsfield, L. Gizzi, J. Gerlach, A. Verl, T. F. Besier, and O. Röhrle. A system for reproducible 3d ultrasound measurements of skeletal muscles. *IEEE Transactions on Biomedical Engineering*, pages 1–12, 2024.

[218] A. S. Sahrmann, N. S. Stott, T. F. Besier, J. W. Fernandez, and G. G. Hands-

field. Soleus muscle weakness in cerebral palsy: Muscle architecture revealed with diffusion tensor imaging. *PLOS ONE*, 14(2):e0205944, feb 2019.

[219] A. S. Sahrmann, L. Vosse, T. Siebert, G. G. Handsfield, and O. Röhrle. 3d ultrasound-based determination of skeletal muscle fascicle orientations. *Biomechanics and Modeling in Mechanobiology*, Mar. 2024.

[220] A. S. Sahrmann, L. Vosse, T. Siebert, G. G. Handsfield, and O. Röhrle. Determination of muscle shape deformations of the tibialis anterior during dynamic contractions using 3d ultrasound. *Frontiers in Bioengineering and Biotechnology*, 2024.

[221] S. E. Salcudean, G. Bell, S. Bachmann, W. H. Zhu, P. Abolmaesumi, and P. D. Lawrence. Robot-assisted diagnostic ultrasound – design and feasibility experiments. In *Medical Image Computing and Computer-Assisted Intervention – MICCAI'99*, pages 1062–1071. Springer Berlin Heidelberg, 1999.

[222] J. M. Sanches and J. S. Marques. A rayleigh reconstruction/interpolation algorithm for 3d ultrasound. *Pattern Recognition Letters*, 21(10):917–926, sep 2000.

[223] A. Scharf, F. Geka, A. Steinborn, H. Frey, A. Schlemmer, and C. Sohn. 3d real-time imaging of the fetal heart. *Fetal Diagnosis and Therapy*, 15(5):267–274, 2000.

[224] P. Schenk, T. Siebert, P. Hiepe, D. Güllmar, J. R. Reichenbach, C. Wick, R. Blickhan, and M. Böl. Determination of three-dimensional muscle architectures: validation of the DTI-based fiber tractography method by manual digitization. *Journal of Anatomy*, 223(1):61–68, may 2013.

[225] T. Schimmoeller, R. Colbrunn, T. Nagle, M. Lobosky, E. E. Neumann, T. M. Owings, B. Landis, J. E. Jelovsek, and A. Erdemir. Instrumentation of off-the-shelf ultrasound system for measurement of probe forces during freehand imaging. *Journal of Biomechanics*, 83:117–124, jan 2019.

[226] S.-H. Schless, B. Hanssen, F. Cenni, L. Bar-On, E. Aertbeliën, G. Molenaers, and K. Desloovere. Estimating medial gastrocnemius muscle volume in children with spastic cerebral palsy: a cross-sectional investigation. *Developmental Medicine & Child Neurology*, 60(1):81–87, oct 2017.

[227] W. Schroeder, K. Martin, and B. Lorensen. *The Visualization Toolkit*. Kitware, 4 edition, 2006.

[228] R. Seydewitz, T. Siebert, and M. Böl. On a three-dimensional constitutive model for history effects in skeletal muscles. *Biomechanics and Modeling in Mechanobiology*, 18(6):1665–1681, may 2019.

[229] O. R. Seynnes and N. J. Cronin. Simple muscle architecture analysis (SMA): An ImageJ macro tool to automate measurements in b-mode ultrasound scans. *PLOS ONE*, 15(2):e0229034, feb 2020.

[230] J. Shen, N. Zemiti, J.-L. Dillenseger, and P. Poignet. Fast and simple automatic 3d ultrasound probe calibration based on 3d printed phantom and an untracked marker. In *2018 40th Annual International Conference of the IEEE Engineering in Medicine and Biology Society (EMBC)*. IEEE, jul 2018.

[231] S. Sherebrin, A. Fenster, R. N. Rankin, and D. Spence. Freehand three-dimensional ultrasound: implementation and applications. In R. L. V. Metter and J. Beutel,

editors, *Medical Imaging 1996: Physics of Medical Imaging*. SPIE, apr 1996.

[232] V. B. Shim, J. W. Fernandez, P. B. Gamage, C. Regnery, D. W. Smith, B. S. Gardiner, D. G. Lloyd, and T. F. Besier. Subject-specific finite element analysis to characterize the influence of geometry and material properties in achilles tendon rupture. *Journal of Biomechanics*, 47(15):3598–3604, nov 2014.

[233] A. P. Shortland, C. A. Harris, M. Gough, and R. O. Robinson. Architecture of the medial gastrocnemius in children with spastic diplegia. *Developmental Medicine and Child Neurology*, 43(12):796, dec 2001.

[234] C. V. Siang and F. Mohamed. A comparison of hole-filling methods for 3d medical data reconstruction and visualization. *International Journal of Innovative Computing*, 9(2), nov 2019.

[235] T. Siebert, M. Günther, and R. Blickhan. A 3d-geometric model for the deformation of a transversally loaded muscle. *Journal of Theoretical Biology*, 298:116–121, apr 2012.

[236] T. Siebert, A. Tomalka, N. Stutzig, K. Leichsenring, and M. Böl. Changes in three-dimensional muscle structure of rabbit gastrocnemius, flexor digitorum longus, and tibialis anterior during growth. *Journal of the Mechanical Behavior of Biomedical Materials*, 74:507–519, oct 2017.

[237] N. Smith-Guerin, L. A. Bassit, G. Poisson, C. Delgorge, P. Arbeille, and P. Vieyres. Clinical validation of a mobile patient-expert tele-echography system using ISDN lines. In *4th International IEEE EMBS Special Topic Conference on Information Technology Applications in Biomedicine, 2003.* IEEE, 2003.

[238] O. V. Solberg, F. Lindseth, H. Torp, R. E. Blake, and T. A. N. Hernes. Freehand 3d ultrasound reconstruction algorithms—a review. *Ultrasound in Medicine & Biology*, 33(7):991–1009, jul 2007.

[239] R. S. Sopher, A. A. Amis, D. C. Davies, and J. R. Jeffers. The influence of muscle pennation angle and cross-sectional area on contact forces in the ankle joint. *The Journal of Strain Analysis for Engineering Design*, 52(1):12–23, sep 2016.

[240] D. Stanigloudi. Design eines phantoms für 3d ultraschallberechnungen von skelettmuskeln. Student research thesis, University of Stuttgart, Feb. 2022.

[241] H. Stark, R. Fröber, and N. Schilling. Intramuscular architecture of the autochthonous back muscles in humans. *Journal of Anatomy*, 222(2):214–222, nov 2012.

[242] E. M. Strasser, T. Draskovits, M. Praschak, M. Quittan, and A. Graf. Association between ultrasound measurements of muscle thickness, pennation angle, echogenicity and skeletal muscle strength in the elderly. *AGE*, 35(6):2377–2388, mar 2013.

[243] N. Stutzig, D. Ryan, J. M. Wakeling, and T. Siebert. Impact of transversal calf muscle loading on plantarflexion. *Journal of Biomechanics*, 85:37–42, mar 2019.

[244] S. Sun, M. Gilbertson, and B. W. Anthony. Probe localization for freehand 3d ultrasound by tracking skin features. In *Medical Image Computing and Computer-Assisted Intervention – MICCAI 2014*, pages 365–372. Springer International Publishing, 2014.

[245] S.-Y. Sun, M. Gilbertson, and B. W. Anthony. 6-DOF probe tracking via skin mapping for freehand 3d ultrasound. In *2013 IEEE 10th International Symposium on Biomedical Imaging*. IEEE, apr 2013.

[246] J. Suthakorn, N. Tanaiutchawoot, and C. Wiratkapan. Ultrasound calibration with ladder phantom at multiple depths for breast biopsy navigation system. *Theoretical and Applied Mechanics Letters*, 10(5):343–353, jul 2020.

[247] M. S. Taljanovic, L. H. Gimber, G. W. Becker, L. D. Latt, A. S. Klauser, D. M. Melville, L. Gao, and R. S. Witte. Shear-wave elastography: Basic physics and musculoskeletal applications. *RadioGraphics*, 37(3):855–870, may 2017.

[248] M. Tanter and M. Fink. Ultrafast imaging in biomedical ultrasound. *IEEE Transactions on Ultrasonics, Ferroelectrics, and Frequency Control*, 61(1):102–119, jan 2014.

[249] J. Thomare, L. Lacourpaille, P. J. McNair, M. Crouzier, R. Ellis, and A. Nordez. A gel pad designed to measure muscle volume using freehand 3-dimensional ultrasonography. *Journal of Ultrasound in Medicine*, 40(6):1245–1250, sep 2020.

[250] C. Tous, A. Jodoin, B. Pontré, D. Grabs, M. Begon, N. J. Bureau, and E. V. Houten. Characterizing the myoarchitecture of the supraspinatus and infraspinatus muscles with mri using diffusion tensor imaging. *Journal of Magnetic Resonance Imaging*, jun 2023.

[251] G. Treece, R. Prager, and A. Gee. Regularised marching tetrahedra: improved iso-surface extraction. *Computers & Graphics*, 23(4):583–598, aug 1999.

[252] G. Treece, R. Prager, A. Gee, and L. Berman. Surface interpolation from sparse cross sections using region correspondence. *IEEE Transactions on Medical Imaging*, 19(11):1106–1114, 2000.

[253] G. M. Treece, A. H. Gee, R. W. Prager, C. J. Cash, and L. H. Berman. High-definition freehand 3-d ultrasound. *Ultrasound in Medicine & Biology*, 29(4):529–546, apr 2003.

[254] G. M. Treece, R. W. Prager, A. H. Gee, and L. Berman. Fast surface and volume estimation from non-parallel cross-sections, for freehand three-dimensional ultrasound. *Medical Image Analysis*, 3(2):141–173, jun 1999.

[255] J. Triboulet, E. Nasr, P. Poignet, E. Dombre, and M. Dauzat. Evaluation of the influence of probe pressure on the b-mode ultrasound measurement of arterial diameter. In *2006 International Conference of the IEEE Engineering in Medicine and Biology Society*. IEEE, aug 2006.

[256] J. W. Trobaugh, W. D. Richard, K. R. Smith, and R. D. Bucholz. Frameless stereotactic ultrasonography: Method and applications. *Computerized Medical Imaging and Graphics*, 18(4):235–246, jul 1994.

[257] J. W. Trobaugh, D. J. Trobaugh, and W. D. Richard. Three-dimensional imaging with stereotactic ultrasonography. *Computerized Medical Imaging and Graphics*, 18(5):315–323, sep 1994.

[258] R. Tsumura, J. W. Hardin, K. Bimbraw, A. V. Grossestreuer, O. S. Odusanya, Y. Zheng, J. C. Hill, B. Hoffmann, W. Soboyejo, and H. K. Zhang. Tele-operative

low-cost robotic lung ultrasound scanning platform for triage of covid-19 patients. *IEEE Robotics and Automation Letters*, 6(3):4664–4671, July 2021.

[259] R. Tsumura and H. Iwata. Robotic fetal ultrasonography platform with a passive scan mechanism. *International Journal of Computer Assisted Radiology and Surgery*, 15(8):1323–1333, Feb. 2020.

[260] T. J. van der Zee and A. D. Kuo. TimTrack: A drift-free algorithm for estimating geometric muscle features from ultrasound images. *PLOS ONE*, 17(3):e0265752, mar 2022.

[261] T. Vaughan, A. Lasso, T. Ungi, and G. Fichtinger. Hole filling with oriented sticks in ultrasound volume reconstruction. *Journal of Medical Imaging*, 2(3):034002, aug 2015.

[262] M. Victorova, D. Navarro-Alarcon, and Y.-P. Zheng. 3d ultrasound imaging of scoliosis with force-sensitive robotic scanning. In *2019 Third IEEE International Conference on Robotic Computing (IRC)*. IEEE, feb 2019.

[263] O. T. von Ramm and S. W. Smith. Real time volumetric ultrasound imaging system. *Journal of Digital Imaging*, 3(4):261–266, nov 1990.

[264] J. M. Wakeling, M. Jackman, and A. I. Namburete. The effect of external compression on the mechanics of muscle contraction. *Journal of Applied Biomechanics*, 29(3):360–364, jun 2013.

[265] Z. Wang, A. Destro, S. Petersson, F. Cenni, and R. Wang. In vivo 3d muscle architecture quantification based on 3d freehand ultrasound and magnetic resonance imaging. *Journal of Biomechanics*, 152:111567, may 2023.

[266] S. R. Ward, C. M. Eng, L. H. Smallwood, and R. L. Lieber. Are current measurements of lower extremity muscle architecture accurate? *Clinical Orthopaedics and Related Research*, 467(4):1074–1082, oct 2008.

[267] G. Weide, S. van der Zwaard, P. A. Huijing, R. T. Jaspers, and J. Harlaar. 3d ultrasound imaging: Fast and cost-effective morphometry of musculoskeletal tissue. *Journal of Visualized Experiments*, (129), nov 2017.

[268] W. Wein and A. Khamene. Image-based method for in-vivo freehand ultrasound calibration. In S. A. McAleavey and J. D'hooge, editors, *SPIE Proceedings*. SPIE, mar 2008.

[269] T. Wen, F. Yang, J. Gu, and L. Wang. A novel bayesian-based nonlocal reconstruction method for freehand 3d ultrasound imaging. *Neurocomputing*, 168:104–118, nov 2015.

[270] T. Wen, Q. Zhu, W. Qin, L. Li, F. Yang, Y. Xie, and J. Gu. An accurate and effective FMM-based approach for freehand 3d ultrasound reconstruction. *Biomedical Signal Processing and Control*, 8(6):645–656, nov 2013.

[271] T. L. Wickiewicz, R. R. Roy, P. L. Powell, and V. R. Edgerton. Muscle architecture of the human lower limb. *Clinical Orthopaedics and Related Research*, 179:275–283, 1983.

[272] A. Wing and P. Beek. Motion analysis: A joint centenary. *Human Movement*

Science, 23(5):iii–iv, nov 2004.

[273] I. Wolf, M. Vetter, I. Wegner, M. Nolden, T. Bottger, M. Hastenteufel, M. Schobinger, T. Kunert, and H.-P. Meinzer. The medical imaging interaction toolkit (MITK): a toolkit facilitating the creation of interactive software by extending VTK and ITK. In R. L. G. Jr., editor, *Medical Imaging 2004: Visualization, Image-Guided Procedures, and Display*, volume 5367, pages 16 – 27. International Society for Optics and Photonics, SPIE, 2004.

[274] M.-X. Xie, X.-F. Wang, T. O. Cheng, Q. Lu, L. Yuan, and X. Liu. Real-time 3-dimensional echocardiography: A review of the development of the technology and its clinical application. *Progress in Cardiovascular Diseases*, 48(3):209–225, nov 2005.

[275] W. Zeng, D. R. Hume, Y. Lu, C. K. Fitzpatrick, C. Babcock, C. A. Myers, P. J. Rullkoetter, and K. B. Shelburne. Modeling of active skeletal muscles: a 3d continuum approach incorporating multiple muscle interactions. *Frontiers in Bioengineering and Biotechnology*, 11, May 2023.

[276] S. Zhang, Z. Zhang, S. C. Chan, H. Wen, and X. Chen. An automatic muscle fiber orientation tracking algorithm using bayesian kalman filter for ultrasound images. In *2015 IEEE International Conference on Image Processing (ICIP)*. IEEE, sep 2015.

[277] X. Zhang, J. Fincke, A. Kuzmin, V. Lempitsky, and B. Anthony. A single element 3d ultrasound tomography system. In *2015 37th Annual International Conference of the IEEE Engineering in Medicine and Biology Society (EMBC)*. IEEE, aug 2015.

[278] W. Zheng, S. Liu, Q.-W. Chai, J.-S. Pan, and S.-C. Chu. Automatic measurement of pennation angle from ultrasound images using resnets. *Ultrasonic Imaging*, 43(2):74–87, feb 2021.

[279] Y. Zhou and Y.-P. Zheng. Enhancement of muscle fibers in ultrasound images using gabor filters. In *2009 IEEE International Ultrasonics Symposium*. IEEE, sep 2009.

[280] N. Zielinska, R. S. Tubbs, F. Paulsen, B. Szewczyk, M. Podgorski, A. Borowski, and L. Olewnik. Anatomical variations of the tibialis anterior tendon insertion: An updated and comprehensive review. *Journal of Clinical Medicine*, 10(16):3684, aug 2021.